

CHARACTERIZATION OF WATER TRANSPORT AND  
LIQUID ACCUMULATION IN PROTON EXCHANGE  
MEMBRANE FUEL CELLS

by

**Fei Wei**

A thesis submitted in partial fulfillment of the requirements for the degree of

**Doctor of Philosophy**

Department of Mechanical Engineering

**University of Alberta**

© Fei Wei, 2023

# Abstract

Hydrogen proton exchange membrane fuel cell (PEMFC) vehicles present a viable solution for decarbonizing the heavy-duty and long-distance transportation sector. They convert the chemical energy of hydrogen directly into electricity, with the only by-products being heat and water and, therefore, they are completely environmental-friendly. However, challenges related to hydrogen infrastructure and PEMFC cost and durability hinder their wider market-adoption. Enhancing the power density of PEMFCs can reduce their size and subsequent costs; however, high current density operation is limited by the cell's ability to efficiently evacuate the water produced from the oxygen reduction reaction (ORR) in the cathode catalyst layer. Efficient removal of fast ORR product water at high currents, from the anode and cathode compartments of the cell, is imperative to prevent the reactant starvation arising from electrode flooding. Water accumulation has also been identified as a factor affecting catalyst degradation and as a result, the durability of PEMFCs. Therefore, a comprehensive understanding of water transport and liquid water accumulation during PEMFCs operation becomes paramount in improving their performance and durability and ultimately reducing their cost.

A water balance setup, enabling real-time quantification of water transport and accumulation inside operating PEMFCs, is developed and validated in this work (see Chapter 2). The setup integrates sensors for measuring relative humidity, temperature, and absolute pressure of the gas-vapor mixture, and dry reactant flow rate. Moreover, a fast and reliable approach is proposed for distinguishing between the water accumulated in the membrane and liquid water within the porous media. This

method holds promise for real-time control strategies aimed at mitigating membrane dehydration and electrode flooding concerns.

The established water balance setup was used to investigate several aspects of interest in the literature: (a) water transport in polymer electrolyte membranes (see Chapter 3); (b) the influence of operating conditions and the addition of a micro-porous layer to cathode gas diffusion layer on cell performance and water transport and accumulation (see Chapter 4); and (c) the influence of the cathode catalyst layer Nafion and platinum loadings on cell performance, water crossover between the electrodes and water accumulation in the membrane-electrode-assembly (see Chapter 5).

Analysis of water transport in proton-exchange (Nafion<sup>®</sup> N211, N212, N115 and N117) and anion-exchange (Aemion<sup>®</sup> AH1-HNN8-50-X, Fumapem<sup>®</sup> FAA-3-30/50, and Versogen<sup>™</sup> PiperION-A40) membranes confirmed that interfacial transport is the key limiting. Using the experimental setup in combination with a numerical model, water desorption rate and its activation energy were estimated. The water desorption rate of AH1-HNN8-50-X aligns closely with Nafion<sup>®</sup> N115 and N117, and the activation energy for this process is similar. In contrast, FAA-3-30/50 and PiperION-A40 exhibit two to three times faster desorption and a lower activation energy.

The study of operating conditions and micro-porous layer (MPL) addition showed that changing operating conditions has a dramatic effect on the water transport across the membrane, while the ratio of water transported to produced water remained relatively constant with current density. Under very dry conditions, water moved from anode to cathode while increasing humidity and decreasing temperature enhanced the cathode-to-anode water crossover. Adding an MPL to the cathode gas diffusion layer increased the cathode-to-anode water crossover at all operating conditions, but the increase was not as pronounced as with changing operating conditions, resulting in only a significant performance increase at 60 °C and 70% RH likely due to increased water vaporization and improved in-plane oxygen pathways.

Lastly, this work demonstrates that increasing the cathode Nafion loading reduces cathode-to-anode water crossover at all conditions, i.e., helps the cathode retain water. Cells with 20 wt.% Nafion loading were able to operate at the highest current density retaining less water inside the electrode. Varying the platinum loading had a negligible influence on water transport between the electrodes at all conditions. This contradicts the common hypothesis that thin CL will flood more quickly.

In summary, this thesis contributed a novel experimental setup and analysis strategy to be able to estimate the real-time water crossover and accumulation in an operating PEMFC. Using the setup, this thesis offers a comprehensive exploration of how modifications to PEMFC components impact the dynamics of water crossover and liquid water accumulation within the operating PEMFCs. The developed water balance setup stands as a reliable tool for real-time measurement of water fluxes and liquid water accumulations, providing insights into water management within operating PEMFCs. These insights can contribute to enhance PEMFCs performance and thus to reduce their cost.

**Keywords:** proton exchange membrane fuel cell, membrane, micro-porous layer, catalyst layer, water management, water crossover, liquid water accumulation.

# Preface

Parts of Chapters 1, 2, 3 and 6 have been published as F. Wei, A. Kosakian, J. Liu, J. Kracher, R. Khan, and M. Secanell, “Water transport in anion and proton exchange membranes,” *Journal of Power Sources*, vol. 557, p. 232 494, 2023. DOI: <https://doi.org/10.1016/j.jpowsour.2022.232494>. A. Kosakian and I contributed equally to that publication. I was responsible for conceptualization; experimental methodology and validation; formal analysis; investigation; experimental data collection; visualization; original draft; and manuscript review and editing. A. Kosakian was responsible for conceptualization; numerical methodology, software implementation and validation; formal analysis; investigation; visualization; original draft; and manuscript review and editing. J. Liu, J. Kracker and R. Khan were responsible for conceptualization, methodology and software implementation, respectively. M. Secanell was the supervising author and was responsible for conceptualization and methodology; and provided help with formal analysis, software implementation, and manuscript writing, review, and editing.

Parts of Chapters 1, 2, 4 and 6 have been published as F. Wei, A. Kosakian, and M. Secanell, “Effect of operating conditions and micro-porous layer on the water transport and accumulation in proton exchange membrane fuel cells,” *Chemical Engineering Journal*, p. 144 423, 2023. DOI: <https://doi.org/10.1016/j.cej.2023.144423>. I was responsible for conceptualization; methodology; validation; formal analysis; investigation; data curation; visualization; original draft; and manuscript review and editing. A. Kosakian was responsible for formal analysis and manuscript review and editing. M. Secanell was the supervising author and was responsible for conceptual-

ization and methodology and provided help with formal analysis, investigation, and manuscript review and editing.

Parts of Chapters 1, 2, 5 and 6 are being prepared for an upcoming publication F. Wei, A. Kosakian, J. Liu, and M. Secanell, “Effect of Cathode Catalyst Layer Nafion and Platinum Loading on the Dynamic Transport and Accumulation of Water Inside an Operating PEMFC,” (under review). I was responsible for conceptualization, methodology; validation; formal analysis; investigation; data curation; visualization; original draft; and manuscript review and editing. A. Kosakian was responsible for investigation and manuscript review and editing. J.F. Liu was responsible for investigation, and manuscript review and editing. M. Secanell was the supervising author and was responsible for conceptualization and methodology and provided help with investigation and manuscript review and editing.

I have also co-authored the following publications, but no material from those publications has been intentionally copied in this thesis:

1. S. Shukla, F. Wei, M. Mandal, J. Zhou, M. S. Saha, J. Stumper, and M. Secanell, “Determination of PEFC Gas Diffusion Layer and Catalyst Layer Porosity Utilizing Archimedes Principle,” *Journal of The Electrochemical Society*, vol. 166, no. 15, F1142, 2019. DOI: 10.1149/2.0251915jes. S. Shukla and I contributed equally to this publication and I was responsible for conceptualization; literature review; conducting buoyancy and mercury intrusion porosimetry experiments; data analysis; and manuscript writing and review.
2. S. Jung, M. Sabharwal, A. Jarauta, F. Wei, M. Gingras, J. Gostick, and M. Secanell, “Estimation of relative transport properties in porous transport layers using pore-scale and pore-network simulations,” *Journal of The Electrochemical Society*, vol. 168, no. 6, p. 064501, 2021. In this publication, I was responsible for manuscript review and experimental work for determination of the pore size distribution via mercury intrusion porosimetry test, effective diffusivity and permeability measurements.

3. Y Kim, T Asset, F Wei, P Atanassov, M Secanell, J Barralet, and J. Gostick, “Fabrication of platinum group metal-free catalyst layer with enhanced mass transport characteristics via an electrospraying technique,” *Materials Today Energy*, vol. 20, p. 100 641, 2021. In this publication, I was responsible for manuscript review and pore size distribution measurements.
4. An upcoming publication A. Kosakian, F. Wei, S. Jung, J. Zhou, A. Punia, J. Liu, and M. Secanell, “Impact of liquid-water accumulation and drainage cycles on fuel-cell performance and stability,” (under review, second revision). In this upcoming publication. I was responsible for conducting experiments; data analysis; and manuscript writing (experimental methodology section) and review.

Fei Wei

November 9, 2023

*To my family*

# Acknowledgments

Studying at the Energy Systems Design Laboratory at the University of Alberta since September 2017 has been an utterly life-changing and immensely rewarding experience. Throughout this transformative journey, I have evolved from a hydrogen proton exchange membrane fuel cell layman to a researcher capable of conducting independent research, writing academic articles, and delivering presentations. While this doctoral thesis represents six years of relentless effort, its realization would not have been possible without the invaluable support and assistance of numerous individuals. Thus, I take this opportunity to express my heartfelt gratitude to all of them.

First and foremost, I extend my deepest thanks to my supervisor, Prof. Marc Secanell, whose guidance and mentorship have made this thesis possible. Relocating to Canada for my doctorate was a big change, but you made me feel welcome and at home throughout these years. Your boundless knowledge and expertise in various scientific and engineering domains amazed me and will continue forever. You have consistently been an inspiration and someone I could look up to and learn from. Your humor and unwavering support will forever be cherished. I distinctly remember our first meeting when I was in China. You believed my English might be good enough for a proper interview but decided to invite Dr. Jie Zhou to help with translation. I was pleasantly surprised when you even joined in the humor, playfully hooking Jie's shoulder during our conversation. Since then, I have had unwavering faith that you would not only be an exceptional research supervisor but also a wonderful friend in my life.

My Ph.D. years at the University of Alberta would not have been nearly as enjoy-

able without my ESDLab mates. Special thanks to Dr. Aslan Kosakian; we had an absolute blast. I fondly remember our collaborations on four papers, our trips to 2022 World Fuel Cell Conference at University of California Irvine, and our adventures in Jasper and Banff National Parks. Your unwavering support and willingness to lend an ear during times of distress meant the world to me. Whether it was engaging in conversations, watching documentary movies, sampling diverse cuisines, or strolling through the North Saskatchewan River valley, you made every moment memorable. I cherish these beautiful memories, and I sincerely hope our paths cross again in the future. I am also deeply grateful to Michael Moore, Luis Padilla Urbina, and Seongyeop Jung for helping me transition to life in Canada. When I first arrived at ESDLab, my English proficiency was limited, and I struggled to understand conversations. Your patient translations and slower, easy-to-understand speech allowed me to adapt smoothly. Your support in helping me improve my English by patiently adjusting your speaking pace was truly invaluable. I would also like to extend my thanks to Jiafei Liu, Jasper Eitzen, Ambuj Punia, Dr. Jie Zhou, Dr. Shantanu Shukla, Dr. Vaishnavi Kale, Dr. Alexandre Jarauta Arabi, Dr. Manas Mandal, Dr. Mayank Sabharwal, and all other past and present ESDLab members for their camaraderie and assistance.

I must acknowledge the financial support I received over the years from CREATE Program in Materials for Electrochemical Energy Solutions (CREATE ME) and the China Scholarship Council (CSC). Without these funding sources, my survival in Canada and pursuit of my research would have been challenging if not impossible.

My heartfelt gratitude also goes to two of my master's classmates, Dazhi Situ and Dr. Yuhong Chen. During times of distress in Canada, you were always willing to lend an empathetic ear and offer valuable suggestions. Additionally, I would like to express my thanks to my co-supervisor during my master's at Shanghai Jiao Tong University, Prof. Zhenyu Liu, who ignited and sustained my interest in research, and motivated me to pursue my Ph.D. degree in Canada.

Lastly, I extend my deepest appreciation to my parents, Genlin Wei and Genxiang Wei, my brother and his family, Guo Wei, Yan Xia, and Xiatian Wei, for their unconditional love and unwavering support. Without you, none of my achievements would have been possible. Thank you for being my rock and standing by me throughout this journey.

Fei Wei

November 9, 2023

# Table of Contents

<b>1</b>	<b>Introduction</b>	<b>1</b>
1.1	Motivation . . . . .	1
1.2	PEMFC background . . . . .	3
1.2.1	Operation principle . . . . .	3
1.2.2	PEMFC configuration . . . . .	4
1.2.2.1	Proton exchange membrane . . . . .	5
1.2.2.2	Gas diffusion layer . . . . .	6
1.2.2.3	Micro-porous layer . . . . .	6
1.2.2.4	Catalyst layer . . . . .	6
1.2.3	Water crossover and liquid water accumulation . . . . .	7
1.2.4	PEMFC performance and characterization . . . . .	9
1.2.4.1	Polarization curve . . . . .	9
1.2.4.2	Ohmic resistance . . . . .	14
1.3	Literature review . . . . .	15
1.3.1	Methods used to measure water transport in fuel cells . . . . .	15
1.3.2	Water transport in polymer electrolyte membrane . . . . .	17
1.3.3	Impact of MPL introduction and operating conditions on water management . . . . .	19
1.3.4	Impact of CL composition and loading on water management	20
1.4	Thesis Objectives . . . . .	22
1.5	Thesis Outline . . . . .	22

<b>2</b>	<b>Methodology</b>	<b>24</b>
2.1	Experimental setup . . . . .	25
2.2	Theory . . . . .	27
2.2.1	Water flux determination . . . . .	27
2.2.2	Water crossover determination . . . . .	28
2.2.3	Determination of accumulation and saturation . . . . .	29
2.2.3.1	Water accumulation in the MEA . . . . .	29
2.2.3.2	Water accumulation in the membrane . . . . .	30
2.2.3.3	Water accumulation and saturation in the PTLs . . . . .	31
2.2.4	Uncertainty analysis . . . . .	33
2.2.5	Bias estimation . . . . .	35
2.3	Validation of experimental setup . . . . .	36
2.3.1	Ex-situ validation . . . . .	36
2.3.2	In-situ validation . . . . .	37
2.4	Electrochemical characterization . . . . .	39
2.4.1	Experimental conditions . . . . .	39
2.4.2	Electrochemical characterization . . . . .	40
2.4.2.1	Cell conditioning . . . . .	40
2.4.2.2	Electrochemical surface area measurement . . . . .	40
2.4.2.3	Polarization curve measurement . . . . .	40
2.4.2.4	Current hold experiment . . . . .	40
2.5	Conclusions . . . . .	41
<b>3</b>	<b>Water Transport in Anion and Proton Exchange Membranes</b>	<b>42</b>
3.1	Materials and experiments . . . . .	43
3.1.1	Sample preparation and cell assembly . . . . .	43
3.1.2	Experimental setup and conditions . . . . .	45
3.2	Mathematical model . . . . .	46

3.2.1	Governing equations . . . . .	48
3.2.1.1	Model 1: Diffusion-dominated transport . . . . .	48
3.2.1.2	Model 2: Desorption-dominated transport . . . . .	50
3.2.1.3	Model 3: Combined diffusion-and-desorption transport . . . . .	51
3.2.2	Water uptake . . . . .	51
3.2.3	Water diffusivity . . . . .	54
3.2.4	Interfacial water transport . . . . .	56
3.2.5	Input parameters . . . . .	56
3.2.6	Fitting methodology . . . . .	56
3.3	Results and discussion . . . . .	58
3.3.1	Nafion <sup>®</sup> proton exchange membranes . . . . .	58
3.3.1.1	Identification of the limiting mode of water transport via experiments and simulations . . . . .	58
3.3.1.2	Rate of water desorption . . . . .	63
3.3.1.3	Activation energy for water desorption . . . . .	65
3.3.1.4	Can liquid-vapor permeation setups be used to mea- sure water diffusivity? . . . . .	65
3.3.2	Anion exchange membranes . . . . .	67
3.3.2.1	Limiting mode of transport . . . . .	67
3.3.2.2	Rate of water desorption . . . . .	70
3.3.2.3	Activation energy for water desorption . . . . .	71
3.4	Conclusions . . . . .	72
<b>4</b>	<b>Effect of Operating Conditions and Micro-porous Layer on the Wa- ter Transport and Accumulation in Proton Exchange Membrane Fuel Cells</b>	<b>74</b>
4.1	Materials and experiments . . . . .	75
4.1.1	Sample preparation and cell assembly . . . . .	75

4.2	Results and Discussion . . . . .	76
4.2.1	Effect of operating conditions . . . . .	76
4.2.1.1	PEMFC performance. . . . .	76
4.2.1.2	Water crossover. . . . .	81
4.2.1.3	Water accumulation. . . . .	85
4.2.2	Effect of cathode MPL . . . . .	86
4.2.2.1	PEMFC performance. . . . .	86
4.2.2.2	Water crossover. . . . .	87
4.2.2.3	Water accumulation. . . . .	89
4.3	Conclusions . . . . .	90
<b>5</b>	<b>Effect of Cathode Catalyst Layer Nafion and Platinum Loading on the Dynamic Transport and Accumulation of Water Inside an Op- erating PEMFC</b>	<b>92</b>
5.1	Materials and experiments . . . . .	93
5.1.1	Sample preparation and cell assembly . . . . .	93
5.1.2	Microstructure characterization . . . . .	95
5.2	Results and Discussion . . . . .	96
5.2.1	Effect of Nafion loading . . . . .	96
5.2.1.1	Thickness, porosity and ECSA . . . . .	96
5.2.1.2	Fuel cell performance . . . . .	98
5.2.1.3	Water crossover . . . . .	100
5.2.1.4	Liquid water accumulation . . . . .	103
5.2.2	Effect of platinum loading . . . . .	109
5.2.2.1	Thickness, porosity and ECSA . . . . .	109
5.2.2.2	Fuel cell performance . . . . .	110
5.2.2.3	Water crossover . . . . .	110
5.2.2.4	Liquid water accumulation . . . . .	110

5.3	Conclusions . . . . .	117
<b>6</b>	<b>Conclusions and Future Work</b>	<b>120</b>
6.1	Conclusions . . . . .	121
6.2	Contributions . . . . .	123
6.3	Future Work . . . . .	124
6.3.1	Membrane property characterization . . . . .	124
6.3.2	Water accumulation validation with imaging data . . . . .	125
6.3.3	Effect of GDL, MPL and CL PSD on water management . . . . .	125
6.3.4	Application to AEMFC . . . . .	125
	<b>Bibliography</b>	<b>127</b>
	<b>Appendix A: Supplementary Information for Chapter 3: Water Trans-</b>	
	<b>port in Anion and Proton Exchange Membranes</b>	<b>152</b>
A.1	Mathematical model . . . . .	152
A.1.1	Water uptake . . . . .	152
A.1.2	Darken factor . . . . .	157
A.2	Results and discussion . . . . .	159
A.2.1	Fitting . . . . .	159

# List of Tables

1.1	Role of MPL in water management of PEMFCs . . . . .	7
2.1	Ex-situ validation of the experimental setup. . . . .	37
3.1	Properties of the membranes used in this work. . . . .	44
3.2	Input parameters of the model: cell geometry and operating conditions.	57
3.3	Fitted scaling factors for diffusion, desorption, and activation energy for Nafion <sup>®</sup> membranes and the corresponding fitting residual and $R^2$ values. . . . .	61
3.4	Fitted scaling factors for diffusion, desorption, and activation energy for AEMs and the corresponding fitting residual and $R^2$ values. The physical properties without scaling ( $\beta_D = \beta_d = \beta_E = 1$ ) are $2.72 \cdot$ $10^{-5}$ cm <sup>2</sup> /s, $4.59 \cdot 10^{-3}$ cm/s, and 20 kJ/mol, respectively. . . . .	69
5.1	Cathode CL under study. . . . .	94
A.1	Coefficients of the water-uptake curve eq. (3.10). . . . .	153
A.2	Coefficients of the inverted water-uptake curve (A.8). . . . .	159
A.3	Coefficients of the Darken factor eq. (3.13). For all membranes, $\delta_0 =$ $\varepsilon_0 = 1$ . . . . .	160

# List of Figures

1.1	A typical cross-sectional schematic of a PEMFC. . . . .	3
1.2	Scanning electron microscopy images of: (a) commercial GDL (SGL 29BA) and (b) inkjet printed CL (30 wt.% Nafion loading). Image courtesy of Dr. Manas Mandal (ESDLab). . . . .	5
1.3	A typical schematic of water transport in a PEMFC. . . . .	8
1.4	Representative PEMFC polarization curve with corresponding voltage losses. . . . .	10
1.5	Representative PEMFC polarization curve (a) without and (b) with significant flooding. . . . .	13
2.1	(a) Experimental setup for the in-situ testing, (b) schematic of the setup, (c) fuel cell flow field and (d) schematic of the water transport. . . . .	26
2.2	Uncertainty analysis for water crossover. . . . .	35
2.3	In-situ validation results obtained from (a) polarization and (b) current hold experiments at 80 °C and 70% RH with 29BC in the cathode. . . . .	38
3.1	Experimental setup for the water transport properties measurements of AEM and PEM materials: a) the experimental setup, b) schematic of the setup and c) schematic of water transport in the cell. . . . .	47
3.2	Comparison of the sorption isotherms for Nafion <sup>®</sup> N11X, Nafion <sup>®</sup> N21X, Aemion <sup>®</sup> AH1-HNN8-50-X (HMT-PMBI), Fumapem <sup>®</sup> FAA-3, and Versogen <sup>™</sup> PiperION-A40 membranes (eq. (3.10) and Table A.1). . . . .	52

3.3	Experimental measurements of water transport through Nafion <sup>®</sup> N115, N117, N211 and N212 at 60, 70 and 80 °C: a), c) and e) water crossover; and b), d) and f) outlet RH. . . . .	59
3.4	Comparison of the water diffusivities fitted for Nafion <sup>®</sup> N117, N211, and N212 with the literature data at a) 50 °C and b) 80 °C. . . . .	62
3.5	Comparison of the water-content drop across Nafion <sup>®</sup> membranes at the dry-channel inlet (solid lines) and outlet (dashed lines) computed with: a) model 1 (diffusion) and b) model 3 (diffusion and desorption). . . . .	63
3.6	Comparison of the fitted water-desorption rates for Nafion <sup>®</sup> N117, N211, N212, Aemion <sup>®</sup> AH1-HNN8-50-X, Fumapem <sup>®</sup> FAA-3-50, and Versogen <sup>™</sup> PiperION-A40 at a) 60 °C and b) 80 °C. . . . .	64
3.7	Experimental measurements of water transport through Aemion <sup>®</sup> AH1-HNN8-50-X, Fumapem <sup>®</sup> FAA-3-30/50, and Versogen <sup>™</sup> PiperION-A40 at 60, 70 and 80 °C: a), c) and e) water crossover; and b), d) and f) outlet RH. . . . .	68
3.8	Comparison of the water-content drop across AEM membranes at the dry-channel inlet (solid lines) and outlet (dashed lines) computed with: a) model 1 (diffusion) and b) model 3 (diffusion and desorption). All data are at 80 °C and 12 or 13% inlet RH in the dry channel. . . . .	70
4.1	Polarization curves (a) without and (b) with MPL and corresponding dimensionless water crossover (c) without and (d) with MPL obtained from galvanodynamic polarization experiments under varying experimental conditions. . . . .	77
4.2	Polarization curves and corresponding current interrupt resistance for cells with (SGL 29BC) and without (SGL 29BA) MPL in the cathode. . . . .	78

4.3	Water crossover obtained from galvanodynamic polarization experiments under varying experimental conditions for cells (a) without and (b) with MPL. . . . .	79
4.4	Real-time (a) voltage, (b) dimensionless water crossover, and (c) cathode PTL water accumulation and (d) saturation obtained from quasi-steady current hold experiments. . . . .	80
4.5	Dimensionless water crossover with comparisons with literature under (a) cold/wet and (b) hot/dry conditions. . . . .	82
4.6	(a) ORR product water flux, (b) outlet RH, (c) the amount of water accumulation and (d) cathode PTL saturation obtained from polarization curve experiments at 60 °C and 70% RH. . . . .	83
4.7	Pore size distribution of SGL 29BA and 29BC measured in-house using mercury intrusion porosimetry. . . . .	88
5.1	Cross-sectional SEM images of the cathode catalyst layers (after all in-situ tests): (a) design 1; (b) design 2; (c) design 3; (d) design 4; (e) design 5; and (f) design 6. . . . .	96
5.2	Cyclic voltammetry results for cells with varying Nafion loadings (a) before and (c) after all tests and platinum loadings (c) before and (d) after all tests. . . . .	97
5.3	Polarization curves and current interrupt resistances for cells with 10, 20, 30 and 40 wt.% Nafion loading obtained at (a) 80 °C and 30% RH, (b) 80 °C and 50% RH, (c) 80 °C and 70% RH and (d) 60 °C and 70% RH. Experimental conditions: 0.5 slpm hydrogen and 0.5 slpm air, 50 kPa(gauge) backpressure, and 5 mA/s scan rate. . . . .	99

5.4	Water transport results for cells with varying Nafion loadings obtained from current hold experiments: (a) real-time cathode-to-anode water crossover at 60 °C and 70% RH, (b) averaged dimensionless cathode-to-anode water crossover during last 5-min, and (c) averaged cathode-to-anode water crossover during last 5-min. . . . .	101
5.5	Real-time cathode-to-anode water crossover for cells with varying Nafion loadings obtained from current-hold experiments at: (a) 80 °C and 30% RH, (b) 80 °C and 50% RH and (c) 80 °C and 70% RH. . . . .	102
5.6	Current hold results at 60 °C and 70% RH for cells with 10, 20, 30 and 40 wt.% Nafion loading: (a) cell voltage, (b) membrane protonic resistance, (c) ORR product water flux, (d) total amount of water accumulation in the MEA, (e) total amount of water accumulation in the membrane, (f) total amount of water accumulation in the porous media, (g) outlet RH, (h) membrane water activity, and (i) cathode PTL saturation. . . . .	104
5.7	Galvanodynamic results at 60 °C and 70% RH for cells with 10, 20, 30 and 40 wt.% Nafion loading: (a) membrane protonic resistance, (b) ORR product water flux, (c) total amount of water accumulation in the MEA, (d) total amount of water accumulation in the membrane, (e) total amount of water accumulation in the porous media, (f) cathode porous media saturation, (g) membrane water activity, and (h) outlet RH. . . . .	105
5.8	Polarization curves and current interrupt resistances for cells with 0.133, 0.219 and 0.317 mg <sub>Pt</sub> /cm <sup>2</sup> <sub>CL</sub> platinum loading obtained at (a) 80 °C and 30% RH, (b) 80 °C and 50% RH, (c) 80 °C and 70% RH and (d) 60 °C and 70% RH. Experimental conditions: 0.5 slpm hydrogen and 0.5 slpm air, 50 kPa(gauge) backpressure, and 5 mA/s scan rate. . . . .	111

5.9	Water transport results for cells with varying platinum loadings obtained from current hold experiments: (a) real-time cathode-to-anode water crossover at 60 °C and 70% RH, (b) averaged dimensionless cathode-to-anode water crossover during last 5-min, and (c) averaged cathode-to-anode water crossover during last 5-min. . . . .	112
5.10	Current hold results at 60 °C and 70% RH for cells with 0.133, 0.219 and 0.317 mg <sub>Pt</sub> /cm <sub>CL</sub> <sup>2</sup> platinum loading: (a) cell voltage, (b) membrane protonic resistance, (c) ORR product water flux, (d) total amount of water accumulation in the MEA, (e) total amount of water accumulation in the membrane, (f) total amount of water accumulation in the porous media, (g) outlet RH, (h) membrane water activity, and (i) cathode PTL saturation. . . . .	113
5.11	Galvanodynamic results at 60 °C and 70% RH for cells with 0.133, 0.219 and 0.317 mg <sub>Pt</sub> /cm <sub>CL</sub> <sup>2</sup> platinum loading: (a) membrane protonic resistance, (b) ORR product water flux, (c) total amount of water accumulation in the MEA, (d) total amount of water accumulation in the membrane, (e) total amount of water accumulation in the porous media, (f) cathode PTL saturation, (g) membrane water activity, and (h) outlet RH. . . . .	114
A.1	Water-uptake curves for the cast Nafion <sup>®</sup> N211 and N212 membranes at 25–80 °C from references [228, 238, 243, 244] and their fit obtained in this work: a) the sorption isotherm (eq. (3.10) and Table A.1) and b) the inverse sorption isotherm (eq. (A.8) and Table A.2). Sorption isotherms for Nafion <sup>®</sup> N117 (eq. (3.10) and Table A.1) and a variety of Nafion membranes (eq. (A.3)) are also shown for comparison. . . .	154

A.2	Water-uptake curves for Aemion <sup>®</sup> AH1-HNN8-50-X (HMT-PMBI) membranes at 30–60 °C from references [245–247] and their fits obtained in this work: a) the sorption isotherm (eq. (3.10) and Table A.1) and b) the inverse sorption isotherm (eq. (A.8) and Table A.2). . . . .	155
A.3	Water-uptake curves for Fumapem <sup>®</sup> FAA3 membranes at 25 and 40 °C from references [231, 247] and their fit obtained in this work: a) the sorption isotherm (eq. (3.10) and Table A.1) and b) the inverse sorption isotherm (eq. (A.8) and Table A.2). . . . .	156
A.4	Water-uptake curves for PiperION <sup>®</sup> PAP-TP-85 from reference [231] and its fit obtained in this work: a) the sorption isotherm (eq. (3.10) and Table A.1) and b) the inverse sorption isotherm (eq. (A.8) and Table A.2). . . . .	156
A.5	Comparison of the Darken factors for Nafion <sup>®</sup> N11X, Nafion <sup>®</sup> N21X, Aemion <sup>®</sup> AH1-HNN8-50-X, Fumapem <sup>®</sup> FAA-3, and Versogen <sup>™</sup> PiperION-A40 membranes (eq. (3.13) and Table A.3). Markers correspond to the maximum water content in vapor-equilibrated membranes at unit water activity found from the sorption isotherms (eq. (3.10) and Table A.1).161	161
A.6	Results of fitting the experimental crossover flux with model 2 (desorption only; see Table 3.3) for Nafion <sup>®</sup> : a) N115; b) N117; c) N211; and d) N212. The shadow is added to guide the eye through the experimental conditions. . . . .	162
A.7	Results of fitting the experimental crossover flux with model 2 (desorption only; see Table 3.4) for: a) Aemion <sup>®</sup> AH1-HNN8-50-X; b) Versogen <sup>™</sup> PiperION-A40; c) Fumapem <sup>®</sup> FAA-3-30; and d) Fumapem <sup>®</sup> FAA-3-50. The shadow is added to guide the eye through the experimental conditions. . . . .	163

A.8	Comparison of the measured and simulated outlet vapor pressure in the dry channel for the fitting results in Table 3.3 and Figure A.6 obtained with model 2 (desorption only) for Nafion <sup>®</sup> : a) N115; b) N117; c) N211; and d) N212. The shadow is added to guide the eye through the experimental conditions. . . . .	164
A.9	Comparison of the measured and simulated outlet vapor pressure in the dry channel for the fitting results in Table 3.4 and Figure A.7 obtained with model 2 (desorption only) for: a) Aemion <sup>®</sup> AH1-HNN8-50-X; b) Versogen <sup>™</sup> PiperION-A40; c) Fumapem <sup>®</sup> FAA-3-30; and d) Fumapem <sup>®</sup> FAA-3-50. The shadow is added to guide the eye through the experimental conditions. . . . .	165
A.10	Residual distributions around the fitted scaling factors in Tables 3.3 and 3.4 for Nafion <sup>®</sup> : a) N115; b) N117; c) N211; and d) N212. . . . .	166
A.11	Residual distributions around the fitted scaling factors in Tables 3.3 and 3.4 for: a) Aemion <sup>®</sup> AH1-HNN8-50-X; b) Versogen <sup>™</sup> PiperION-A40; c) Fumapem <sup>®</sup> FAA-3-30; and d) Fumapem <sup>®</sup> FAA-3-50. . . . .	167
A.12	Comparison of the fitted water-desorption rates for Nafion <sup>®</sup> N117, N211, N212, Aemion <sup>®</sup> AH1-HNN8-50-X, Fumapem <sup>®</sup> FAA-3-50, and Versogen <sup>™</sup> PiperION-A40 at a) 60 °C and b) 80 °C. . . . .	168
A.13	Comparison of the water diffusivities fitted for Nafion <sup>®</sup> N117, N211, and N212 with the literature data at a) 50 °C and b) 80 °C. . . . .	169

# Chapter 1

## Introduction<sup>1</sup>

### 1.1 Motivation

Anthropogenic greenhouse gas (GHG) emissions have become an urgent worldwide issue due to their global warming potential, prompting the establishment of the Paris Agreement in 2015 aimed at reducing them [9]. Countries such as the United States, China, Canada, and Germany, have committed to decarbonizing their energy systems by 2050 or 2060 [10–13]. According to the Intergovernmental Panel on Climate Change, approximately 15% of total anthropogenic GHG emissions came from the transportation sector in 2019 [14]. Proton exchange membrane fuel cell vehicles are a feasible technology to decarbonize the heavy-duty and long-distance transportation sector [15, 16]. Hydrogen PEMFCs electrochemically convert the chemical energy of hydrogen into electricity and heat with water and heat as the by-products. Because of the direct energy conversion, the overall efficiency of PEMFCs is higher than

---

<sup>1</sup>Parts of this chapter are reproduced from the following publications:

1. F. Wei, A. Kosakian, J. Liu, J. Kracher, R. Khan, and M. Secanell, “Water transport in anion and proton exchange membranes,” *Journal of Power Sources*, vol. 557, p. 232 494, 2023. DOI: <https://doi.org/10.1016/j.jpowsour.2022.232494>.
2. F. Wei, A. Kosakian, and M. Secanell, “Effect of operating conditions and micro-porous layer on the water transport and accumulation in proton exchange membrane fuel cells,” *Chemical Engineering Journal*, p. 144 423, 2023. DOI: <https://doi.org/10.1016/j.cej.2023.144423>.
3. F. Wei, A. Kosakian, J. Liu, and M. Secanell, “Effect of Cathode Catalyst Layer Nafion and Platinum Loading on the Dynamic Transport and Accumulation of Water Inside an Operating PEMFC,” (under review).

Author contributions are detailed in the Preface of this thesis.

that of the conventional internal combustion engines [17, 18]. Compared with other fuel cells, e.g., phosphoric acid fuel cell, solid oxide fuel cell and molten carbonate fuel cell, hydrogen PEMFCs operate under relatively low temperatures, i.e., generally 60–80 °C, which allows them to start up and shut down quickly, making them well suited for vehicles [19, 20]. Fast refueling time and longer driving range also allow hydrogen PEMFCs vehicles to compete with the battery-powered counterparts, despite the higher efficiency of the latter [21].

Although hydrogen PEMFCs have already met the U.S. Department of Energy (DOE) targets for specific power (650 W/kg), power density (650 W/L), and cold start-up time (start from  $-20\text{ °C} < 30$  seconds) [22, 23], the cost and durability of fuel-cell systems still need to be addressed to meet the ultimate DOE targets, i.e., a cost of \$30/kW and 8,000-hour durability [23, 24], and thus to increase their market adoption. One of the key factors negatively impacting both the cost and durability of PEMFCs is the accumulation of liquid water within the cells. For example, increasing fuel cell current density at the same cell voltage can reduce its size and, therefore, cost; however, high current density operation is currently limited by the cell’s ability to efficiently evacuate the water produced in the oxygen reduction reaction in the cathode catalyst layer. Excessive liquid water must be removed efficiently to avoid electrode flooding and thus blockage of the reactant transport pathways [19, 25–27]. Moreover, previous studies have demonstrated that water accumulation can have a detrimental effect on catalyst degradation and, consequently, the durability of PEMFCs [28–32].

During the past two decades, efforts have been made to improve water management by modifying PEMFC components [33–37]; however, rarely is the quantified effect of these modifications studied in terms of their importance on real-time water transport and accumulation via experimental approach. The overall objective of this thesis is, therefore, to experimentally quantify the impact of modifications to PEMFC components on the crucial processes of dynamic water transport and liquid

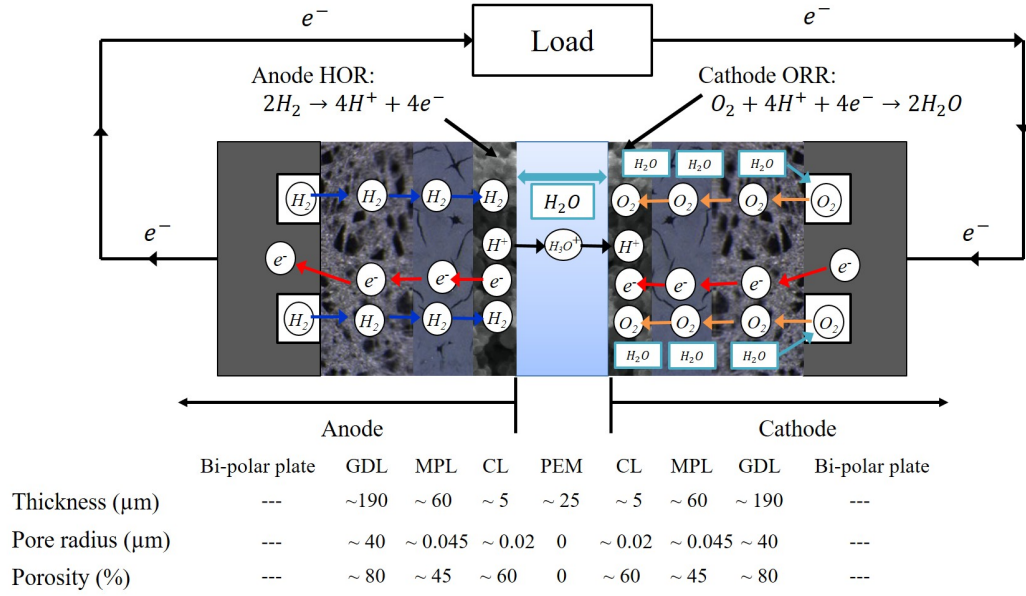


Figure 1.1: A typical cross-sectional schematic of a PEMFC. Entrained water in the reactant gases is neglected.

water accumulation within the cell.

## 1.2 PEMFC background

### 1.2.1 Operation principle

Figure 1.1 shows a schematic of PEMFC components and their corresponding thickness, porosity, and characteristic pore size. As shown in the figure, a typical PEMFC consists of a PEM, two CLs, MPLs, GDLs, and graphite bipolar plates (BPPs). The PEM is used to transport protons and prevent the crossover of the reactant gas and electrons. In order to catalyze the electrochemical reactions, each side of the PEM is coated with a CL, and the complete assembly is termed as catalyst-coated-membrane (CCM). Hydrogen oxidizes at the anode CL, releasing protons ( $\text{H}^+$ ), electrons ( $\text{e}^-$ ) and heat according to the hydrogen oxidation reaction (HOR):

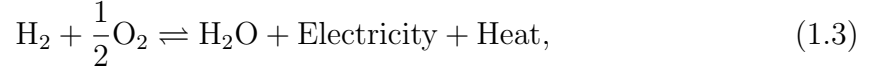


The HOR products protons and electrons are transported to the cathode CL through the PEM and an external circuit, respectively. At the cathode CL, they react with

oxygen, producing water and heat according to the oxygen reduction reaction (ORR):



The overall electrochemical reaction taking place in a PEMFC is



where the produced water can be in the liquid and/or vapor form, depending on the operating condition; electricity is gained by passing the HOR product electrons through the external circuit before they take place in ORR; the overall electrochemical reaction is exothermic, and the majority of the total heat is generated from the ORR [38–41].

### 1.2.2 PEMFC configuration

A gas diffusion layer with a micro-porous layer, termed as porous transport layer (PTL), is commonly introduced to each side of the CCM, which is used to: 1) distribute the reactant gases to the CLs uniformly, 2) collect electrons and heat from the catalyst layer, 3) protect the thin CLs from mechanical deformation, and 4) facilitate water removal [25, 42]. The assembly of the CCM, MPLs, and GDLs, termed as membrane electrode assembly (MEA), is sandwiched between two electron-conductive flow field plates (FFPs), which are electrically connected by an external circuit. The flow fields, engraved or stamped on the surface of the plates, serve to deliver reactants to the CLs and to remove the produced water. Both reactant gases and produced water, in either vapor or liquid form, are transported through the void spaces of the CLs, MPLs, and GDLs. Electrons transport through the carbon in the MPLs and GDLs, and platinum and carbon black support in the CLs. Protons and sorbed water are transported through the PEM and the ionomer presented in the CLs. Due to their multi-functional nature, PEM, CLs, MPLs, and GDLs are made up of multiple materials and have complex micro-structures. A detailed description of the PEM, GDL, MPL, and CL is provided below.

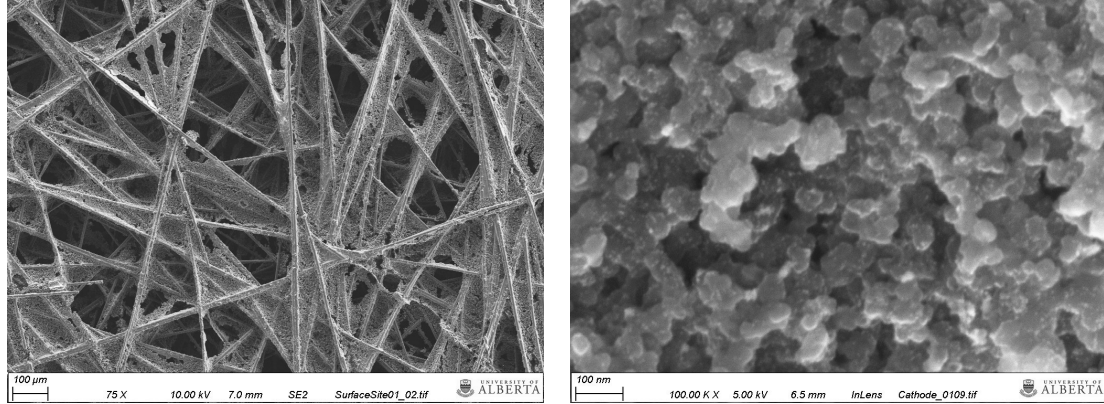


Figure 1.2: Scanning electron microscopy images of: (a) commercial GDL (SGL 29BA) and (b) inkjet printed CL (30 wt.% Nafion loading). Image courtesy of Dr. Manas Mandal (ESDLab).

### 1.2.2.1 Proton exchange membrane

The proton exchange membrane employed in PEMFCs, typically a Nafion<sup>®</sup> membrane, is a proton-conductive polymer membrane composed of an electrically neutral semicrystalline polymer backbone (polytetrafluoroethylene, PTFE) and a randomly tethered side-chain (polysulfonyl fluoride vinyl ether) with a pendant ionic group ( $\text{SO}_3^-$ ) [43, 44]. Kusoglu and Weber [43] conducted a comprehensive review of proton exchange membranes. Membrane thickness is on the order of 1–100  $\mu\text{m}$ , with the state-of-art PEMs being 5–25  $\mu\text{m}$  thick [43, 45]. The pendant ionic group is associated with a proton to form  $\text{SO}_3\text{H}$  [43, 44, 46], to which water is bound via the hydrogen bond ( $\text{SO}_3^- \cdot \text{H}_3\text{O}^+$ ) [43]. Water uptake by the membrane (from the surrounding vapor or liquid water) enables hydrogen-proton dissociation from  $\text{SO}_3\text{H}$  and proton conduction by two mechanisms: the translational motion of hydronium ( $\text{H}_3\text{O}^+$ ) [43] and Grotthuss hopping (exchange of  $\text{H}^+$  in the hydrogen bonds of water molecules) [43, 44, 46]. Protonic conductivity of Nafion<sup>®</sup> membranes increases with water content [43, 44] and, therefore, it is imperative to maintain the membrane hydrated to make it protonic conductive and thus to minimize ohmic losses.

### 1.2.2.2 Gas diffusion layer

There exist two distinct categories of commercially accessible GDL materials [47, 48], i.e., carbon paper (non-woven, see Figure 1.2a) and carbon cloth (woven). Both of them are based on electrically conductive carbon fibers derived from polyacrylonitrile [49]. The electrically conductive nature of the GDLs enables the electron transfer between CLs and BPPs. Owing to their porous structure, GDLs serve as mediators, uniformly conveying reactants to the CLs, thus enhancing catalyst utilization. Moreover, GDLs furnish pathways that facilitate the removal of ORR product water at the cathode CL [50]. In order to prevent the blockage of pores with liquid water, a hydrophobic agent, e.g., polytetrafluoroethylene (PTFE), is usually integrated into the GDLs [49, 51, 52]. Additionally, GDL provides structural support for the CLs, which are highly susceptible to mechanical deformation.

### 1.2.2.3 Micro-porous layer

The MPL is usually introduced between CL and GDL to improve PEMFC performance and water management at high current density, especially under wet conditions [50, 53–56]. For example, Owejan et al. [50] observed a 20% to 30% polarization performance increase under fully humidified conditions after adding an MPL. Generally, the MPL is fabricated by brush painting or spraying a slurry of solvents (e.g., deionized water and IPA), carbon black, and hydrophobic binder (e.g., PTFE) or hydrophilic binder (e.g., ionomer), over the GDL which acts as a substrate [57–60]. Table 1.1 lists the proposed mechanisms by which MPL improves PEMFC performance and water management. As shown in the table, the effect of MPL on water removal from anode or cathode is still under debate.

### 1.2.2.4 Catalyst layer

Catalyst layers (see Figure 1.2b), where the ORR and HOR take place, are the heart of the PEMFC. Besides their imperative role of catalyzing the electrochemical reactions,

Table 1.1: Role of MPL in water management of PEMFCs

MPL effect on water management	References	
	Support	Against
Increased water back diffusion from cathode to anode	[54, 61–63]	[53, 64, 65]
Increased liquid water removal from CL to GDL	[54, 61–64, 66–68]	[50, 55]
Enhanced O <sub>2</sub> transport due to water distribution improvement	[50, 61, 69, 70]	
Forms a liquid water barrier which hinders the condensed water at GDL from reaching CL	[50, 71]	–
Decreased electrode saturation by increasing electrode temperature and removing water in vapor phase	[25, 50, 71]	–
Effective role of MPL cracks in the water management as water removal pathways	[50, 55, 72–76]	–

catalyst layers are also responsible for the reactants (hydrogen and oxygen), charges (electrons and protons), and produced water transport. Therefore, catalyst layers must consist of three phases, i.e., the void phase for reactants and water transport, the electron-conductive phase, and the proton-conductive phase. In order to achieve these functionalities, catalyst layers are commonly fabricated by depositing a catalyst ink consisting of solvents, e.g., propylene glycol and IPA, ionomer, and catalyst, e.g., carbon black supported platinum particles (Pt/C), over each side of the PEM [77, 78] or the PTL [79–82].

### 1.2.3 Water crossover and liquid water accumulation

Cost reduction can be accomplished by increasing the fuel cell power output per gram of catalyst [83]. This requires optimization in PEMFC components to enable operation at higher current density at a given voltage, for which enhanced water management is of crucial importance. Water is necessary for maintaining sufficient electrolyte conductivity [43, 44], but fast ORR water production at high current may induce electrode flooding, causing instability and performance degradation [84–

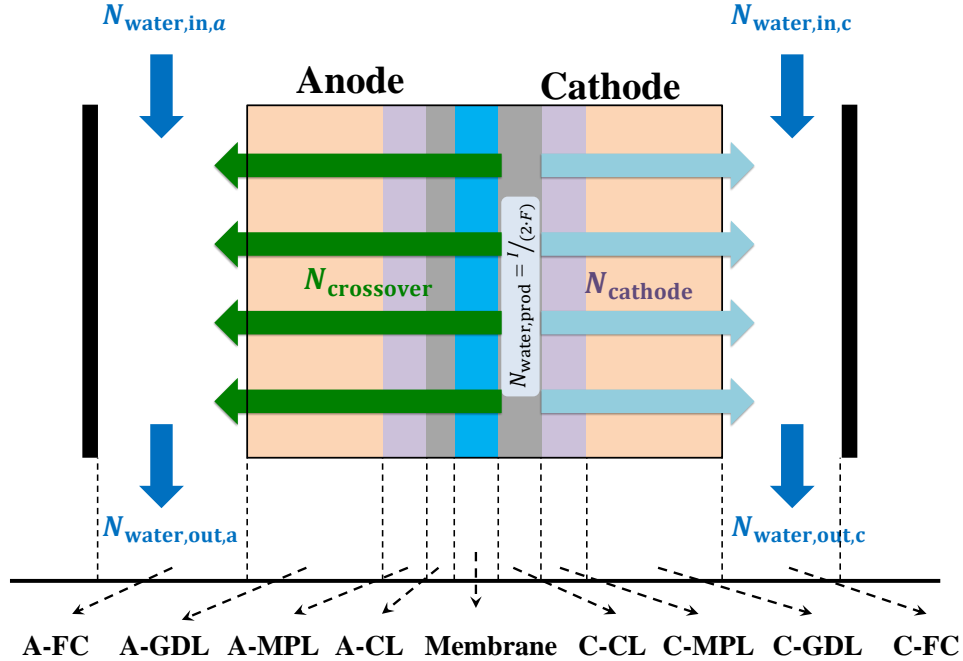


Figure 1.3: A typical schematic of water transport in a PEMFC.

91] and accelerating platinum degradation and thus shortening the lifetime of PEMFCs [28, 30].

The water produced at the cathode CL can be removed not only through the cathode gas flow channels, but also through the anode gas flow channels via the membrane, as depicted in Figure 1.3. To increase the water removal rate from the cathode, strategies such as adding an MPL to the GDL [25, 54, 56, 61–63, 92–100], vaporizing the water [25, 50, 55], creating groove or perforation on a PTL to provide pathways for liquid water removal [72, 101–104], creating cracks on an MPL [33, 50, 70, 72, 96, 97, 105–108], changing wettability and microstructure of CL [36, 37, 109–111], MPL [25, 34, 35, 54, 72, 112, 113] and GDL [33, 56, 62, 101, 103, 114, 115] have been proved to be applicable.

Water removal from cathode to anode not only enables higher hydration of the membrane, increasing the protonic conductivity to reduce ohmic resistance, but also enhances the removal rate of ORR product water, eliminating the flooding in the MEA. There are four kinds of water transport mechanisms through the mem-

brane, i.e., electro-osmotic drag, back diffusion, thermo-osmosis, and hydraulic permeation [116–119]. Due to the difficulty of experimentally separating water transport values through the membrane for each mechanism, the combined effect of all mechanisms is generally considered instead, which is termed as water crossover [61, 120, 121]. To enhance the cathode-to-anode water crossover, strategies such as applying temperature and/or RH gradient between the cathode and anode [55, 122] and introducing an MPL to the cathode [54, 61–63, 123] have been demonstrated to be applicable.

Understanding the water transport behaviors inside an operating PEMFC is critical in designing strategies of the PEM, CL, MPL, and GDL to promote water crossover and to eliminate flooding, and thus to improve PEMFC performance and durability and cut down its cost. Therefore, the accurate measurement of water crossover and liquid water accumulation must be an integral part of the fuel cell performance analysis, which is either not reported in the experimental work or only studied with numerical models.

## 1.2.4 PEMFC performance and characterization

### 1.2.4.1 Polarization curve

The polarization curve (or *iV* curve), describing the relationship between cell voltage and current, is commonly used to characterize PEMFC electrochemical performance. Since the active area (in-plane area) of the MEA may vary between analyzed fuel cells, the current is generally normalized per MEA area to give current density so that the performance of different cells can be compared. Figure 1.4 shows a schematic of typical polarization curve with corresponding voltage losses.

The standard theoretical potential (thermodynamic potential) of a PEMFC is determined from the change in the standard Gibbs free energy ( $\Delta G^0$ ) of the reaction eq. (1.3) [124]:

$$E_{\text{theor}}^0 = -\frac{\Delta G^0}{n \cdot F}, \quad (1.4)$$

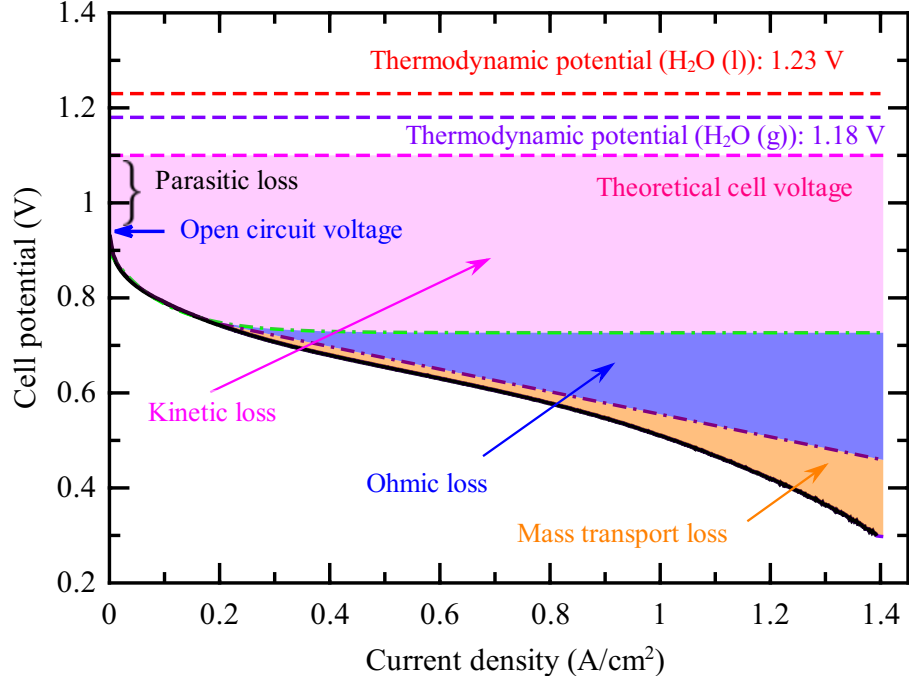


Figure 1.4: Representative PEMFC polarization curve with corresponding voltage losses.

where  $n$  is the number of electrons per mole of hydrogen required to complete the reaction ( $n = 2$ ) and  $F$  is the Faraday's constant (94,485 C/mol). At standard conditions, i.e., 298.15 K and 1 atm,  $E_{\text{theor}}^0$  is approximately 1.23 V and 1.18 V when the ORR product water is in liquid and vapor form, respectively [124]. To correct for the activity of the reactants and products, the temperature at which the reactions occurs, and the final phase of the water, Nernst equation is generally used to calculate the theoretical cell voltage ( $E_{\text{theor}}$ ) at non-standard conditions [38, 124]:

$$E_{\text{theor}} = E_{\text{theor}}^0 + \frac{\Delta S}{2 \cdot F} (T - T^0) + \frac{R \cdot T}{2 \cdot F} \ln \left( \frac{a_{\text{H}_2} (a_{\text{O}_2})^{1/2}}{a_{\text{H}_2\text{O}}} \right), \quad (1.5)$$

where  $E_{\text{theor}}^0$  is the theoretical potential determined at temperature  $T^0$ ,  $\Delta S$  is the additional entropy generated at temperature  $T$ , and  $a_{\text{H}_2}$ ,  $a_{\text{O}_2}$  and  $a_{\text{H}_2\text{O}}$  are the activities of hydrogen, oxygen and ORR product water, respectively.

A potential difference (over-potential) between  $E_{\text{theor}}$  and the operating cell voltage leads to the generation of the faradaic current. However, not all of faradaic current flows through the external circuit. A few milliamperes of current generated in the

cathode due to hydrogen crossover through the membrane, which are offset by the ORR thereby requiring an over-potential [124, 125]. This compensation, known as parasitic loss, results in an offset of the potential at which the net current is zero from the theoretical potential to a lower value named open circuit voltage (OCV). The magnitude of this deviation depends on the rate of reactant crossover and, therefore, membrane that is impermeable to reactants can sensationally reduce the parasitic loss.

When the over-potential is further increased, current starts to flow through the external circuit, forming a relationship between voltage and current, i.e., polarization curve. As current is drawn from the cell, three types of irreversible voltage losses occur: a) kinetic loss, predominant at low current; b) ohmic loss; and c) mass-transport loss, predominant at high current.

The sharp non-linear drop in cell voltage at low current densities in Figure 1.4, known as the kinetic or activation losses, is associated with overcoming the energy barriers to the HOR and, mainly, the ORR. Kinetic losses can be reduced by increasing the concentration and pressure of the reactant, elevating cell operating temperature, and employing more active catalyst.

The linear cell potential drop in Figure 1.4 represents the ohmic losses, which are due to the proton transport resistance in the polymer electrolyte, electron transport resistance in the electrodes, external circuit and FFPs, and contact resistances between layers. Ohmic losses due to electron transport resistances are usually much smaller than those that arise from the resistance to protons transport through the PEM and CLs [19, 124]. The ohmic losses due to the protonic resistance can be substantially reduced by increasing the hydration of the membrane and ionomer phase in CLs [19, 43]. Reducing the thickness of each MEA components, using more conductive materials, and improving the contact between each layer can also help to reduce the ohmic losses [124].

The last sharp non-linear cell voltage drop in Figure 1.4 is due to mass transport

losses, which arise from the insufficient reactant supply to the catalyst sites. The higher the current, the greater rates of reactants supply are required to align with the electrochemical consumption rate and, therefore, mass transport can be influenced by the rate at which the ORR product water is being removed. At high current densities, more water is produced at the cathode CL. If this produced water cannot be efficiently removed from the MEA, it can flood the pores of CLs, MPLs, and GDLs, and thus block reactant transport pathways [25, 50, 72, 108, 126]. During the past two decades, efforts such as modifying the structure and wettability of the GDLs [33, 56, 62, 101, 103, 114, 115], MPLs [25, 34, 35, 54, 72, 112, 113] and CLs [36, 37, 109–111] have been found to be capable of improving the water management towards the electrode flooding due to the fast ORR water production at high currents.

Polarization curves are usually measured by applying a linear or staircase sweep, either in voltage or current, to the cell. A comprehensive sweep generally encompasses a forward scan from high to low voltage (or from low to high current), followed by a backward scan conducted in the converse direction. Depending on the cell operating conditions and the scan rate, dynamic membrane hydration and platinum oxide, and liquid water accumulation may result in the appearance of hysteresis in the measured polarization curves [84–86, 88–90]. If no significant flooding occurs, as shown in Figure 1.5a, cell performance during the backward scan is better than the forward scan due to the better hydration of the electrolyte from the ORR product water [86, 88, 90, 127–129] and/or the reduced platinum-oxide coverage during the backward scan [130, 131]. Conversely, in the scenario where electrode flooding becomes prevalent, reactant transport is impeded by liquid water blockage in the pore space of the porous media and thus, the backward-scan performance is worse than the forward-scan performance [84–90], as seen in Figure 1.5b.

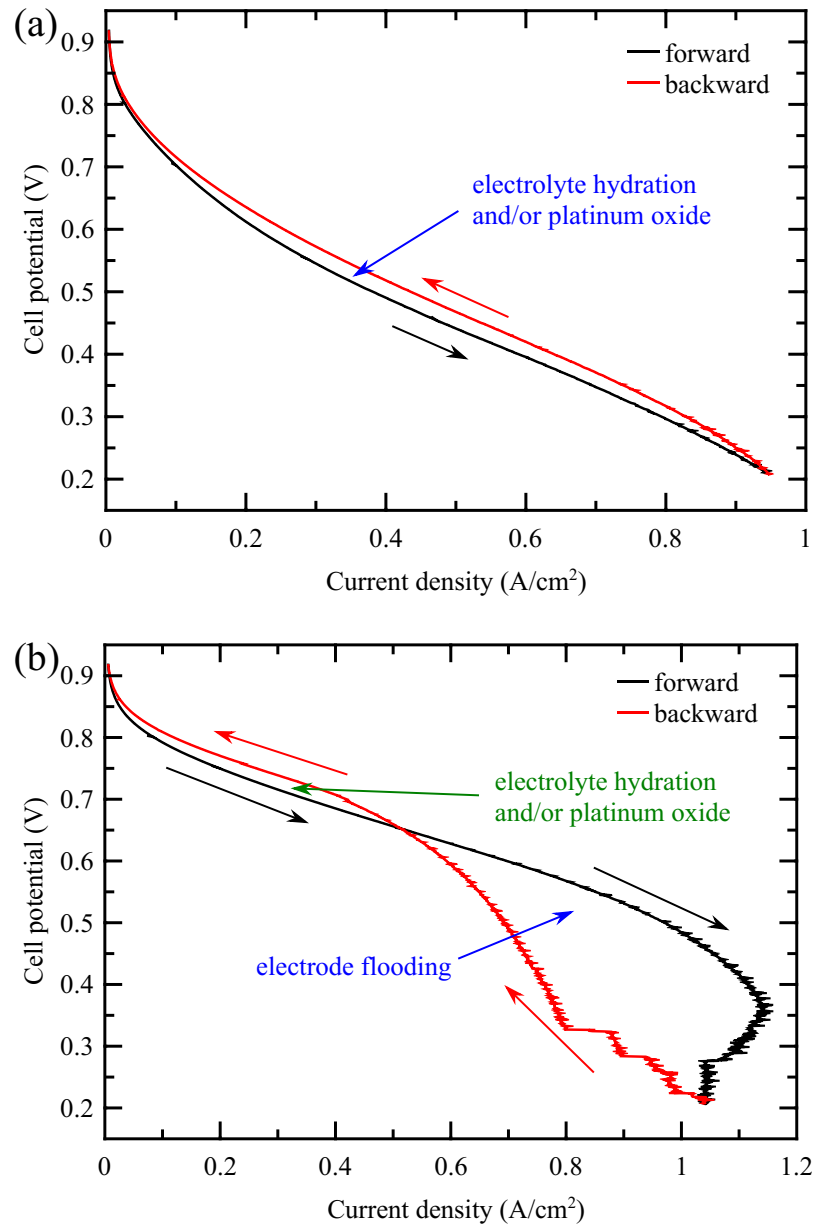


Figure 1.5: Representative PEMFC polarization curve (a) without and (b) with significant flooding.

#### 1.2.4.2 Ohmic resistance

As discussed above, ohmic resistance plays a significant role in the fuel cell performance. Albeit a typical ohmic resistance of a fuel cell is on the order of milliohms, the cell voltage loss due to the ohmic loss becomes significant at high current densities. Since the ohmic losses of the MEA are dominated by the proton transport resistance through the membrane, the protonic resistance of the membrane can be an indicator to assess the water management in an operating PEMFC.

To be capable of being integrated into operating fuel cell systems, the approach employed for measuring the protonic resistance of the membrane must be non-intrusive to avoid interfering with cell performance, easy to implement, and yield results that are easily interpreted. Typically, there are four methods used to measure the ohmic resistance, i.e., current interrupt resistance (CIR) method, AC resistance method, electrochemical impedance spectroscopy (EIS) method, and high frequency resistance (HFR) method. A detailed discussion of these ohmic resistance measurement techniques can be found in Refs. [124, 132]

During the polarization curve measurement, a single data value of the membrane protonic resistance at each current is preferred as multiple data points may affect the polarization curve. As such, the CIR and HFR methods are suitable. Current interrupt resistance method is based on the principle that the resistive potential drop within the cell disappears almost instantaneously when the steady-state current is momentarily interrupted for a short duration [124, 132]. The protonic resistance of the membrane is then calculated by subtracting the resistance of fuel cell hardware, PTLs and CLs from the instantaneous voltage change divided by the cell current just before the interrupt event. High frequency resistance method applies a small AC signal to the electronic load to modulate the dc load current. The resulting magnitude and phase of the AC voltage and current response are measured by a frequency response analyzer. The CIR method is reported to over-estimate the protonic resistance of the

membrane, which is attributed to the additional voltage change as a result of a rapid potential change after the interrupt that arises because of the potential distribution within porous electrodes with non-negligible electrolyte resistance [132]. The inherent difference in the response of a porous electrode with non-negligible ohmic resistance to a large perturbation (current interrupt event) as compared to a small perturbation (impedance measurement) is the source of discrepancy in measured ohmic resistance for current interrupt resistance and high frequency resistance methods. However, due to the limited accessibility of the frequency response analyzer to conduct HFR measurements and in order to simplify the experiments, the current interrupt resistance method was used in this thesis to measure the protonic resistance of the membrane during the electrochemical experiments as this technique is integrated in the fuel cell test stand used.

## **1.3 Literature review**

The initial segment of this literature review section presents a comprehensive overview of the existing experimental setups employed for quantifying water fluxes within operational PEMFCs. Subsequently, the focus shifts towards a thorough exploration of the water transport within polymer electrolyte membranes. The literature review extends further to encompass a comprehensive scrutiny of the impact of operating conditions and the introduction of an MPL to the cathode GDL. Finally, a literature review on the effect of cathode CL Nafion and platinum loadings on cell performance is conducted.

### **1.3.1 Methods used to measure water transport in fuel cells**

Different experimental setups have been developed in the literature to measure the water fluxes in operating PEMFCs. The net water flux between the electrodes is normally estimated as the difference between the inlet and outlet water fluxes in the anode and cathode electrode. Inlet water fluxes are usually estimated by assuming

that the dew point and absolute pressure are equal to the prescribed reactant temperature and backpressure, respectively. However, care is needed when estimating the inlet flux, as the cell backpressure can differ from the inlet pressure, resulting in an inaccurate estimation. Outlet water fluxes are commonly measured by weighing the condensed water that has been collected downstream of the fuel cell using devices such as ice baths [133], cold traps [99, 134, 135], water chilled condensers [55, 65, 136–138] and desiccants [139]. These devices are precise and easy to incorporate into a fuel cell setup. However, a lengthy collecting period (from 30 min to 3 hours) and a sizable active area are needed to collect enough condensed water to study the impact of operating conditions or transport layer modifications on the water crossover between the cathode and anode electrodes [55, 99, 140]. The inaccurate inlet flux, combined with the long collection period, means that these methods only give a time-averaged estimation and cannot be used for real-time water flux tracking. Furthermore, these methods cannot distinguish between liquid and vapor that exit the electrodes. To address these limitations, techniques for transient water measurement in fuel cells have been developed, including infrared adsorption sensors [100, 120, 141, 142], gas chromatography [143, 144], and setups involving relative humidity and temperature sensors [145, 146]. Among these, the relative humidity and temperature sensors are the cheapest and can be used to quantify transient water transport in PEMFCs with high accuracy.

To study water transport in operating PEMFCs, a reliable technique is also needed to quantify the amount of liquid water in the electrodes. To date, this has been done with either ex-situ experiments [63, 147], analyzing in-situ tomography images [27, 33–35, 93, 105, 107, 108, 148–154] or via two-phase numerical modeling [25, 54, 155–164]. The use of imaging techniques requires specialized equipment and training, thus is costly and takes a long time, and the accuracy of the results is limited by spatial and temporal resolutions and the domain size. To the best of the authors’ knowledge, there is no experimental work except imaging on estimating the real-time

porous transport layer saturation in an operating PEMFC.

### 1.3.2 Water transport in polymer electrolyte membrane

The water transport properties of Nafion<sup>®</sup> membranes have been widely measured using techniques such as dynamic vapor sorption (DVS) [165, 166], pulsed field gradient nuclear magnetic resonance (PFG-NMR) spectroscopy [167–169], quasi-elastic neutron scattering (QENS) [170, 171], dynamic infrared spectroscopy [172], and liquid-vapor (L-V) or vapor-vapor (V-V) permeation [133, 173–177]. Kusoglu and Weber [43] conducted a comprehensive review of these techniques and observed that the reported bulk diffusivities of Nafion<sup>®</sup> (proton exchange membrane) varied widely, i.e., from  $10^{-9}$  to  $10^{-5}$  cm<sup>2</sup>/s, depending on experimental techniques used to obtain and interpret the measured data (whether or not interfacial resistances were considered). For example, the L-V [133, 173–176, 178] and V-V permeation methods [133, 174, 175, 179] provided very different diffusivity estimates because the exchange of water at the interfaces limited the overall transport in Nafion<sup>®</sup> membranes [133, 166, 173–175, 180–183]. The challenge of using the V-V setup is that it involves bulk and interfacial transport across two interfaces: absorption on the wet side and desorption on the dry side. The L-V configuration allows for the wet interface to be eliminated from the analysis, as the interfacial transport resistance across the boundary between liquid water and the membrane is negligible [43, 175, 177, 184]. The relative importance of interfacial exchange depends on the thickness and water content of the membranes. Monroe et al. [174] argued that interfacial transport was limiting in Nafion<sup>®</sup> membranes of thickness less than 300  $\mu\text{m}$ , which is significantly thicker than commercial PEMs of 20–50  $\mu\text{m}$  [146, 178, 185–187]. Kienitz et al. [175] concluded that interfacial resistance can be dominant, especially in thin and dry membranes. Based on the previous literature, L-V permeation setups are well established for the estimation of the rate of water desorption from membranes. This rate can then be used as an initial estimate in the V-V analysis, where, according to Ge et al. [133],

the desorption rate might be lower and depends on the membrane water content.

Only a few articles have discussed the water transport properties of anion exchange membranes [146, 178, 185–187]. Marino et al. [186] measured the water diffusion coefficient for the Fumapem<sup>®</sup> FAA-3 membrane using PFG-NMR method. Eriksson et al. [146] and Myles et al. [185] used the permeation setup to measure the water diffusivity for the Tokuyama A201 (L-V and V-V) and SnowPure Excellion<sup>™</sup> I-200 (V-V), respectively. However, interfacial resistances were not considered in the data analysis [146, 185, 186]. Luo et al. [178] used the L-V permeation method to measure the water diffusivity and the interfacial desorption rate for the HMT-PMBI (Aemion<sup>®</sup>) and Fumapem<sup>®</sup> FAA-3 membranes. During their measurements, the dry side was equilibrated with water vapor at a fixed relative humidity (RH) of 40% and a membrane temperature of 70 °C, and the diffusivity and interfacial desorption rate were given under this specific condition. Li et al. [187] measured the bulk diffusivity and the interfacial desorption rate of the Tokuyama A201 membrane using an L-V permeation setup, where the wet and dry sides were equilibrated with liquid water and dry oxygen, respectively. When the water diffusivity and the interfacial desorption rate were determined from the experimental data, the RH variation along the dry flow channel due to water crossover was not considered and instead the membrane was assumed to be equilibrated with an averaged RH on the dry side. As a result, the reported interfacial exchange rate varied with the gas flow rate. The literature review shows that interfacial transport rates were either not considered in the data analysis [146, 185, 186] or not given as a function of the membrane water content [178, 187]. Thus, development of an experimental methodology and an appropriate model to interpret the data and to quantify the interfacial transport rate as a function of the water content and temperature for anion exchange membranes is required.

### 1.3.3 Impact of MPL introduction and operating conditions on water management

Although there is a consensus in the literature that the introduction of MPLs in membrane electrode assemblies improves interfacial contact [32, 72, 94, 114, 188] and prevents the carbon fibers of GDL from penetrating the membrane and shorting the cell [114, 188], there is less agreement on the exact influence of MPLs on water management. Some researchers concluded that the cathode MPL increases the amount of water transport from the cathode to the anode to facilitate the removal of water from the anode side [25, 54, 56, 61–63, 92–100]; however, others showed that the impact of MPL on water crossover is limited [55, 65, 136–138].

It is hypothesized that the contradictory conclusions on the impact of the MPL on water transport between the cathode and anode might be due to the varying operating conditions and the water phase in the catalyst-coated-membrane. For example, fully humidified or over-saturated conditions were used in at least one side of the electrodes in [55, 65, 136–138]. Under these conditions, the membrane can come into contact with liquid water and become fully hydrated [1, 43, 133, 189]. This likely switches the primary mode of bulk water transport in the membrane from diffusive to hydraulic [43, 44, 123, 159, 190], and overall water transport might increase compared to the case where the PEM is vapor equilibrated.

Previous water transport studies have not measured the average water saturation in the electrodes; however, operating conditions and the MPL also have a crucial impact on the water accumulation. The small and hydrophobic pores of the MPL might prevent small interfacial droplets at the CL surface from growing into large ones, merging and eventually forming a liquid water film [15, 34, 35, 50, 56, 61, 72, 93, 94, 96, 155, 156]. Similarly, high temperature operation could result in the quick evaporation of produced liquid water in the electrode [25, 50, 55]. Thus, high temperature and MPLs might reduce the saturation level at the CL and PTL interface and increases the supply of reactant to the catalyst sites by providing pathways for

the reactant to diffuse around the localized liquid water blockages in the GDL [25, 50, 61]. Cracks in MPLs, such as those observed in commercial SGL BC-series [33, 72, 191], were also found to increase the removal rate of liquid water by providing additional transport pathways [33, 50, 70, 72, 96, 97, 105–108]. With higher capillary pressure due to the small pores of MPL, the rate of liquid water removal at break-through from cathode CL to cathode gas flow channels [33, 63, 188, 192] is increased. For example, Gostick et al. [63] showed that liquid water break-through from the CL to the GDL via the MPL resulted in a reduction of overall water saturation in GDL from 27% to 3%.

Based on the above, it is of paramount importance to study the effect of operating conditions on water crossover and accumulation. Furthermore, the effect of the MPL on water crossover and accumulation should be evaluated at varying conditions to assess the reason for the discrepancies observed in the literature. Basically, does the MPL improve the cathode-to-anode water crossover? And under what conditions?

### **1.3.4 Impact of CL composition and loading on water management**

Catalyst layer ionomer loading affects the reactant supply to the catalyst sites, the removal of ORR product water, and proton transport [43, 193, 194]. It has been reported that high Nafion loading can substantially enhance proton conductivity of CLs, but result in a high resistance to oxygen transport to the active site by reducing the porosity of the catalyst layers [111, 195], thereby reducing transport and possibly inducing significant water flooding [110], especially when operating the PEMFC at high current densities under wet/cold conditions. Furthermore, Nafion has a different wettability than carbon and, therefore, changes in ionomer loading are likely to influence water retention in the catalyst layer. Therefore, an optimal Nafion loading that achieves a balance between protonic conductivity and water transport and accumulation is needed. Many studies have been conducted in the literature to

explore the optimal Nafion loading [78, 110, 196–207], as well as ionomer-gradient designs [202, 208–214]; however, these studies have focused on the impact of Nafion loading on in-situ performance, e.g., electrochemical surface area, protonic resistance, and polarization-curve, but none have quantified its effect on water transport and liquid water accumulation in operating PEMFCs.

Developing low platinum loading CL while preserving fuel cell performance is crucial for reducing PEMFC cost; however, water management of low PL catalyst layers is more critical, due to their inherently low water capacity, which has been suggested to make them more susceptible to flooding [91, 159]. For example, Kongkanand and Sinha [91] experimentally found that thin CL showed large voltage undershoots during current up-transients from 0.02 to 1.0 A/cm<sup>2</sup> at 80 °C and 100% RH, whereas thicker CLs exhibited a more robust voltage response. They postulated that thin CLs, owing to their limited water storage capacity, do not allow sufficient time for water removal and, therefore, are easier to flood during current up-transients at wet condition; however, this conclusion was based on a non-isothermal transient model but was not experimentally validated. Zenyuk et al. [159] also observed a significant impact of CL thickness on saturation in catalyst layer via mathematical modeling, e.g., 2.2 times higher at 5 μm than 2 μm. An experimental study analyzing the relationship between CL loading and flooding for carbon-supported platinum electrodes is needed to validate numerical results and has not yet been reported.

Adachi et al. [215] demonstrated that the introduction of a catalyst layer onto one or both sides of the PEM did not discernibly alter the water transport flux crossing the membrane via ex-situ vapor-vapor permeation method. This indicates that the CL might have a negligible effect on water transport across the membrane, implying that water crossover should not be modified by CL composition and loading; however, in-situ polarization-curve measurements suggested that both Nafion loading [78, 110, 196–207] and CL thickness [91, 159] have a noticeable influence on cell performance. The divergent observations obtained from ex-situ and in-situ experiments

underscore the importance of accurately quantifying the impact of these changes on water transport in operating PEMFCs.

## 1.4 Thesis Objectives

The overall objective of this thesis is to experimentally quantify the impact of cell component and operating conditions modifications on the real-time water transport and liquid water accumulation within an operating PEMFC. To achieve this goal, the following objectives will be addressed:

1. Objective #1: Develop a water balance setup that enables the real-time measurement of water transport between the anode and cathode electrodes and liquid water accumulation in the MEA inside operating PEMFCs.
2. Objective #2: Characterize water transport in proton and anion exchange membranes using the developed water balance setup.
3. Objective #3: Study the impact of operating conditions and MPL addition to the cathode transport layer on the performance, water transport and liquid water accumulation in PEMFCs using the developed water balance setup.
4. Objective #4: Study the impact of cathode CL Nafion and platinum loadings on the performance, water transport and liquid water accumulation in PEMFCs using the developed water balance setup.

## 1.5 Thesis Outline

There are six chapters in this thesis. The current chapter establishes the foundational context by presenting the motivation for this thesis, introducing the background of PEMFC operation principles, conducting a literature review of the pertinent subject matter, and outlining the set objectives. A detailed description of the developed water balance setup, which allows for real-time measurement of water fluxes entering

and leaving the anode and cathode of an operating PEMFC and liquid water accumulations in PTL, is given in Chapter 2. The developed water balance setup is then used in Chapters 3–5 to address the objectives formulated above. The water balance setup was first used to quantify the water transport in proton and anion exchange membranes in Chapter 3. Then, the impact of operating conditions and micro-porous layers on the water transport and accumulation in PEMFCs was studied in Chapter 4. Lastly, the impact of cathode catalyst layer Nafion and platinum loadings on the water transport and accumulation in PEMFCs was studied in Chapter 5. Summarizing the culmination of these extensive investigations, Chapter 6 provides an overview of the main findings from this thesis. Moreover, it serves as a launchpad for future research endeavors, outlining prospective avenues that merit exploration.

# Chapter 2

## Methodology<sup>1</sup>

The focus of this chapter is to introduce the water balance setup used in the next chapters to quantify the real-time water transport and liquid water accumulation in operating PEMFCs. Ex-situ and in-situ experiments were conducted to validate the developed water balance setup, and an uncertainty analysis was also performed based on error propagation of relative humidity and temperature sensors, absolute pressure transducers and gas flowmeters uncertainties. Based on the measured water fluxes entering and leaving the anode and cathode of the operating PEMFC, a comprehensive approach is proposed for estimating the cathode-to-anode water crossover and distinguishing the water accumulated in the membrane from the liquid water in the porous media. This chapter also outlines the experimental conditions and electrochemical characterizations used to analyze the impact of operating conditions and MPL addition to cathode GDL (see Chapter 4) and cathode catalyst layer Nafion

---

<sup>1</sup>Parts of this chapter are reproduced from the following publications:

- a F. Wei, A. Kosakian, J. Liu, J. Kracher, R. Khan, and M. Secanell, “Water transport in anion and proton exchange membranes,” *Journal of Power Sources*, vol. 557, p. 232 494, 2023. DOI: <https://doi.org/10.1016/j.jpowsour.2022.232494>.
- b F. Wei, A. Kosakian, and M. Secanell, “Effect of operating conditions and micro-porous layer on the water transport and accumulation in proton exchange membrane fuel cells,” *Chemical Engineering Journal*, p. 144 423, 2023. DOI: <https://doi.org/10.1016/j.cej.2023.144423>.
- c F. Wei, A. Kosakian, J. Liu, and M. Secanell, “Effect of Cathode Catalyst Layer Nafion and Platinum Loading on the Dynamic Transport and Accumulation of Water Inside an Operating PEMFC,” (under review).

Author contributions are detailed in the Preface of this thesis.

and platinum loading (see Chapter 5) on water management.

## 2.1 Experimental setup

The experimental setup to measure water transport, shown in Figure 2.1a and 2.1b, consisted mainly of a Scribner 850e fuel cell testing station, four custom-built sensor boxes (referred as water balances in this thesis), and fuel cell hardware. The four water balances, consisting of a relative humidity and temperature sensor (Sensirion SHT85) and a pressure transducer (Omega MMA030USBHK2C0T8A6CE), were located at the inlet and outlet of the tested cell to measure the relative humidity, temperature, and absolute pressure of the gas-vapor mixture. Special measures were taken to eliminate the presence of liquid water in the tubing so as to not underestimate the water flux and to avoid electrical shorts in the RH and temperature sensors. To achieve a stable temperature at the sensors and prevent condensation, the inlet and outlet water balances were immersed in heated water baths set to 95 °C, and heating tape was used to cover the exposed pipes between the fuel cell and the water balance. The heating tape at the cell inlet (tape #1 in Figure 2.1b) was set to 5 °C higher than the cell temperature, and the tapes down stream of the cell (tapes #2 and #3) were set to 115 °C. During the experiments, the flow rates of dry reactants entering the fuel cell were measured separately from the test station mass flow controllers using two flowmeters (Alicat, M-5SLPM-D/5M) located between the gas cylinders and the test station as shown in Figure 2.1b in order to increase the accuracy of the inlet water flux estimation. The temperature of the anode and cathode end plates of the fuel cell hardware was controlled separately to provide accurate temperature control.

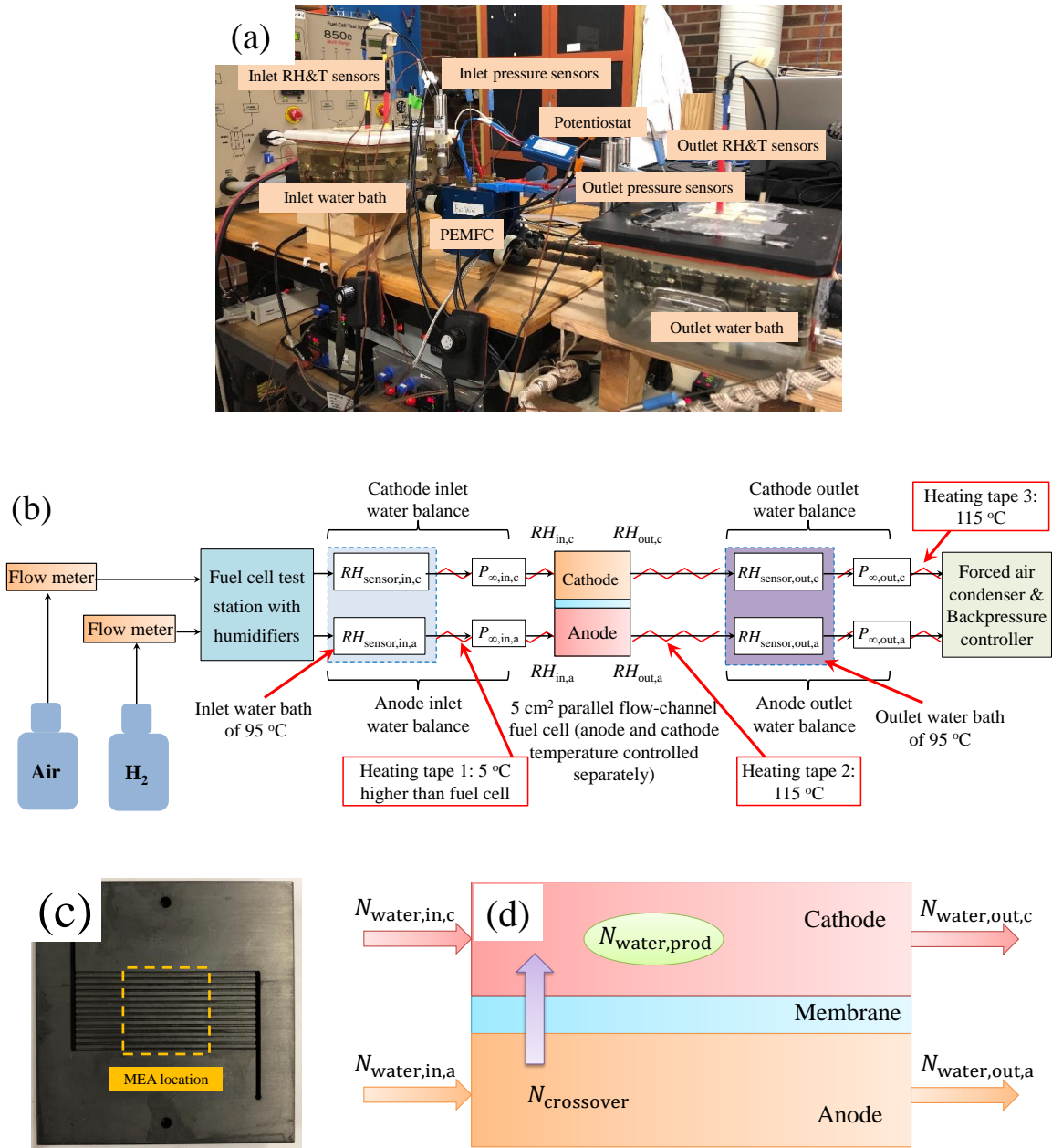


Figure 2.1: (a) Experimental setup for the in-situ testing, (b) schematic of the setup, (c) fuel cell flow field and (d) schematic of the water transport.

## 2.2 Theory

### 2.2.1 Water flux determination

The molar flow rates of the water entering the anode and cathode of the operating PEMFC were calculated using the dry flow rates of the gas supply (hydrogen and air in the anode and cathode, respectively) corrected to standard conditions of 101.325 kPa and 273.15 K ( $\dot{V}_{\text{gas,in}}$ ), the relative humidity ( $RH_{\text{sensor,in}}$ ), temperature ( $T_{\text{sensor,in}}$ ), and the absolute pressure ( $P_{\infty,\text{in}}$ ) of the gas-vapor mixture. The molar flow rates of dry hydrogen and air were calculated using the ideal gas law as

$$N_{\text{dry,gas,in}} = \frac{P_0 \cdot (\dot{V}_{\text{gas,in}} [\text{slpm}])}{R \cdot T_0 \cdot (60 [\text{s}])}, \quad (2.1)$$

where  $P_0$  is 101.325 kPa,  $T_0$  is 273.15 K, and  $R$  is the gas constant, i.e., 8.3145 J/(mol·K). The molar flow rates of water entering the anode and cathode of the tested cell were calculated as

$$N_{\text{water,in}} = N_{\text{dry,gas,in}} \cdot \frac{P_{\text{vapor,in}}}{P_{\infty,\text{in}} - P_{\text{vapor,in}}}, \quad (2.2)$$

where  $P_{\text{vapor,in}}$  is the inlet vapor pressure calculated using the Buck equation [216]:

$$P_{\text{vapor,in}} = RH_{\text{sensor,in}} \cdot 0.61121 \cdot \exp \left( \left[ 18.678 - \frac{T_{\text{sensor,in}}}{234.5} \right] \left( \frac{T_{\text{sensor,in}}}{257.14 + T_{\text{sensor,in}}} \right) \right). \quad (2.3)$$

It should be noted that  $T_{\text{sensor}}$  deviated from the water bath temperature, i.e., 95 °C. This is because the gas-vapor mixtures were pre-heated, either by the Scribner test station or custom-built heating tapes, before their temperature was measured by the SHT85 sensors.

Due to the higher temperature of the water baths than the cell, the RH readings from the Sensirion SHT85 sensors ( $RH_{\text{sensor,in}}$ ) were different from the inlet ( $RH_{\text{in}}$ ) and outlet ( $RH_{\text{out}}$ ) RHs in the gas flow channels; therefore,  $RH_{\text{in}}$  and  $RH_{\text{out}}$  were calculated as

$$RH_{\text{in}} = \frac{P_{\text{vapor,in}}}{P_{\text{sat}}}, \quad (2.4)$$

and

$$RH_{\text{out}} = \frac{P_{\text{vapor,out}}}{P_{\text{sat}}}, \quad (2.5)$$

where  $P_{\text{sat}}$  is the saturation pressure calculated using eq. (2.3) with  $RH$  and  $T$  equal to 100% and cell temperature, respectively;  $P_{\text{vapor,out}}$  is the outlet vapor pressure calculated using eq. (2.3) with  $RH$  and  $T$  measured by the outlet relative humidity and temperature sensors.

Calculating the molar flow rates of the water leaving the anode and cathode of the operating PEMFC ( $N_{\text{water,out}}$ ) is similar to the water entering the fuel cell using eq. (2.2). However, the dry molar gas flow rate leaving the fuel cell ( $N_{\text{dry,gas,out}}$ ) must be corrected to account for the consumption of hydrogen in the HOR and oxygen in the ORR and for the reactant crossover. Since reactant crossover was found negligible, the dry molar flow rate of hydrogen and nitrogen-oxygen mixture leaving the anode and cathode of the operating PEMFC at given cell current were calculated as

$$N_{\text{dry,gas,out,a}} = N_{\text{dry,gas,in,a}} - \frac{I}{2 \cdot F} \quad (2.6)$$

and

$$N_{\text{dry,gas,out,c}} = N_{\text{dry,gas,in,c}} - \frac{I}{4 \cdot F} \quad (2.7)$$

for the anode and the cathode, respectively, where  $I$  is the current and  $F$  is the Faraday constant, i.e., 96485 C/mol.

### 2.2.2 Water crossover determination

The anode and cathode electrodes were considered to be two coupled control volumes separated by the membrane, as indicated in Figure 2.1d, in order to calculate the overall water distribution and net water flux across the membrane within an operating PEMFC. The net molar water crossover flux through the membrane ( $N_{\text{crossover}}$ ) was defined as the difference in the molar flow rates between the water entering and leaving the anode or cathode. A positive value represented a net water transport from anode

to cathode. Note that, in Chapter 5, the direction of water crossover was reversed as the net water was found to transport from the cathode to the anode. For the anode, the water crossover flux was

$$N_{\text{crossover,a}} = N_{\text{water,in,a}} - N_{\text{water,out,a}}, \quad (2.8)$$

and for the cathode,

$$N_{\text{crossover,c}} = N_{\text{water,out,c}} - N_{\text{water,in,c}} - N_{\text{water,prod}}, \quad (2.9)$$

where  $N_{\text{water,prod}}$  is the molar flow rate of water produced in ORR calculated as

$$N_{\text{water,prod}} = \frac{I}{2 \cdot F}. \quad (2.10)$$

In the absence of liquid water accumulation,  $N_{\text{crossover}} = N_{\text{crossover,a}} = N_{\text{crossover,c}}$ . When  $RH_{\text{out}}$  at the cathode was 100%,  $N_{\text{crossover,a}} \neq N_{\text{crossover,c}}$  due to water accumulation in the cathode. In this case,  $N_{\text{crossover}}$  was measured using the anode water crossover, i.e.,  $N_{\text{crossover,a}}$ .

In this thesis, the dimensionless water crossover ( $\beta$ ) represents the water flux ratio of crossover to produced water by the ORR, which was calculated as

$$\beta = \frac{N_{\text{crossover}}}{N_{\text{water,prod}}}. \quad (2.11)$$

## 2.2.3 Determination of accumulation and saturation

### 2.2.3.1 Water accumulation in the MEA

If water is accumulated in the MEA at a given time instant, the total amount of water leaving the operating PEMFC ( $N_{\text{water,out,a}} + N_{\text{water,out,c}}$ ) will be lower than the sum of the amounts of water entering the cell ( $N_{\text{water,in,a}} + N_{\text{water,in,c}}$ ) and water produced in ORR ( $N_{\text{water,prod}}$ ). Thus, the total amount of water accumulated in the MEA ( $V_{\text{MEA,water}}(t)$ ) can be determined by

$$V_{\text{MEA,water}}(t) = \frac{M_{\text{water}}}{\rho_{\text{water}}} \int_{t_0}^t (N_{\text{water,in,a}} + N_{\text{water,in,c}} + N_{\text{water,prod}} - N_{\text{water,out,a}} - N_{\text{water,out,c}}) dt, \quad (2.12)$$

where  $M_{\text{water}}$  and  $\rho_{\text{water}}$  are the molecular weight and density of liquid water, respectively.

The total amount of water in the MEA can be divided into water accumulated in the polymer electrolyte and in the porous media. Compared with the membrane and the PTLs, accumulation of water in the ionomer and pore phases of catalyst layers can be neglected due to their relatively small volume, and thus

$$V_{\text{MEA,water}}(t) = \Delta V_{\text{PEM,water}}(t) + V_{\text{PTL,water}}(t), \quad (2.13)$$

where  $\Delta V_{\text{PEM,water}}(t)$  and  $V_{\text{PTL,water}}(t)$  are the amounts of water accumulated in the membrane and in the PTLs, respectively.

### 2.2.3.2 Water accumulation in the membrane

The volume of water accumulated in the membrane ( $\Delta V_{\text{PEM,water}}(t)$ ) was determined as the difference between the water content at a given time  $t$  ( $V_{\text{PEM,water}}(t)$ ) and the initial water content ( $V_{\text{PEM,water}}^0$ ), i.e.,

$$\Delta V_{\text{PEM,water}}(t) = V_{\text{PEM,water}}(t) - V_{\text{PEM,water}}^0. \quad (2.14)$$

The total volume of water contained inside the membrane was calculated as

$$V_{\text{PEM,water}} = \frac{\rho_{\text{PEM}}}{\text{EW}_{\text{PEM}}} \cdot \lambda_{\text{PEM}} \cdot \frac{M_{\text{water}}}{\rho_{\text{water}}} \cdot V_{\text{PEM}}, \quad (2.15)$$

where  $\lambda_{\text{PEM}}$  is the water content of the membrane,  $\rho_{\text{PEM}}$  is the dry polymer density (2 g<sub>PEM</sub>/cm<sup>3</sup><sub>PEM</sub> [43, 217, 218]), EW<sub>PEM</sub> is its equivalent weight (1100 g<sub>PEM</sub>/mol<sub>SO<sub>3</sub><sup>-</sup></sub> [218, 219]), and  $V_{\text{PEM}}$  is the volume of the dry membrane, calculated as

$$V_{\text{PEM}} = L_{\text{PEM}} \cdot A_{\text{PEM}} = 25 \mu\text{m} \cdot 5 \text{ cm}^2 = 1.25 \times 10^{-2} \text{ cm}^3_{\text{PEM}}, \quad (2.16)$$

where  $L_{\text{PEM}}$  and  $A_{\text{PEM}}$  are the dry thickness and active area of the Nafion NR-211 membrane, respectively. The initial water content for the calculation of  $V_{\text{PEM,water}}^0$  in eq. (2.14) was determined from the sorption isotherm (see Chapter 3), assuming the water activity ( $a_w$ ) of the inlet,

$$\lambda_{\text{PEM}} = 14.25a_w - 23.95a_w^2 + 21.11a_w^3. \quad (2.17)$$

For the real-time measurements, the water content was estimated based on [220]

$$\sigma_{\text{PEM,H}^+} = (-0.020634 + 0.01052 \lambda_{\text{PEM}} - 1.0125 \cdot 10^{-4} \lambda_{\text{PEM}}^2) \exp \left[ \frac{6248}{R} \left( \frac{1}{303} - \frac{1}{T_{\text{cell}}} \right) \right], \quad (2.18)$$

where  $R$  is the gas constant (8.3145 J/(mol·K)), and  $T_{\text{cell}}$  is the cell temperature, and  $\sigma_{\text{PEM,H}^+}$  is the protonic conductivity of the membrane, determined from the current interrupt resistance (CIR) using

$$\sigma_{\text{PEM,H}^+} = \frac{L_{\text{PEM}}}{\text{CIR} - R_{\text{extra}}}, \quad (2.19)$$

where  $R_{\text{extra}}$  is the resistance from fuel cell hardware, PTLs and CLs, and it was found to be approximately 28 mOhm·cm<sup>2</sup> by measuring the ohmic resistance of an electrochemical cell with a CCM replaced with a 3-mil-thick copper foil.

In order to make sure the method outlined above provided physically meaningful values, the water activity was estimated and compared to the outlet RH assuming the membrane is in equilibrium with the water vapor. In this case, the water activity was estimated from the inverse of eq. (2.17),

$$a_w = \frac{1.77\lambda_{\text{PEM}} + 0.121\lambda_{\text{PEM}}^2 + 0.0317\lambda_{\text{PEM}}^3}{28.3 - 5.32\lambda_{\text{PEM}} + 0.907\lambda_{\text{PEM}}^2}. \quad (2.20)$$

### 2.2.3.3 Water accumulation and saturation in the PTLs

With the amount of water accumulated in the MEA ( $V_{\text{MEA,water}}(t)$ ) and the change in the water content in the membrane ( $\Delta V_{\text{PEM,water}}(t)$ ) known, the amount of water accumulated in the PTLs ( $V_{\text{PTL,water}}(t)$ ) at a given time instant was found from eq. (2.13). Due to the relatively small density of vapor, water accumulated in the PTLs was assumed to be in liquid form, and the corresponding saturation was found using

$$S_{\text{PTL}}(t) = \frac{V_{\text{PTL,water}}(t)}{V_{\text{void}}}, \quad (2.21)$$

where  $V_{\text{void}}$  is the total PTL pore volume. The method described above does not allow for the direct differentiation between liquid water accumulation in the anode

and cathode PTLs. In the calculations, the pore volume of the cathode PTL was used under the assumption of predominant cathode flooding. The assumption is based on observations showing the  $RH$  first reaches 100% at the cathode outlet. Saturation above one would indicate flooding of both anode and cathode PTLs. In this thesis, either the SGL 29BA or 29BC with a pinch of approximately  $68\mu\text{m}$  was used as the cathode PTL.

The total pore volume of SGL 29BA was calculated as

$$V_{\text{void}} = \varepsilon AL = 82.87\% \cdot 5 \text{ cm}^2 \cdot 122 \mu\text{m} = 5.055 \times 10^{-8} \text{ m}^3, \quad (2.22)$$

where  $A$  is the in-plane area of the GDL ( $5 \text{ cm}^2$ ),  $L$  is the thickness of the compressed GDL ( $122 \mu\text{m}$ ) based on the 5 mil rigid gasket used, and  $\varepsilon$  is the porosity of the compressed GDL, which was calculated as [92]

$$\varepsilon = 1 - \frac{L_0}{L}(1 - \varepsilon_0) = 1 - \frac{190 \mu\text{m}}{122 \mu\text{m}} (1 - 0.89) = 82.87\%, \quad (2.23)$$

where  $L_0$  and  $\varepsilon_0$  are the thickness and porosity of the uncompressed GDL, respectively.

SGL BC samples are composed of three sub-regions, i.e., pure MPL, MPL-GDL intermediate and pure GDL regions [107, 221, 222]. Unfortunately, there are no studies in the literature that characterize the thickness and porosity of each sub-region of SGL 29BC with the same pinch as in this thesis. Porosity profile of SGL 25BC, a predecessor of 29BC, under the pinch of  $75 \mu\text{m}$  has been measured using  $\mu\text{CT}$  technique by Lee et al. [107] The thickness of pure MPL, MPL-GDL intermediate and pure GDL regions were 22, 119 and  $35 \mu\text{m}$ , respectively. The porosity profile was found to monotonically increase from the pure MPL to the pure GDL regions as the amount of MPL intrusion diminished. In this thesis, the total pore volume of the SGL 29BC was found by integrating the local 25BC porosity reported in [107], which gave  $4.144 \times 10^{-8} \text{ m}^3$ . The total pore volume of SGL 25BC is lower than that of SGL 29BA with the pinch of  $68 \mu\text{m}$  due to the intrusion of MPL into the GDL.

## 2.2.4 Uncertainty analysis

In this thesis, the dry nitrogen flow rate,  $RH$ , temperature, and absolute pressure were measured using the sensors discussed above. An uncertainty analysis was performed based on error propagation [223, 224] from each of the sensors. The estimated overall error for the water crossover measurements was

$$\omega_{N_{\text{crossover}}} = \sqrt{\omega_{N_{\text{water,in}}}^2 + \omega_{N_{\text{water,out}}}^2}, \quad (2.24)$$

where  $\omega_{N_{\text{wv,in}}}$  and  $\omega_{N_{\text{wv,out}}}$  are the uncertainties for the inlet and outlet water flux in the anode or cathode side, respectively. They are given as

$$\begin{aligned} \omega_{N_{\text{water}}} &= \sqrt{\left(\omega_{N_{\text{gas}}} \frac{\partial N_{\text{water}}}{\partial N_{\text{gas}}}\right)^2 + \left(\omega_{P_{\text{vap}}} \frac{\partial N_{\text{water}}}{\partial P_{\text{vap}}}\right)^2 + \left(\omega_{P_{\infty}} \frac{\partial N_{\text{water}}}{\partial P_{\infty}}\right)^2} \\ &= \sqrt{\left(\omega_{N_{\text{gas}}} \frac{P_{\text{vap}}}{P_{\infty} - P_{\text{vap}}}\right)^2 + \left(\omega_{P_{\text{vap}}} \frac{N_{\text{gas}} P_{\infty}}{(P_{\infty} - P_{\text{vap}})^2}\right)^2 + \left(\omega_{P_{\infty}} \frac{N_{\text{gas}} P_{\text{vap}}}{(P_{\infty} - P_{\text{vap}})^2}\right)^2}, \end{aligned} \quad (2.25)$$

where  $\omega_{N_{\text{gas}}}$ ,  $\omega_{P_{\infty}}$  and  $\omega_{P_{\text{vap}}}$  are the uncertainty for the dry gas flow rate, absolute pressure and vapor pressure, respectively. The uncertainty for the dry gas flow rate ( $\omega_{N_{\text{gas}}}$ ) is calculated using the manufacturer data (Alicat M-5SLPM-D/5M flow meter):

$$\begin{aligned} \omega_{N_{\text{gas}}} &= \frac{P_0 \cdot \left(\sqrt{B_{N_{\text{gas}}}^2 + P_{N_{\text{gas}}}^2} \text{ [slpm]}\right)}{R \cdot T_0 \cdot (60 \text{ [s]})} \text{ [mol/s]} \\ &= \frac{101.325 \text{ [kPa]} \cdot \left(\sqrt{(0.1\% \cdot 5 \text{ [slpm]})^2 + (0.0063 \text{ [slpm]})^2}\right)}{8.3145 \text{ [J/(mol}\cdot\text{K)]} \cdot 273.15 \text{ [K]} \cdot (60 \text{ [s]})} \text{ [mol/s]} \\ &= 5.981 \times 10^{-6} \text{ [mol/s]}, \end{aligned} \quad (2.26)$$

where  $B_{N_{\text{gas}}}$  is the systematic or bias uncertainty provided by the manufacturer, and  $P_{N_{\text{gas}}}$  is the precision uncertainty determined from the standard deviation of the measurements. The accuracy of the Alicat M-5SLPM-D/5M flow meter is  $\pm 0.1\%$  of full scale (5 slpm), and the precision uncertainty was found to be  $\pm 0.0063$  slpm.

Next, the uncertainty for the absolute pressure ( $\omega_{P_\infty}$ ) in eq. (2.25) was calculated as

$$\begin{aligned}\omega_{P_\infty} &= \sqrt{B_{P_\infty}^2 + P_{P_\infty}^2} \\ &= \sqrt{(0.05\% \cdot 200 \text{ [kPa]})^2 + (0.040 \text{ [kPa]})^2} \\ &= 0.11 \text{ [kPa]},\end{aligned}\tag{2.27}$$

where  $\pm 0.05\%$  of full scale (200 kPa) is the accuracy of the pressure transducers and  $\pm 0.040$  kPa is the precision uncertainty found in this thesis.

The uncertainty for the vapor pressure ( $\omega_{P_{\text{vap}}}$ ) in eq. (2.25) is calculated as

$$\begin{aligned}\omega_{P_{\text{vap}}} &= \left\{ \left( \omega_{RH} \cdot \frac{\partial P_{\text{vap}}}{\partial RH} \right)^2 + \left( \omega_T \cdot \frac{\partial P_{\text{vap}}}{\partial T} \right)^2 \right\}^{1/2} \\ &= \left\{ \left( 2\% \cdot \frac{P_{\text{vap}}}{RH} \right)^2 \right. \\ &\quad \left. + \left[ (0.0033 \cdot T - 0.06) \cdot P_{\text{vap}} \cdot \left( \left( -\frac{T}{234.5 \cdot (257.14 + T)} \right) \right. \right. \right. \\ &\quad \left. \left. \left. + \left( \frac{257.14}{(257.14 + T)^2} \right) \left( 18.678 - \frac{T}{234.5} \right) \right) \right]^2 \right\}^{1/2},\end{aligned}\tag{2.28}$$

where  $\omega_{RH}$  and  $\omega_T$  are the accuracies of the relative humidity and temperature measured using the Sensirion SHT85 sensors [225], respectively. They are given as

$$\begin{cases} \omega_{RH} = \pm 2\% \\ \omega_T = \pm (0.0033 \cdot T - 0.06). \end{cases}\tag{2.29}$$

Once the individual uncertainties are known, rearranging eq. (2.25) gives,

$$\begin{aligned}\omega_{N_{\text{wv}}} &= \left\{ \left( 5.981 \times 10^{-6} \frac{P_{\text{vap}}}{P_\infty - P_{\text{vap}}} \right)^2 \right. \\ &\quad \left. + \left( \omega_{P_{\text{vap}}} \frac{4.05 \times 10^{-4} P_\infty}{(P_\infty - P_{\text{vap}})^2} \right)^2 + \left( 0.11 \frac{4.05 \times 10^{-4} P_{\text{vap}}}{(P_\infty - P_{\text{vap}})^2} \right)^2 \right\}^{1/2}.\end{aligned}\tag{2.30}$$

The relative uncertainty in the water crossover, i.e.,

$$\frac{\omega_{N_{\text{crossover}}}}{N_{\text{crossover}}},\tag{2.31}$$

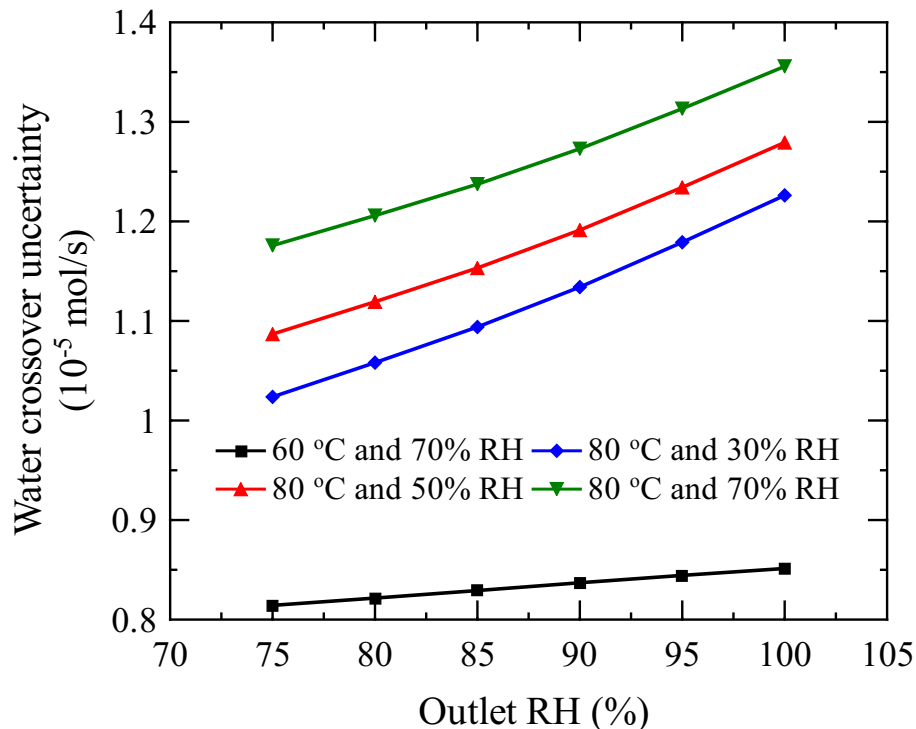


Figure 2.2: Uncertainty analysis for water crossover.

was found to be less than 23.6% in this thesis. Figure 2.2 shows the water crossover uncertainty (calculated using eqs. (2.24) to (2.30)) at varying operating conditions for the outlet  $RH$  ranged from 75 to 100%. A lower relative uncertainty of water crossover could be achieved by increasing the active area and thus water crossover flux ( $N_{\text{crossover}}$ ). However, this would have likely resulted in either super-saturated conditions or large pressure drops in the channels as larger flow rates would have been necessary to avoid super-saturation of the gas stream.

### 2.2.5 Bias estimation

Two bias estimation experiments were performed, before and after any electrochemical experiment at each operating condition, by holding the cell at OCV for 10 minutes and measuring any difference between the inlet and outlet water fluxes. The second bias estimation experiment was conducted to make sure that the water flux bias was the same after the experiments. The averaged bias between the two experiments was

assumed to be due to the measurement uncertainty and used to correct the measured water fluxes.

## 2.3 Validation of experimental setup

The capability of the developed water balance setup to accurately track the water fluxes that enter and leave the anode and cathode of the PEMFC was verified via ex-situ and in-situ validation tests.

### 2.3.1 Ex-situ validation

Before any water transport measurements were conducted, the capability of the experimental setup to accurately measure the water flux in the gas-vapor stream was verified. To validate the experimental setup developed in this thesis, humidified nitrogen was routed from the fuel cell test station directly to the inlet water balance setup, then the outlet water balance, and finally a forced air condensing unit. The inlet and outlet water balances were connected using a stainless steel tube heated to 105 °C; the tested cell was not included in the validation experiments. The experimental setup was validated by comparing the mass of water measured by the inlet and outlet water balances and the combined mass of the condensed water and the water vapor retained in the exhaust gas-vapor mixture. The exhaust gas-vapor stream was assumed to be fully saturated (100% RH) under the room temperature (around 25 °C) and pressure (around 93.5 kPa). The water mass in the nitrogen-vapor stream was calculated using eqs. (2.1) to (2.3), and the condensed water was weighed with a precision balance (Denver Instruments SI-603,  $\pm 0.1$  mg).

In this thesis, validation experiments were carried out using 1.0 slpm nitrogen flow with dew points corresponding to approximately 30, 50 and 70% RH at 80 °C. To accumulate enough condensed water, the three experiments were run for 2, 1 and 1 hours, respectively. The results of the ex-situ validation experiments are summarized in Table 2.1. As shown in the table, the three water masses in all three cases were in

Table 2.1: Ex-situ validation of the experimental setup.

Validation		Water mass by inlet water balance <sup>a</sup> (g)	Water mass by outlet water balance <sup>a</sup> (g)	Water mass by condenser <sup>b</sup> (g)
Anode	30% RH	18.16±0.25	18.55±0.26	18.12±0.01
	50% RH	16.14±0.24	16.33±0.25	16.51±0.01
	70% RH	26.09±0.44	26.28±0.45	26.63±0.01
Cathode	30% RH	18.01±0.25	17.76±0.25	18.09±0.01
	50% RH	16.06±0.24	16.01±0.25	16.26±0.01
	70% RH	25.76±0.44	26.00±0.45	26.32±0.01

<sup>a</sup> The error is the uncertainty of the water balance setup.

<sup>b</sup> The error is the uncertainty of the precision balance used to weigh the condensed water.

good agreement with each other, confirming the capability of the experimental setup developed in this thesis to measure water flux in the gas-vapor mixture.

### 2.3.2 In-situ validation

The in-situ validation experiments were carried out using the same experimental configuration as later discussed in Chapter 4 under 80 °C with 70% RH. The water balance setup was validated by comparing: (1) the molar rates of water produced in ORR measured using the developed water balance and estimated using eq. (2.10); and (2) the molar rates of water transport between the electrodes measured using the anode and cathode water balances during galvanodynamic polarization sweeps and current holds. The molar rate of water production in ORR measured using the developed water balance was calculated as the difference in the molar rates of water leaving and entering the fuel cell, and the molar rates of water transport between the electrodes measured using anode and cathode water balances were calculated using eqs. (2.8) and (2.9), respectively. The results of the in-situ validation experiments in Figure 2.3 show that the molar rate of water production that was measured using the developed water balance was in good agreement with the theoretical value

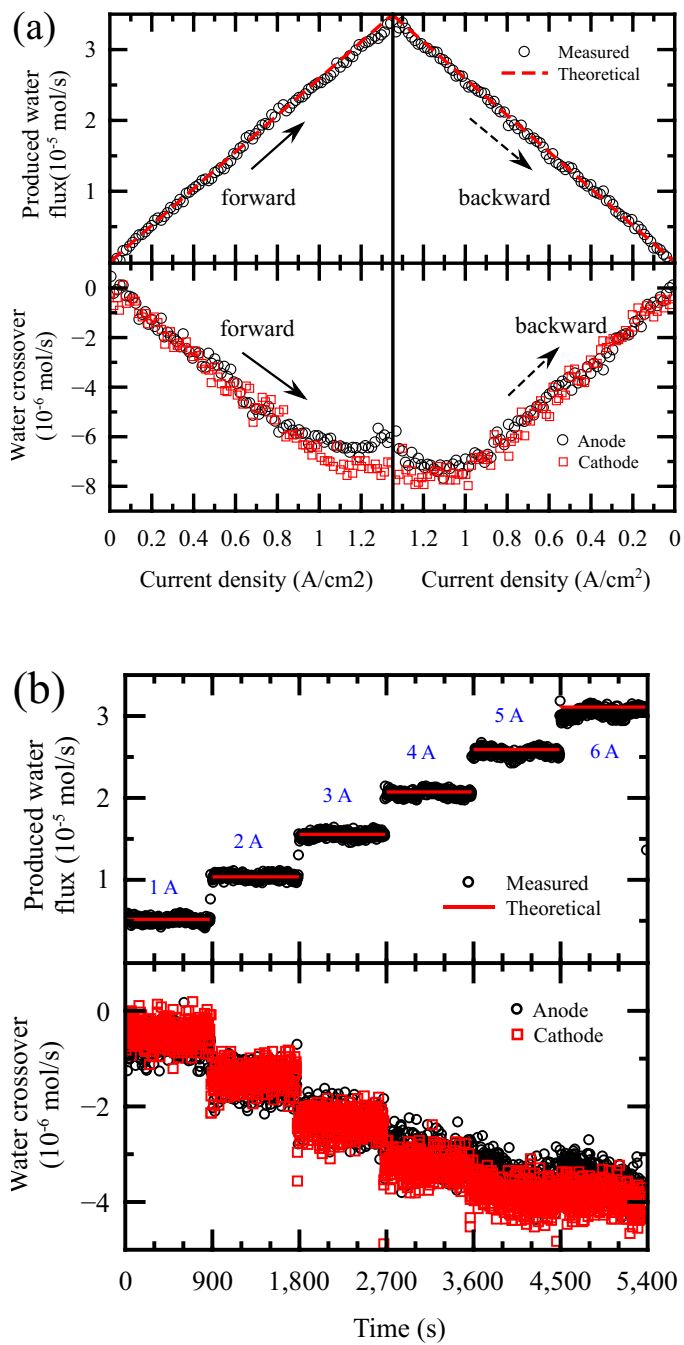


Figure 2.3: In-situ validation results obtained from (a) polarization and (b) current hold experiments at 80 °C and 70% RH with 29BC in the cathode. Positive values of water crossover direct from the anode to the cathode electrode.

estimated using eq. (2.10). This also indicates that there was no significant liquid water accumulation in the porous media under 80 °C and 70% RH. The molar rate of water transport between the electrodes measured using the anode and cathode water balances was also in good agreement. Furthermore, as seen in Figure 2.3a, both anode and cathode results indicated that the water crossover stopped increasing when current density reached approximately 1.1 A/cm<sup>2</sup>, which was likely due to the increased electro-osmotic drag of water from anode to cathode. These observations confirm the capability of the water balance setup developed in this thesis to track the real-time water fluxes entering and leaving the anode and cathode of an operating PEMFC and thus to calculate the water crossover and liquid water accumulation in the electrodes.

## **2.4 Electrochemical characterization**

### **2.4.1 Experimental conditions**

In this thesis, two cells were assembled and tested for each PEMFC configuration to verify the reproducibility of the measurements. Water transport in PEMFCs was investigated under four conditions using hydrogen in the anode (0.5 slpm) and air in the cathode (0.5 slpm): 1) 60 °C with 70% RH; 2) 80 °C with 30% RH; 3) 80 °C with 50% RH; and 4) 80 °C with 70% RH. The flow rates were fixed at 0.5 slpm for hydrogen and air, respectively corresponding to stoichiometric factors between 8.5 and 11.2 and from 3.5 to 4.7 at 1 A/cm<sup>2</sup> for the selected operating conditions. In all tests, a backpressure of 50 kPa (gauge) was applied and controlled by an automatic backpressure regulator (Scribner 850BP). During all experiments, absolute pressures, RHs, temperatures and reactant flow rates were recorded every second to calculate the real-time fluxes of water that enter and leave the anode and cathode of the operating PEMFCs.

## **2.4.2 Electrochemical characterization**

In this thesis, electrochemical characterizations were carried out as follows. During polarization-curve and current hold experiments, current density, voltage and current interrupt resistance (CIR, estimated using the current interrupt method [132]) were measured every second.

### **2.4.2.1 Cell conditioning**

After fuel cell assembly, the cell was conditioned at 80 °C and 80% RH using hydrogen (fixed 0.3 slpm) and air (fixed 0.6 slpm) for 16 half-hour-long steps from 0.1 to 4 A (except 0.1 to 0.5 A for CL design 3 with 40 wt.% NL in Chapter 5) with 30-second open circuit voltage (OCV) intervals between each step.

### **2.4.2.2 Electrochemical surface area measurement**

Electrochemical surface area was obtained from cyclic voltammetry (CV), before and after all in-situ tests, with 40 mV/s scan rate from 0.05 to 0.8 V at 50 °C using fully humidified hydrogen (0.2 slpm) and nitrogen (0.05 slpm) as the gas supply to the anode and cathode, respectively. The ECSAs at the beginning of tests (BOT) and the end of tests (EOT) were estimated from the hydrogen adsorption and desorption peaks (between 0.05 and 0.4 V) using the method discussed in Ref. [132].

### **2.4.2.3 Polarization curve measurement**

At each operating condition, the cell was first preconditioned by holding for 10 minutes at 0.2 A/cm<sup>2</sup>. The polarization curve was then measured forward and backward in the galvanodynamic mode with currents ranging from 0 A (OCV) to 10 A (or 0.3 V, whichever was reached earlier) in 5 mA steps every second with one full sweep.

### **2.4.2.4 Current hold experiment**

Current hold experiments were performed by holding the cell at current densities from 0.2 to 1.4 A/cm<sup>2</sup> for 15 minutes at each current density. The initial 10 minutes

were used to stabilize the cell under the given current density, and the averaged data measured during the last 5 minutes were used to calculate the water fluxes.

## **2.5 Conclusions**

An experimental water balance setup for quantifying the real-time water transport between the electrodes and accumulation in the operating PEMFCs was developed and validated in this chapter. The water balance setup, composed of four relative humidity and temperature sensors, four absolute pressure transducers and two gas flowmeters, was used to track the real-time molar flow rates of water that enter and leave the anode and cathode of the operating PEMFCs. The developed setup makes it possible to detect when flooding starts in the MEA and in which compartment it takes place. Therefore, the presented setup can be turned into a relatively simple and cost-effective strategy for real-time monitoring, detection, and prevention of flooding in industrial applications.

## Chapter 3

# Water Transport in Anion and Proton Exchange Membranes<sup>1</sup>

Water transport in proton exchange membrane fuel cells is crucial because water not only affects the supply of reactant but also the durability of the catalyst. In anion exchange membrane fuel cells, water transport is even more important because water not only is produced in the anode but also functions as a reactant in the cathode. Therefore, accurate measurement of water transport properties of proton and anion exchange membranes is paramount for membrane design to improve fuel cell performance and durability. The water transport properties of Nafion<sup>®</sup> membranes have been widely measured, and the relative importance of interfacial exchange was found to depend on the thickness and water content; however, results in the literature for diffusivity and interfacial rates in Nafion<sup>®</sup> vary by several orders of magnitude. Only few studies reported water transport properties of AEMs; and even in those limited studies, interfacial transport rates were either not considered in data analysis or not given as a function of water activity. In this chapter, the water balance setup,

---

<sup>1</sup>Parts of this chapter are reproduced from the following publication:

1. F. Wei, A. Kosakian, J. Liu, J. Kracher, R. Khan, and M. Secanell, “Water transport in anion and proton exchange membranes,” *Journal of Power Sources*, vol. 557, p. 232 494, 2023. DOI: <https://doi.org/10.1016/j.jpowsour.2022.232494>.
2. F. Wei, A. Kosakian, J. Liu, J. Kracher, R. Khan, and M. Secanell, “Corrigendum to “Water transport in anion and proton exchange membranes” [J. Power Sources 557 (2023) 232494],” *Journal of Power Sources*, vol. 576, p. 233 214, 2023, ISSN: 0378-7753

Author contributions are detailed in the Preface of this thesis.

based on the liquid-vapor permeation method, was used to determine the water flux across the Nafion<sup>®</sup> N211, N212, N115 and N117 with varying thicknesses (from 1 to 7 mil) and fabrication methods (cast and extruded) at multiple operating conditions. Using three numerical models developed in this chapter, i.e., diffusion-dominated, desorption-dominated and combined diffusion-and-desorption transport, the results of water flux across the membrane were analyzed. The measured rates of water desorption were compared with literature to verify whether the developed setup is capable of correctly identifying interfacial transport as limiting water transport mode in liquid-equilibrated Nafion<sup>®</sup> membranes. The same methodology was applied to analyze the anion exchange membranes, i.e., Aemion<sup>®</sup> AH1-HNN8-50-X, Fumapem<sup>®</sup> FAA-3-30/50, and Versogen<sup>™</sup> PiperION-A40.

## 3.1 Materials and experiments

### 3.1.1 Sample preparation and cell assembly

Four proton exchange (Nafion<sup>®</sup> N115, N117, N211 and N212) and four anion exchange (Aemion<sup>®</sup> AH1-HNN8-50-X, Fumapem<sup>®</sup> FAA-3-30, Fumapem<sup>®</sup> FAA-3-50 and Versogen<sup>™</sup> PiperION-A40) membranes were investigated (Table 3.1). Two samples, 4 cm by 4 cm in size, of each membrane (three samples in the case of N117) were prepared and tested to assess repeatability. Nafion<sup>®</sup> N115 and N117 were pre-treated in boiling deionized (DI) water for 30 minutes before testing, while N211 and N212 were tested as received. Anion exchange membranes were converted to bicarbonate form ( $\text{HCO}_3^-$ ) by first immersing them in an aqueous solution of 1 M sodium bicarbonate ( $\text{NaHCO}_3$ ) at room temperature for 48 hours, replacing the solution after the first 24 hours, and then soaking them in DI water for 24 hours before rinsing them with DI water three times to remove the residual sodium bicarbonate.

The membranes were sandwiched between 25 mm by 25 mm SGL 29AA gas diffusion layers (GDLs). The GDL-membrane assembly was then introduced into a

Table 3.1: Properties of the membranes used in this work.

Membrane	Thickness <sup>a</sup> , $\mu\text{m}$	Dry density, $\text{g}/\text{cm}^3$	Equivalent weight, $\text{g}/\text{mol}_{\text{ion}}$	Liquid-equilibrated water content, $\text{mol}_{\text{H}_2\text{O}}/\text{mol}_{\text{ion}}$
Nafion <sup>®</sup> N115	127	2 [43, 217]	1100 [46, 227, 228]	22 [43, 227, 229, 230]
Nafion <sup>®</sup> N117	183	2 [43, 217]	1100 [46, 227, 228]	22 [43, 227, 229, 230]
Nafion <sup>®</sup> N211	25	2 [43, 217, 218]	1100 [218, 219]	22 [43, 230]
Nafion <sup>®</sup> N212	50	2 [43, 217, 218]	1100 [218, 219]	22 [43, 230]
Aemion <sup>®</sup> AH1-HNN8-50-X	50	1.15 <sup>b</sup> [178]	441 <sup>c</sup> [178]	25 [178]
Fumapem <sup>®</sup> FAA-3-30	30	1.46 [231]	552 <sup>c</sup> [231]	12.5 [231]
Fumapem <sup>®</sup> FAA-3-50	50	1.46 [231]	552 <sup>c</sup> [231]	12.5 [231]
Versogen <sup>™</sup> PiperION-A40	40	1.30 [231]	469 <sup>c</sup> [231]	13.8 [231]

<sup>a</sup> Provided by the manufacturer.

<sup>b</sup> Computed using equations (14)–(16) and data from Table 1 of Ref. [178].

<sup>c</sup> Equivalent weight is computed as a reciprocal of the reported ion-exchange capacity.

Scribner fuel cell hardware with 14 parallel flow channels. The length, width, depth and number of the flow channels was 25 mm, 0.86 mm, 1 mm and 14, respectively. The width of the land between two flow channels was 0.82 mm. Two 6-mil PTFE-coated fiberglass gaskets with a 25 mm by 25 mm window were used on each side of the GDL-membrane assembly to prevent gas leakage and provide consistent contact between the membrane and GDL, which was confirmed using pressure-sensitive paper.

### 3.1.2 Experimental setup and conditions

Figure 3.1 shows the experimental setup used to measure the water transport properties of the membranes. As shown in Figures 3.1a and 3.1b, the setup consisted mainly of a Scribner 850e fuel cell station, two custom-built water balances, the cell hardware and a peristaltic pump (GILSON<sup>®</sup> MINIPULS 3). The temperature of the anode and cathode end plates of the fuel cell hardware was controlled separately. In this chapter, the water transport properties were measured at 60, 70 and 80 °C. The two sides of the tested cell were fed a nitrogen-vapor mixture and liquid water, respectively. On the dry side, nitrogen gas at 0.5 slpm with varying RH (10–50%) was fed to the cell. On the wet side, DI water was first preheated to a temperature of 10 °C higher than that of the cell and then circulated through the cell using the peristaltic pump at a fixed rate of 150 cm<sup>3</sup>/min, where it was assumed to have reached thermal equilibrium with the cell hardware. Two custom-built water balances, consisting of relative humidity and temperature sensors (Sensirion SHT85) and pressure transducers (Omega MMA030USBHK2C0T8A6CE), were located at the inlet and outlet of the tested cell to measure the relative humidity, temperature, and absolute pressure of the gas-vapor mixture. Special measures were taken to eliminate the presence of liquid water in the cell's channel and the setup's tubing so as to not underestimate the water flux and to avoid electrical short of the RH and temperature sensors. To prevent condensation, the inlet and outlet water balances were immersed in heated

water baths set at the same temperature as the tested cell and heating tapes were used to cover exposed pipes with the inlet and outlet heating tape temperature set to the cell temperature and 105 °C, respectively. The outlet water balance was open to the atmosphere.

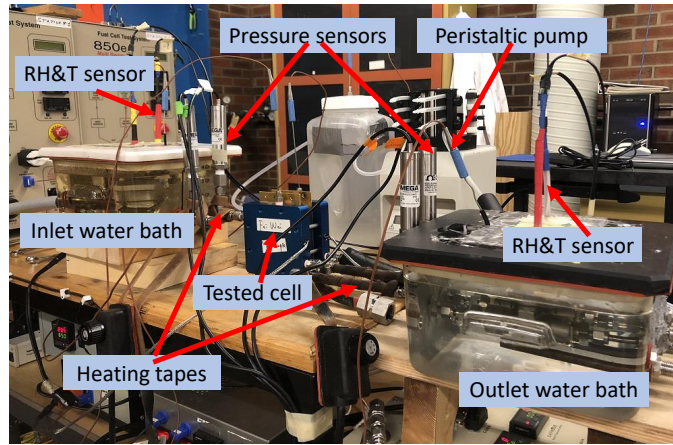
During the experiments, the dry nitrogen flow rate measured using an Alicat flowmeter (M-5SLPM-D/5M), the RH and temperature, and the absolute pressure were recorded at 1 Hz. For each experimental condition in this chapter, the measurement was carried out for 1.5 hours and the experimental data obtained in the last 30 minutes were averaged and used in the simulations discussed in Section 3.2.

## 3.2 Mathematical model

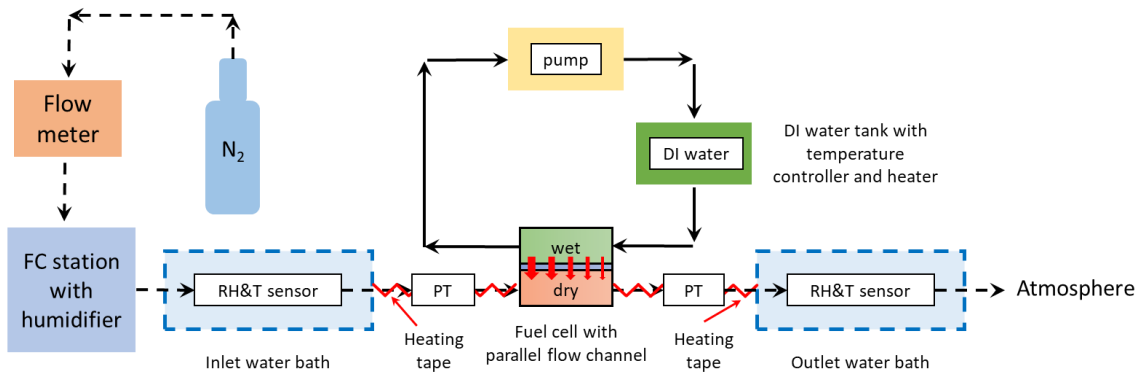
The experimental data measured in this chapter was analyzed with the mathematical model developed by Aslan Kosakian, a post-doctoral fellow at ESDLab. The model is described in detail as follows.

The developed model is pseudo-2D, with the first dimension across the membrane ( $z$ ) and the second dimension along the dry channel ( $x$ ), as shown in Figure 3.1c. A single dry channel of effective width equal to the product of the number of the parallel channels and the width of a single channel is considered. Assuming the interfacial resistance to water transport across the membrane-liquid boundary is negligible [43, 175, 177, 184], the water content on that side of the membrane is assumed constant and equal to the known liquid-equilibrated value. Therefore, mass transport in the wet channel is not considered. Since GDLs do not contribute significantly to the overall resistance to water transport in permeation setups [232], mass transport in those layers is not modeled, and distribution of water vapor in GDLs is assumed uniform. The rest of the model assumptions are as follows:

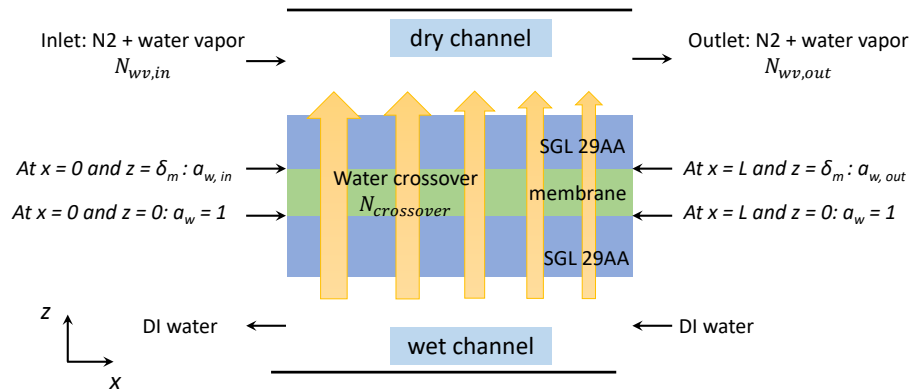
- the setup is operated at steady state;
- membrane swelling is not considered, and its thickness is assumed constant;



a)



b)



c)

Figure 3.1: Experimental setup for the water transport properties measurements of AEM and PEM materials: a) the experimental setup, b) schematic of the setup and c) schematic of water transport in the cell.

- all gases are assumed to obey the ideal-gas law;
- bulk transport of water in the membrane is governed by Fick’s law;
- since both sides of the cell are maintained at similar pressure, diffusion is assumed to be the main mode of transport of water within the membrane, and its permeation is assumed negligible.

To analyze the relative contribution of the bulk and interfacial transport mechanisms to the overall water transport across the membrane, three model modifications were considered. In the first mathematical model, identical to that of Motupally et al. [189], only the diffusion of water across the sample was simulated. In that case, the exchange of water at the membrane-gas interface was assumed infinitely fast. In the second model, the membrane was assumed to be fully liquid-equilibrated with no concentration gradient within it, and the transport was assumed to be fully governed by desorption at the membrane-gas interface. Both diffusion and desorption were taken into account in the third model.

### 3.2.1 Governing equations

#### 3.2.1.1 Model 1: Diffusion-dominated transport

Water conservation and transport in the dry channel is described with the following equation [189]:

$$\frac{dN_{\text{wv},x}}{dx} - \frac{w_{\text{PEM}}}{w_{\text{ch}}h} N_{\text{wv},z} = 0, \quad (3.1)$$

where  $N_{\text{wv}}$  is the molar flux of water vapor ( $\text{mol}/(\text{cm}^2 \cdot \text{s})$ ),  $w_{\text{PEM}}$  and  $w_{\text{ch}}$  are the width of the membrane (cm) and the effective width of the channel (cm), respectively, and  $h$  is the channel depth (cm). The flux of water vapor along the channel is related to the inlet flux of nitrogen through

$$N_{\text{wv},x} = \frac{x_{\text{wv}}}{1 - x_{\text{wv}}} N_{\text{N}_2,x}. \quad (3.2)$$

Note that the nitrogen flux is constant along the channel due to the assumption that no gas crosses the membrane. Inside the membrane,  $N_{\text{wv},z}$  is a diffusive flux of absorbed water and is given by [189]

$$N_{\text{wv},z} = -\frac{\rho_{\text{m,dry}}}{\text{EW}} D_{\lambda}(\lambda, T) \frac{d\lambda}{dz}, \quad (3.3)$$

where  $\rho_{\text{m,dry}}$  is the dry membrane density ( $\text{g}/\text{cm}^3$ ), EW is its equivalent weight ( $\text{g}/\text{mol}_{\text{SO}_3^-}$  in Nafion<sup>®</sup> and  $\text{g}/\text{mol}_{\text{mol}_{\text{N}^+}}$  in the alkaline counterparts),  $\lambda$  is the water content ( $\text{mol}_{\text{H}_2\text{O}}/\text{mol}_{\text{SO}_3^-}$  for Nafion<sup>®</sup> and  $\text{mol}_{\text{H}_2\text{O}}/\text{mol}_{\text{N}^+}$  for AEMs), and  $D_{\lambda}(\lambda, T)$  is the diffusion coefficient ( $\text{cm}^2/\text{s}$ ). At a given location along the channel and at steady state, the water vapor flux in eq. (3.3) is the same throughout the membrane, and thus its integration across the membrane gives

$$N_{\text{wv},z} = -\frac{\rho_{\text{m,dry}}}{\text{EW}\delta_{\text{m}}} \int_{\lambda(z=0)}^{\lambda(z=\delta_{\text{m}})} D_{\lambda}(\lambda, T) d\lambda, \quad (3.4)$$

where  $\delta_{\text{m}}$  is membrane thickness (cm),  $\lambda(z=0)$  is the known liquid-equilibrated water content, and  $\lambda(z=\delta_{\text{m}})$  is the water content at the membrane-gas interface. Substituting this result into eq. (3.1), the following ordinary differential equation (ODE) is obtained with respect to the molar fraction of water vapor in the channel,  $x_{\text{wv}}$  [189]:

$$\frac{dx_{\text{wv}}}{dx} = -\frac{w_{\text{m}}}{w_{\text{ch}}h} \frac{(1-x_{\text{wv}})^2}{N_{\text{N}_2,x}} \frac{\rho_{\text{m,dry}}}{\text{EW}\delta_{\text{m}}} \int_{\lambda(z=0)}^{\lambda(z=\delta_{\text{m}})} D_{\lambda}(\lambda, T) d\lambda. \quad (3.5)$$

The molar fraction of water vapor at the starting point of the channel,  $x_{\text{wv}}^{\text{in}}$ , is used as the initial condition. It is calculated from the experimentally measured inlet vapor pressure,  $p_{\text{wv}}^{\text{in}}$ , and the absolute gas pressure at the inlet,  $p_{\text{tot}}^{\text{in}}$ :

$$x_{\text{wv}}^{\text{in}} = \frac{p_{\text{wv}}^{\text{in}}}{p_{\text{tot}}^{\text{in}}}.$$

While the lower limit of the integral in eq. (3.5) is the liquid-equilibrated water content in the membrane and is constant, the upper limit depends on the relative

humidity at the given location  $z$  of the channel. This relative humidity is related to the molar fraction of water vapor through

$$\text{RH} = \frac{x_{\text{wv}} p_{\text{tot}}}{p_{\text{wv,sat}}}, \quad (3.6)$$

where  $p_{\text{wv,sat}}$  is the pressure of saturated water vapor at the given temperature. Because the upper limit of the integration depends on the solution variable and because  $D_\lambda$  is a highly nonlinear function of  $\lambda$ , ODE eq. (3.5) is solved numerically using the `solve_ivp` function from SciPy [233] with the adaptive LSODA algorithm [234, 235]. The absolute and relative solution tolerances of  $10^{-3}$  in the ODE solver were found optimal in terms of accuracy and computational time. Ten times stricter tolerances resulted in an insignificant change in the outlet vapor molar fractions (e.g., within 0.05% for Nafion<sup>®</sup> N211). The computational time of each diffusion simulation for a single experimental condition was on the order of 0.1 s using Intel<sup>®</sup> Xeon<sup>®</sup> E5-2690 v2 CPU at 3.00 GHz.

### 3.2.1.2 Model 2: Desorption-dominated transport

Equations (3.1) and (3.2) describe the change in water molar fraction along the dry channel due to the crossover through the membrane. They are still valid in this modification of the model where only desorption at the membrane-gas interface is considered. However, the crossover flux  $N_{\text{wv},z}$  in eq. (3.1) is no longer assumed to be diffusive. This flux is now described by the desorption of water at the membrane-gas interface:

$$N_{\text{wv},z} = \frac{\rho_{\text{m,dry}}}{\text{EW}} k_{\text{des}}(\lambda(z = \delta_{\text{m}}) - \lambda_{\text{eq}}(x_{\text{wv}})), \quad (3.7)$$

where  $k_{\text{des}} = k_{\text{des}}(\lambda(z = \delta_{\text{m}}), T)$  is the desorption rate that depends on water content at the interface and temperature [133]. Equilibrium water content,  $\lambda_{\text{eq}}(x_{\text{wv}})$ , is determined from a sorption isotherm. Substituting eqs. (3.2) and (3.7) into eq. (3.1) and rearranging, one obtains an ODE for the water molar fraction along the dry channel:

$$\frac{dx_{\text{wv}}}{dx} = \frac{w_{\text{m}}}{w_{\text{ch}} h} \frac{(1 - x_{\text{wv}})^2}{N_{\text{N}_2,x}} \frac{\rho_{\text{m,dry}}}{\text{EW}} k_{\text{des}}(\lambda(z = \delta_{\text{m}}) - \lambda_{\text{eq}}(x_{\text{wv}})). \quad (3.8)$$

Due to the assumption of no concentration gradient across the membrane, the water content at the membrane-gas interface,  $\lambda(z = \delta_m)$ , is known in this case and is equal to the equilibrium water content of the given membrane in contact with liquid water. Equation (3.8) is solved the same way as eq. (3.5). The computational time was on the order of 1 ms for a single simulation.

### 3.2.1.3 Model 3: Combined diffusion-and-desorption transport

When the concentration gradient across the membrane cannot be neglected,  $\lambda(z = \delta_m)$  in eq. (3.8) is unknown. It is determined from the balance of the flux of water diffusion across the membrane (eq. (3.4)) and the flux of water desorption (eq. (3.7)):

$$-\frac{1}{\delta_m} \int_{\lambda(z=0)}^{\lambda(z=\delta_m)} D_\lambda d\lambda = k_{\text{des}}(\lambda(z = \delta_m) - \lambda_{\text{eq}}(x_{\text{wv}})). \quad (3.9)$$

Equations (3.8) and (3.9) represent a system of governing equations for the diffusion-desorption model. This system must be solved iteratively, as it is implicit in  $\lambda(z = \delta_m)$ .

At the first iteration of the ODE solver,  $x_{\text{wv}}$  corresponds to the known inlet RH. Therefore,  $\lambda_{\text{eq}}(x_{\text{wv}})$  is known at that point, and eq. (3.9) is solved with respect to  $\lambda(z = \delta_m)$  using Brent's bracketing method [236, 237] from SciPy [233]. Then, eq. (3.8) is advanced to determine  $x_{\text{wv}}$  at the next channel location, and the process repeats. The computational time for a single simulation was on the order of 1 s.

## 3.2.2 Water uptake

Equations (3.5), (3.8), and (3.9) involve the water content at the membrane-gas interface,  $\lambda_{\text{eq}}(x_{\text{wv}})$ . Its value is found through the sorption isotherm (the water-uptake curve) for the given material. For all of the samples tested in this chapter, the sorption isotherm is given by the following polynomial for water activity,  $a_w$  (equilibrium RH):

$$\lambda_{\text{eq}} = \alpha_0 + \alpha_1 a_w + \alpha_2 a_w^2 + \alpha_3 a_w^3, \quad 0 < a_w < 1. \quad (3.10)$$

Equation (3.10) does not contain a temperature correction due to the weak dependence of water uptake in Nafion<sup>®</sup> membranes on temperature (the available uptake data at 25–80 °C [168, 227, 228, 238–244] does not exhibit a clear temperature trend and has a relatively low sensitivity to the change in temperature) and the scarcity of data for AEMs.

The polynomial coefficients for each membrane are listed in Table A.1. The uptake curve for Nafion<sup>®</sup> N117 was obtained by Springer et al. [239] by fitting Zawodzinski et al.’s [168] measurements at 30 °C. The same uptake was assumed for Nafion<sup>®</sup> N115, which differs from N117 only in thickness. The rest of the sorption isotherms were obtained in this chapter as discussed in Section A.1.1 of the Appendix by fitting experimental data from Refs. [228, 231, 238, 243–247].

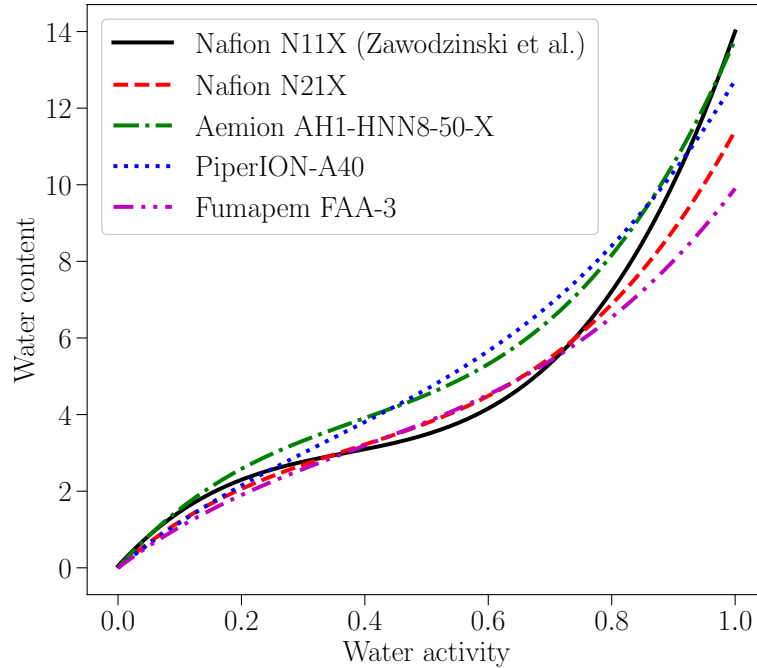


Figure 3.2: Comparison of the sorption isotherms for Nafion<sup>®</sup> N11X, Nafion<sup>®</sup> N21X, Aemion<sup>®</sup> AH1-HNN8-50-X (HMT-PMBI), Fumapem<sup>®</sup> FAA-3, and Versogen<sup>™</sup> PiperION-A40 membranes (eq. (3.10) and Table A.1). The individual fits are shown in Figures A.1a, A.2a, A.3a, and A.4a.

Figure 3.2 shows a comparison of the sorption isotherms (eq. (3.10)) with coeffi-

cients from Table A.1. It can be seen from the comparison (Figures 3.2 and A.1a) that the fabrication method of Nafion<sup>®</sup> does not seem to have a strong influence on its water uptake. The water uptake by the considered alkaline membranes is not too different from that by acidic Nafion<sup>®</sup>. The uptake by Aemion<sup>®</sup> and Fumapem<sup>®</sup> materials (Figures 3.2, A.2a and A.3a), similarly to that by Nafion<sup>®</sup>, does not appear to have a strong dependence on temperature, although more experimental data are needed to verify this conclusion.

The maximum water content in vapor-equilibrated Nafion<sup>®</sup> is  $14.0 \text{ mol}_{\text{H}_2\text{O}}/\text{mol}_{\text{SO}_3^-}$  and  $11.4 \text{ mol}_{\text{H}_2\text{O}}/\text{mol}_{\text{SO}_3^-}$  for N11X and N21X, respectively, as seen in Figure 3.2. Both values are significantly lower than the water content in liquid-equilibrated Nafion<sup>®</sup>,  $22 \text{ mol}_{\text{H}_2\text{O}}/\text{mol}_{\text{SO}_3^-}$  (Table 3.1). This discrepancy in the amount of water in Nafion<sup>®</sup> equilibrated with saturated vapor and with liquid water is known as Schröder’s paradox [43, 248]. One possible explanation for this phenomenon is the difference in the morphological structure of Nafion<sup>®</sup> in contact with gaseous and liquid water: a hydrophobic, fluorine-rich skin layer is formed at the Nafion<sup>®</sup>-gas interface and causes an additional transport resistance as compared with the Nafion<sup>®</sup>-liquid boundary [43, 172, 184, 249]. It is noteworthy that Schröder’s paradox does not imply discontinuity in the water content. For instance, Hwang et al. [184] conducted X-ray microtomography measurements of water-content distribution across a Nafion<sup>®</sup> membrane exposed to dry gas and liquid water on its opposite sites; the reported distributions are continuous with no abrupt changes in the internal water content.

Schröder’s paradox appears to occur in AEMs as well. It is as significant in Aemion<sup>®</sup> AH1-HNN8-50-X as it is in Nafion<sup>®</sup>, with the water content changing from  $13.8 \text{ mol}_{\text{H}_2\text{O}}/\text{mol}_{\text{N}^+}$  under vapor-equilibrated conditions (Figure 3.2) to  $25 \text{ mol}_{\text{H}_2\text{O}}/\text{mol}_{\text{N}^+}$  in contact with liquid water (Table 3.1). This difference in the water content is far less noticeable in Versogen<sup>™</sup> PiperION-A4 ( $12.7$  and  $13.8 \text{ mol}_{\text{H}_2\text{O}}/\text{mol}_{\text{N}^+}$ ) and Fumapem<sup>®</sup> FAA-3 ( $9.9$  and  $12.5 \text{ mol}_{\text{H}_2\text{O}}/\text{mol}_{\text{N}^+}$ ).

### 3.2.3 Water diffusivity

Water diffusivity in the polymer electrolyte in eqs. (3.5) and (3.9) was computed as [133, 168, 189, 190, 239]

$$D_\lambda = \frac{\partial \ln a_w}{\partial \ln \lambda} D_\mu = \frac{\partial \ln a_w}{\partial \ln \lambda} \beta_D \alpha_\lambda f_V \exp \left[ \beta_E \frac{E_a}{R} \left( \frac{1}{303} - \frac{1}{T} \right) \right], \quad (3.11)$$

where  $D_\mu$  is the empirical expression for the diffusion coefficient of water related to the chemical-potential gradient suggested by Weber and Newman [190] based on the analysis of experimental data. Coefficient  $\alpha_\lambda$  (cm<sup>2</sup>/s) in eq. (3.11) is a constant prefactor,

$$f_V = \frac{\lambda V_w}{V_e + \lambda V_w}$$

is the volume fraction of water in the ionomer,

$$V_w = \frac{M_{\text{H}_2\text{O}}}{\rho_{\text{lw}}}$$

is the molar volume of water (cm<sup>3</sup>/mol),

$$V_e = \frac{\text{EW}}{\rho_{\text{m, dry}}}$$

is the molar volume of the dry polymer (cm<sup>3</sup>/mol), and  $E_a$  is the activation energy (J/mol). Scaling factors  $\beta_D$  and  $\beta_E$  in eq. (3.11) that modify the values of  $\alpha_\lambda$  and  $E_a$  were estimated based on the experimental data obtained in this chapter as discussed later. This approach was selected over the direct quantification of  $\alpha_\lambda$  and  $E_a$  in an attempt to make the optimization parameters as close to each other by magnitude as possible and thus improve the quality of the fit. For all membranes, reference values  $\alpha_\lambda = 2.72 \cdot 10^{-5}$  cm<sup>2</sup>/s and  $E_a = 20$  kJ/mol were used as estimated by Ge et al. [133] and Yeo and Eisenberg [250] for Nafion<sup>®</sup>. The fitted scaling factors indicate the relative change in the diffusivity prefactor and the activation energy with respect to their reference values.

The Darken factor [43, 133, 189, 190],

$$\mathcal{D} = \frac{\partial \ln a_w}{\partial \ln \lambda} \quad (3.12)$$

in eq. (3.11) was computed by inverting the experimentally measured isotherms from Refs. [228, 231, 238, 239, 243, 244, 247], fitting the resulting curves with eq. (A.8) using the SLSQP algorithm in SciPy [233] following the same procedure that was used for the water-uptake curves, and analytically differentiating the fit using Maxima [251]. The details of this approach are provided in Section A.1.2 of the Appendix. As discussed in that section, this approach results in a single diffusivity expression (as opposed to the separate expressions for the low and high water content [133, 189]) and involves only one curve-fitting procedure, which minimizes the numerical error.

The fitted inverse sorption isotherms are provided in eq. (A.8) and Table A.2. The analytically computed Darken factor was of the form

$$\mathcal{D} = \frac{\delta_0 + \delta_1\lambda + \delta_2\lambda^2 + \delta_3\lambda^3 + \delta_4\lambda^4}{\varepsilon_0 + \varepsilon_1\lambda + \varepsilon_2\lambda^2 + \varepsilon_3\lambda^3 + \varepsilon_4\lambda^4 + \varepsilon_5\lambda^5}. \quad (3.13)$$

The coefficients of the equation above are given in Table A.3. The Darken factors derived in this chapter for Nafion<sup>®</sup> N11X, Nafion<sup>®</sup> N21X, Aemion<sup>®</sup> AH1-HNN8-50-X, Fumapem<sup>®</sup> FAA-3, and Versogen<sup>™</sup> PiperION-A40 membranes are compared in Figure A.5.

The peak in the Darken factor at the water content of about 2–3 mol<sub>H<sub>2</sub>O</sub>/mol<sub>ion</sub> is due to the plateau in the sorption isotherms at the intermediate water activity (Figure 3.2). The Darken factors shown in Figure A.5 are extended beyond the maximum water content in vapor-equilibrated membranes at unit water activity found from the sorption isotherms (eq. (3.10) and Table A.1) to the liquid-equilibrated water content from Table 3.1. In that region, the Darken factors are quasi-linear, in agreement with the results of Motupally et al. [189] and Ge et al. [133]. As in references [133, 189], it was assumed in this chapter that the derived Darken factors and thus diffusion coefficients of water were valid between the vapor-equilibrated and liquid-equilibrated water contents.

### 3.2.4 Interfacial water transport

The expression for the rate of water desorption at the membrane-gas interface was adopted from Ge et al. [133]:

$$k_{\text{des}} = \beta_{\text{d}} \alpha_{\text{des}} f_{\text{V}} \exp \left[ \beta_{\text{E}} \frac{E_{\text{a}}}{R} \left( \frac{1}{303} - \frac{1}{T} \right) \right], \quad (3.14)$$

where  $\alpha_{\text{des}} = 4.59 \cdot 10^{-3}$  cm/s and  $E_{\text{a}}$  is assumed the same as for the diffusion coefficient (eq. (3.11)) [133]. Coefficients  $\beta_{\text{d}}$  and  $\beta_{\text{E}}$  are scaling factors that are determined as discussed later. The fitted scaling factors indicate the relative change in  $\alpha_{\text{des}}$  and  $E_{\text{a}}$  with respect to their reference values.

### 3.2.5 Input parameters

Cell-geometry parameters of the model and operating conditions are listed in Table 3.2. Properties of the membranes that were considered in this chapter are summarized in Table 3.1.

### 3.2.6 Fitting methodology

The scaling factors  $\beta_{\text{D}}$ ,  $\beta_{\text{E}}$ , and  $\beta_{\text{d}}$  in eqs. (3.11) and (3.14) were used as fitting parameters and were adjusted so that the model reproduced the experimentally measured water flux across the given membrane. The residual of the fit was defined as

$$\text{Residual} = \sqrt{\frac{\sum_{i=1}^N \left( \frac{N_{\text{wv},i}^{\text{exp}} - N_{\text{wv},i}^{\text{sim}}}{N_{\text{wv},i}^{\text{exp}}} \right)^2}{N}}, \quad (3.15)$$

where  $N$  is the total number of the experimental data points.

The fitting was performed in Python in two stages. First, a grid search was performed for the scaling factors with the `brute-force` method from SciPy [233]. Once the grid point with the lowest residual was found, it was supplied as an initial guess to the `Nelder-Mead` method [233] so that a more optimal solution would be found. The `Nelder-Mead` iterations were considered converged when the residual stopped changing within the given absolute tolerance, which was set to  $10^{-4}$ .

Table 3.2: Input parameters of the model: cell geometry and operating conditions.

<b>Parameter</b>	<b>Value</b>
<b>Geometry</b>	
Number of channels ( $n_{\text{ch}}$ )	14
Effective channel width ( $w_{\text{ch}}$ ), mm	11.48
Width of each channel ( $w_{\text{ch}}/n_{\text{ch}}$ ), mm	0.82
Channel depth ( $h$ ), mm	1
Channel length ( $L_{\text{ch}}$ ), cm	2.5
Membrane width ( $w_{\text{PEM}}$ ), cm	2.5
Membrane thickness ( $\delta_{\text{m}}$ ), cm	Table 3.1
<b>Operating conditions</b>	
Flow rate of dry N <sub>2</sub> , slpm	0.545
Temperature, °C	60, 70, 80
Inlet RH, %	10–50%

For all of the three models discussed in Section 3.2, the search bounds were  $10^{-3} \leq \beta_D \leq 10$ ,  $0.1 \leq \beta_E \leq 5$ , and  $10^{-3} \leq \beta_d \leq 100$ . Due to the large variation in the order of magnitude in  $\beta_D$  and  $\beta_d$ , the respective search bounds were split into smaller regions, and fitting was repeated until a solution that did not lie at the boundary was obtained. For model 1 (diffusion), fifty points were used in each direction ( $\beta_D$  and  $\beta_E$ ). Fifty nodes in  $\beta_E$  and two hundred nodes in  $\beta_d$  were used for model 2 (desorption). Twenty points in each direction ( $\beta_D$ ,  $\beta_E$ , and  $\beta_d$ ) were used in model 3 (diffusion and desorption).

## 3.3 Results and discussion

### 3.3.1 Nafion<sup>®</sup> proton exchange membranes

#### 3.3.1.1 Identification of the limiting mode of water transport via experiments and simulations

The molar flow rate of water crossing the tested membrane was measured and compared for Nafion<sup>®</sup> materials of different thickness in order to verify that the developed experimental setup and mathematical model correctly capture the dominance of the interfacial exchange in the overall transport of water [133, 166, 173–175, 178, 180–183]. Four Nafion<sup>®</sup> membranes were used for this purpose: N211 (25  $\mu\text{m}$ ), N212 (50  $\mu\text{m}$ ), N115 (127  $\mu\text{m}$ ), and N117 (183  $\mu\text{m}$ ).

The experimentally measured outlet RH and water flux across the Nafion<sup>®</sup> membranes are shown in Figure 3.3. The error bars are a combination of the experimental uncertainty (see Section 2.2.4 for their calculation) and the standard deviation between the measurements. As shown in the figure, outlet RH increased with the inlet RH but never reached saturation for the considered operating conditions and membranes. There were no significant differences in the measured outlet RH and water flux across the membranes of the same type (N21X or N11X) at 60, 70 and 80 °C. Since the water flux was independent of the sample thickness in each membrane pair (extruded or cast), the interfacial exchange was likely limiting the overall transport of water in Nafion<sup>®</sup>, in agreement with the previous literature [133, 166, 173–175, 178, 180–183]. The water flux measured across the cast N21X membranes was significantly different from that across the extruded N11X samples, and the discrepancy increased with temperature. One possible explanation for this could be that Nafion<sup>®</sup> N11X dried out more than N21X at the elevated temperature and thus bulk transport became non-negligible. Alternatively, the N11X and N21X samples may have had different sensitivity of water desorption to temperature due to their distinct fabrication methods. The mathematical models developed and discussed in Section 3.2 were used to analyze the measurements and to test the aforementioned hypotheses.

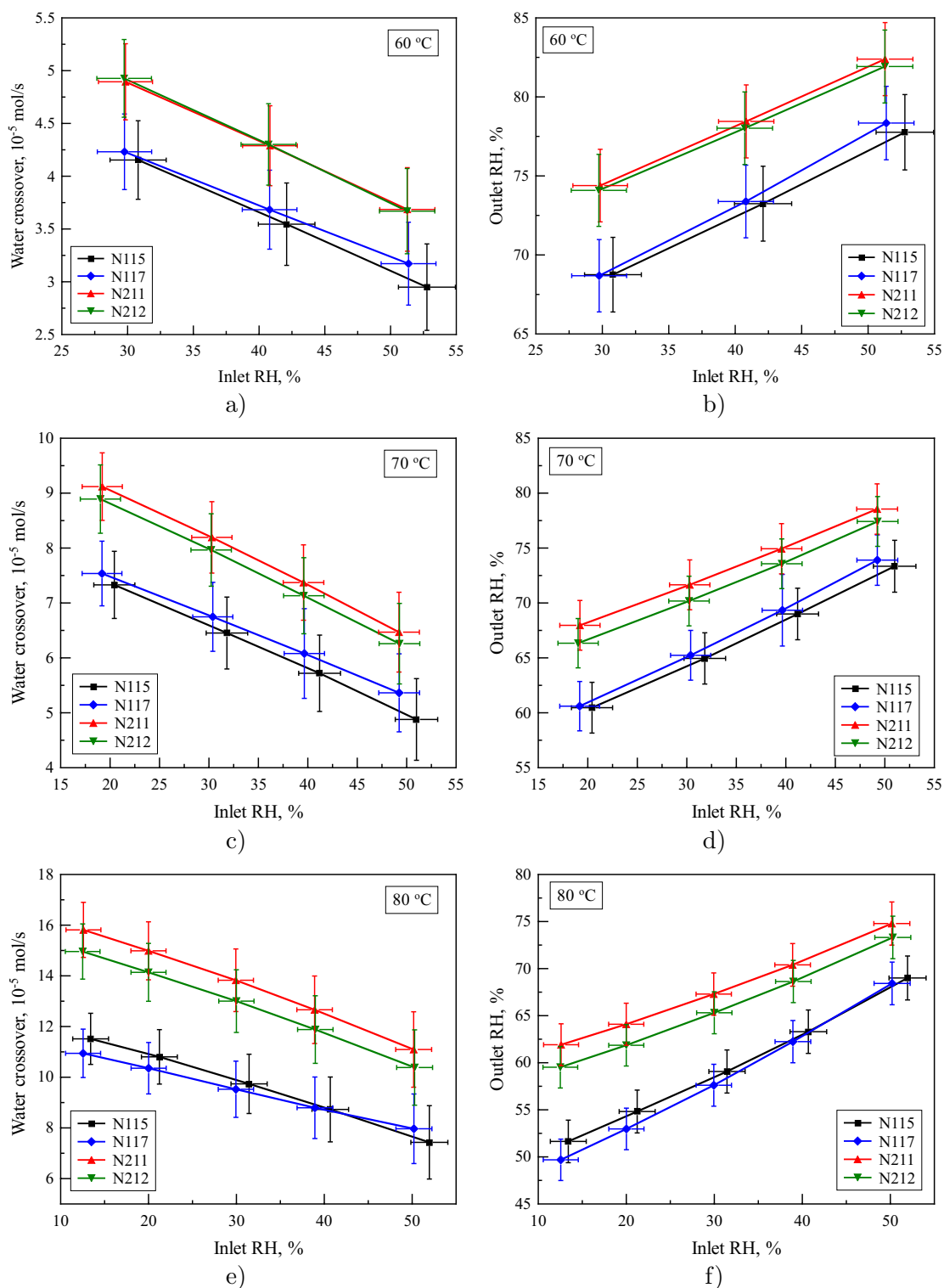


Figure 3.3: Experimental measurements of water transport through Nafion<sup>®</sup> N115, N117, N211 and N212 at 60, 70 and 80 °C: a), c) and e) water crossover; and b), d) and f) outlet RH.

The scaling factors for diffusivity, activation energy, and desorption rate (eqs. (3.11) and (3.14)) obtained by fitting the measured water fluxes are provided in Table 3.3. A good fit was obtained in all cases with the relative residual (eq. (3.15)) of 9–12%, which was reasonable considering the experimental water-flux uncertainty within 23.6%. The three fits were equivalent in the sense that the fitting residual was lower than the experimental uncertainty. The example data fits obtained with model 2 (desorption) are shown in Figure A.6 and discussed in Section A.2.1 of the Appendices. Models 1 (diffusion) and 3 (diffusion and desorption) produced nearly identical activation-energy scaling factors for each individual Nafion<sup>®</sup> membrane but an order of magnitude different diffusivity scaling factors. Models 2 (desorption) and 3, on the other hand, resulted not only in a matching activation energy but also in similar desorption coefficients. Since the combined model 3 encapsulates both diffusion- and desorption-limited scenarios, it is possible for it to achieve the same solution as the diffusion-limited model 1 if a large desorption scaling factor is used (making desorption fast). However, the fits with models 2 and 3 are more in line with the observation of desorption-limited transport made earlier based on the experimental data in Figure 3.3, where water flux across Nafion<sup>®</sup> N11X and N21X samples did not scale with their thickness. Therefore, the fits obtained with models 2 and 3 are deemed more realistic as compared with the results of the diffusion-dominated model 1. Since diffusion likely did not contribute significantly to the overall water transport through Nafion<sup>®</sup> membranes, it is possible that the lower water flux through the N11X membranes at the elevated temperature seen in Figure 3.3 was due to the different surface morphology of the considered Nafion<sup>®</sup> samples prepared with extrusion (N11X) and casting (N21X).

To further verify the dominance of interfacial transport in Nafion<sup>®</sup>, water-content drop across all membranes, computed with models 1 (diffusion) and 3 (diffusion and desorption), was plotted as illustrated in Figure 3.5 at the dry-channel inlet (solid lines) and outlet (dashed lines). All data are shown for the extreme case of 80 °C and

Table 3.3: Fitted scaling factors for diffusion, desorption, and activation energy for Nafion<sup>®</sup> membranes and the corresponding fitting residual and  $R^2$  values. The physical properties without scaling ( $\beta_D = \beta_d = \beta_E = 1$ ) are  $2.72 \cdot 10^{-5}$  cm<sup>2</sup>/s,  $4.59 \cdot 10^{-3}$  cm/s, and 20 kJ/mol, respectively.

Result	Model 1	Model 2	Model 3
	Diffusion	Desorption	Diffusion and desorption
<b>Nafion<sup>®</sup> N115</b>			
Diffusion ( $\beta_D$ )	0.158	—	3.74
Desorption ( $\beta_d$ )	—	0.0175	0.0184
Activation energy ( $\beta_E$ )	2.31	2.29	2.29
Relative residual, %	10.8	11.6	11.5
$R^2$	0.918	0.900	0.902
<b>Nafion<sup>®</sup> N117</b>			
Diffusion ( $\beta_D$ )	0.268	—	2.74
Desorption ( $\beta_d$ )	—	0.0202	0.0224
Activation energy ( $\beta_E$ )	2.17	2.17	2.18
Relative residual, %	10.1	10.8	10.8
$R^2$	0.930	0.913	0.913
<b>Nafion<sup>®</sup> N211</b>			
Diffusion ( $\beta_D$ )	0.0231	—	0.260
Desorption ( $\beta_d$ )	—	0.0158	0.0160
Activation energy ( $\beta_E$ )	2.72	2.72	2.79
Relative residual, %	9.37	9.52	9.59
$R^2$	0.950	0.948	0.947
<b>Nafion<sup>®</sup> N212</b>			
Diffusion ( $\beta_D$ )	0.0530	—	0.314
Desorption ( $\beta_d$ )	—	0.0179	0.0211
Activation energy ( $\beta_E$ )	2.54	2.55	2.54
Relative residual, %	8.79	9.02	9.14
$R^2$	0.951	0.948	0.947

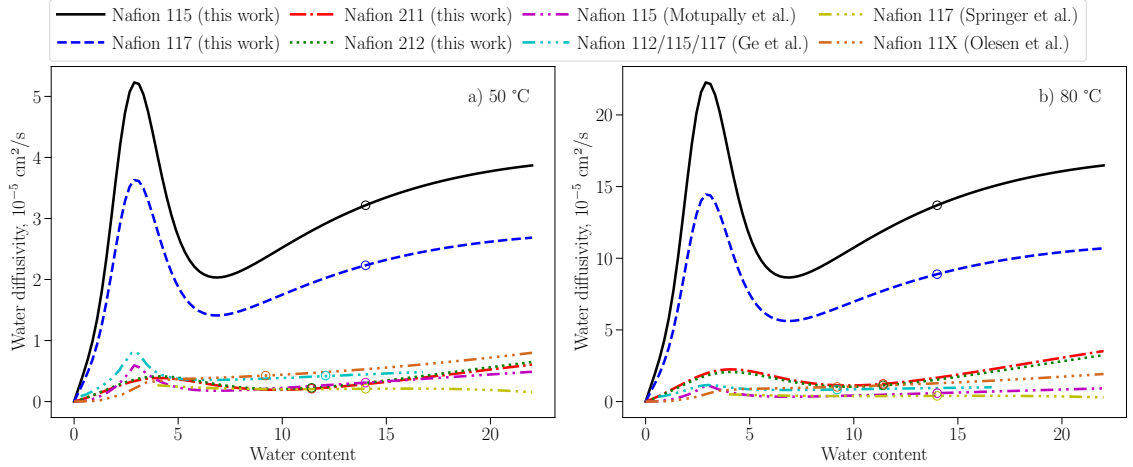


Figure 3.4: Comparison of the water diffusivities fitted for Nafion<sup>®</sup> N117, N211, and N212 with the literature data at a) 50 °C and b) 80 °C. The results were obtained with model 3 (diffusion and desorption). Markers indicate the vapor-equilibrated water content at 100% RH from Figure 3.2. Each graph is plotted up to the liquid-equilibrated water content from Table 3.1. The literature data are from Refs. [133, 189, 239, 252, 253].

12 or 13% inlet RH in the dry channel; the water-content drop was smaller at the lower temperature and/or higher inlet RH. Since the diffusive flux was integrated (eqs. (3.5) and (3.9)) and the water content in the membrane was not solved for, the distributions in the figure are shown as linear approximations. Both models resulted in similar equilibrium water activity in the dry channel for each membrane, with a higher water concentration upstream due to vapor accumulation, since the inlet RH was taken from the experiments and the outlet RH was fitted to the same data for each sample. However, the model with infinitely fast desorption (model 1) predicted a large drop in water content across each membrane while the concentration gradient obtained with model 3 was insignificant and nearly all of the water-content change occurred at the dry-channel interface. These results are consistent with the observation of significant water-transport resistance at the Nafion<sup>®</sup>-gas interface in the literature [133, 166, 173–175, 178, 180–183].

The low sensitivity of the overall transport across membranes equilibrated with liquid water on one side to the bulk transport made the determination of water dif-

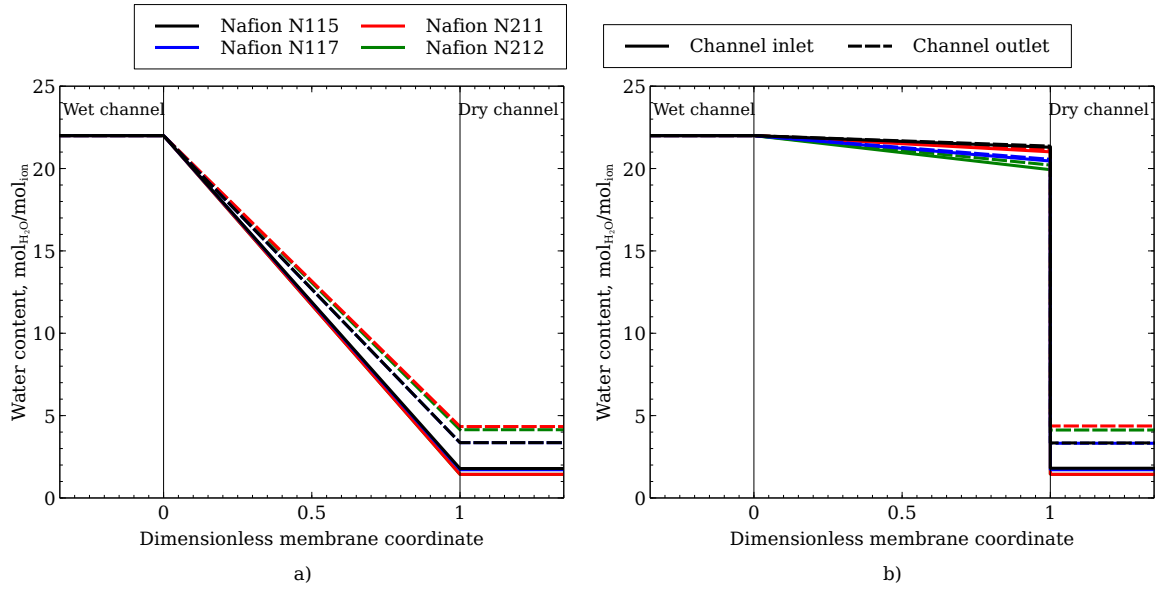


Figure 3.5: Comparison of the water-content drop across Nafion<sup>®</sup> membranes at the dry-channel inlet (solid lines) and outlet (dashed lines) computed with: a) model 1 (diffusion) and b) model 3 (diffusion and desorption). All data are at 80 °C and 12 or 13% inlet RH in the dry channel.

fusivity using liquid-vapor permeation setups challenging and potentially inaccurate. This is illustrated in Figure 3.4, where diffusion coefficients of water in Nafion<sup>®</sup> fitted with model 3 (diffusion and desorption) are compared with the literature values from Refs. [43, 133, 189, 239, 252, 253] [20, 151, 232, 310, 326, 327].

### 3.3.1.2 Rate of water desorption

The desorption coefficients calculated with eq. (3.14) and the fitted scaling factors from Table 3.3 are plotted in Figure 3.6 at 60 and 80 °C. The presented results were obtained with model 2 (desorption), as the contribution of diffusion to the overall transport was small. The desorption rates may have been underestimated with model 2 which does not account for the plausible (albeit small) change in the water content across the membranes suggested by the simulations with model 3 (Figure 3.5b). On the other hand, transport in the bulk of the membrane was assumed to be purely diffusive in model 3, which might not have been the case [43]. Nevertheless, both

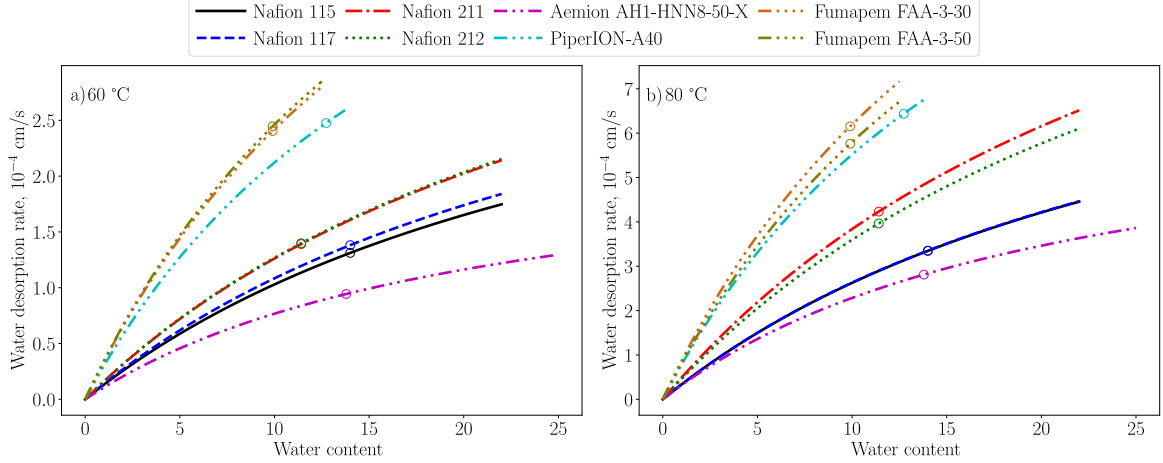


Figure 3.6: Comparison of the fitted water-desorption rates for Nafion<sup>®</sup> N117, N211, N212, Aemion<sup>®</sup> AH1-HNN8-50-X, Fumapem<sup>®</sup> FAA-3-50, and Versogen<sup>™</sup> PiperION-A40 at a) 60 °C and b) 80 °C. The results were obtained with model 2 (desorption). Markers indicate the vapor-equilibrated water content at 100% RH from Figure 3.2. Each graph is plotted up to the liquid-equilibrated water content from Table 3.1.

models 2 and 3 yielded relatively similar desorption rates for each membrane. The desorption rates obtained with model 3 are reported in Figure A.12.

The desorption rates for Nafion<sup>®</sup> membranes obtained in this chapter are of the order  $10^{-5}$ – $10^{-4}$  cm/s at 60–80 °C, which is in agreement with some of the previous literature [92, 175, 180, 181, 183, 254–256]. A significantly higher desorption rate, sometimes by several orders of magnitude, was reported in other studies [133, 166, 172–174, 176, 178, 182, 257, 258]. There appears to be no correlation between the reported interfacial transport rate and the experimental technique used to measure it, the operating temperature, or the type and thickness of the samples. Therefore, the causes for the wide range of the desorption rates reported in the literature ( $10^{-5}$ – $10$  cm/s by magnitude) might be the specifics of the experimental apparatus and methods, as well as the varying complexity of the mathematical models employed in the data analysis.

As expected, the fitted exchange rate is similar for the Nafion<sup>®</sup> membranes of the same type (N11X or N21X; Figure 3.6). Despite the higher desorption scaling factor, a lower overall desorption rate (3.14) was estimated for Nafion<sup>®</sup> N11X than

for N21X due to the lower activation energy for the former, as will be shown later. It is hypothesized that the desorption rate and its activation energy depend on the nature of the sites at the Nafion<sup>®</sup> surface that water is leaving (water clusters, sulfonic groups, and fluoropolymers) [172]. Therefore, it is natural to expect some variability in the measured desorption rate with the fabrication method of these membranes that may affect the surface morphology.

### 3.3.1.3 Activation energy for water desorption

The activation energy calculated using the reference value of 20 kJ/mol [250] and the scaling factors from Table 3.3 is 45.8 kJ/mol for Nafion<sup>®</sup> N115, 43.4 kJ/mol for N117, 54.4 kJ/mol for N211, and 51.0 kJ/mol for N212. These values were obtained with the desorption model; the diffusion-desorption model resulted in similar, within 2.6%, activation energies. Activation energy estimated in this chapter for Nafion<sup>®</sup> is in line with that measured for the interfacial transport of water by Romero and Mérida [257] but higher than experimentally estimated by others [166, 172, 255]. The activation energy for desorption obtained in this chapter and in the literature is higher than the activation energy for water diffusion in Nafion<sup>®</sup> (20 kJ/mol [250], 9.1/11.6 kJ/mol [254], 18 kJ/mol [259], and 23 kJ/mol [260]), suggesting different sensitivity of the interfacial and bulk water transport in these materials to temperature. The activation energy for diffusion and desorption was assumed the same in the mathematical model developed in this chapter (eqs. (3.11) and (3.14) share the same scaling factor  $\beta_d$ ). However, as discussed before, the overall contribution of bulk transport was small.

### 3.3.1.4 Can liquid-vapor permeation setups be used to measure water diffusivity?

Since the concentration gradient across the membrane in liquid-vapor permeation setups was small (Figure 3.5b), the fits with the diffusion-desorption model were relatively insensitive to the diffusion coefficient as compared with the desorption rate.

This is illustrated in Figure A.10, where the distributions of the residual (3.15) around the fitted scaling factors  $\beta_D$ ,  $\beta_E$ , and  $\beta_d$  (Table 3.3) are shown.

Diffusion coefficients of water in Nafion<sup>®</sup> fitted with model 3 (diffusion and desorption) are shown in Figure 3.4. As expected, the measured water diffusivities for Nafion<sup>®</sup> N211 and N212 matched. At the lower temperature (50 or 60 °C), these coefficients were of the order  $10^{-6}$  cm<sup>2</sup>/s, which was within the range  $10^{-9}$ – $10^{-5}$  cm<sup>2</sup>/s reported in a number of experimental studies using various techniques, such as transient gravimetric measurements, steady-state permeation, and nuclear magnetic resonance [43, 133, 189, 239, 252, 253]. However, the N211 and N212 diffusivities estimated in this chapter exceeded the expected range at 80 °C. The diffusion coefficients for N115 and N117 were an order of magnitude higher than that for the cast membranes at both low and high temperature and nearly two orders higher than reported for Nafion<sup>®</sup> N11X with similar liquid-vapor permeation setups [133, 189]. Additionally, the diffusivities estimated for N115 and N117 did not match, even though the two membranes differ only in their thickness. The observed discrepancy is due to the low sensitivity of the overall transport of water to diffusion in membranes that are liquid-equilibrated on one side. The relatively insignificant contribution of diffusion makes it challenging to accurately estimate the water diffusivity using liquid-vapor permeation setups. Furthermore, the high value of the activation energy fitted in this chapter that mainly corresponded to the desorption process and not diffusion resulted in a more rapid increase in diffusivity with temperature than expected from the literature (Figure 3.4). Therefore, a combination of liquid-vapor and vapor-vapor permeation setups with accurate numerical models for each case is recommended for water-transport characterization of PEMs and AEMs. A vapor-vapor permeation setup and a model where activation energy is different for diffusion and interfacial transport may improve the diffusivity estimate. In that case, the number of fitting scaling factors would increase from three (diffusivity, desorption rate, combined activation energy) to five (diffusivity and its activation energy, desorption and absorption

rates, and activation energy of the interfacial transport). Vapor-vapor experiments will be performed in future work to complement the current analysis.

### 3.3.2 Anion exchange membranes

#### 3.3.2.1 Limiting mode of transport

The measured outlet RH and the crossover water flux for Aemion<sup>®</sup> AH1-HNN8-50-X, Fumapem<sup>®</sup> FAA-3-30 and FAA-3-50, and Versogen<sup>™</sup> PiperION-A40 are shown in Figure 3.7. The crossover flux and the outlet RH measured with Fumapem<sup>®</sup> FAA-3-30 and FAA-3-50 samples (30  $\mu\text{m}$  and 50  $\mu\text{m}$ , respectively) were within the experimental uncertainty in all cases. This suggests that the interfacial transport was dominating in Fumapem<sup>®</sup> membranes, in agreement with the results of Luo et al. [178]. The difference between the water fluxes across the four AEMs was the lowest at 60 °C and increased with temperature. Since the tested samples had similar thickness (30 to 50  $\mu\text{m}$ ), the observed variability in the water flux was likely due to the difference in the membrane materials and morphology.

Because Aemion<sup>®</sup> and Versogen<sup>™</sup> PiperION samples of different thickness were not available, conclusions on the limiting mode of transport could not be made based on the experimental data. The measured water flux was processed with the three developed mathematical models as discussed before. The fitted scaling factors for diffusion, desorption, and activation energy are listed in Table 3.4. As it was the case for Nafion<sup>®</sup>, models 1 (diffusion) and 3 (diffusion and desorption) resulted in similar activation-energy scaling factors for each membrane but an order of magnitude different diffusivity scaling factors while models 2 (desorption) and 3 produced similar activation energy and desorption coefficients.

Water-content drop across the tested AEMs computed with models 1 (diffusion) and 3 (diffusion and desorption) is illustrated in Figure 3.8 for the extreme case of 80 °C and 12 or 13% inlet RH. Similarly to Nafion<sup>®</sup>, AEMs exhibited a large water-content drop when infinitely fast desorption was assumed (Figure 3.8a) and

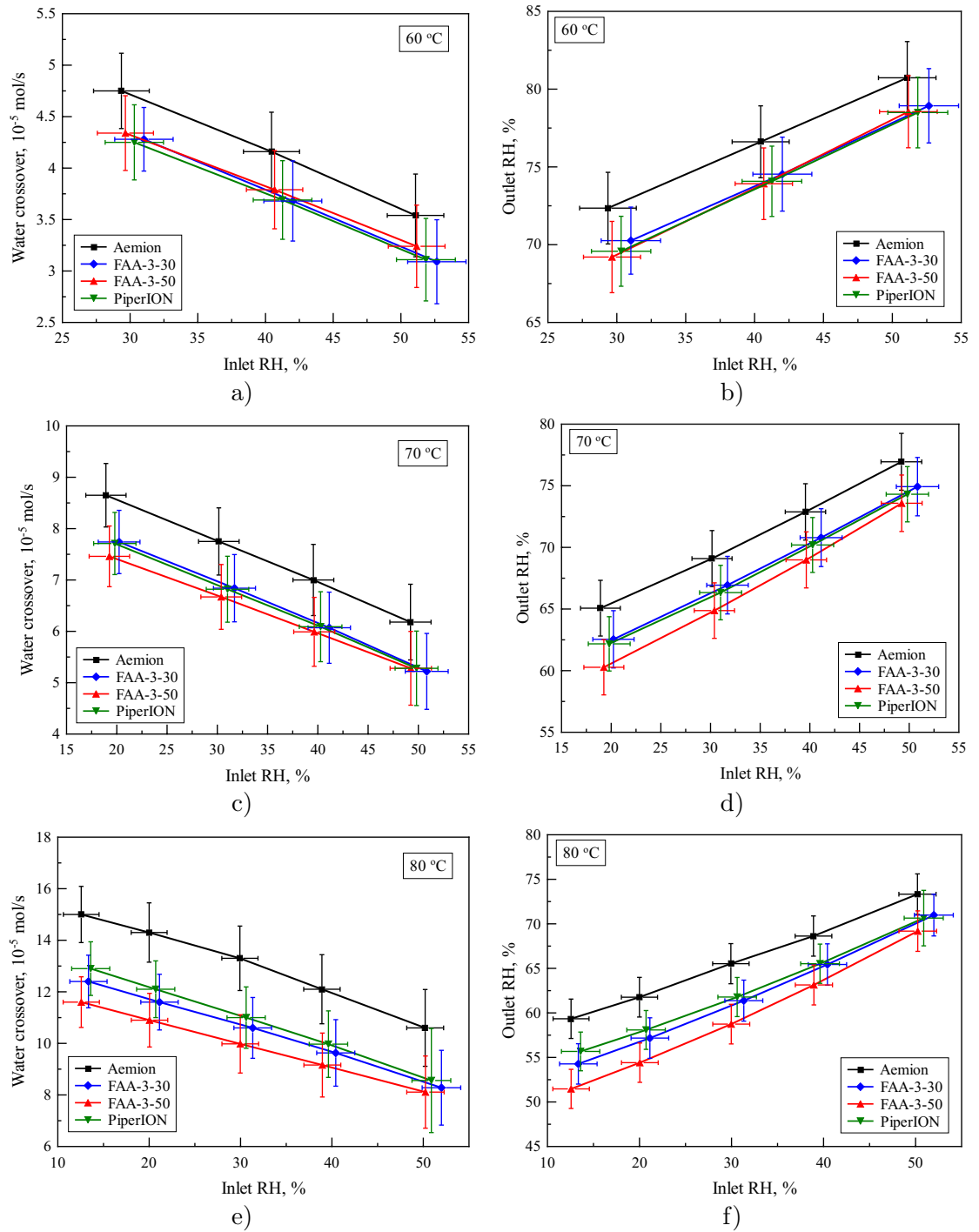


Figure 3.7: Experimental measurements of water transport through Aemion<sup>®</sup> AH1-HNN8-50-X, Fumapem<sup>®</sup> FAA-3-30/50, and Versogen<sup>™</sup> PiperION-A40 at 60, 70 and 80 °C: a), c) and e) water crossover; and b), d) and f) outlet RH.

Table 3.4: Fitted scaling factors for diffusion, desorption, and activation energy for AEMs and the corresponding fitting residual and  $R^2$  values. The physical properties without scaling ( $\beta_D = \beta_d = \beta_E = 1$ ) are  $2.72 \cdot 10^{-5}$  cm<sup>2</sup>/s,  $4.59 \cdot 10^{-3}$  cm/s, and 20 kJ/mol, respectively.

Result	Model 1	Model 2	Model 3
	Diffusion	Desorption	Diffusion and desorption
<b>Aemion<sup>®</sup> AH1-HNN8-50-X</b>			
Diffusion ( $\beta_D$ )	0.0183	—	0.111
Desorption ( $\beta_d$ )	—	0.00768	0.0109
Activation energy ( $\beta_E$ )	2.67	2.67	2.56
Relative residual, %	8.17	8.26	8.76
$R^2$	0.961	0.959	0.959
<b>Fumapem<sup>®</sup> FAA-3-30</b>			
Diffusion ( $\beta_D$ )	0.0387	—	0.366
Desorption ( $\beta_d$ )	—	0.0313	0.0358
Activation energy ( $\beta_E$ )	2.30	2.30	2.29
Relative residual, %	5.97	6.75	6.89
$R^2$	0.977	0.971	0.970
<b>Fumapem<sup>®</sup> FAA-3-50</b>			
Diffusion ( $\beta_D$ )	0.0776	—	0.577
Desorption ( $\beta_d$ )	—	0.0369	0.0448
Activation energy ( $\beta_E$ )	2.07	2.09	2.07
Relative residual, %	5.06	5.73	5.95
$R^2$	0.983	0.977	0.976
<b>Versogen<sup>™</sup> PiperION-A40</b>			
Diffusion ( $\beta_D$ )	0.0335	—	0.270
Desorption ( $\beta_d$ )	—	0.0259	0.0307
Activation energy ( $\beta_E$ )	2.37	2.34	2.31
Relative residual, %	5.64	5.08	5.27
$R^2$	0.979	0.983	0.982

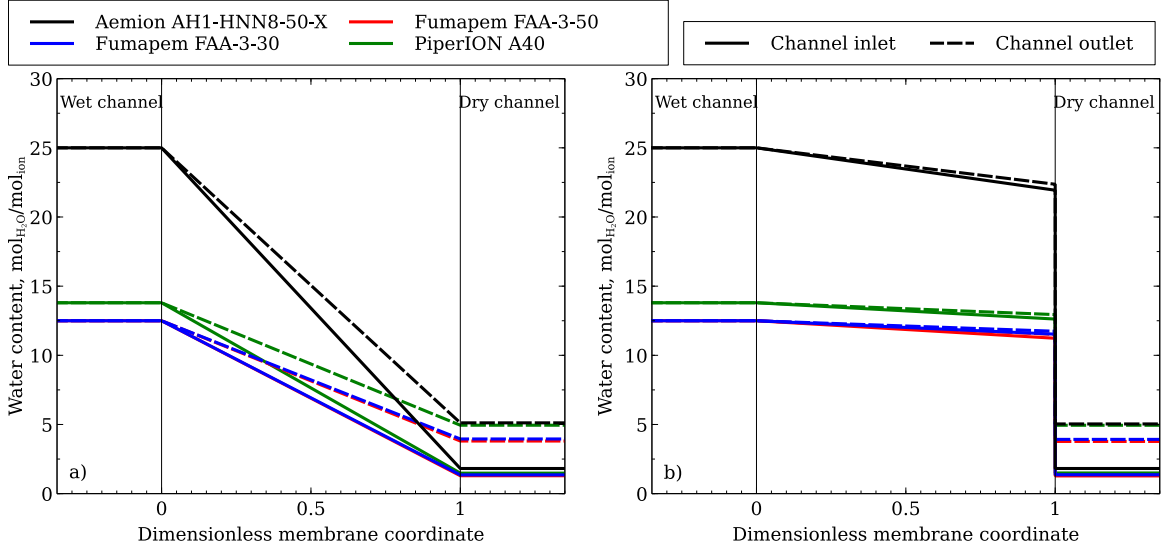


Figure 3.8: Comparison of the water-content drop across AEM membranes at the dry-channel inlet (solid lines) and outlet (dashed lines) computed with: a) model 1 (diffusion) and b) model 3 (diffusion and desorption). All data are at 80 °C and 12 or 13% inlet RH in the dry channel.

a negligible concentration gradient when finite diffusion was included in the model (Figure 3.8b). The nearly uniform water content close to the liquid-equilibrated value for each membrane is consistent with the similarity of the fitted scaling factors between the desorption-dominated and the combined diffusion-desorption models in Table 3.4.

The experimentally measured water flux and the simulation results for Aemion<sup>®</sup> and Versogen<sup>™</sup> PiperION samples followed the same trends as those observed for Nafion<sup>®</sup> and Fumapem<sup>®</sup> membranes where multiple thicknesses were available and for which desorption was identified as the limiting mode of water transport in the liquid-vapor scenario. Therefore, it is likely that desorption was limiting in Aemion<sup>®</sup> and Versogen<sup>™</sup> PiperION membranes as well. These results are in agreement with the AEM literature [146, 178, 187].

### 3.3.2.2 Rate of water desorption

As shown in Figure 3.6, the exchange rates estimated for AEMs at 60–80 °C are of the same order of magnitude as those for Nafion<sup>®</sup>,  $10^{-5}$ – $10^{-4}$  cm/s. They are an

order of magnitude lower than reported for Tokuyama A201 AEM (28  $\mu\text{m}$ ) by Li et al. [187] ( $1.5 \cdot 10^{-4}$ – $2.5 \cdot 10^{-3}$  cm/s at 30–40 °C). Luo et al. [178] measured the interfacial exchange rate to be  $2.6 \cdot 10^{-3}$  cm/s for HMT-PMBI (Aemion<sup>®</sup>, 12–70  $\mu\text{m}$ ) and  $3.0 \cdot 10^{-3}$  cm/s for Fumapem<sup>®</sup> FAA3 (19–50  $\mu\text{m}$ ) at 70 °C and 40% RH. The corresponding desorption rates estimated in this chapter are about  $8.9 \cdot 10^{-5}$  cm/s and  $2.0 \cdot 10^{-4}$  cm/s at the same conditions, i.e., 29 and 15 times lower, respectively. It is not clear how the interfacial exchange rate was computed by Luo et al., so the discrepancy could be either due to the experimental setup or the method used to extract this quantity, which might have resulted in coefficients with slightly different physical interpretation. Given the scarcity of AEM data in the literature and the large variability in the interfacial exchange rates in Nafion<sup>®</sup>, the desorption rates obtained in this chapter for alkaline membranes are deemed reasonable.

As seen in Figure 3.6, Aemion<sup>®</sup> AH1-HNN8-50-X exhibits an exchange rate similar to that of Nafion<sup>®</sup> N117. The smaller discrepancy between liquid- and vapor-equilibrated water content (Schröder’s paradox) in Fumapem<sup>®</sup> FAA-3 and Versogen<sup>™</sup> PiperION-A40 results in a less substantial differential water content in equation (3.7). Despite the smaller water flux (Figures 3.3 and 3.7), this leads to two to three times higher desorption rate measured for these materials as compared with those obtained for Nafion<sup>®</sup> and Aemion<sup>®</sup> membranes. However, it is difficult to correlate the measured desorption rates directly with the magnitude of Schröder’s paradox: it is weaker in Fumapem<sup>®</sup> FAA-3 and Versogen<sup>™</sup> PiperION-A40 than in Aemion<sup>®</sup> AH1-HNN8-50-X and also weaker in N11X than in N21X, yet the desorption rates follow the opposite trends for AEMs and PEMs.

### 3.3.2.3 Activation energy for water desorption

The activation energy for water desorption from Aemion<sup>®</sup> AH1-HNN8-50-X was found to be 53.4 kJ/mol, which is close to 52.7 kJ/mol estimated for Nafion<sup>®</sup> N21X (average of N211 and N212). Nevertheless, the overall desorption rate for Aemion<sup>®</sup>

shown in Figure 3.6 is lower than for N211 and N212 due to the lower scaling factor  $\beta_d$  (Table 3.4). Conversely, the lower activation energy of 46.0 kJ/mol and 41.8 kJ/mol for Fumapem<sup>®</sup> FAA-3-30 and FAA-3-50, respectively, and 46.8 kJ/mol for Versogen<sup>™</sup> PiperION-A40 did not result in a lower desorption rate in Figure 3.6 due to the significantly higher  $\beta_d$  (Tables 3.3 and 3.4). The provided activation energies for AEMs were obtained with model 2 (desorption), and model 3 (diffusion and desorption) resulted in activation energies that were within 4.3%.

### 3.4 Conclusions

An experimental setup and a numerical model were developed for the characterization of water transport in proton-exchange and anion-exchange membranes. The presented setup, conceptually similar to the one described in Chapter 2, was used to measure water flux across proton-exchange and anion-exchange membranes equilibrated with liquid water on one side and vapor on the other side. These are the first such measurements reported for Versogen<sup>™</sup> PiperION membranes and the first for Aemion<sup>®</sup> and Fumapem<sup>®</sup> performed at multiple temperature and RH conditions. Three 1D mathematical models accounting for water diffusion, desorption, or the combined transport were then used to analyze the experimental measurements. In agreement with the literature [133, 146, 166, 173–175, 178, 180–183, 187], interfacial exchange of water at the membrane-gas interface was identified as the limiting mode of water transport in both PEMs and AEMs.

The rate of water desorption from Nafion<sup>®</sup> membranes measured in this chapter was of the order  $10^{-5}$ – $10^{-4}$  cm/s at 60–80 °C, within the range previously reported in the literature [43], thereby validating the experimental setup and the analysis approach used in this chapter. Water was found to desorb from Aemion<sup>®</sup> AH1-HNN8-50-X at about the same rate as Nafion<sup>®</sup> N115 and N117, and the activation energy for this process is also similar at 53.4 kJ/mol. On the other hand, Fumapem<sup>®</sup> FAA-3-30 and FAA-3-50 and Versogen<sup>™</sup> PiperION-A40 exhibit two to three times faster

desorption and a lower activation energy: 46.0, 41.8, and 46.8 kJ/mol, respectively.

The liquid-vapor permeation analysis performed in this chapter allowed for the isolation of the desorption process from the bulk transport and absorption of water that would otherwise also take place in a vapor-vapor setup. This simplified the experimental apparatus, the mathematical model used for the analysis, and the optimization algorithm for fitting the measured data. The desorption rate and the corresponding activation energy reported in this chapter can be used as initial estimates for the combined absorption, diffusion, and desorption characterization of PEMs and AEMs with vapor-vapor permeation setups.

## Chapter 4

# Effect of Operating Conditions and Micro-porous Layer on the Water Transport and Accumulation in Proton Exchange Membrane Fuel Cells<sup>1</sup>

The water balance developed in Chapter 2 was used to measure water crossover between the anode and cathode electrodes and water accumulation in the MEA inside operating PEMFCs and thus to understand the impact of operating conditions and transport layer configurations on cell performance. The impact of operating conditions on water crossover had not been previously studied in the literature. Similarly, the literature was ambiguous regarding the role of the MPL on modifying water transport across the membrane.

---

<sup>1</sup>Parts of this chapter are reproduced from the following publication:

1. F. Wei, A. Kosakian, and M. Secanell, “Effect of operating conditions and micro-porous layer on the water transport and accumulation in proton exchange membrane fuel cells,” *Chemical Engineering Journal*, p. 144 423, 2023. DOI: <https://doi.org/10.1016/j.cej.2023.144423>

Author contributions are detailed in the Preface of this thesis.

## 4.1 Materials and experiments

### 4.1.1 Sample preparation and cell assembly

Catalyst coated membranes were manufactured by inkjet printing  $5 \text{ cm}^2$  of catalyst ink on a Nafion membrane (Ion Power, NR-211,  $25.4 \text{ }\mu\text{m}$ ) [77, 261, 262]. The relatively small active area was chosen to minimize the changes in concentration along the channel and reduce the occurrence of two-phase flow in the channel, as large liquid droplets might not be detected by the sensors. The catalyst layer ink, with a 30 wt.% Nafion loading, was first prepared by mixing isopropyl alcohol, propylene glycol, Nafion ionomer solution (Ion Power, Liquion solution LQ-1105 1100EW 5 wt.%) and Pt/C catalyst (HyPlat, 40 wt.% platinum supported on Ketjenblack EC-300J) using the procedures described in Refs. [25, 261]. A commercial piezo-electric printer (Dimatix DMP-2831, Fujifilm Inc.) was then used to fabricate the cathode CL by printing the ink layer-by-layer over the membrane until it reached a platinum loading of  $0.2 \text{ mg}_{\text{Pt}}/\text{cm}_{\text{CL}}^2$ . Once the cathode CL was printed, it was dried overnight under ambient conditions before printing the anode CL using the same protocol. The anode side had a catalyst loading of  $0.1 \text{ mg}_{\text{Pt}}/\text{cm}_{\text{CL}}^2$ . The inkjet printed anode CL of  $0.1 \text{ mg}_{\text{Pt}}/\text{cm}_{\text{CL}}^2$  was found to have a thickness of  $2.8 \text{ }\mu\text{m}$  based on SEM measurement in Ref. [92] and the cathode CL of  $0.2 \text{ mg}_{\text{Pt}}/\text{cm}_{\text{CL}}^2$  was assumed to have a thickness of  $5.6 \text{ }\mu\text{m}$ .

The catalyst-coated-membrane was then sandwiched between a  $5 \text{ cm}^2$  Sigracet SGL 29BC (GDL and MPL) on the anode and either a  $5 \text{ cm}^2$  SGL 29BA (only GDL) or 29BC on the cathode. The MEA was then introduced into a Scribner fuel cell hardware with 14 parallel flow channels, as shown in Figure 2.1c. The channel length, width and depth were 22.4 mm, 0.86 mm and 1 mm, respectively. The width of the land between two flow channels was 0.82 mm. Rigid gaskets of 7 mil and 5 mil with a  $5 \text{ cm}^2$  window were used on the side of SGL 29BC and 29BA, respectively, to prevent gas leakage and provide consistent contact between the CCM and the porous

transport layers. The thickness and porosity were  $182.8 \pm 3.9 \text{ }\mu\text{m}$  and  $88.6 \pm 0.2\%$  for uncompressed SGL 29BA (GDL only), respectively; and for uncompressed SGL 29BC (MPL + GDL), they were  $210.3 \pm 2.2 \text{ }\mu\text{m}$  and  $77.2 \pm 0.3\%$ , respectively [4]. Assuming CL deformation is negligible [92], and the compression is uniformly distributed for SGL 29BA but not for SGL 29BC based on the literature results of imaging-based analysis in the through-plane direction [107], the average thickness of compressed SGL 29BA and 29BC is around 122 and 170  $\mu\text{m}$ , respectively, i.e., approximate 34% and 20% pinch.

## 4.2 Results and Discussion

Figure 4.1 shows polarization curve and dimensionless water crossover vs. current density for two cells with (SGL 29BC) and without (SGL 29BA) MPL in the cathode under varying operating conditions (current interrupt resistance and water crossover are provided in Figure 4.2 and 4.3, respectively). Excellent reproducibility was achieved between two cells. Figure 4.4 shows the real-time voltage, dimensionless water crossover, and liquid water accumulation and saturation in the cathode electrode obtained from the quasi-steady current hold experiments with 15 min for current density ranging from 0.2 to 1.2  $\text{A}/\text{cm}^2$ . The dimensionless water crossover in this chapter represents the ratio of the water crossover flux to the water production flux with positive values indicating water transport from the anode to the cathode.

### 4.2.1 Effect of operating conditions

#### 4.2.1.1 PEMFC performance.

Figure 4.1a shows that the best galvanodynamic performance with the cells without an MPL in the cathode was achieved at 80 °C and 70% RH. At 60 °C and 70% RH, a decrease in performance was observed at high current densities due to water accumulation in the cathode (will be discussed in Section 4.2.1.3); and for 80 °C and 30 and 50% RH, ohmic losses reduced cell performance substantially. A similar effect

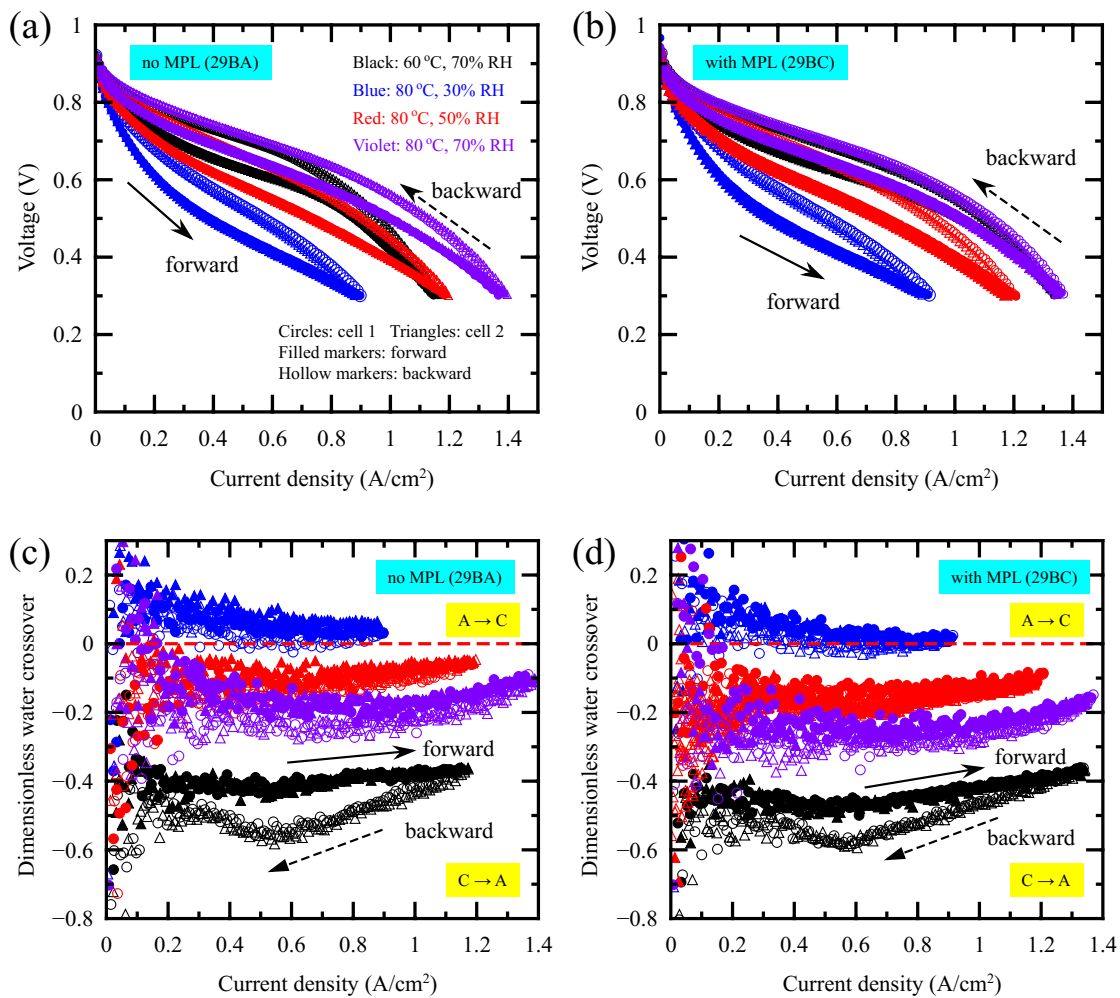


Figure 4.1: Polarization curves (a) without and (b) with MPL and corresponding dimensionless water crossover (c) without and (d) with MPL obtained from galvanodynamic polarization experiments under varying experimental conditions.

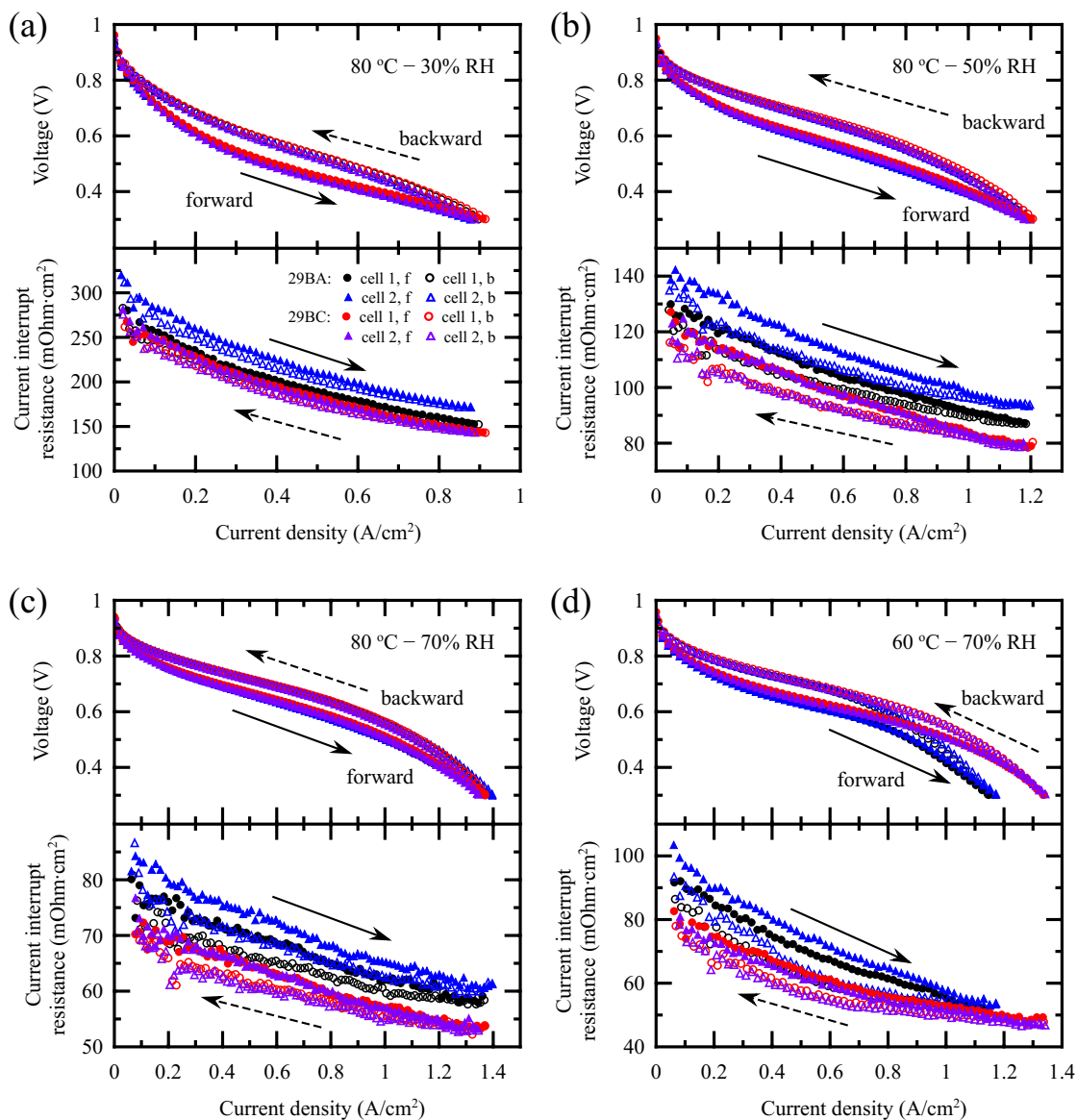


Figure 4.2: Polarization curves and corresponding current interrupt resistance for cells with (SGL 29BC) and without (SGL 29BA) MPL in the cathode. Scan rate: 5 mA/s between OCV and 0.3 V with a full forward and backward scan. Experimental conditions: (a) 80 °C and 30% RH, (b) 80 °C and 50%, (c) 80 °C and 70% and (d) 60 °C and 70% RH. Reactant: 0.5 slpm hydrogen (anode) and 0.5 slpm air (cathode). Backpressure: 50 kPa (gauge).

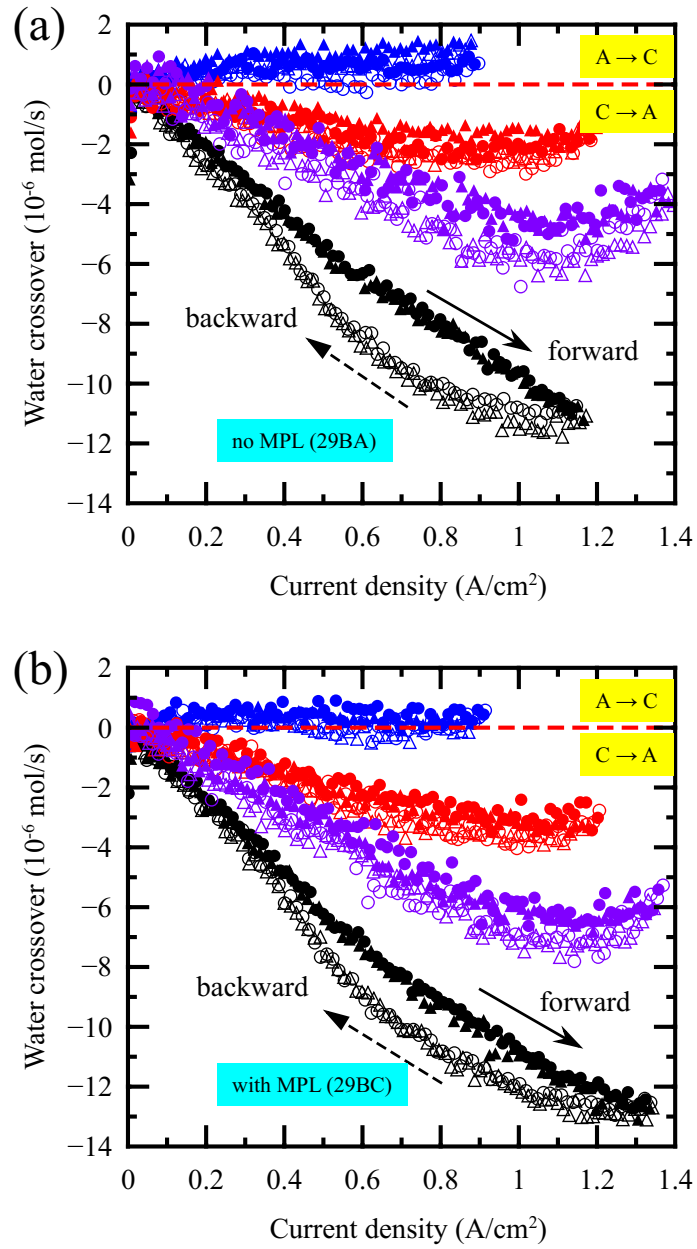


Figure 4.3: Water crossover obtained from galvanodynamic polarization experiments under varying experimental conditions for cells (a) without and (b) with MPL.

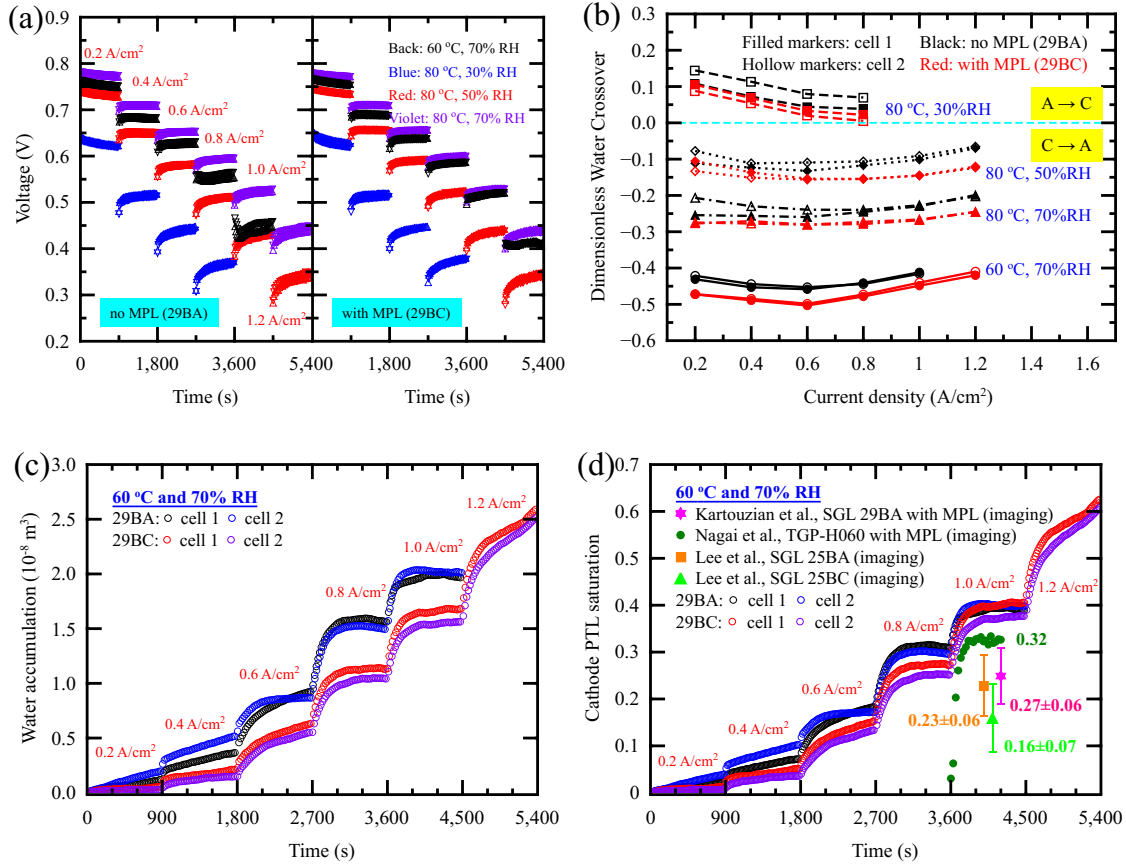


Figure 4.4: Real-time (a) voltage, (b) dimensionless water crossover, and (c) cathode PTL water accumulation and (d) saturation obtained from quasi-steady current hold experiments. Kartouzian et al. [154]: neutron imaging taken after 30 min current hold at 1 A/cm<sup>2</sup> and then shut down reactant supply, 8 cm<sup>2</sup> cell with 3-channel serpentine flow fields, 0.3/0.3 mg<sub>pt</sub>/cm<sub>CL</sub><sup>2</sup> CLs, NR212 Nafion membrane, anode of SGL 29BC, 0.2 nL/min 120% RH hydrogen and 70 kPa backpressure, cathode of MPL (40 μm and 20 wt.% PTFE) on SGL 29BA, 0.5 nL/min 120% RH air and 60 kPa backpressure, 50 °C cell temperature. Nagai et al. [34]: operando X-ray tomographic microscopy taken at 1 A/cm<sup>2</sup>, 0.4/0.4 mg<sub>pt</sub>/cm<sub>CL</sub><sup>2</sup> CLs, anode with MPL (30-40 μm and 61% porosity) on TGP-H060 GDL and 153 mL/min 100% RH hydrogen, cathode with MPL (30-40 μm and 46% porosity) on TGP-H060 GDL and 219 mL/min 105% RH air, no backpressure, 40 °C cell temperature. Lee et al. [107]: XTM taken at 1 A/cm<sup>2</sup>, 20.3 μm Nafion HP membrane, 0.3/0.3 mg<sub>pt</sub>/cm<sub>CL</sub><sup>2</sup> CLs, anode with SGL 25BA or 25BC and 1 slpm 100% RH hydrogen, cathode with 25BA or 25BC and 1 slpm 100% RH air, 150 kPa backpressure, 60 °C cell temperature.

of operating conditions was observed for the quasi-steady performance obtained from the current hold experiments (shown in Figure 4.4a).

Hysteresis in the galvanodynamic polarization was observed at all experimental conditions, with the backward scan showing better performance (hollow markers) than the forward scan performance (solid markers). Such polarization hysteresis is commonly attributed to the better membrane hydration during the backward scan [86, 88, 90, 127–129]. Indeed, the current interrupt resistance was lower during the backward scan (hollow markers in Figure 4.2) than during the forward scan (solid markers in Figure 4.2) due to increased membrane hydration; however, the measured reduction in the current interrupt resistance was not sufficient to result in such significant improvement in polarization during the backward scan. For example, at the current density of  $0.6 \text{ A/cm}^2$  at  $60 \text{ }^\circ\text{C}$  and  $70\% \text{ RH}$ , the voltage hysteresis magnitude was  $72 \text{ mV}$  but the change in the current interrupt resistance of  $8.27 \text{ m}\Omega\text{-cm}^2$  could only result in a  $5 \text{ mV}$  improvement. Therefore, membrane hydration was not the main contributor to the polarization-curve hysteresis; instead, it might have been induced mostly by the platinum oxide dynamics [130, 131]; however, further research is needed in this area.

#### **4.2.1.2 Water crossover.**

The galvanodynamic and quasi-steady dimensionless water crossover is shown in Figure 4.1c and Figure 4.4b, respectively. The dimensionless water crossover shown in Figure 4.1c was measured using the anode water balances, since liquid water accumulation occurred in the cathode electrode (see Section 4.2.1.3). The dimensionless water crossover shown in Figure 4.4b was determined by averaging the dimensionless water crossover values measured using the anode and cathode water balances for the last 5 min of 15 min for each current as the water transport reached stabilization.

The operating conditions were found to have a considerable effect on the water crossover. At  $80 \text{ }^\circ\text{C}$  and  $30\% \text{ RH}$ , water crossover was from the anode to the cathode,

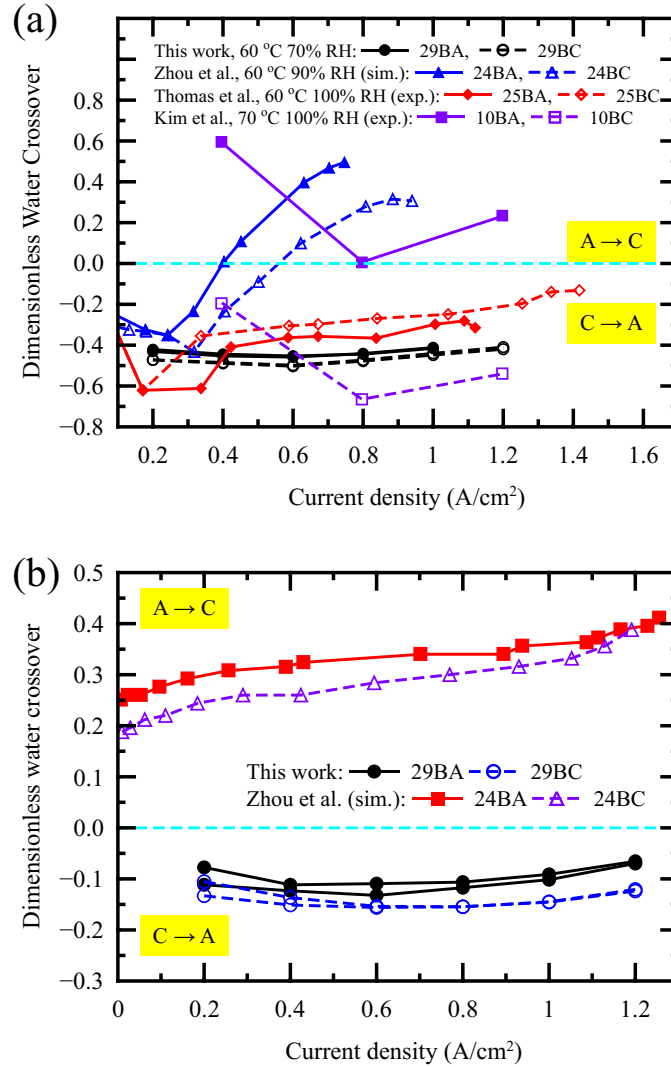


Figure 4.5: Dimensionless water crossover with comparisons with literature under (a) cold/wet and (b) hot/dry conditions. Zhou et al. [25]: simulation work, 25  $\mu\text{m}$  N211 membrane, 0.1/0.1  $\text{mg}_{\text{pt}}/\text{cm}_{\text{CL}}^2$ , 5  $\text{cm}^2$  parallel channel, SGL 24BA (190  $\mu\text{m}$ ) and 24BC (235  $\mu\text{m}$ ), no back-pressure, no along-the-channel effects in the model. Thomas et al. [55]: experimental work, 30  $\mu\text{m}$  perfluorosulfonated membrane, 0.2/0.6  $\text{mg}_{\text{pt}}/\text{cm}_{\text{CL}}^2$ , 25  $\text{cm}^2$  parallel channel, SGL 25BA (190  $\mu\text{m}$ ) and 25BC (235  $\mu\text{m}$ ), no back-pressure, 1.4/3.0 stoich  $\text{H}_2/\text{air}$ . Kim et al. [99]: experimental work, 18  $\mu\text{m}$  membrane (Gore-PRIMEA-18), 0.4/0.4  $\text{mg}_{\text{pt}}/\text{cm}_{\text{CL}}^2$ , 25  $\text{cm}^2$  single-serpentine channel, SGL 10BA (400  $\mu\text{m}$ ) and 10BC (420  $\mu\text{m}$ ), no back-pressure, 1/1 slpm  $\text{H}_2/\text{air}$ .

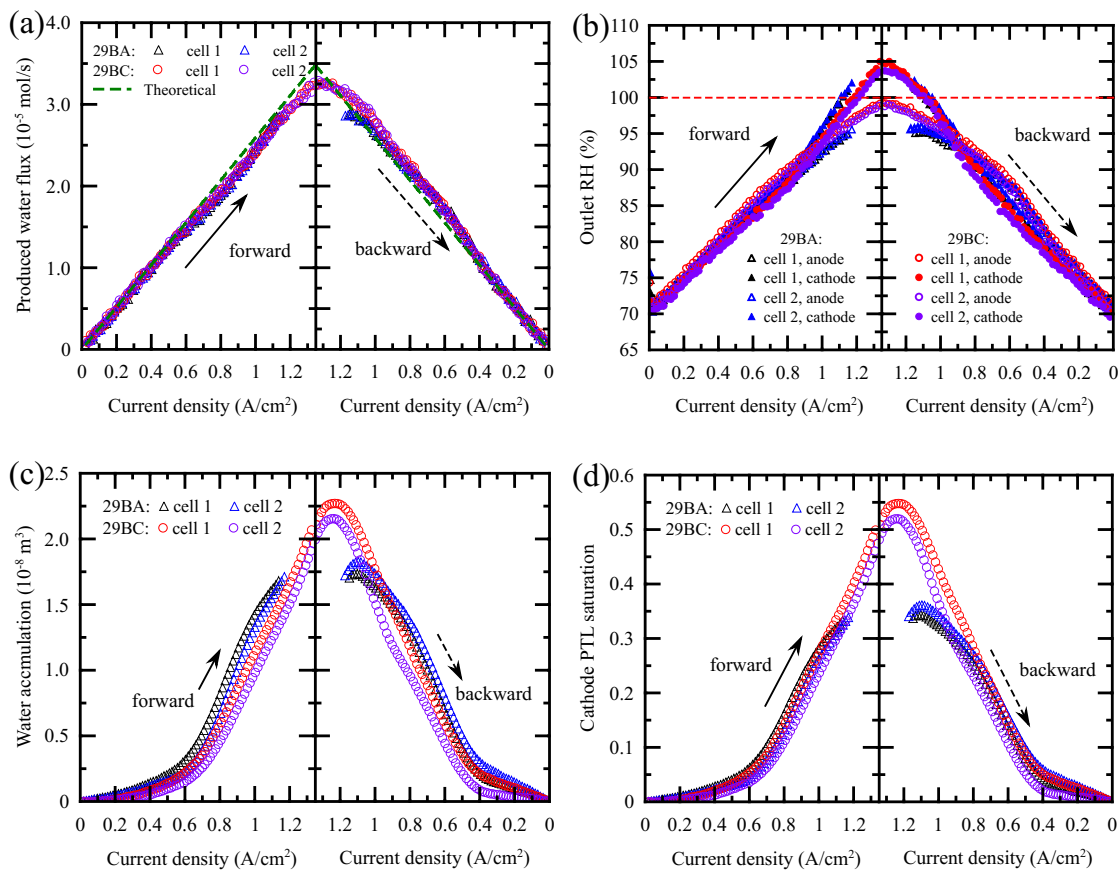


Figure 4.6: (a) ORR product water flux, (b) outlet RH, (c) the amount of water accumulation and (d) cathode PTL saturation obtained from polarization curve experiments at 60 °C and 70% RH.

while for the other three cases it was in the opposite direction. The total amount of water transported from the cathode to the anode during the backward scan was higher than during the forward scan, and the difference at 60 °C and 70% RH was the highest because liquid water accumulated in the cathode electrode during the forward scan at high current densities and was removed during the backward scan. Figures 4.1c and 4.4b also show that at 80 °C, the net water that transports from the cathode to the anode increased with increasing inlet RH, mainly due to the improved water transport properties of the Nafion membrane [43, 133, 189]. At 60 °C and 70% RH, the total amount of water crossing the membranes was the highest among all experimental conditions. When cells were operated at lower cell temperature, the saturation pressure calculated using eq. (2.3) was lower and the RH gradient across the CCM was higher at 60 °C than at 80 °C. Therefore, more water was transported from the cathode to the anode at 60 °C and 70% RH as a result of the larger RH gradient.

The measured dimensionless water crossover flux is compared in Figure 4.5 with the literature. At 60 °C with 70% RH, a dimensionless water crossover of about  $-0.42$  was measured in this chapter. A similar value was reported by Thomas et al. [55] (solid red diamond markers in Figure 4.5a), although in their work it was higher below  $0.4 \text{ A/cm}^2$  and lower above  $0.4 \text{ A/cm}^2$ . This discrepancy might be because of either the different cells or the assumption made by Thomas et al. that the inlet absolute pressure was equal to the backpressure, which could have affected the estimation of the inlet water flux. Deviation from the experimental work of Kim et al. [99] (solid violet square markers) was more significant. They reported water transport in the opposite direction, i.e., from the anode to the cathode, which might have been the result of increased vaporization due to the thicker GDLs (400 vs. 190  $\mu\text{m}$ ). The water flux measured in this chapter at 60 °C with 80% RH and 60 °C with 50% RH did not agree with the modeling results of Zhou et al. [25] (solid blue triangular markers), who reported a net water flux from the anode to the cathode at both conditions except for

low current density at 60 °C with 70% RH highlighting the importance of validating water fluxes in addition to cell performance. Zhou et al. [25] also reported that the water flux predicted with their model did not agree with the experimental data from Thomas et al. [55] and was highly sensitive to the selection of the membrane transport properties [263].

#### 4.2.1.3 Water accumulation.

Figure 4.6a shows the comparison of the measured molar rate of ORR product water and the theoretical values obtained from galvanodynamic polarization experiments at 60 °C and 70% RH. A difference between the two can be observed starting in the forward scan at high current densities. During the forward scan, less than the theoretical amount of water was leaving the cell, while during the backward scan the water flux was higher than the theoretical. It was hypothesized that the deviation was due to the accumulation of liquid water in the MEA. Since only the cathode outlet RH reached 100% at high current densities (shown in Figure 4.6b), it is more likely that liquid water accumulated in the cathode.

Using the methodology discussed in Section 2.2.3, the total amount of water accumulation in the cathode 29BA and its saturation at 60 °C and 70% RH were determined and shown in Figures 4.4c, 4.4d, 4.6c and 4.6d. Figure 4.6c shows that, at the same current density, more water accumulated in the cathode without an MPL, and that with an MPL higher current densities could be achieved even though there was more water. Saturation was obtained using eq. (2.21), and a value as high as 35% was estimated at the highest current density without an MPL in the cathode.

Current hold experiments can be used to study the dynamics of water accumulation. Figures 4.4c and 4.4d show that, at current densities of 0.2–0.6 A/cm<sup>2</sup>, the water accumulation and saturation in SGL 29BA increased with operating time and did not stabilize during the 15 min of operation at constant current density, indicating a higher rate of water accumulation than removal. The lower rate of water removal

was probably because less heat was produced in the ORR at these current densities, and the small interfacial gas-liquid area in SGL 29BA at low saturation also limited liquid water evaporation. At current densities of 0.8 and 1.0 A/cm<sup>2</sup>, the water accumulation and saturation in SGL 29BA were initially increased with operating time and finally stabilized, indicating the balance between the rates of liquid water accumulation and water removal. The saturation in SGL 29BA stabilized around 0.31 and 0.4 at 0.8 and 1.0 A/cm<sup>2</sup>, respectively. At these current densities, the rate of liquid water accumulation was lower as a result of the faster evaporation due to the increased heat production in the ORR and the higher interfacial liquid-gas area in the GDL at higher saturation. Therefore, it took a shorter time to achieve a water transport balance in the SGL 29BA at high current densities. The rate of water production increased at 1.2 A/cm<sup>2</sup>, tipping the balance again in favor of accumulation.

Figure 4.4d compares the estimated cathode saturation with data obtained from the literature. In our case, the measured saturation of SGL 29BA at 1 A/cm<sup>2</sup> stabilized around 0.4, which is higher than reported by Lee et al. [107] using X-ray tomographic microscopy (XTM), 0.23±0.06. This deviation could be due to errors in the estimation of the pore volume, errors associated with imaging setup resolution (10 μm [35]) and segmentation in the XTM, and whether water transport has reached the steady-state, which was not mentioned in [107].

## 4.2.2 Effect of cathode MPL

### 4.2.2.1 PEMFC performance.

In the literature, the introduction of an MPL in the cathode has been shown to have little effect under dry conditions other than a reduction in the current interrupt resistance [25, 96], but to significantly improve the PEMFC performance under wet conditions [27, 50, 54–56, 94–96, 107, 137, 188, 264]. In this chapter, a similar effect was observed. As shown in Figure 4.2, at 80 °C with 30, 50 and 70% RH, the addition of an MPL had only a limited effect on the galvanodynamic polarization

performance and hysteresis. This was likely because the small decrease in current interrupt resistance with the introduction of a cathode MPL (see Figure 4.2) resulted in only a small voltage recovery (up to 8 mV), which could also have been offset by the increased loss of reactant transport due to the small size of the MPL pores [32, 33, 265]. However, at 60 °C and 70% RH (Figure 4.2d), the improvement in PEMFC performance was considerable, i.e., 14% increase in the maximum power density. This was likely because the addition of an MPL to the cathode helped reduce water accumulation, including increasing water back-diffusion from the cathode to the anode (see Section 4.2.2.2), increasing water vaporization, and creating in-plane oxygen pathways around the localized liquid water blockages in the GDL (see Section 4.2.2.3). After adding an MPL to the cathode GDL, the best cell performance was achieved at 60 °C with 70% RH and 80 °C with 70% RH as shown in Figure 4.1b. Furthermore, as shown in Figure 4.4a, the voltage vs. time results obtained from the quasi-steady current hold experiments indicate that the cathode MPL enabled stable fuel cell operation at high current densities during 15 min even at 60 °C and 70% RH (note that water accumulation at 1.2 A/cm<sup>2</sup> was still increasing after 15 min, see Figure 4.4c).

#### 4.2.2.2 Water crossover.

Figures 4.1d and 4.4b show that the impact of introducing an MPL to the cathode was significant. Under the four experimental conditions, the cathode MPL increased the amount of net water transported from the cathode to the anode. For example, Figure 4.4b shows that the increase in the quasi-steady dimensionless water crossover with the MPL introduction was around 0.05 at all operating conditions. This improved membrane hydration and reduced current interrupt resistance, as shown in Figure 4.2. Furthermore, the galvanodynamic water crossover shown in Figure 4.1d indicates that the cathode MPL reduced the hysteresis in the dimensionless water crossover between the forward and backward scans. The low reproducibility of dimensionless water crossover observed at low current densities, was most likely due to

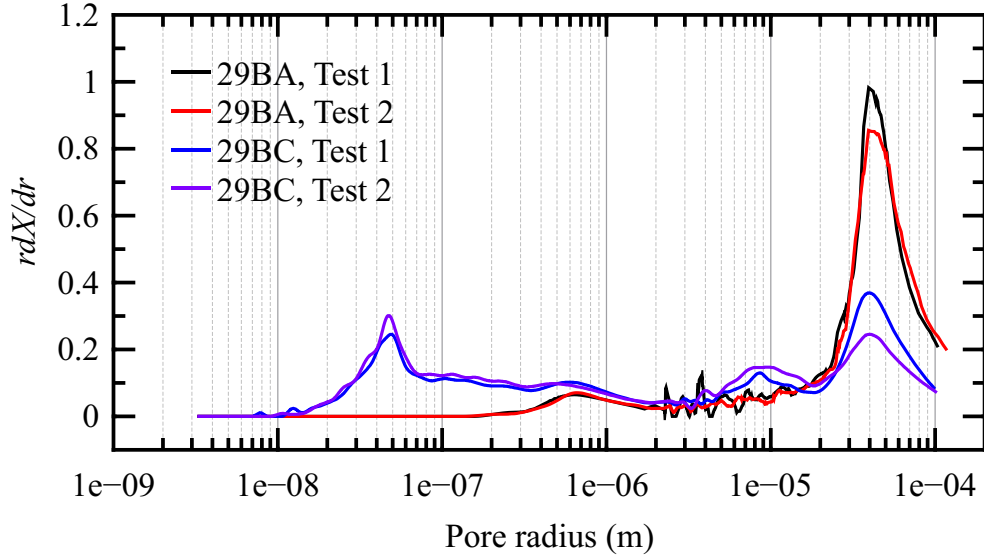


Figure 4.7: Pore size distribution of SGL 29BA and 29BC measured in-house using mercury intrusion porosimetry.

the accuracy of the water balance setup, as a very small amount of water was transported through the membrane, which is also the reason for the low reproducibility at 80 °C and 30% RH.

The quasi-steady current hold experiments in Figure 4.4b also suggest that cathode MPL increased the reproducibility of dimensionless water crossover. The low reproducibility is most likely due to the large morphological pores in SGL 29BA adjacent to the cathode CL. As shown in the pore size distribution of SGL 29BA and 29BC based on mercury intrusion porosimetry (see Figure 4.7), the pore radius of the GDL is much larger than that of MPL, i.e., 40  $\mu\text{m}$  vs. 45 nm for the main peak.

The observed increased back-diffusion was in agreement with Refs. [25, 99], albeit this effect was stronger in the literature. However, Thomas et al. [55] observed a decrease in back-diffusion with the addition of the cathode MPL. This comparison highlights the significant discrepancy in the direction of water transport across the membrane and the impact of the cathode MPL on it that exists in the literature. Because the experimental setup developed in this chapter was thoroughly validated, it is possible that the differences in the observations are due to the dissimilarities of

the equipment, methods, and membranes used.

#### 4.2.2.3 Water accumulation.

When an MPL was introduced to the cathode, the measured molar rates of the ORR product water at 60 °C with 70% RH still deviated from the theoretical values starting in the forward scan at high current densities as shown in Figure 4.6a, indicating that MPL did not prevent the water accumulation in the cathode. This was also validated by only the cathode outlet RH reaching 100% RH in Figure 4.6b.

The impact of cathode MPL on water accumulation and saturation in SGL 29BC is illustrated in Figures 4.4c, 4.4d, 4.6c, and 4.6d. As shown in Figure 4.6c, at the same current density, the total amount of water accumulated in the cells without MPL (29BA shown in triangles) was higher than for cells with MPL (29BC shown in circles). This is because the addition of a cathode MPL increased the electrode temperature [19, 25, 50, 266], which led to an increase in the water vaporization. This difference in the total amount of water accumulation between cells with and without MPL was observed to increase during the current hold experiments with the operating time as shown in Figure 4.4d. However, due to the estimated smaller total pore volume, i.e., 4.144 vs.  $5.055 \times 10^{-8} \text{ m}^3$ , the saturation in SGL 29BC was similar to that of 29BA shown in Figures 4.4d and 4.6d.

At high current density (1.2 A/cm<sup>2</sup>), the current hold experiment was not carried out for cells without MPL because their voltage was lower than 0.3 V as shown in Figure 4.1b. With an MPL, Figure 4.4a show that, although the saturation in the SGL 29BC reached values of nearly 60%, the cells were still able to achieve good performance and stability. It is hypothesized the reason is that the MPL prevented liquid water accumulation in the large pores of the GDL on the cathode CL surface from contacting and forming liquid water films as discussed in [50]. Furthermore, the MPL could provide an in-plane oxygen diffusion pathway around such liquid water blockages [25, 50, 61]. It should be noted that at the highest current density with an

MPL water accumulation did not reach an equilibrium (see Figure 4.4c); therefore, it is likely that eventually the cell would start to show transport limitations. This behavior was observed in our laboratory with different cell configurations and will be reported in a future study.

Figure 4.4d compares the measured saturation in SGL 29BC with the results determined by imaging [34, 107, 154]. In this chapter, the saturation stabilized around 0.39, higher than  $0.27 \pm 0.06$  [154],  $0.16 \pm 0.07$  [107] and 0.32 [34] reported in the literature. The deviation in saturation might be induced by the different cells used, imaging resolution and segmentation, and the different experimental configurations and conditions. The saturation stabilized in this chapter after around 300 s, which is longer than 200 s reported by Nagai et al. [34] This was likely due to the higher cell temperature (60 °C vs. 40 °C) and lower inlet RH (70% vs. 105%) in this chapter.

### 4.3 Conclusions

Operating conditions have the most significant impact on PEMFC performance, water crossover, and water accumulation. For PEMFC with a cathode MPL, performance improved with increasing inlet RH from 30% to 70% at 80 °C, and performance at 60 °C and 70% RH was similar to 80 °C and 50% RH. The water crossover to produced water ratio remained nearly constant with the current density and only at 80 °C and 30% RH, it was from the anode to the cathode. Water crossover changed from approximately 0.1 moles of water per mole of water produced going from anode to cathode (80 °C and 30% RH) to 0.6 moles of water per mole of water produced going from cathode to anode (60 °C and 70% RH). At 80 °C, the total amount of water crossover increased with increasing inlet RH, likely due to increased PEM humidification. Furthermore, due to the low saturation pressure at 60 °C, the total amount of water transported from the cathode to the anode was the highest among the four experimental conditions in this chapter. Liquid water accumulation in the MEA was tracked with the developed setup at 60 °C and 70% RH. The cathode

outlet RH reached 100% in the course of the measurements, indicating that flooding took place in that compartment, and the saturation was estimated to reach 40% at 1 A/cm<sup>2</sup>.

The impact of adding an MPL to the cathode on the performance, water crossover, and water accumulation was also considerable. The addition of an MPL had only a limited effect on the performance at 80 °C and 30, 50 and 70% RH, but significantly improved the performance at 60 °C and 70% RH. The MPL was found to marginally increase the water back-diffusion from the cathode to the anode, i.e., approximately an extra 0.05 moles per mole of water produced. Although the cathode MPL did not prevent water accumulation in the cathode, the overall amount of liquid water was reduced possibly due to the increased internal MEA temperature and thus vaporization. Cells with a cathode MPL were found to achieve higher and more stable performance at higher current densities, despite reaching a saturation of nearly 70% at the highest current density (1.2 A/cm<sup>2</sup>). The improved performance was rationalized by the provision of in-plane oxygen transport pathways in the MPL around the local water blockage sites in the cathode GDL, as well as by their inhibition by improving the mismatch in pore sizes between the CL and the GDL.

## Chapter 5

# Effect of Cathode Catalyst Layer Nafion and Platinum Loading on the Dynamic Transport and Accumulation of Water Inside an Operating PEMFC<sup>1</sup>

Previous proton exchange membrane fuel cell (PEMFC) catalyst layer (CL) composition and loading optimization studies focused on improving cell performance but did not quantify the impact of these changes on water transport and liquid water accumulation. Considering water transport and accumulation have a significant impact on ohmic and mass-transport losses as well as catalyst degradation, understanding how they change with changing CL ionomer and platinum loading could help elucidate its relationship to cell performance and durability. In this chapter, the custom-built device described in Chapter 2 was used to measure the real-time water transport and liquid water accumulation in the electrode of PEMFCs with cathode CLs fabricated using varying Nafion (NLs, 10–40 wt.%) and platinum loadings (PLs, 0.133–0.317 mg<sub>Pt</sub>/cm<sub>CL</sub><sup>2</sup>) under multiple operating conditions ranging from hot/dry

---

<sup>1</sup>Parts of this chapter are reproduced from the following publication:

1. F. Wei, A. Kosakian, J. Liu, and M. Secanell, “Effect of Cathode Catalyst Layer Nafion and Platinum Loading on the Dynamic Transport and Accumulation of Water Inside an Operating PEMFC,” (under review).

Author contributions are detailed in the Preface of this thesis.

to cold/wet.

## 5.1 Materials and experiments

### 5.1.1 Sample preparation and cell assembly

Six cathode catalyst layer designs were studied, as summarized in Table 5.1. To verify the reproducibility of the measurements, two cells were assembled and tested for each cathode catalyst layer design. Cathode CL designs 1-3 had a cathode platinum loading (PL) of  $0.2 \text{ mg}_{\text{Pt}}/\text{cm}_{\text{CL}}^2$  and Nafion loadings (NLs) of 10, 20 and 30 wt.%, respectively, and designs 4-6 had 30 wt.% NL and PLs of 0.133, 0.219 and  $0.317 \text{ mg}_{\text{Pt}}/\text{cm}_{\text{CL}}^2$ , respectively. Designs 4-6 were chosen to have 30 wt.% NL as it is close to the optimal ionomer loading previously reported in the literature [78, 198, 205]. The anode CL PL was maintained at  $0.1 \text{ mg}_{\text{Pt}}/\text{cm}_{\text{CL}}^2$  with 30 wt.% NL.

Catalyst coated membranes (CCMs) were manufactured by inkjet printing  $5 \text{ cm}^2$  (approximately 2.24 cm by 2.24 cm) of catalyst ink using a piezo-electric printer (Dimatix DMP-2831, Fujifilm Inc.) on a Nafion membrane (Ion Power, NR-211,  $25.4 \mu\text{m}$ ) [77, 261, 262]. The relatively small active area was chosen to minimize the changes in concentration along the channel and reduce the occurrence of two-phase flow in the channel, as large liquid droplets might not be detected by the sensors. The catalyst layer ink, with varying NLs, was first prepared by mixing isopropyl alcohol, propylene glycol, Nafion ionomer solution (Ion Power, Liquion solution LQ-1105 1100EW 5 wt.%) and Pt/C catalyst (HyPlat, 40 wt.% platinum supported on Ketjenblack EC-300J) using the procedures described in Refs. [25, 261].

The catalyst coated membrane was then sandwiched between two  $5 \text{ cm}^2$  Sigracet SGL 29BC porous transport layers (PTLs). Subsequently, the membrane electrode assembly (MEA) was integrated into a Scribner fuel cell hardware with an in-house flow field plate with 14 parallel flow channels (see Figure 2.1c). The gas flow channel width and depth were 0.86 mm and 1 mm, respectively. The width of the land

Table 5.1: Cathode CL under study.

Cathode CL	Nafion loading (wt.%)	Platinum loading ( $\text{mg}_{\text{Pt}}/\text{cm}^2_{\text{CL}}$ )	SEM thickness <sup>a</sup> ( $\mu\text{m}$ )	Porosity <sup>b</sup> (%)	ECSA-BOT <sup>c</sup> ( $\text{m}^2_{\text{Pt}}/\text{g}_{\text{Pt}}$ )	ECSA-EOT <sup>c</sup> ( $\text{m}^2_{\text{Pt}}/\text{g}_{\text{Pt}}$ )
Design 1	10	0.194	6.2 $\pm$ 0.8	70.4 $\pm$ 3.7	57.3, 67.7	60.9, 69.6
Design 2	20	0.205	6.2 $\pm$ 0.9	62.6 $\pm$ 5.1	58.6, 63.9	60.8, 63.5
Design 3	40	0.206	4.3 $\pm$ 0.8	19.5 $\pm$ 15.9	59.4 <sup>d</sup>	61.8 <sup>d</sup>
Design 4	30	0.133	3.2 $\pm$ 0.4	43.6 $\pm$ 6.8	58.2 <sup>d</sup>	58.7 <sup>d</sup>
Design 5	30	0.219	5.9 $\pm$ 0.5	49.1 $\pm$ 4.8	59.0, 61.4	60.1, 64.0
Design 6	30	0.317	7.8 $\pm$ 0.5	44.8 $\pm$ 3.3	55.6, 55.1	56.2, 54.9

<sup>a</sup> The uncertainty of CL thickness was calculated as the standard deviation of 60 measurements (three images with 20 measurements each).

<sup>b</sup> The uncertainty of CL porosity was estimated using the error propagation in equations (5.1) from the uncertainty of CL thickness.

<sup>c</sup> ECSA for two cells of each cathode CL configuration.

<sup>d</sup> CV result showed one of the two cells had a internal cell shorting and, therefore, ECSA is not reported.

between two flow channels was 0.82 mm. Two 7 mil rigid gaskets (composed of one 2-mil Kapton Polyimide film (2271K2) and one 5 mil PTFE-coated fiberglass fabric sheet (8577K82) from McMASTER-CARR) with a 5 cm<sup>2</sup> window were used on each side of the MEA to prevent gas leakage and provide consistent contact between the CCM and the PTLs. The thickness and porosity of the uncompressed SGL 29BC was 210.3±2.2 μm and 77.2±0.3%, respectively [4]. Assuming CL and membrane deformation is negligible [92], the average thickness of compressed SGL 29BC in each side was approximately 170 μm, i.e., about 20% pinch.

### 5.1.2 Microstructure characterization

After all electrochemical characterization tests, cathode CLs were embedded in epoxy, polished to expose the CL edge, and coated with carbon powder to become electronically conductive. Their cross-sectional scanning electron microscopy images were then taken using back-scattered mode at three different locations (SEM, conducted with 300 VP-FESEM, Zeiss Sigma). Catalyst layer thickness was measured at 20 locations in each cross-sectional SEM image using the software ImageJ 1.52v [267]. The porosity of each cathode CL was estimated based on the density of each component and SEM thickness using the following equations [4]:

$$\left\{ \begin{array}{l} V_{\text{CL,pore}} = V_{\text{CL,bulk}} - V_{\text{CL,solid}}, \\ V_{\text{CL,bulk}} = A \cdot L, \\ V_{\text{CL,solid}} = A \cdot m_{\text{Pt}} \left( \frac{1}{\rho_{\text{Pt}}} + \frac{1-\omega_{\text{Pt}}}{\omega_{\text{Pt}} \rho_{\text{C}}} + \frac{\omega_{\text{N}}}{(1-\omega_{\text{N}}) \omega_{\text{Pt}} \rho_{\text{N}}} \right), \\ \epsilon_{\text{CL}} = \frac{V_{\text{CL,pore}}}{V_{\text{CL,bulk}}}, \end{array} \right. \quad (5.1)$$

where  $V_{\text{CL,solid}}$ ,  $V_{\text{CL,bulk}}$ ,  $V_{\text{CL,pore}}$ ,  $m_{\text{Pt}}$ ,  $\omega_{\text{N}}$  and  $\epsilon_{\text{CL}}$  are solid volume, bulk volume, pore volume, platinum loading, Nafion loading and porosity of the CL, respectively;  $A$  and  $L$  are the in-plane area (5 cm<sup>2</sup>) and SEM thickness of the CL, respectively;  $\rho_{\text{C}}$ ,  $\rho_{\text{Pt}}$  and  $\rho_{\text{N}}$  are the densities of the carbon black support (2 g/cm<sup>3</sup>), platinum (21.5 g/cm<sup>3</sup>) and Nafion (2 g/cm<sup>3</sup>), respectively [4, 208];  $\omega_{\text{Pt}}$  is the mass fraction of platinum in Pt/C catalyst (40 wt.%).

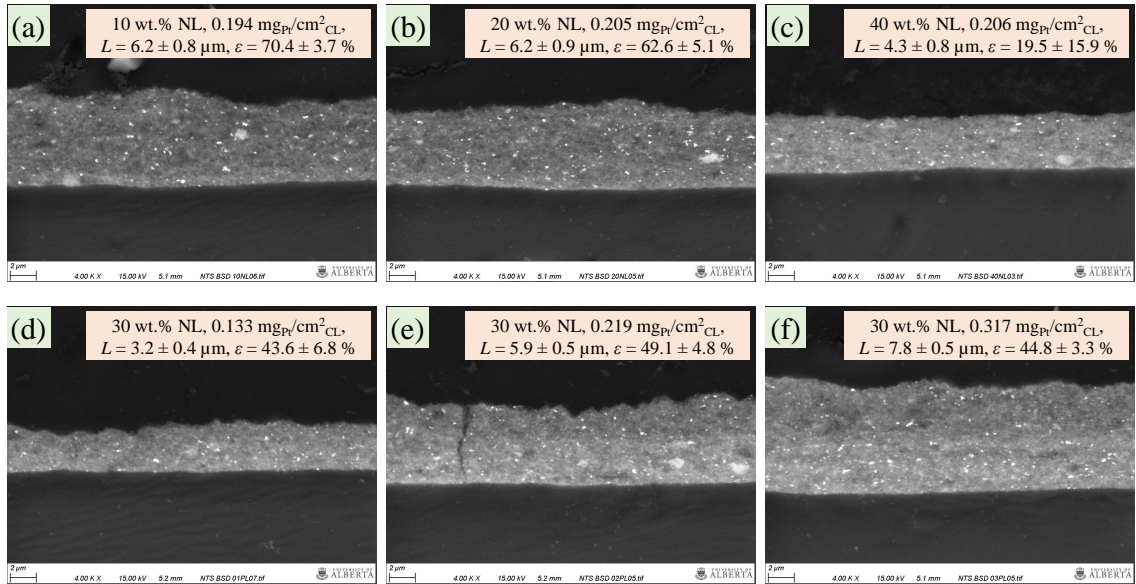


Figure 5.1: Cross-sectional SEM images of the cathode catalyst layers (after all in-situ tests): (a) design 1; (b) design 2; (c) design 3; (d) design 4; (e) design 5; and (f) design 6.

## 5.2 Results and Discussion

### 5.2.1 Effect of Nafion loading

#### 5.2.1.1 Thickness, porosity and ECSA

Cross-sectional SEM images, shown in Figure 5.1, were used to estimate CL thickness and porosity. The SEM thickness and porosity of each analyzed CL design are shown in Table 5.1 and Figure 5.1. Catalyst layer thicknesses decreased from  $6.2 \pm 0.8 \mu\text{m}$  to  $4.3 \pm 0.8 \mu\text{m}$  as Nafion loading increased from 10 to 40 wt.%. In this work, when the Nafion loading increased from 10 to 20 wt.%, catalyst layer thickness remained unchanged. Further increasing Nafion loading from 20 to 40 wt.% reduced the thickness of CL, which is consistent with Shukla et al. [4] (29.6 to 39.8 wt.% NL) and Soboleva et al. [110] (30 to 50 wt.% NL) but not with Gode et al. [268], where a negligible impact of Nafion loading (30 to 43 wt.%) on CL thickness was observed. The reduction in CL thickness in this case could be due to the ionomer shrinking the CL upon drying.

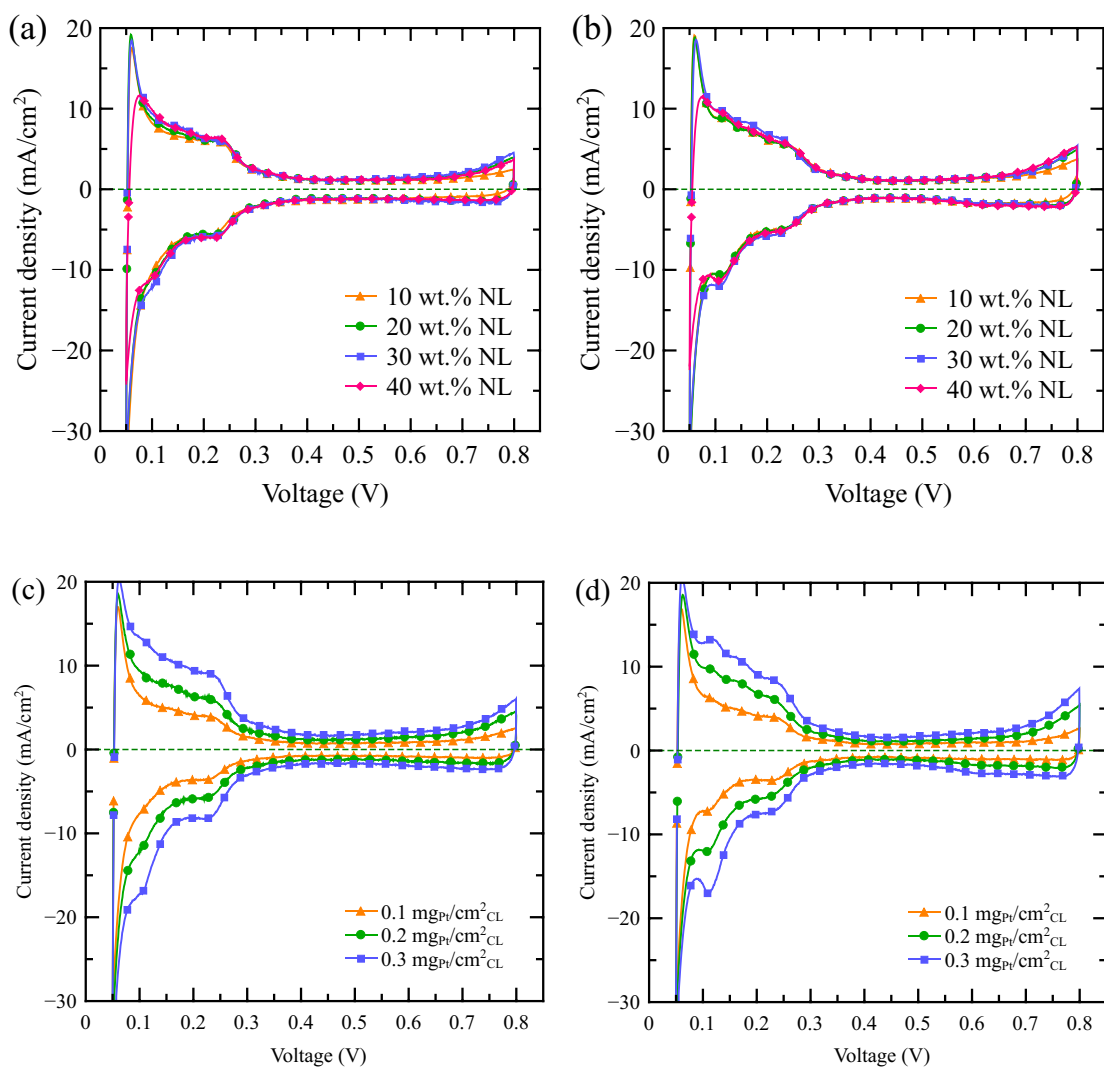


Figure 5.2: Cyclic voltammetry results for cells with varying Nafion loadings (a) before and (c) after all tests and platinum loadings (c) before and (d) after all tests.

Catalyst layer porosity, estimated using eq. (5.1), was observed to decrease with increasing Nafion loading [4, 78, 269]. Porosity decreased only slightly from 10 to 20 wt.% NL, whereas it decreased dramatically from 20 to 40 wt.% NL, in agreement with the observations by Gode et al. [268]

Figures 5.2a and 5.2b show the cyclic voltammetry results for the cathode CL designs with varying Nafion loadings. Table 5.1 lists the ECSAs estimated from these measurements. Nafion loading was found to have a negligible impact on ECSA, which was about  $60 \text{ m}^2_{\text{Pt}}/\text{g}_{\text{Pt}}$  in all cases (10–40 wt.%), in agreement with the observations in Ref. [78] for inkjet printed CLs.

### 5.2.1.2 Fuel cell performance

Figure 5.3 shows the polarization curves and current interrupt resistances for cells with 10, 20, 30, and 40 wt.% Nafion loading under varying operating conditions. Nafion loading was found to have a significant impact on PEMFC performance. Under all operating conditions, the cell with 40 wt.% NL exhibited the worst performance likely due to the highest resistance to oxygen transport through the bulk void space of the CL, since its porosity was the lowest (19.5%, see Table 5.1 and Figure 5.1).

**Dry and intermediate conditions** At 80 °C and 30, 50 and 70% RH, the best performance was achieved at 20 wt.% NL. For cells with 30 wt.% NL, a lower performance was obtained at high current densities as compared with 20 wt.% NL, which could be attributed to significant oxygen transport resistance because of lower porosity (49.1% vs. 62.6%). The cathode CL with 10 wt.% NL is likely limited by CL protonic transport resistance and, therefore, it exhibited the largest sensitivity to RH.

**Cold/wet condition** The observations made above were also valid for 60 °C and 70% RH; however, stability of the cell performance varied significantly among Nafion loadings due to liquid water accumulation in the MEA. As shown in Figure 5.3d, cells with 10 and 20 wt.% NLs shut down at high current densities during the backward

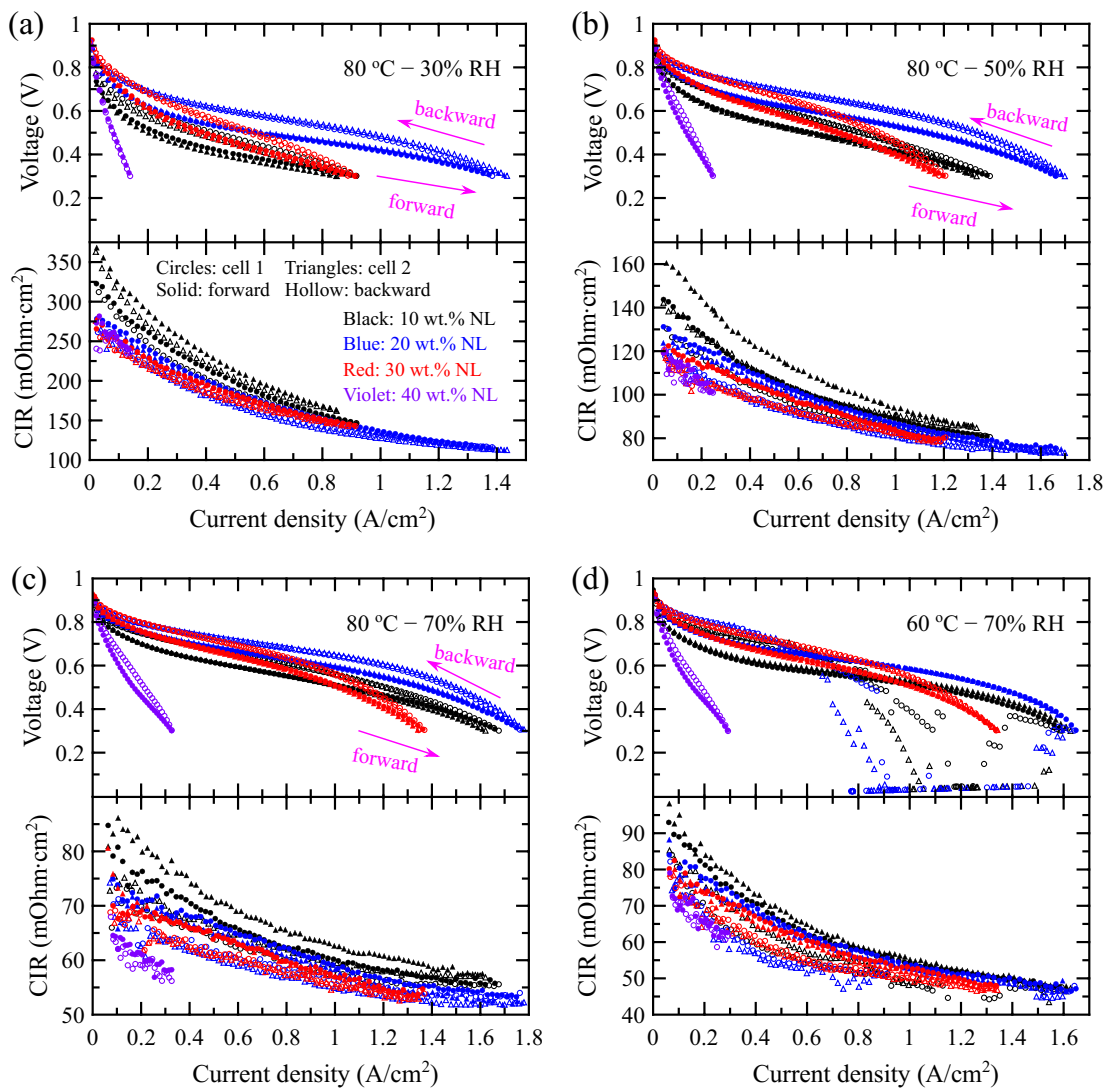


Figure 5.3: Polarization curves and current interrupt resistances for cells with 10, 20, 30 and 40 wt.% Nafion loading obtained at (a) 80 °C and 30% RH, (b) 80 °C and 50% RH, (c) 80 °C and 70% RH and (d) 60 °C and 70% RH. Experimental conditions: 0.5 slpm hydrogen and 0.5 slpm air, 50 kPa(gauge) backpressure, and 5 mA/s scan rate.

scan due to MEA flooding. The performance progressively recovered likely due to the removal of liquid water, with the cell having 10 wt.% NL recovering first. Despite the comparable amount of liquid water in the MEA with 30 wt.% NL at the same current densities (about from 0 to 1.3 A/cm<sup>2</sup> shown in Figure 5.7c), those cells continued to operate normally, as the maximum amount of liquid water in the electrode was lower due to the lower maximum current density at 0.3 V (at which point the scan reversed direction).

### 5.2.1.3 Water crossover

Figure 5.4a shows the real-time water crossover flux during current hold experiments at 60 °C and 70% RH. In all cases, water moves from cathode to anode and the flux increases with current density. At low current densities, i.e., 0.2–0.6 A/cm<sup>2</sup>, the water crossover measured using the anode water balance quickly matched the cathode, and water crossover promptly stabilized. At higher current densities, i.e., 0.8–1.2 A/cm<sup>2</sup>, the anode and cathode measured water crossover did not match after the current was increased and then progressively converged to the same value, after about 5 min. The discrepancy in water crossover is attributed to liquid water accumulation in the PEM and cathode electrode. At a current density of 1.4 A/cm<sup>2</sup>, a much higher water crossover was measured using the cathode water balance than the anode, due to significant liquid water accumulation in the cathode, as evidenced by the poor cell voltage stability (see Figure 5.6a). As shown in Figure 5.5, at 80 °C, the measured anode and cathode water crossover instantly matched and converged to the same value at all current densities because liquid water accumulation is negligible at this condition due to increased evaporation rate [119, 270].

Figures 5.4b and 5.4c show the averaged cathode-to-anode water crossover results during the last 5-min of current hold experiments. The cathode-to-anode water crossover decreased with increasing Nafion loading at all operating conditions, likely as a result of increasing ORR activity closer to the CCL-PTL interface due to the CL

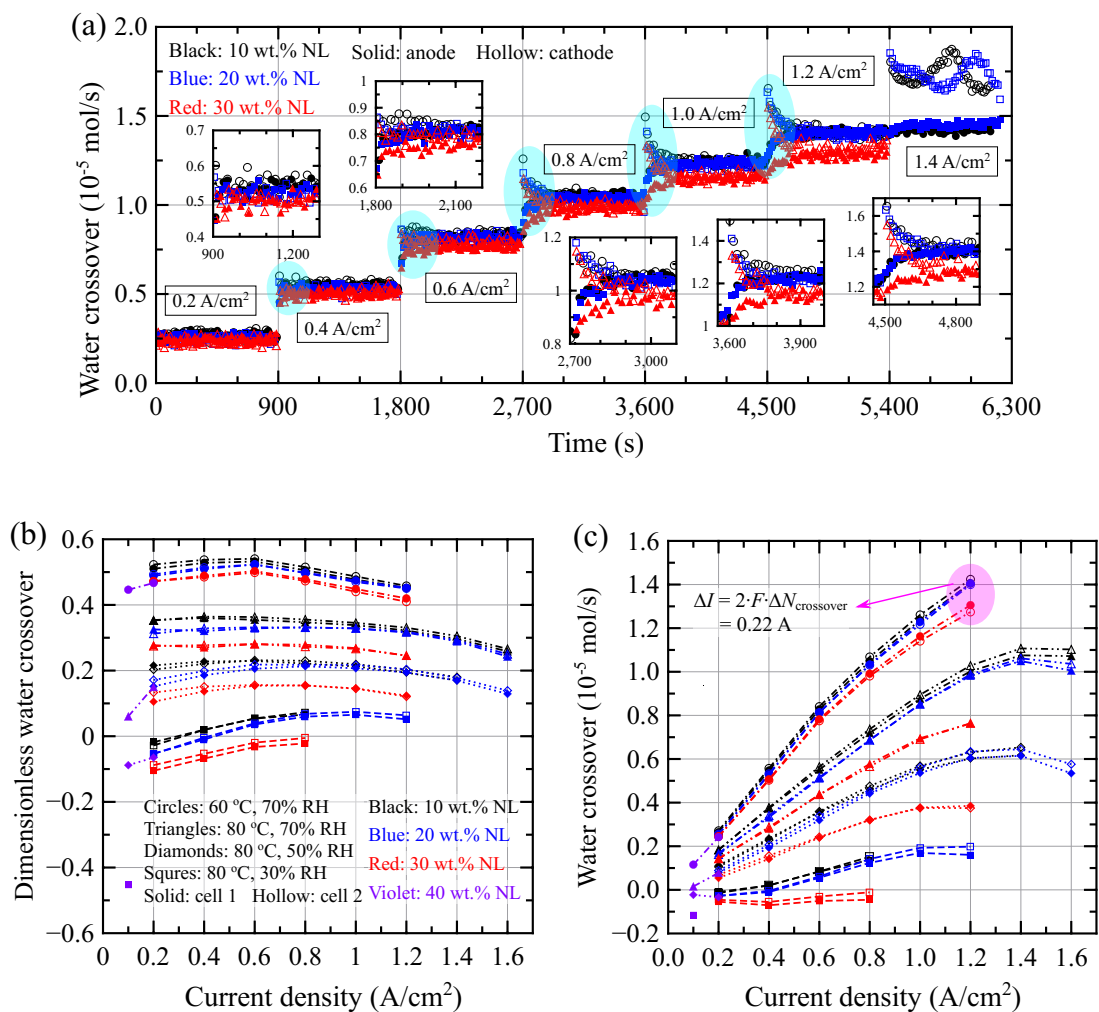


Figure 5.4: Water transport results for cells with varying Nafion loadings obtained from current hold experiments: (a) real-time cathode-to-anode water crossover at 60 °C and 70% RH, (b) averaged dimensionless cathode-to-anode water crossover during last 5-min, and (c) averaged cathode-to-anode water crossover during last 5-min.

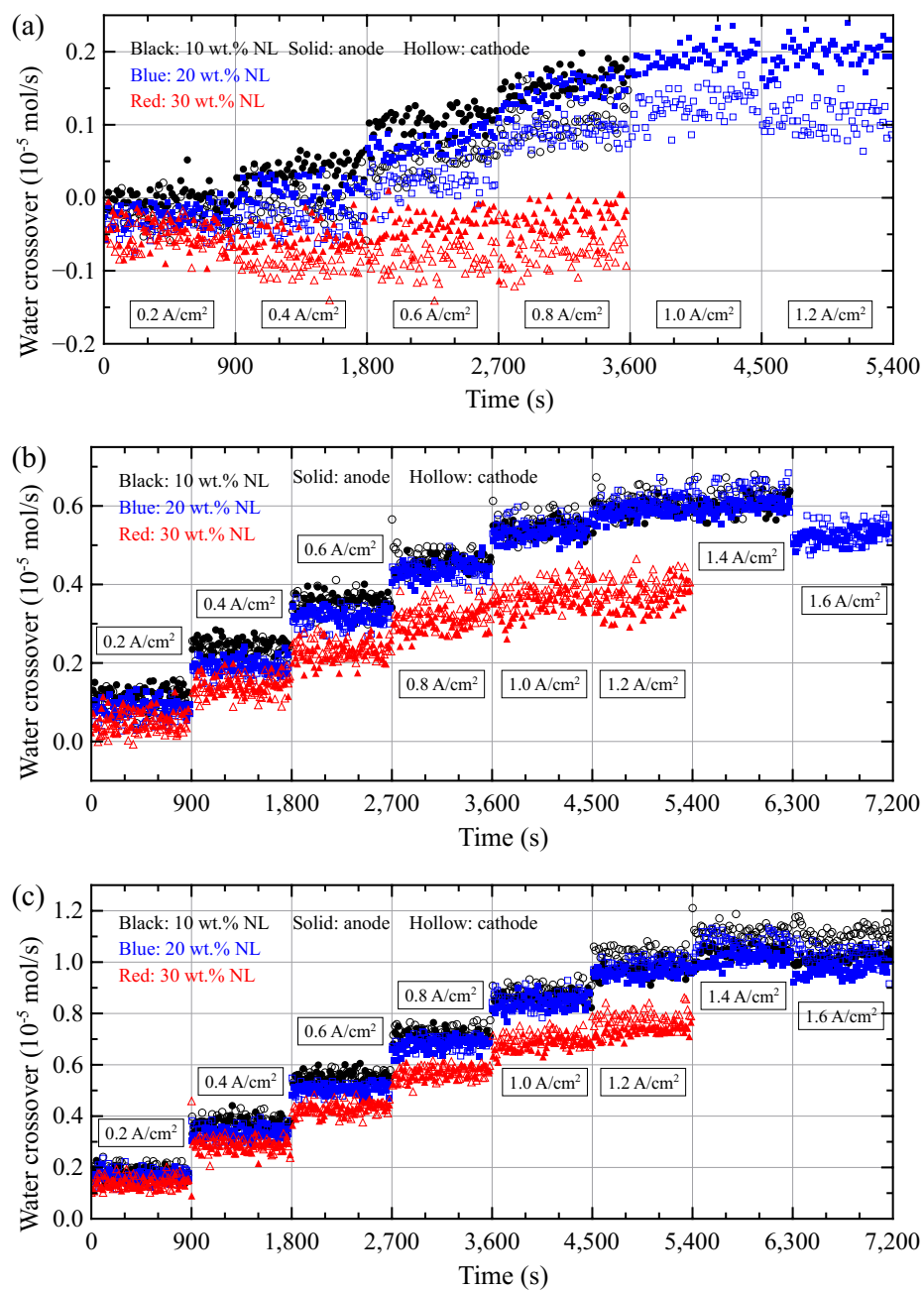


Figure 5.5: Real-time cathode-to-anode water crossover for cells with varying Nafion loadings obtained from current-hold experiments at: (a) 80 °C and 30% RH, (b) 80 °C and 50% RH and (c) 80 °C and 70% RH.

reduced porosity and increased protonic conductivity. This promoted water removal from the cathode and, therefore, decreased the crossover flux of water to the anode. This effect was especially prominent in the cells with 40 wt.% NL (porosity is around 19.5%). The increase in water crossover flux from cells with 20 wt.% to 30 wt.% NL at 1.2 A/cm<sup>2</sup> is approximately equivalent to removing the water produced by 0.044 A/cm<sup>2</sup> of current.

Figures 5.4b and 5.4c show that operating condition had a significant effect on water crossover, in agreement with our previous publication [2]. At 80 °C, water crossover from cathode to anode increased with increasing inlet RH, likely due to the improved water transport properties of the humidified Nafion membrane [1, 43, 133, 189]. At 60 °C and 70% RH, the total amount of water crossing the membranes was the highest among all experimental conditions. When cells operate at lower cell temperature, the saturation pressure is lower, resulting in higher water vapor activity at low current and thus, ionomer water content even at low current, leading to a larger water content gradient in the membrane enhancing the cathode-to-anode water transport.

#### 5.2.1.4 Liquid water accumulation

**Current-hold measurements** Figure 5.6 shows water accumulation results obtained from current hold experiments at 60 °C and 70% RH. Figure 5.6a shows that the cell voltage during the current hold was stable for all cells until 1.4 A/cm<sup>2</sup>. The cell voltage was also in agreement with polarization curve voltage at the same current density during forward scan, as seen in Figure 5.3d. Figure 5.6b shows that the membrane protonic resistance decreases with increasing current density as the membrane is hydrated.

The measured ( $N_{\text{ORR,measured}}$ ) and theoretical ORR product water fluxes are shown in Figure 5.6c and are obtained using

$$N_{\text{ORR,measured}} = (N_{\text{water,out,a}} + N_{\text{water,out,c}}) - (N_{\text{water,in,a}} + N_{\text{water,in,c}}) \quad (5.2)$$

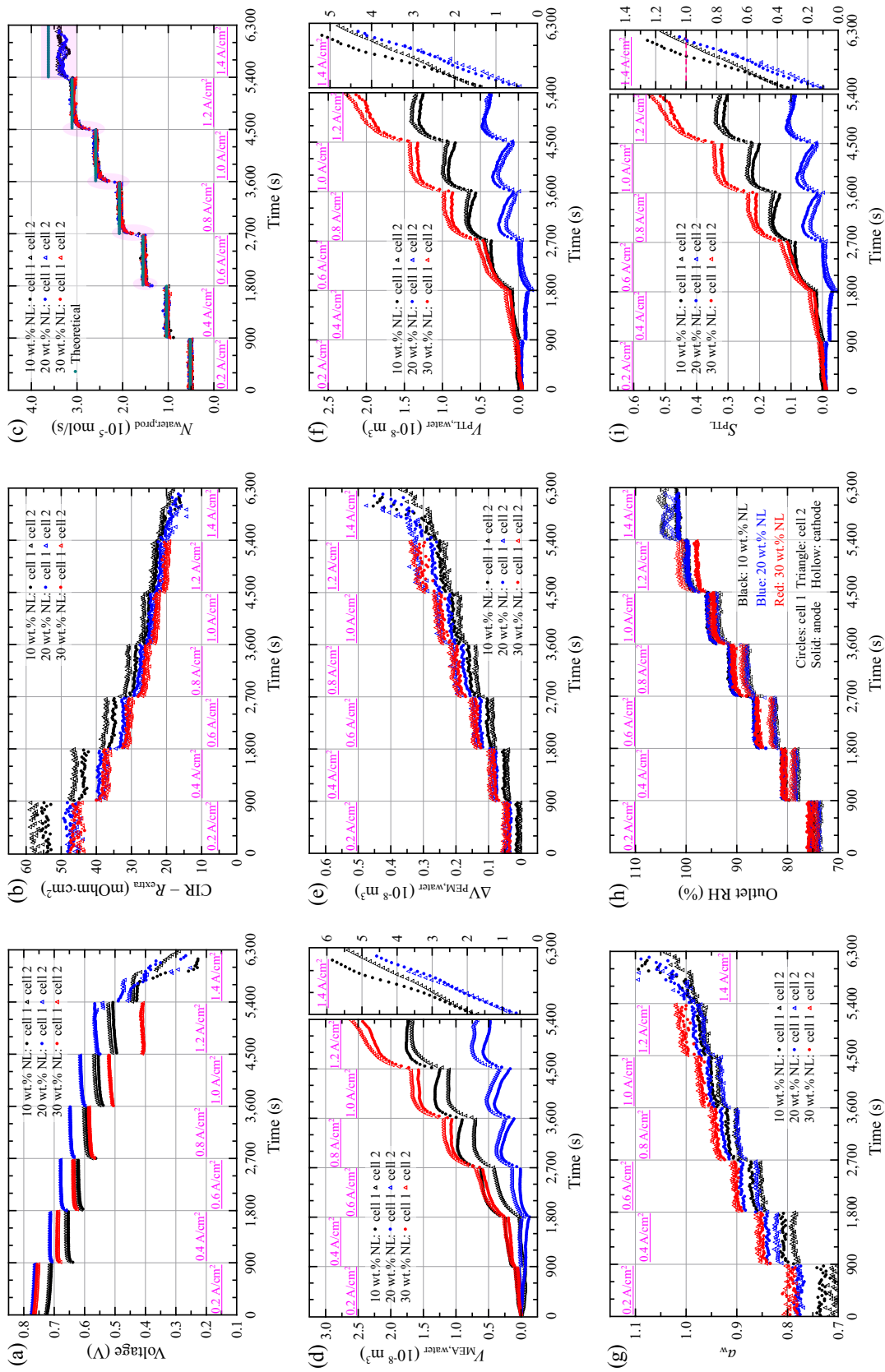


Figure 5.6: Current hold results at 60 °C and 70% RH for cells with 10, 20, 30 and 40 wt.% Nafion loading: (a) cell voltage, (b) membrane protonic resistance, (c) ORR product water flux, (d) total amount of water accumulation in the MEA, (e) total amount of water accumulation in the porous media, (f) total amount of water accumulation in the porous media, (g) outlet RH, (h) membrane water activity, and (i) cathode PTL saturation.

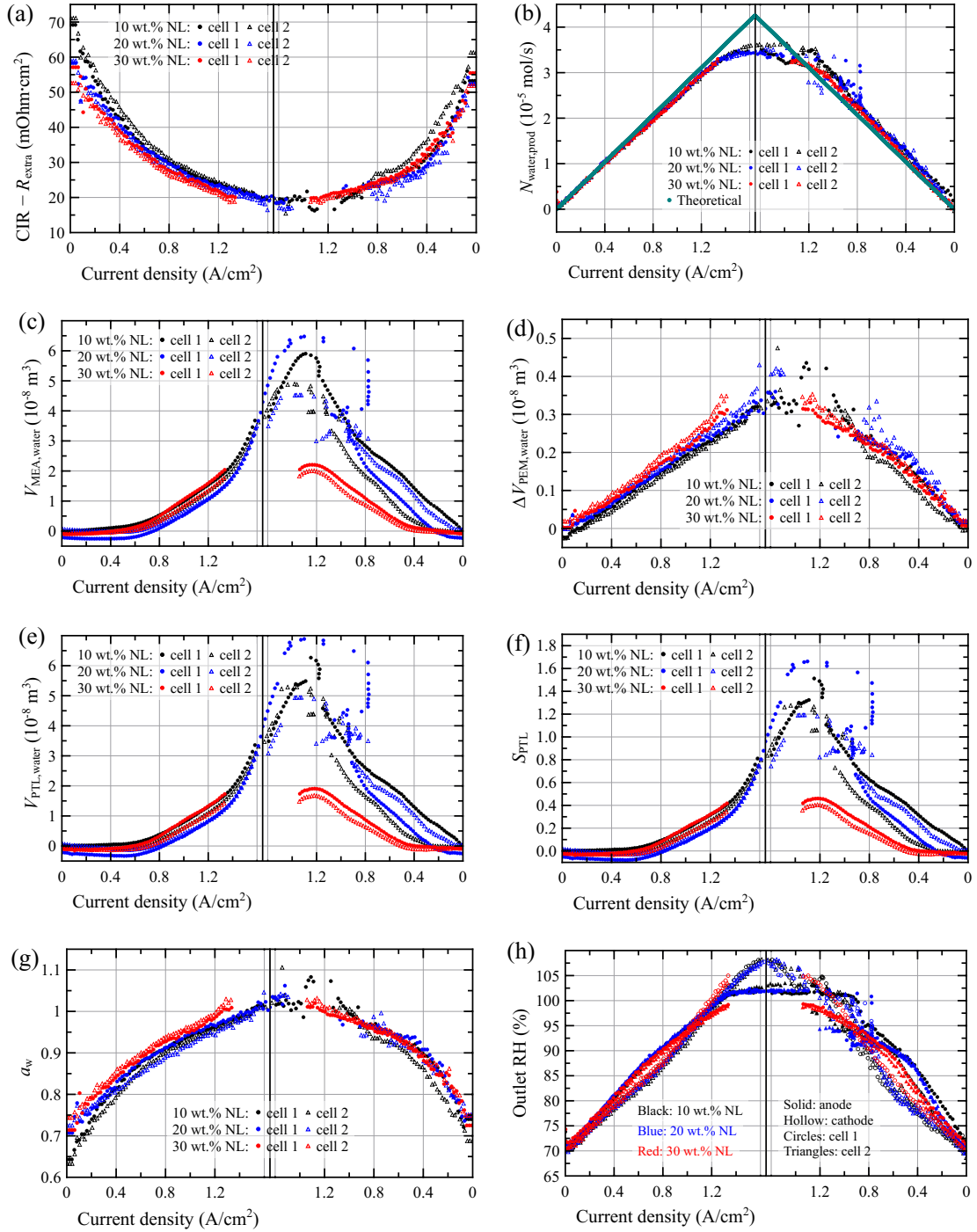


Figure 5.7: Galvanodynamic results at 60 °C and 70% RH for cells with 10, 20, 30 and 40 wt.% Nafion loading: (a) membrane protonic resistance, (b) ORR product water flux, (c) total amount of water accumulation in the MEA, (d) total amount of water accumulation in the membrane, (e) total amount of water accumulation in the porous media, (f) cathode porous media saturation, (g) membrane water activity, and (h) outlet RH.

and eq. (2.10), respectively. These fluxes noticeably deviated at the initial stages of the current hold from 0.6 to 1.2 A/cm<sup>2</sup> and at all times at 1.4 A/cm<sup>2</sup>. This deviation is hypothesized to be due to water accumulation in the membrane and in the porous media.

Figure 5.6d shows the total amount of water accumulation in the MEA estimated using eq. (2.12), i.e., by integrating the difference between theoretical and measured ORR product water flux in Figure 5.6c. The negative values at the current densities of 0.2 and 0.4 A/cm<sup>2</sup> for the cells with 20 wt.% NL were assumed to be a result of experimental uncertainty, and the total amount of accumulated water is considered negligible. The amount of water accumulated in the MEA was then separated into water accumulation in the membrane (Figure 5.6e) and in the cathode PTL (Figure 5.6f) using the approach discussed in Section 2.2.3. Initially, water accumulated in the membrane, followed by water accumulation in the porous media at current densities above 0.4 A/cm<sup>2</sup>.

To verify that the membrane-conductivity-based approach to estimate the water content in the membrane was physically meaningful, the average water activity obtained using eq. (2.20), and shown in Figure 5.6g, was compared to the outlet RH in Figure 5.6h. Both the estimated water activity and outlet RH follow similar trend and have similar values. The average water activity exceeded unity at 1.4 A/cm<sup>2</sup> likely because eq. (2.20) was obtained for vapor-equilibrated Nafion membrane while the membrane might be in contact with liquid water (Figure 5.6f).

Figures 5.6f and 5.6i show that Nafion loading has a significant impact on the dynamics of liquid water accumulation and saturation in the porous media, where saturation was obtained from water accumulation using eq. (2.21). For cells with 30 wt.% NL, at each current hold between 0.2 to 1.0 A/cm<sup>2</sup>, the total saturation in the porous media quickly increased with operating time and then stabilized. The stable region indicated that a balance was established between water evaporation, which increases with increasing liquid-vapor interfacial area [119], water crossover

and water production. As current density increased to 1.2 A/cm<sup>2</sup>, this balance could no longer be established and liquid water accumulated in the porous media during the full duration of the current hold step, indicating that cells were not stable at this current density.

For cells with 10 and 20 wt.% NL on the other hand, at 0.8–1.2 A/cm<sup>2</sup>, PTL saturation increased but then decreased over time as seen in Figures 5.6f and 5.6i. In these cells, liquid water content reduced over time after a brief increase due to the increased current density (and thus increased water production rate). The reason for the reduction in liquid water is not clear, as the cathode over-potential is similar (Figure 5.6a), but might have been due to the higher CL porosity allowing a larger vapor flux, thereby tipping the balance between water rejection and water accumulation towards the former. At 1.4 A/cm<sup>2</sup>, water could not be evaporated at a sufficient rate, and the amount of liquid water in the PTLs significantly increased over time. This rapid increase in saturation resulted in the cell voltage instability seen in Figure 5.6a. Saturation exceeded unity at 1.4 A/cm<sup>2</sup> in Figure 5.6i, possibly indicating either flooding of both cathode and anode PTLs or water in the cathode channel.

In the entire tested range of current densities, the cells with 30 wt.% NL had the highest saturation in the porous media compared with the cells with lower Nafion loadings. This was likely due to the reduced cathode-to-anode water crossover flux (see Figures 5.4b and 5.4c) and hindered water vapor diffusion toward the cathode channel as a result of lower porosity (see Table 5.1). The difference in water crossover between 10 and 20 wt.% NL in Figures 5.4b and 5.4c was marginal, however the overall PTL saturation was considerably lower for the 20 wt.% NL cells compared with 10 wt.% NL. This might have been due to the shift of the ORR in the cathode CL from the PEM-CCL interface at low Nafion loading to a more uniform distribution at higher Nafion loading. The more uniform production of water in the cathode CL could result in a larger liquid-vapor interfacial area, leading to a higher rate of

evaporation.

**Galvanodynamic measurements** Figure 5.7 shows the water accumulation results during the galvanodynamic polarization curve experiments in Figure 5.3d which were obtained at a scan rate of 5 mA/s, 60 °C and 70% RH. Figure 5.7a shows the membrane protonic resistance. Since reliable CIR measurements could not be obtained during the flooding-induced voltage drop (see Figure 5.3d), the missing data was interpolated so as to enable the conversion of the CIR into water content as discussed in Section 2.2.3.2.

A significant difference between the measured and theoretical ORR product water fluxes at 60 °C and 70% RH was observed at high current densities as seen in Figure 5.7b. Similar to that in the current hold experiments, this discrepancy was attributed to water accumulation in the membrane and in the porous media.

The total amount of water accumulation in the MEA, membrane and porous media estimated using the methodology discussed in Section 2.2.3 is shown in Figures 5.7c, 5.7d and 5.7e, respectively. During the galvanodynamic experiments, a steady increase in membrane water content and PTL saturation is observed as a balance between water production and water rejection cannot be established.

Figure 5.7f shows that the PTL saturation for cells with 10 and 20 wt.% NL reached 100% at the end of the forward scan and even 170% during the backward scan, indicating that liquid water accumulated in either both anode and cathode electrodes or cathode PTL and channel. This is in line with the cell voltage instability during the backward scan (see Figure 5.3d) and the membrane water activity being greater than 1 as seen in Figure 5.7g, which implies presence of liquid water near the membrane. In contrast, saturation only reached 40% for cells with 30 wt.% NL, likely due to lower maximum current density achieved in the galvanodynamic measurements. At the same current densities during the forward scan, Nafion loading had a negligible impact on the water accumulation, because the scan rate (5 mA/s) was too fast to

accumulate enough water to affect cell performance. The cells with 30 wt.% NL accumulated significantly less liquid water during backward scan because they spent less time operating at high current densities.

Figure 5.7h shows the measured cell outlet RHs. For the cells with 30 wt.% NL, only the cathode outlet RH reached 100% at high current densities and, therefore, it is likely that most of the liquid water was accumulated in the cathode. However, for 10 and 20 wt.% NLs, both anode and cathode outlet RHs reached 100% at high current densities, indicating the possible presence of liquid water in both electrodes. This was in agreement with saturation being greater than 1 shown in Figure 5.7f.

## 5.2.2 Effect of platinum loading

### 5.2.2.1 Thickness, porosity and ECSA

Table 5.1 and Figure 5.1 show the SEM thickness and porosity for the inkjet printed CLs with varying platinum loadings. An approximately linear increase in the SEM thickness was observed, with a relatively small variation in the volumetric platinum loading (371, 406, and 416  $\text{mg}_{\text{Pt}}/\text{cm}^3_{\text{CL}}$ ). This is in contrast to the nonlinear increase in thickness of inkjet printed CLs observed in Ref. [261], where the volumetric loading changed from 74 to 205  $\text{mg}_{\text{Pt}}/\text{cm}^3_{\text{CL}}$ . This difference is attributed to the use of propylene glycol instead of ethylene glycol in the CL ink preparation. As discussed in Ref. [271], the lower boiling point of propylene glycol decreases drying time and increases CL porosity.

Catalyst layer porosity was found to be nearly independent of platinum loading, which is consistent with the nearly constant volumetric platinum loading but contrary to the observations in Ref. [261] that PL negatively impacts CL porosity. The difference in the CL ink preparation discussed above might be the reason for the different impact of platinum loading on CL porosity made in this work and Ref. [261]

Figures 5.2c and 5.2d show the CV results for cathode CL designs with varying platinum loadings, and the corresponding ECSAs are listed in Table 5.1. As shown

in the table, there was no clear trend in the impact of platinum loading on ECSA, which was around 55–60  $\text{m}_{\text{Pt}}^2/\text{g}_{\text{Pt}}$ .

### 5.2.2.2 Fuel cell performance

Figure 5.8 shows the polarization curves and CIRs of cells with varying platinum loadings. The best performance was achieved with 0.317  $\text{mg}_{\text{Pt}}/\text{cm}_{\text{CL}}^2$  PL at all operating conditions, with the largest improvement observed at low RH and high temperature, i.e., 80 °C and 30% RH shown in Figure 5.8a. Cells with 0.133 and 0.219  $\text{mg}_{\text{Pt}}/\text{cm}_{\text{CL}}^2$  PL had comparable performance at all operating conditions but in the kinetic region where performance correlated with loading, in agreement with Shukla et al. [261] and Saha et al. [272]

### 5.2.2.3 Water crossover

Figure 5.9a shows the cathode-to-anode water crossover flux during current holds at 60 °C and 70% RH. The same behavior was observed at all platinum loadings. Figures 5.9b and 5.9c show that increasing platinum loading had a negligible effect on cathode-to-anode water crossover, in contrast with the significant influence of Nafion loading shown in Figures 5.4b and 5.4c. The limited impact of PL on water crossing the membrane contradicts the numerical modeling results of Zenyuk et al. [159], where they reported a significant increase in water crossover with increasing CL thickness, such as approximately twice higher at 5  $\mu\text{m}$  compared to 2  $\mu\text{m}$ .

### 5.2.2.4 Liquid water accumulation

**Current hold measurements** Figure 5.10 shows current hold results for cells with varying platinum loadings at 60 °C and 70% RH. As seen in Figure 5.10a, all cells had stable voltage until 1.2  $\text{A}/\text{cm}^2$ . Additionally, the voltage of cells with 0.133  $\text{mg}_{\text{Pt}}/\text{cm}_{\text{CL}}^2$  was comparable with 0.219  $\text{mg}_{\text{Pt}}/\text{cm}_{\text{CL}}^2$  but was significantly lower than 0.317  $\text{mg}_{\text{Pt}}/\text{cm}_{\text{CL}}^2$ . The cell voltage, as in the previous case, was similar to the polarization curve cell voltage during the forward scan at the same current density.

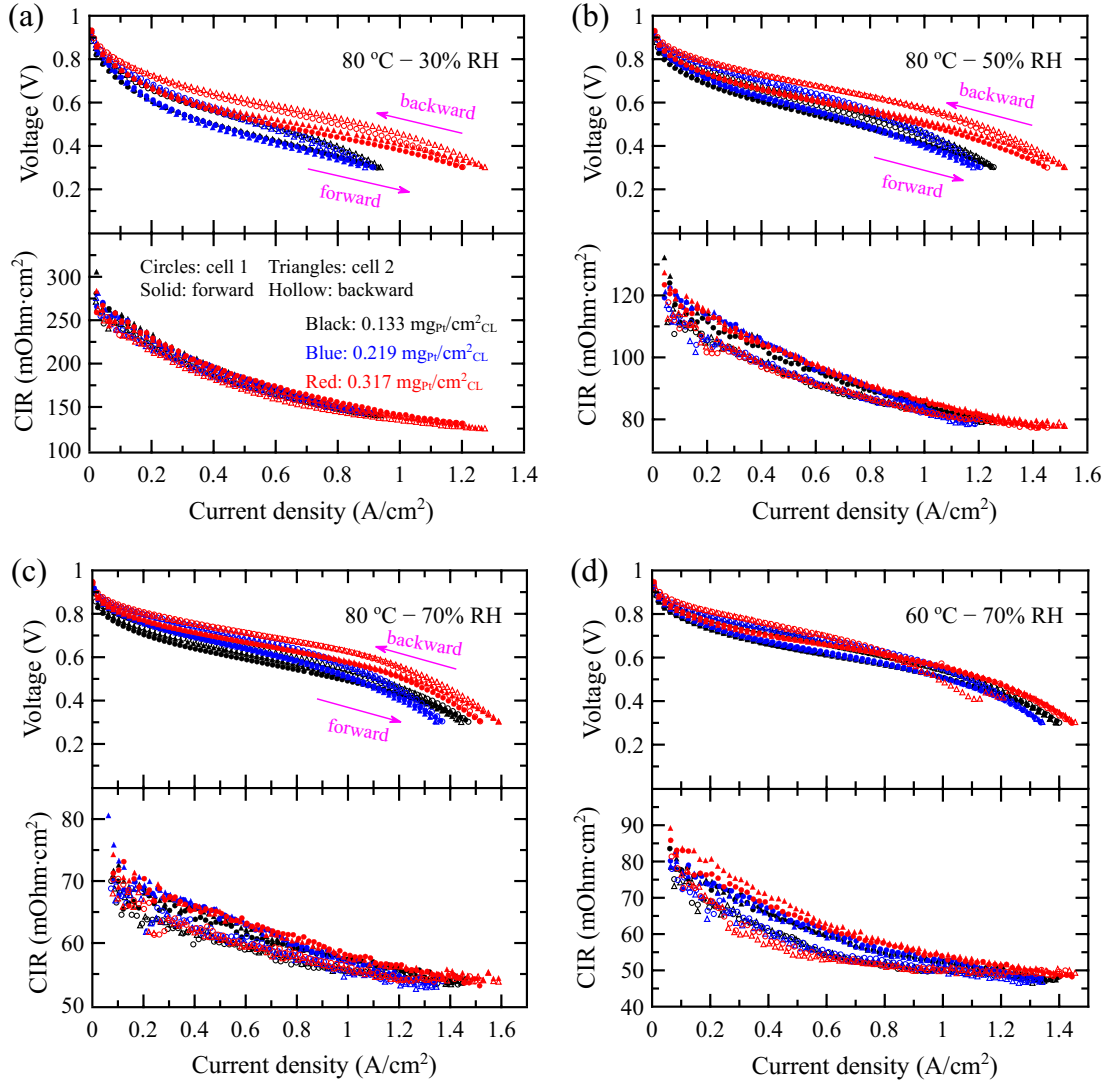


Figure 5.8: Polarization curves and current interrupt resistances for cells with 0.133, 0.219 and 0.317  $\text{mg}_{\text{Pt}}/\text{cm}_{\text{CL}}^2$  platinum loading obtained at (a) 80 °C and 30% RH, (b) 80 °C and 50% RH, (c) 80 °C and 70% RH and (d) 60 °C and 70% RH. Experimental conditions: 0.5 slpm hydrogen and 0.5 slpm air, 50 kPa(gauge) backpressure, and 5 mA/s scan rate.

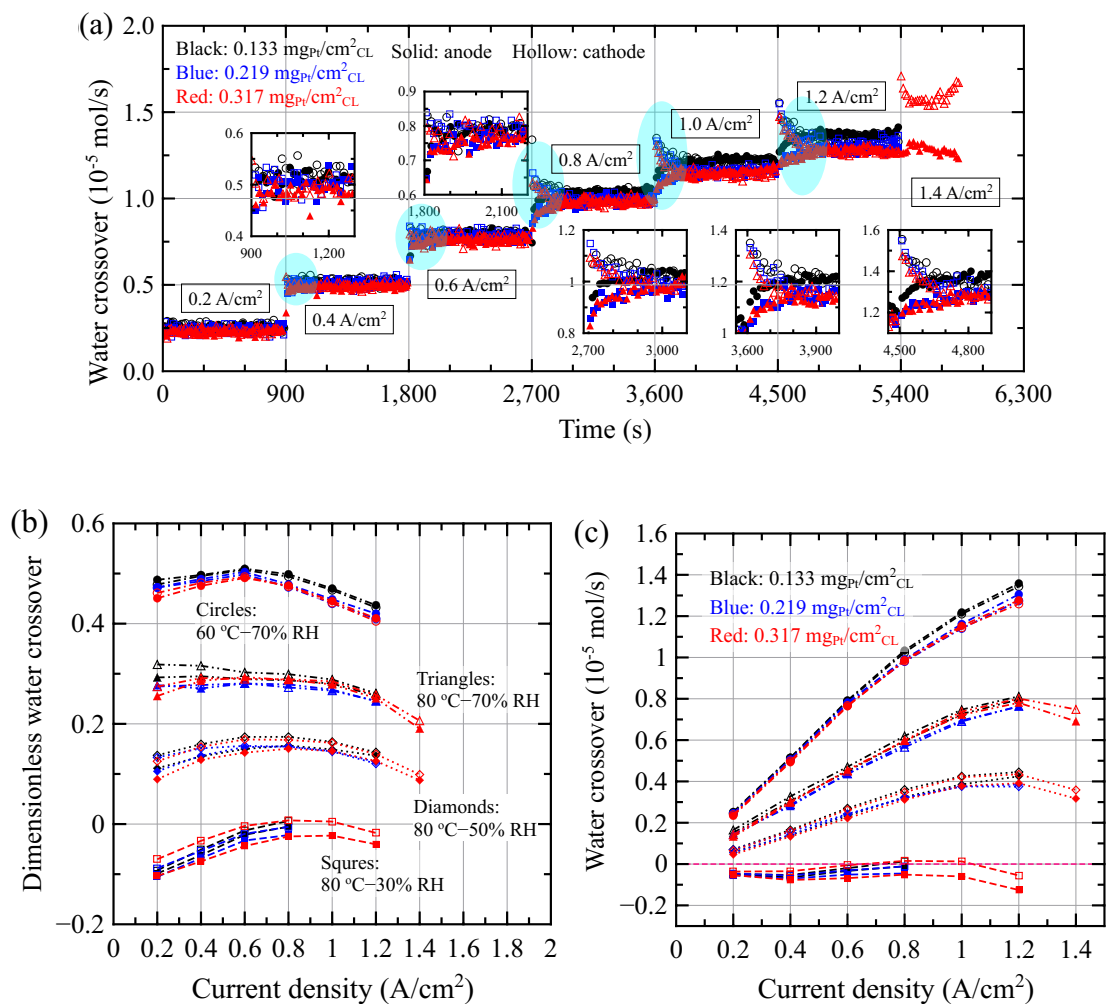


Figure 5.9: Water transport results for cells with varying platinum loadings obtained from current hold experiments: (a) real-time cathode-to-anode water crossover at 60 °C and 70% RH, (b) averaged dimensionless cathode-to-anode water crossover during last 5-min, and (c) averaged cathode-to-anode water crossover during last 5-min.

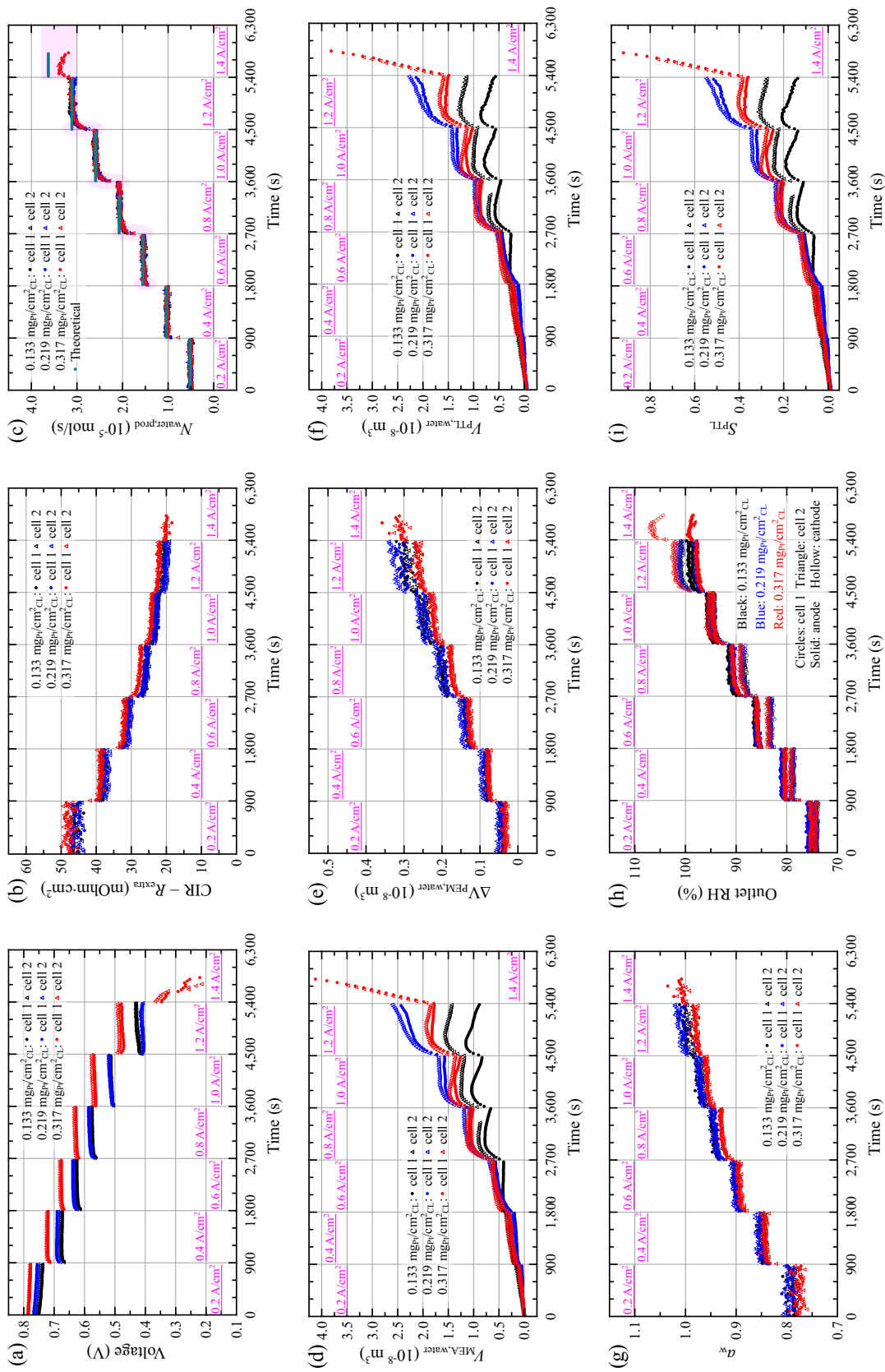


Figure 5.10: Current hold results at 60 °C and 70% RH for cells with 0.133, 0.219 and 0.317 mgPt/cm<sub>CL</sub> platinum loading: (a) cell voltage, (b) membrane protonic resistance, (c) ORR product water flux, (d) total amount of water accumulation in the MEA, (e) total amount of water accumulation in the membrane, (f) membrane water activity, and (i) cathode PTL saturation.

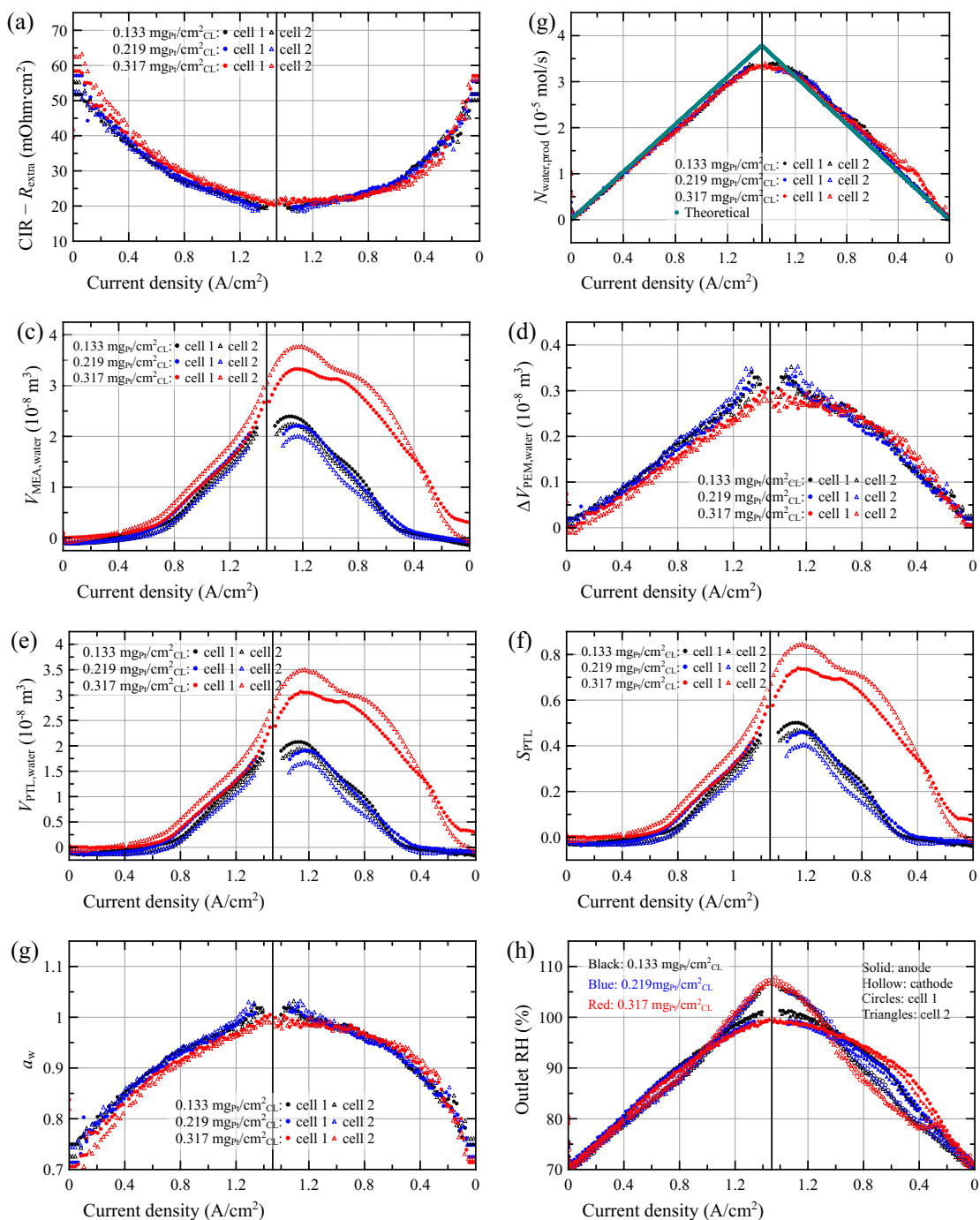


Figure 5.11: Galvanodynamic results at 60 °C and 70% RH for cells with 0.133, 0.219 and 0.317  $\text{mg}_{\text{Pt}}/\text{cm}^2_{\text{CL}}$  platinum loading: (a) membrane protonic resistance, (b) ORR product water flux, (c) total amount of water accumulation in the MEA, (d) total amount of water accumulation in the membrane, (e) total amount of water accumulation in the porous media, (f) cathode PTL saturation, (g) membrane water activity, and (h) outlet RH.

The membrane protonic resistance in Figure 5.10b decreases with current density as a result of increased membrane hydration.

Figure 5.10c compares the measured and theoretical ORR product water fluxes, where the former is significantly lower at the initial stages of the current hold from 0.6 to 1.2 A/cm<sup>2</sup> and at all times at 1.4 A/cm<sup>2</sup>. Similar to the hypothesis made regarding the impact of Nafion loading on liquid water accumulation (Section 5.2.1.4), the discrepancy in the ORR product water flux was attributed to water accumulation in the membrane and in the porous media.

The total amount of water accumulation in the MEA, membrane and porous media for cells with varying platinum loadings is shown in Figures 5.10d, 5.10e and 5.10f, respectively. The observation of water initially accumulating in the MEA and then in the porous media made earlier for cells with varying Nafion loading was also made herein. Furthermore, both the estimated water activity (Figure 5.10g) and outlet RH (Figure 5.10h) exhibit similar trends and values, ensuring the estimated water content in the membrane was physically meaningful.

Figures 5.10f and 5.10i show that platinum loading affects the dynamics of liquid water accumulation and saturation in the porous media. In the case of cells with 0.219 and 0.317 mg<sub>Pt</sub>/cm<sup>2</sup><sub>CL</sub>, at each current hold from 0.2 to 1.0 A/cm<sup>2</sup>, PTL saturation exhibited a quick increase over time, followed by a subsequent stabilization, as discussed in Section 5.2.1.4. When current density increased to 1.2 A/cm<sup>2</sup>, however this balance could no longer be established for cells with 0.219 mg<sub>Pt</sub>/cm<sup>2</sup><sub>CL</sub> and liquid water significantly accumulated in the porous media but did not noticeably affect cell voltage shown in Figure 5.10a. In the case of 0.317 mg<sub>Pt</sub>/cm<sup>2</sup><sub>CL</sub>, the current density had to increase to 1.4 A/cm<sup>2</sup> for water accumulation to dominate. This prompt increase in PTL saturation resulted in the significant cell voltage instability seen in Figure 5.10a.

Cells with 0.133 mg<sub>Pt</sub>/cm<sup>2</sup><sub>CL</sub> did not show the same behavior. At 0.8 to 1.2 A/cm<sup>2</sup>, PTL saturation initially increased but then decreased over operating time as seen in

Figures 5.10f and 5.10i. This occurred because the balance was tipped toward water crossover and evaporation, and flooding reduced over time after a brief increase due to the increased water production. The authors do not have a clear explanation for this imbalance, as the cathode over-potential was almost identical to  $0.219 \text{ mg}_{\text{Pt}}/\text{cm}_{\text{CL}}^2$  (Figure 5.6a) and thus heat production was similar. A possible reason might be a larger vapor transport flux through the thin CL with  $0.133 \text{ mg}_{\text{Pt}}/\text{cm}_{\text{CL}}^2$ .

Figures 5.10f and 5.10i shows that at current densities from  $0.2$  to  $0.6 \text{ A}/\text{cm}^2$ , PTL saturation was nearly independent of platinum loading. When current density was increased to  $0.8 \text{ A}/\text{cm}^2$  and above, cells with  $0.133 \text{ mg}_{\text{Pt}}/\text{cm}_{\text{CL}}^2$  and  $0.219 \text{ mg}_{\text{Pt}}/\text{cm}_{\text{CL}}^2$  PL had the lowest and highest saturation, respectively. Different electrode designs achieved different saturation levels once a balance between water production and rejection via evaporation and cathode-to-anode water crossover was established. The lowest loading CL was able to reach that balance at lower PTL saturation, which is in line with numerical findings of Goshtasbi et al. [158] but contradicts the simulation results of Zenyuk et al. [159]. To the best of authors' knowledge, there is no experimental work estimating PTL saturation in operating PEMFCs with varying PLs.

**Galvanodynamic measurements** Figure 5.11 shows the water accumulation results during galvanodynamic experiments for cells with varying platinum loadings at  $60 \text{ }^\circ\text{C}$  and  $70\% \text{ RH}$ . Figure 5.11a shows the membrane protonic resistance steadily decreased with increasing current density as the membrane was hydrated with the ORR product water and then increased as the current was reduced. An asymmetric shape was observed; however, indicating the scan rate ( $5 \text{ mA}/\text{s}$ ) is faster than the time required to re-equilibrate the membrane.

A significant disparity between the measured and theoretical ORR product water fluxes was observed at high current densities, as seen in Figure 5.11b. This discrepancy was used to estimate the total amount of water accumulation in the MEA,

membrane and porous media, as shown in Figures 5.11c, 5.11d and 5.11e, respectively. During the galvanodynamic experiments, water was first used to hydrate the membrane and, from  $0.8 \text{ A/cm}^2$  onward, started to fill the pore space in the PTL. Furthermore, the estimated water content in the membrane was verified to be physically meaningful: the estimated water activity (Figure 5.11g) was similar to the outlet RH (Figure 5.11h).

As seen in Figure 5.11f, at the same current densities during the forward scan, the impact of platinum loading on the PTL saturation was marginal as compared with the current hold experiments. This was likely because the operating period was insufficient to accumulate larger amounts of liquid water. The cells with  $0.317 \text{ mg}_{\text{Pt}}/\text{cm}^2_{\text{CL}}$  flooded to a greater extent during the backward scan, which was due to higher maximum current density achieved at the end of the forward scan (0.3 V). The high level of saturation however did not result in cell instabilities, as also observed in the Nafion loading study when loading was 30 wt.%.

### 5.3 Conclusions

In this chapter, the water balance setup described in Chapter 2 was employed to concurrently quantify the impact of cathode catalyst layer Nafion (10–40 wt.%) and platinum ( $0.133\text{--}0.317 \text{ mg}_{\text{Pt}}/\text{cm}^2_{\text{CL}}$ ) loadings on cell performance, real-time cathode-to-anode water crossover, and dynamics of water accumulation in the MEA at four operating conditions ranging from hot/dry to cold/wet.

The influence of cathode catalyst layer composition and loading on porosity, thickness and ECSA was first analyzed. Increasing ionomer loading from 10 to 20 wt.% decreased the CL porosity by 8% and increasing it from 20 to 40 wt.% resulted in a 43% reduction. Furthermore, catalyst layer porosity was found to be nearly independent of platinum loading. Nafion and platinum loadings did not have a significant impact on ECSA, yielding a value of approximately  $60 \text{ m}^2_{\text{Pt}}/\text{g}_{\text{Pt}}$  for all layer compositions.

Nafion loading in the CCL notably influenced fuel cell performance, water crossover, and water accumulation. The cathode-to-anode water crossover decreased with increasing Nafion loading at all operating conditions, possibly because of the shift of the ORR away from the PEM-CL interface with increasing NL due to the lower porosity and higher protonic conductivity. Under all experimental conditions, the best and worst fuel cell performance during the forward polarization scan (from low to high current) was achieved at 20 and 40 wt.% NL, respectively, likely as a result of the interplay between proton and reactant transport. Significant PTL flooding caused shut down of the cells with 10 and 20 wt.% Nafion loadings during the backward scan at 60 °C and 70% RH. The cells with 30 wt.% NL showed stable polarization curves; however, it could not reach the same maximum currents due to already large water accumulation.

Current hold and galvanodynamic measurements did not show a clear trend between water accumulation and Nafion loading. The cells with 30 wt.% NL retained more water in the electrode and as a result were able to achieve: i) lower maximum current density; and, ii) reduced sensitivity to RH. However, the 20 wt.% NL cells repeatedly showed lower levels of saturation than the 10 wt.% counter part. It is hypothesized the former is due to a better reaction distribution due to enhanced protonic conductivity. Overall, the cells with 20 wt.% NL performed better under any conditions while the 30 wt.% NL cells were the least sensitive to RH.

For cells with 30 wt.% NL, the impact of cathode CL platinum loading on the performance, water crossover, and water accumulation in PEMFCs was less prominent than the effect of Nafion loading. Cathode-to-anode water crossover was not affected by platinum loading. Cells with 0.317 mg<sub>Pt</sub>/cm<sub>CL</sub><sup>2</sup> PL had the best performance under all experimental conditions, but the improvement over 0.133 and 0.219 mg<sub>Pt</sub>/cm<sub>CL</sub><sup>2</sup> was reduced with increasing RH and/or lowering cell temperature. Overall, porous media saturation increased when more current was produced but then quickly stabilized during low current holds. At higher current densities, steady state could not be

achieved due to steadily increasing water accumulation. A clear trend between water accumulation and platinum loading was not observed, contradicting the commonly held hypothesis that thin CL would flood more quickly.

# Chapter 6

## Conclusions and Future Work<sup>1</sup>

A widespread hydrogen infrastructure, and cost and durability of PEMFC stacks are the primary limitations to the market penetration of hydrogen PEMFCs [273]. One of the promising methods to cut down the cost of PEMFCs is by increasing fuel cell current density at the same cell voltage while using the same amount of platinum [273]. However, fuel cell performance improvement is affected by its ability to efficiently remove the ORR product water, since water accumulation in the porous media will result in reactant starvation. The ORR product water can be removed from anode and cathode compartments of a PEMFC and, therefore, it is necessary to increase the water removal rates from both sides. The overall objective of this thesis was to experimentally quantify the impact of modifications to PEMFC components on the crucial processes of dynamic water transport and liquid water accumulation within the PEMFCs.

---

<sup>1</sup>Parts of this chapter are reproduced from the following publications:

1. F. Wei, A. Kosakian, J. Liu, J. Kracher, R. Khan, and M. Secanell, "Water transport in anion and proton exchange membranes," *Journal of Power Sources*, vol. 557, p. 232 494, 2023. DOI: <https://doi.org/10.1016/j.jpowsour.2022.232494>.
2. F. Wei, A. Kosakian, and M. Secanell, "Effect of operating conditions and micro-porous layer on the water transport and accumulation in proton exchange membrane fuel cells," *Chemical Engineering Journal*, p. 144 423, 2023. DOI: <https://doi.org/10.1016/j.cej.2023.144423>.
3. F. Wei, A. Kosakian, J. Liu, and M. Secanell, "Effect of Cathode Catalyst Layer Nafion and Platinum Loading on the Dynamic Transport and Accumulation of Water Inside an Operating PEMFC," (under review).

Author contributions are detailed in the Preface of this thesis.

## 6.1 Conclusions

To study water management inside operating PEMFCs, a reliable technique is required to quantify the real-time water removal fluxes from both compartments of the cell and liquid water accumulation in the electrodes. In Chapter 2, a water balance setup, which enables real-time measurement of water fluxes that enter and leave the anode and cathode of an operating PEMFC, was developed and validated. The water balance setup not only allows for the quantification of water fluxes but it also provides a fast and reliable method to estimate the water accumulated in the membrane and liquid water in the porous media. The developed setup and the proposed methodology to analyze the results can be used in real-time control strategies addressing membrane dehydration and electrode flooding.

Increasing the cathode-to-anode water crossover rate is one of the promising ways to mitigate cathode flooding arising from inefficient removal of the fast ORR water production at high current. However, this water crossover rate is affected by the water transport properties of the proton exchange membrane. Therefore, in Chapter 3, the developed water balance setup, along with three proposed 1D mathematical models, was used to estimate water desorption rate of PEMs, i.e., Nafion<sup>®</sup> N211, N212, N115 and N117 with varying thickness and fabrication methods, at multiple conditions. Results indicate that interfacial transport is limiting for all the analyzed membrane samples. The obtained desorption rate was found to be similar for the Nafion<sup>®</sup> membranes of the same type (cast N21X or extruded N11X), but a lower overall desorption rate was estimated for Nafion<sup>®</sup> N11X than for N21X due to the lower activation energy for the former. Furthermore, the desorption rate was found to increase with operating temperature and RH gradient between the membrane and the surroundings. The developed methodology was also employed to analyze water transport in several types of AEMs (Aemion<sup>®</sup> AH1-HNN8-50-X, Fumapem<sup>®</sup> FAA-3-30/50, and Versogen<sup>™</sup> PiperION-A40), for which only limited data is available in

the literature.

Accurate measurement of the cathode-to-anode water crossover and water accumulation in the porous media inside operating PEMFCs is crucial for understanding the impact of modifications to cell operating conditions and component designs on cell performance and thus, providing strategies for mitigating electrode flooding at high current operation. Therefore, in Chapters 4 and 5 of this thesis, the developed water balance setup was employed to quantify the impact of operating conditions, MPL addition to the cathode transport layer and cathode CLs fabricated with varying Nafion (10–40 wt.%) and platinum loadings ( $0.133\text{--}0.317\text{ mg}_{\text{Pt}}/\text{cm}_{\text{CL}}^2$ ) on cell performance, cathode-to-anode water crossover and liquid water accumulation.

Operating conditions were found to have the most significant impact. Increasing reactant relative humidity and/or decreasing cell temperature enhanced cathode-to-anode water movement. Among the experimental conditions, liquid water accumulation in the MEA was only tracked at 60 °C and 70% RH and found to occur within the cathode, leading to an estimated saturation of approximately 40% at 1 A/cm<sup>2</sup>. Cell performance also improved with increasing inlet RH at hot conditions, and performance at 60 °C and 70% RH was similar to 80 °C and 50% RH. The ratio of water crossover to produced remained relatively constant with current density and only at hot/dry condition, net water moved from anode to cathode.

The addition of an MPL was found to lead to a slight increase in the cathode-to-anode water crossover, i.e., approximately 0.05 moles per mole of water produced, but it substantially reduced the total amount of liquid water accumulation. The cathode MPL significantly improved fuel cell performance at cold/wet condition, while its effect at hot conditions was limited. Even though a saturation of nearly 70% was reached at 1.2 A/cm<sup>2</sup> under cold/wet condition, cells with a cathode MPL continued to operate normally and achieved a higher and more stable performance than cells without MPL. The performance improvement at cold/wet condition in the case of MPL addition was attributed to the increased water vaporization, as a result of

enhanced internal MEA temperature, and the provision of in-plane oxygen pathways in the MPL around the local water blockage sites in the cathode GDL.

Cathode catalyst layer Nafion loading also had a significant impact. Increasing Nafion loading reduced the cathode-to-anode water crossover, possibly because of the shift of the ORR away from the PEM-CL interface due to reduced porosity and higher protonic conductivity. Due to the trade-off between proton and reactant transport resistance arising from the Nafion loading, at all operating conditions, the best and worst fuel cell performance during the forward polarization scan was achieved at 20 and 40 wt.% NL, respectively. It was also found that the maximum attainable current for cells with 40 wt.% NL was too low to result in liquid water accumulation, but cells with 30 wt.% NL retained the most water in the electrode. Furthermore, the 10 wt.% NL cells exhibited higher levels of saturation than the 20 wt.% counter part, which is hypothesized to be to a better ORR reaction distribution because of enhanced protonic conductivity.

For cells with 30 wt.% NL, cathode CL platinum loading have minimal impact. Increasing platinum loading had a negligible effect on cathode-to-anode water crossover. At all experimental conditions, cells with  $0.317 \text{ mg}_{\text{Pt}}/\text{cm}_{\text{CL}}^2$  PL had the best performance, but the improvement over  $0.133$  and  $0.219 \text{ mg}_{\text{Pt}}/\text{cm}_{\text{CL}}^2$  was reduced with increasing RH and/or lowering cell temperature. Surprisingly, a clear trend between water accumulation and platinum loading was not observed and the  $0.133 \text{ mg}_{\text{Pt}}/\text{cm}_{\text{CL}}^2$  CL appeared to have the smallest water accumulation at  $1.2 \text{ A}/\text{cm}^2$ , contradicting the commonly held hypothesis that thin CL would flood more quickly.

## 6.2 Contributions

The contributions of this dissertation to the advancement of the scientific knowledge in the area of water management in PEMFCs are:

1. the development of a cost-effective and accurate water balance setup for the

real-time measurement of water crossover between the electrodes and liquid water accumulation in the electrodes of operating PEMFCs (see Chapter 2 and publications [1, 2]);

2. the measurement of water desorption rate of proton and anion exchange membranes (see Chapter 3 and publication [1]);
3. quantifying the impact of operating conditions and addition of an MPL to the cathode GDL on cell performance, water transport and liquid water accumulation of operating PEMFCs (see Chapter 4 and publication [2]);
4. quantifying the impact of cathode CL Nafion and platinum loadings on cell performance, water transport and liquid water accumulation of operating PEMFCs (see Chapter 5 and upcoming publication);

Three journal papers [1, 2, 4] were published as the first or co-first author during this Ph.D. Research findings were presented at a number of domestic and international conferences. Another journal paper, based on Chapter 5, is currently under review.

## 6.3 Future Work

### 6.3.1 Membrane property characterization

Liquid-vapor (L-V) [133, 173–176, 178] and vapor-vapor (V-V) permeation methods [133, 174, 175, 179] have measured very different diffusivity of Nafion membranes. This disparity was hypothesized to be due to the effect of the interfaces, which limit the overall water transport through the Nafion<sup>®</sup> membranes [133, 166, 173–175, 180–183]. The challenge of using a V-V setup is that it involves bulk and interfacial transport across two interfaces: absorption on the wet side and desorption on the dry side. In Chapter 3, a L-V permeation method was used to characterize the water desorption rate of membranes. Liquid-vapor permeation setups are well established for the estimation of the rate of water desorption from membranes but can not estimate

the absorption rate. Therefore, in the future, a V-V permeation method based on the developed water balance setup and the combined diffusion-and-desorption transport model will be used to estimate the sorption rates at the interfaces and diffusion coefficient through the bulk volume of the proton and anion exchange membranes.

### **6.3.2 Water accumulation validation with imaging data**

In the literature, the liquid water accumulation in the porous media is generally quantified by either ex-situ experiments [63, 147], analyzing in-situ tomography images [27, 33–35, 93, 105, 107, 108, 148–154] or via two-phase numerical modeling [25, 54, 155–164]. This thesis introduces a water balance setup that allows to measure the real-time water accumulation in operating PEMFCs. In Chapter 4, the measured saturation using the water balance was compared with the results determined by imaging [34, 107, 154]. A deviation was observed and it was attributed to the different cells used, imaging resolution and segmentation, and the different experimental configurations and conditions. In the future, the accuracy of the water balance to quantify the liquid water accumulation can be validated by imaging technique.

### **6.3.3 Effect of GDL, MPL and CL PSD on water management**

Water crossover between the anode and cathode electrodes and liquid water accumulation in the MEA have been found to be affected by the pore size distribution of GDL, MPL and CL using numerical models [109, 119]; however, experimental work is limited in the literature on studying the effect of pore size on water transport and accumulation. The proposed water balance setup can be used for this purpose.

### **6.3.4 Application to AEMFC**

In anion exchange membrane fuel cells, water balance is even more important because water not only is produced in the anode but also functions as a reactant in the cathode. Therefore, the developed water balance setup can be used to optimize the membrane,

CL, MPL, GDL and operating conditions to achieve better water management in AEMFCs and thus improved cell performance and durability.

Over the past two decades, numerous efforts have been made to reduce platinum loading, including the designs of: (1) novel carbon supports that enable high platinum utilization, e.g., carbon nanotube [274], graphene [275], carbon aerogel [276], N-doped mesoporous graphitized carbon [277, 278], and mesoporous carbon materials [279]; (2) new architectures of platinum-based catalyst with high activity, e.g., nanocages [280], core shell [281], nanowires [282], nanocrystals [283], and nanoframes [284]; and (3) platinum-free catalysts [285–288]. In the literature, the electrochemical surface area, current densities in the kinetic region and polarization curves are the main characteristic parameters used to evaluate the success of newly designed catalyst layers. However, durable catalyst layers require a better understanding of their impact on water management, which requires evaluation of water transport and liquid water accumulation in operating AEMFCs. Therefore, in the future, the developed water balance setup can be used to understand the impact of these changes on water transport and liquid water accumulation in operating AEMFCs, which will provide additional insights that cannot be developed based on ECSA, mass activity, and polarization curve measurements alone.

# Bibliography

- [1] F. Wei, A. Kosakian, J. Liu, J. Kracher, R. Khan, and M. Secanell, “Water transport in anion and proton exchange membranes,” *Journal of Power Sources*, vol. 557, p. 232 494, 2023. DOI: <https://doi.org/10.1016/j.jpowsour.2022.232494>.
- [2] F. Wei, A. Kosakian, and M. Secanell, “Effect of operating conditions and micro-porous layer on the water transport and accumulation in proton exchange membrane fuel cells,” *Chemical Engineering Journal*, p. 144 423, 2023. DOI: <https://doi.org/10.1016/j.cej.2023.144423>.
- [3] F. Wei, A. Kosakian, J. Liu, and M. Secanell, “Effect of Cathode Catalyst Layer Nafion and Platinum Loading on the Dynamic Transport and Accumulation of Water Inside an Operating PEMFC,” (under review).
- [4] S. Shukla, F. Wei, M. Mandal, J. Zhou, M. S. Saha, J. Stumper, and M. Secanell, “Determination of PEFC Gas Diffusion Layer and Catalyst Layer Porosity Utilizing Archimedes Principle,” *Journal of The Electrochemical Society*, vol. 166, no. 15, F1142, 2019. DOI: 10.1149/2.0251915jes.
- [5] S. Jung, M. Sabharwal, A. Jarauta, F. Wei, M. Gingras, J. Gostick, and M. Secanell, “Estimation of relative transport properties in porous transport layers using pore-scale and pore-network simulations,” *Journal of The Electrochemical Society*, vol. 168, no. 6, p. 064 501, 2021.
- [6] Y Kim, T Asset, F Wei, P Atanassov, M Secanell, J Barralet, and J. Gostick, “Fabrication of platinum group metal-free catalyst layer with enhanced mass transport characteristics via an electro-spraying technique,” *Materials Today Energy*, vol. 20, p. 100 641, 2021.
- [7] A. Kosakian, F. Wei, S. Jung, J. Zhou, A. Punia, J. Liu, and M. Secanell, “Impact of liquid-water accumulation and drainage cycles on fuel-cell performance and stability,” (under review, second revision).
- [8] F. Wei, A. Kosakian, J. Liu, and M. Secanell, “Effect of Cathode Catalyst Layer Nafion and Platinum Loading on the Dynamic Transport and Accumulation of Water Inside an Operating PEMFC,” (under review).
- [9] P. Agreement, “Paris agreement,” in *Report of the Conference of the Parties to the United Nations Framework Convention on Climate Change (21st Session, 2015: Paris)*. Retrived December, HeinOnline, vol. 4, 2015, p. 2017.

- [10] R. Zhang and T. Hanaoka, “Cross-cutting scenarios and strategies for designing decarbonization pathways in the transport sector toward carbon neutrality,” *Nature Communications*, vol. 13, no. 1, p. 3629, 2022.
- [11] S. Garimella, K. Lockyear, D. Pharis, O. El Chawa, M. T. Hughes, and G. Kini, “Realistic pathways to decarbonization of building energy systems,” *Joule*, vol. 6, no. 5, pp. 956–971, 2022, ISSN: 2542-4351.
- [12] O. Bahn, M. Marcy, K. Vaillancourt, and J.-P. Waaub, “Electrification of the Canadian road transportation sector: A 2050 outlook with TIMES-Canada,” *Energy Policy*, vol. 62, pp. 593–606, 2013.
- [13] M. Victoria, K. Zhu, T. Brown, G. B. Andresen, and M. Greiner, “Early decarbonisation of the European energy system pays off,” *Nature communications*, vol. 11, no. 1, pp. 1–9, 2020.
- [14] Intergovernmental Panel on Climate Change, *Climate Change 2022 Mitigation of Climate Change: Summary for Policymakers*, [https://www.ipcc.ch/report/ar6/wg3/downloads/report/IPCC\\_AR6\\_WGIII\\_SPM.pdf](https://www.ipcc.ch/report/ar6/wg3/downloads/report/IPCC_AR6_WGIII_SPM.pdf), Accessed: 2023-03-23, 2022.
- [15] K. Jiao, J. Xuan, Q. Du, Z. Bao, B. Xie, B. Wang, Y. Zhao, L. Fan, H. Wang, Z. Hou, *et al.*, “Designing the next generation of proton-exchange membrane fuel cells,” *Nature*, vol. 595, no. 7867, pp. 361–369, 2021.
- [16] O. Gröger, H. A. Gasteiger, and J.-P. Suchsland, “Review—Electromobility: Batteries or Fuel Cells?” *Journal of The Electrochemical Society*, vol. 162, no. 14, A2605, 2015.
- [17] S. Ramachandran and U. Stimming, “Well to wheel analysis of low carbon alternatives for road traffic,” *Energy & Environmental Science*, vol. 8, no. 11, pp. 3313–3324, 2015.
- [18] *Where the Energy Goes: Gasoline Vehicles*, <https://www.fueleconomy.gov/feg/atv.shtml>, Accessed: 07th September, 2023, no date.
- [19] A. Z. Weber, R. L. Borup, R. M. Darling, P. K. Das, T. J. Dursch, W. Gu, D. Harvey, A. Kusoglu, S. Litster, M. M. Mench, *et al.*, “A critical review of modeling transport phenomena in polymer-electrolyte fuel cells,” *Journal of The Electrochemical Society*, vol. 161, no. 12, F1254, 2014.
- [20] I. Staffell, D. Scamman, A. V. Abad, P. Balcombe, P. E. Dodds, P. Ekins, N. Shah, and K. R. Ward, “The role of hydrogen and fuel cells in the global energy system,” *Energy & Environmental Science*, vol. 12, no. 2, pp. 463–491, 2019.
- [21] C. Thomas, “Fuel cell and battery electric vehicles compared,” *International Journal of Hydrogen Energy*, vol. 34, no. 15, pp. 6005–6020, 2009.
- [22] U.S. Department of Energy, *Fuel cell technologies office multi-year research, development, and demonstration plan: Fuel cells*, [https://energy.gov/sites/prod/files/2017/05/f34/fcto\\_myRDD\\_fuel\\_cells.pdf](https://energy.gov/sites/prod/files/2017/05/f34/fcto_myRDD_fuel_cells.pdf), 2017, Accessed June 1, 2023.

- [23] D. Papageorgopoulos, *Fuel cell R&D overview*, [https://www.hydrogen.energy.gov/pdfs/review19/plenary\\_fuel\\_cell\\_papageorgopoulos\\_2019.pdf](https://www.hydrogen.energy.gov/pdfs/review19/plenary_fuel_cell_papageorgopoulos_2019.pdf), 2019, Accessed June 1, 2023.
- [24] R. Borup and A. Weber, *Fuel cell R&D overview: Fuel cell performance and durability consortium*, [https://www.hydrogen.energy.gov/pdfs/review20/fc135\\_borup\\_weber\\_2020\\_o.pdf](https://www.hydrogen.energy.gov/pdfs/review20/fc135_borup_weber_2020_o.pdf), 2019, Accessed June 1, 2023.
- [25] J. Zhou, S. Shukla, A. Putz, and M. Secanell, “Analysis of the role of the microporous layer in improving polymer electrolyte fuel cell performance,” *Electrochimica Acta*, vol. 268, pp. 366–382, 2018, ISSN: 0013-4686.
- [26] A. Kosakian, “Transient numerical modeling of proton-exchange-membrane fuel cells,” PhD dissertation, University of Alberta (Canada), 2021.
- [27] J. Lee, J. Hinebaugh, and A. Bazylak, “Synchrotron X-ray radiographic investigations of liquid water transport behavior in a PEMFC with MPL-coated GDLs,” *Journal of Power Sources*, vol. 227, pp. 123–130, 2013.
- [28] K. Khedekar, M. Rezaei Talarposhti, M. M. Besli, S. Kuppan, A. Perego, Y. Chen, M. Metzger, S. Stewart, P. Atanassov, N. Tamura, *et al.*, “Probing Heterogeneous Degradation of Catalyst in PEM Fuel Cells under Realistic Automotive Conditions with Multi-Modal Techniques,” *Advanced Energy Materials*, vol. 11, no. 35, p. 2101794, 2021.
- [29] K. Khedekar, P. Satjaritanun, S. Stewart, J. Braaten, P. Atanassov, N. Tamura, L. Cheng, C. M. Johnston, and I. V. Zenyuk, “Effect of Commercial Gas Diffusion Layers on Catalyst Durability of Polymer Electrolyte Fuel Cells in Varied Cathode Gas Environment,” *Small*, vol. 18, no. 33, p. 2201750, 2022.
- [30] L. Cheng, K. Khedekar, M. Rezaei Talarposhti, A. Perego, M. Metzger, S. Kuppan, S. Stewart, P. Atanassov, N. Tamura, N. Craig, *et al.*, “Mapping of heterogeneous catalyst degradation in polymer electrolyte fuel cells,” *Advanced Energy Materials*, vol. 10, no. 28, p. 2000623, 2020.
- [31] R. L. Borup, A. Kusoglu, K. C. Neyerlin, R. Mukundan, R. K. Ahluwalia, D. A. Cullen, K. L. More, A. Z. Weber, and D. J. Myers, “Recent developments in catalyst-related PEM fuel cell durability,” *Current Opinion in Electrochemistry*, vol. 21, pp. 192–200, 2020.
- [32] L. Zuo, Q. Jian, and Y. Yang, “Durability improvement mechanism of proton exchange membrane fuel cell by microporous layer,” *International Journal of Energy Research*, vol. 46, no. 13, pp. 18809–18818, 2022.
- [33] R. W. Atkinson III, Y. Garsany, B. D. Gould, K. E. Swider-Lyons, and I. V. Zenyuk, “The role of compressive stress on gas diffusion media morphology and fuel cell performance,” *ACS Applied Energy Materials*, vol. 1, no. 1, pp. 191–201, 2017.

- [34] Y. Nagai, J. Eller, T. Hatanaka, S. Yamaguchi, S. Kato, A. Kato, F. Marone, H. Xu, and F. N. Büchi, “Improving water management in fuel cells through microporous layer modifications: Fast operando tomographic imaging of liquid water,” *Journal of Power Sources*, vol. 435, p. 226 809, 2019.
- [35] J Lee, R Yip, P Antonacci, N Ge, T Kotaka, Y Tabuchi, and A Bazylak, “Synchrotron investigation of microporous layer thickness on liquid water distribution in a PEM fuel cell,” *Journal of The Electrochemical Society*, vol. 162, no. 7, F669, 2015.
- [36] Y. Wan, D. Qiu, P. Yi, L. Peng, and X. Lai, “Design and optimization of gradient wettability pore structure of adaptive PEM fuel cell cathode catalyst layer,” *Applied Energy*, vol. 312, p. 118 723, 2022.
- [37] S. A. Berlinger, A. Chowdhury, T. Van Cleve, A. He, N. Dagan, K. C. Neyerlin, B. D. McCloskey, C. J. Radke, and A. Z. Weber, “Impact of platinum primary particle loading on fuel cell performance: Insights from catalyst/ionomer ink interactions,” *ACS Applied Materials & Interfaces*, vol. 14, no. 32, pp. 36 731–36 740, 2022.
- [38] A. A. Kulikovsky, *Analytical modelling of fuel cells*. Elsevier, 2019.
- [39] M. Eikerling and A. Kulikovsky, *Polymer electrolyte fuel cells: physical principles of materials and operation*. CRC Press, 2014.
- [40] A. Z. Weber and J. Newman, “Coupled thermal and water management in polymer electrolyte fuel cells,” *Journal of The Electrochemical Society*, vol. 153, no. 12, A2205, 2006.
- [41] H. Ju, H. Meng, and C.-Y. Wang, “A single-phase, non-isothermal model for PEM fuel cells,” *International Journal of Heat and Mass Transfer*, vol. 48, no. 7, pp. 1303–1315, 2005.
- [42] J. Zhou, “Analyzing Multiphase Flow in Membrane Electrode Assembly Using a Mixed Wettability Mathematical Model,” Ph.D. dissertation, University of Alberta, 2018.
- [43] A. Kusoglu and A. Z. Weber, “New insights into perfluorinated sulfonic-acid ionomers,” *Chemical Reviews*, vol. 117, no. 3, pp. 987–1104, 2017.
- [44] K. Karan, “Interesting facets of surface, interfacial, and bulk characteristics of perfluorinated ionomer films,” *Langmuir*, vol. 35, no. 42, pp. 13 489–13 520, 2019.
- [45] L. Yu, F. Lin, L. Xu, and J. Xi, “Structure–property relationship study of Nafion XL membrane for high-rate, long-lifespan, and all-climate vanadium flow batteries,” *RSC advances*, vol. 7, no. 50, pp. 31 164–31 172, 2017.
- [46] K. A. Mauritz and R. B. Moore, “State of understanding of Nafion,” *Chemical Reviews*, vol. 104, no. 10, pp. 4535–4586, 2004.
- [47] A. El-kharouf and B. G. Pollet, “Gas diffusion media and their degradation,” in *Polymer Electrolyte Fuel Cell Degradation*, Academic Press New York, NY, 2012, pp. 215–247.

- [48] S. Park and B. N. Popov, "Effect of a GDL based on carbon paper or carbon cloth on PEM fuel cell performance," *Fuel*, vol. 90, no. 1, pp. 436–440, 2011.
- [49] R. Schweiss, C. Meiser, T. Damjanovic, I. Galbiati, and N. Haak, "SIGRACET gas diffusion layers for PEM fuel cells, electrolyzers and batteries," *White paper SGL Group*, 2016.
- [50] J. P. Owejan, J. E. Owejan, W. Gu, T. A. Trabold, T. W. Tighe, and M. F. Mathias, "Water transport mechanisms in PEMFC gas diffusion layers," *Journal of The Electrochemical Society*, vol. 157, no. 10, B1456, 2010.
- [51] G.-G. Park, Y.-J. Sohn, T.-H. Yang, Y.-G. Yoon, W.-Y. Lee, and C.-S. Kim, "Effect of PTFE contents in the gas diffusion media on the performance of PEMFC," *Journal of Power Sources*, vol. 131, no. 1-2, pp. 182–187, 2004.
- [52] M Prasanna, H. Ha, E. Cho, S.-A. Hong, and I.-H. Oh, "Influence of cathode gas diffusion media on the performance of the PEMFCs," *Journal of Power Sources*, vol. 131, no. 1-2, pp. 147–154, 2004.
- [53] K. Karan, H. Atiyeh, A. Phoenix, E. Halliop, J. Pharoah, and B. Peppley, "An experimental investigation of water transport in PEMFCs the role of microporous layers," *Electrochemical and Solid-state Letters*, vol. 10, no. 2, B34–B38, 2007.
- [54] A. Z. Weber and J. Newman, "Effects of microporous layers in polymer electrolyte fuel cells," *Journal of The Electrochemical Society*, vol. 152, no. 4, A677–A688, 2005.
- [55] A. Thomas, G. Maranzana, S. Didierjean, J. Dillet, and O. Lottin, "Thermal and water transfer in PEMFCs: investigating the role of the microporous layer," *International Journal of Hydrogen Energy*, vol. 39, no. 6, pp. 2649–2658, 2014.
- [56] G. Lin and T. Van Nguyen, "Effect of thickness and hydrophobic polymer content of the gas diffusion layer on electrode flooding level in a PEMFC," *Journal of The Electrochemical Society*, vol. 152, no. 10, A1942–A1948, 2005.
- [57] X. Wang, H. Zhang, J. Zhang, H. Xu, Z. Tian, J. Chen, H. Zhong, Y. Liang, and B. Yi, "Micro-porous layer with composite carbon black for PEM fuel cells," *Electrochimica Acta*, vol. 51, no. 23, pp. 4909–4915, 2006.
- [58] L. R. Jordan, A. Shukla, T. Behrsing, N. Avery, B. C. Muddle, and M. Forsyth, "Diffusion layer parameters influencing optimal fuel cell performance," *Journal of Power Sources*, vol. 86, no. 1-2, pp. 250–254, 2000.
- [59] E Passalacqua, G Squadrito, F Lufrano, A Patti, and L Giorgi, "Effects of the diffusion layer characteristics on the performance of polymer electrolyte fuel cell electrodes," *Journal of Applied Electrochemistry*, vol. 31, no. 4, pp. 449–454, 2001.
- [60] Z. Qi and A. Kaufman, "Improvement of water management by a microporous sublayer for PEM fuel cells," *Journal of Power Sources*, vol. 109, no. 1, pp. 38–46, 2002.

- [61] M. Blanco and D. P. Wilkinson, "Investigation of the effect of microporous layers on water management in a proton exchange membrane fuel cell using novel diagnostic methods," *International Journal of Hydrogen Energy*, vol. 39, no. 29, pp. 16 390–16 404, 2014.
- [62] R. B. Ferreira, D. Falcão, V. Oliveira, and A. Pinto, "Experimental study on the membrane electrode assembly of a proton exchange membrane fuel cell: Effects of microporous layer, membrane thickness and gas diffusion layer hydrophobic treatment," *Electrochimica Acta*, vol. 224, pp. 337–345, 2017.
- [63] J. T. Gostick, M. A. Ioannidis, M. W. Fowler, and M. D. Pritzker, "On the role of the microporous layer in PEMFC operation," *Electrochemistry Communications*, vol. 11, no. 3, pp. 576–579, 2009.
- [64] D. Malevich, E. Halliop, B. A. Peppley, J. G. Pharoah, and K. Karan, "Investigation of charge-transfer and mass-transport resistances in PEMFCs with microporous layer using electrochemical impedance spectroscopy," *Journal of The Electrochemical Society*, vol. 156, no. 2, B216–B224, 2009.
- [65] H. K. Atiyeh, K. Karan, B. Peppley, A. Phoenix, E. Halliop, and J. Pharoah, "Experimental investigation of the role of a microporous layer on the water transport and performance of a PEM fuel cell," *Journal of Power Sources*, vol. 170, no. 1, pp. 111–121, 2007.
- [66] P. Deevanhxay, T. Sasabe, S. Tsushima, and S. Hirai, "Effect of liquid water distribution in gas diffusion media with and without microporous layer on PEM fuel cell performance," *Electrochemistry Communications*, vol. 34, pp. 239–241, 2013.
- [67] J. H. Nam, K.-J. Lee, G.-S. Hwang, C.-J. Kim, and M. Kaviany, "Microporous layer for water morphology control in PEMFC," *International Journal of Heat and Mass Transfer*, vol. 52, no. 11-12, pp. 2779–2791, 2009.
- [68] J. H. Chun, D. H. Jo, S. G. Kim, S. H. Park, C. H. Lee, E. S. Lee, J.-Y. Jyoung, and S. H. Kim, "Development of a porosity-graded micro porous layer using thermal expandable graphite for proton exchange membrane fuel cells," *Renewable Energy*, vol. 58, pp. 28–33, 2013.
- [69] J. H. Kang, K.-J. Lee, S. H. Yu, J. H. Nam, and C.-J. Kim, "Demonstration of water management role of microporous layer by similarity model experiments," *International Journal of Hydrogen Energy*, vol. 35, no. 9, pp. 4264–4269, 2010.
- [70] Z. Lu, M. M. Daino, C. Rath, and S. G. Kandlikar, "Water management studies in pem fuel cells, part iii: Dynamic breakthrough and intermittent drainage characteristics from gdls with and without mpl," *International Journal of Hydrogen Energy*, vol. 35, no. 9, pp. 4222–4233, 2010.
- [71] T. Sasabe, P. Deevanhxay, S. Tsushima, and S. Hirai, "Investigation on the effect of microstructure of proton exchange membrane fuel cell porous layers on liquid water behavior by soft x-ray radiography," *Journal of Power Sources*, vol. 196, no. 20, pp. 8197–8206, 2011.

- [72] I. Zenyuk, R Taspinar, A. Kalidindi, E. Kumbur, and S Litster, “Computational and experimental analysis of water transport at component interfaces in polymer electrolyte fuel cells,” *Journal of The Electrochemical Society*, vol. 161, no. 11, F3091, 2014.
- [73] O. S. Burheim, H. Su, S. Pasupathi, J. G. Pharoah, and B. G. Pollet, “Thermal conductivity and temperature profiles of the micro porous layers used for the polymer electrolyte membrane fuel cell,” *International Journal of Hydrogen Energy*, vol. 38, no. 20, pp. 8437–8447, 2013, ISSN: 0360-3199.
- [74] H. Ito, Y. Heo, M. Ishida, A. Nakano, S. Someya, and T. Munakata, “Application of a self-supporting microporous layer to gas diffusion layers of proton exchange membrane fuel cells,” *Journal of Power Sources*, vol. 342, pp. 393–404, 2017.
- [75] S. F. Burlatsky, V. V. Atrazhev, M. Gummalla, D. A. Condit, and F. Liu, “The impact of thermal conductivity and diffusion rates on water vapor transport through gas diffusion layers,” *Journal of Power Sources*, vol. 190, no. 2, pp. 485–492, 2009.
- [76] G. Xu, J. LaManna, J. Clement, and M. Mench, “Direct measurement of through-plane thermal conductivity of partially saturated fuel cell diffusion media,” *Journal of Power Sources*, vol. 256, pp. 212–219, 2014.
- [77] S. Shukla, S. Bhattacharjee, A. Z. Weber, and M. Secanell, “Experimental and Theoretical Analysis of Ink Dispersion Stability for Polymer Electrolyte Fuel Cell Applications,” *Journal of The Electrochemical Society*, vol. 164, no. 6, F600, 2017.
- [78] S. Shukla, K. Domican, K. Karan, S. Bhattacharjee, and M. Secanell, “Analysis of Low Platinum Loading Thin Polymer Electrolyte Fuel Cell Electrodes Prepared by Inkjet Printing,” *Electrochimica Acta*, vol. 156, pp. 289–300, 2015, ISSN: 0013-4686.
- [79] S.-J. Shin, J.-K. Lee, H.-Y. Ha, S.-A. Hong, H.-S. Chun, and I.-H. Oh, “Effect of the catalytic ink preparation method on the performance of polymer electrolyte membrane fuel cells,” *Journal of Power Sources*, vol. 106, no. 1-2, pp. 146–152, 2002.
- [80] S Martin, P. Garcia-Ybarra, and J. Castillo, “Electrospray deposition of catalyst layers with ultra-low Pt loadings for PEM fuel cells cathodes,” *Journal of Power Sources*, vol. 195, no. 9, pp. 2443–2449, 2010.
- [81] X. Wang, F. W. Richey, K. H. Wujcik, and Y. A. Elabd, “Ultra-low platinum loadings in polymer electrolyte membrane fuel cell electrodes fabricated via simultaneous electrospinning/electrospraying method,” *Journal of Power Sources*, vol. 264, pp. 42–48, 2014.
- [82] S. Hirano, J. Kim, and S. Srinivasan, “High performance proton exchange membrane fuel cells with sputter-deposited Pt layer electrodes,” *Electrochimica Acta*, vol. 42, no. 10, pp. 1587–1593, 1997.

- [83] C. S. Gittleman, A. Kongkanand, D. Masten, and W. Gu, “Materials research and development focus areas for low cost automotive proton-exchange membrane fuel cells,” *Current Opinion in Electrochemistry*, vol. 18, pp. 81–89, 2019.
- [84] W. He, G. Lin, and T. Van Nguyen, “Diagnostic tool to detect electrode flooding in proton-exchange-membrane fuel cells,” *AIChE Journal*, vol. 49, no. 12, pp. 3221–3228, 2003.
- [85] C. Ziegler, H. M. Yu, and J. O. Schumacher, “Two-phase dynamic modeling of PEMFCs and simulation of cyclo-voltammograms,” *Journal of The Electrochemical Society*, vol. 152, no. 8, A1555–A1567, 2005.
- [86] H. Yu and C. Ziegler, “Transient behavior of a proton exchange membrane fuel cell under dry operation,” *Journal of The Electrochemical Society*, vol. 153, no. 3, A570–A575, 2006.
- [87] A. Shah, G.-S. Kim, P. Sui, and D Harvey, “Transient non-isothermal model of a polymer electrolyte fuel cell,” *Journal of Power Sources*, vol. 163, no. 2, pp. 793–806, 2007.
- [88] L. Hao, H. Yu, J. Hou, W. Song, Z. Shao, and B. Yi, “Transient behavior of water generation in a proton exchange membrane fuel cell,” *Journal of Power Sources*, vol. 177, no. 2, pp. 404–411, 2008.
- [89] D. Gerteisen, T. Heilmann, and C. Ziegler, “Modeling the phenomena of dehydration and flooding of a polymer electrolyte membrane fuel cell,” *Journal of Power Sources*, vol. 187, no. 1, pp. 165–181, 2009.
- [90] J. Hou, “A study on polarization hysteresis in PEM fuel cells by galvanostatic step sweep,” *International Journal of Hydrogen Energy*, vol. 36, no. 12, pp. 7199–7206, 2011.
- [91] A. Kongkanand and P. K. Sinha, “Load transients of nanostructured thin film electrodes in polymer electrolyte fuel cells,” *Journal of The Electrochemical Society*, vol. 158, no. 6, B703, 2011.
- [92] A. Kosakian, L. P. Urbina, A. Heaman, and M. Secanell, “Understanding single-phase water-management signatures in fuel-cell impedance spectra: A numerical study,” *Electrochimica Acta*, vol. 350, p. 136 204, 2020, ISSN: 0013-4686.
- [93] A. Mohseninia, D. Kartouzian, H. Markötter, U. U. Ince, I. Manke, and J. Scholta, “Neutron Radiographic Investigations on the Effect of Hydrophobicity Gradients within MPL and MEA on Liquid Water Distribution and Transport in PEMFCs,” *ECS Transactions*, vol. 85, no. 13, p. 1013, 2018.
- [94] L Daniel, A Bonakdarpour, J Sharman, and D. Wilkinson, “New CCL— MPL architecture reducing interfacial gaps and enhancing PEM fuel cell performance,” *Fuel Cells*, vol. 20, no. 2, pp. 224–228, 2020.

- [95] E. Carcadea, M. Varlam, M. Ismail, D. B. Ingham, A. Marinoiu, M. Raceanu, C. Jianu, L. Patularu, and D. Ion-Ebrasu, “PEM fuel cell performance improvement through numerical optimization of the parameters of the porous layers,” *International Journal of Hydrogen Energy*, vol. 45, no. 14, pp. 7968–7980, 2020.
- [96] G. Chen, G. Zhang, L. Guo, and H. Liu, “Systematic study on the functions and mechanisms of micro porous layer on water transport in proton exchange membrane fuel cells,” *International Journal of Hydrogen Energy*, vol. 41, no. 9, pp. 5063–5073, 2016.
- [97] Y. Hou, X. Li, Q. Du, K. Jiao, and N. Zamel, “Pore-scale investigation of the effect of micro-porous layer on water transport in proton exchange membrane fuel cell,” *Journal of The Electrochemical Society*, vol. 167, no. 14, p. 144504, 2020.
- [98] X. Xie, R. Wang, K. Jiao, G. Zhang, J. Zhou, and Q. Du, “Investigation of the effect of micro-porous layer on PEM fuel cell cold start operation,” *Renewable Energy*, vol. 117, pp. 125–134, 2018.
- [99] T. Kim, S. Lee, and H. Park, “A study of water transport as a function of the micro-porous layer arrangement in PEMFCs,” *International Journal of Hydrogen Energy*, vol. 35, no. 16, pp. 8631–8643, 2010.
- [100] T. C. Yau, M. Cimenti, X. Bi, and J. Stumper, “Effects of cathode gas diffusion layer design on polymer electrolyte membrane fuel cell water management and performance,” *Journal of Power Sources*, vol. 196, no. 22, pp. 9437–9444, 2011.
- [101] D. Gerteisen, T. Heilmann, and C. Ziegler, “Enhancing liquid water transport by laser perforation of a GDL in a PEM fuel cell,” *Journal of Power Sources*, vol. 177, no. 2, pp. 348–354, 2008.
- [102] D. Gerteisen and C. Sadeler, “Stability and performance improvement of a polymer electrolyte membrane fuel cell stack by laser perforation of gas diffusion layers,” *Journal of Power Sources*, vol. 195, no. 16, pp. 5252–5257, 2010.
- [103] M. Manahan and M. Mench, “Laser perforated fuel cell diffusion media: engineered interfaces for improved ionic and oxygen transport,” *Journal of The Electrochemical Society*, vol. 159, no. 7, F322, 2012.
- [104] K. Nishida, T. Murakami, S. Tsushima, and S. Hirai, “Measurement of liquid water content in cathode gas diffusion electrode of polymer electrolyte fuel cell,” *Journal of Power Sources*, vol. 195, no. 11, pp. 3365–3373, 2010.
- [105] S. S. Alrwashdeh, I. Manke, H. Markötter, M. Klages, M. Göbel, J. Haußmann, J. Scholta, and J. Banhart, “In operando quantification of three-dimensional water distribution in nanoporous carbon-based layers in polymer electrolyte membrane fuel cells,” *ACS Nano*, vol. 11, no. 6, pp. 5944–5949, 2017.

- [106] S. Wang, S. Guan, L. Zhang, F. Zhou, J. Tan, and M. Pan, “Enhancing the properties of water and gas management for proton exchange membrane fuel cells via tailored intersected cracks in a microporous layer,” *Journal of Power Sources*, vol. 533, p. 231 402, 2022.
- [107] J Lee, R Banerjee, M. George, D Muirhead, P Shrestha, H Liu, N Ge, S Chevalier, and A Bazylak, “Multiwall carbon nanotube-based microporous layers for polymer electrolyte membrane fuel cells,” *Journal of The Electrochemical Society*, vol. 164, no. 12, F1149, 2017.
- [108] D. Spornjak, R. Mukundan, R. L. Borup, L. G. Connolly, B. I. Zackin, V. De Andrade, M. Wojcik, D. Y. Parkinson, D. L. Jacobson, D. S. Hussey, *et al.*, “Enhanced water management of polymer electrolyte fuel cells with additive-containing microporous layers,” *ACS Applied Energy Materials*, vol. 1, no. 11, pp. 6006–6017, 2018.
- [109] J Zhou, D Stanier, A Putz, and M Secanell, “A mixed wettability pore size distribution based mathematical model for analyzing two-phase flow in porous electrodes II. Model validation and analysis of micro-structural parameters,” *Journal of The Electrochemical Society*, vol. 164, no. 6, F540–F556, 2017.
- [110] T. Soboleva, K. Malek, Z. Xie, T. Navessin, and S. Holdcroft, “PEMFC Catalyst Layers: The Role of Micropores and Mesopores on Water Sorption and Fuel Cell Activity,” *ACS Applied Materials & Interfaces*, vol. 3, no. 6, pp. 1827–1837, 2011.
- [111] M. Sabharwal and M. Secanell, “Understanding the effect of porosity and pore size distribution on low loading catalyst layers,” *Electrochimica Acta*, vol. 419, p. 140 410, 2022.
- [112] Z. Lu, J. Waldecker, X. Xie, M.-C. Lai, D. S. Hussey, and D. L. Jacobson, “Investigation of water transport in perforated gas diffusion layer by neutron radiography,” *ECS Transactions*, vol. 58, no. 1, p. 315, 2013.
- [113] T. Kitahara, H. Nakajima, M. Inamoto, and K. Shinto, “Triple microporous layer coated gas diffusion layer for performance enhancement of polymer electrolyte fuel cells under both low and high humidity conditions,” *Journal of Power Sources*, vol. 248, pp. 1256–1263, 2014.
- [114] K. D. Baik, S. I. Kim, B. K. Hong, K. Han, and M. S. Kim, “Effects of gas diffusion layer structure on the open circuit voltage and hydrogen crossover of polymer electrolyte membrane fuel cells,” *International Journal of Hydrogen Energy*, vol. 36, no. 16, pp. 9916–9925, 2011.
- [115] S. Kandlikar, M. Garofalo, and Z Lu, “Water management in a pemfc: Water transport mechanism and material degradation in gas diffusion layers,” *Fuel Cells*, vol. 11, no. 6, pp. 814–823, 2011.
- [116] M. Secanell Gallart, “Computational modeling and optimization of proton exchange membrane fuel cells,” Ph.D. dissertation, University of Victoria, 2007.

- [117] K. B. Daly, J. B. Benziger, A. Z. Panagiotopoulos, and P. G. Debenedetti, “Molecular dynamics simulations of water permeation across Nafion membrane interfaces,” *The Journal of Physical Chemistry B*, vol. 118, no. 29, pp. 8798–8807, 2014.
- [118] Q. Duan, H. Wang, and J. Benziger, “Transport of liquid water through Nafion membranes,” *Journal of Membrane Science*, vol. 392, pp. 88–94, 2012.
- [119] J. Zhou, A. Putz, and M. Secanell, “A mixed wettability pore size distribution based mathematical model for analyzing two-phase flow in porous electrodes i. mathematical model,” *Journal of The Electrochemical Society*, vol. 164, no. 6, F530–F539, 2017.
- [120] T. C. Yau, M. Cimenti, X. T. Bi, and J. Stumper, “Water transport and schröder’s paradox in fuel cell membrane electrode assemblies,” *Journal of Power Sources*, vol. 224, pp. 285–289, 2013.
- [121] J. R. Kracher, “Experimental Analysis of Transient Water Fluxes in PEM Fuel Cells,” M.S. thesis, University of Alberta, 2018.
- [122] A. Thomas, G. Maranzana, S. Didierjean, J. Dillet, and O. Lottin, “Measurements of electrode temperatures, heat and water fluxes in PEMFCs: conclusions about transfer mechanisms,” *Journal of The Electrochemical Society*, vol. 160, no. 2, F191–F204, 2013.
- [123] A. Z. Weber, R. M. Darling, and J. Newman, “Modeling two-phase behavior in PEFCs,” *Journal of The Electrochemical Society*, vol. 151, no. 10, A1715, 2004.
- [124] K. R. Cooper, V. Ramani, J. M. Fenton, and H. R. Kunz, *Experimental Methods and Data Analyses for Polymer Electrolyte Fuel Cells*. Scribner Associates, Inc., 2009.
- [125] M. Moore, S. Shukla, S. Voss, K. Karan, A. Weber, I. Zenyuk, and M. Secanell, “A numerical study on the impact of cathode catalyst layer loading on the open circuit voltage in a proton exchange membrane fuel cell,” *Journal of The Electrochemical Society*, vol. 168, no. 4, p. 044 519, 2021.
- [126] E. F. Medici, I. V. Zenyuk, D. Y. Parkinson, A. Z. Weber, and J. S. Allen, “Understanding Water Transport in Polymer Electrolyte Fuel Cells Using Coupled Continuum and Pore-Network Models,” *Fuel Cells*, vol. 16, no. 6, pp. 725–733, 2016.
- [127] J. Hamelin, K. Agbossou, A. Laperriere, F. Laurencelle, and T. K. Bose, “Dynamic behavior of a PEM fuel cell stack for stationary applications,” *International Journal of Hydrogen Energy*, vol. 26, no. 6, pp. 625–629, 2001.
- [128] F. Laurencelle, R. Chahine, J. Hamelin, K. Agbossou, M. Fournier, T. K. Bose, and A. Laperriere, “Characterization of a Ballard MK5-E Proton Exchange Membrane Fuel Cell Stack,” *Fuel cells*, vol. 1, no. 1, pp. 66–71, 2001.

- [129] K.-S. Choi, H.-M. Kim, and S.-M. Moon, “An experimental study on the enhancement of the water balance, electrochemical reaction and power density of the polymer electrolyte fuel cell by under-rib convection,” *Electrochemistry Communications*, vol. 13, no. 12, pp. 1387–1390, 2011, ISSN: 1388-2481.
- [130] S. Sugawara, Y. Suzuki, S. S. Kocha, and K. Shinohara, “Electrocatalytic activity analysis of PEFC cathode by 1-D macrohomogeneous model of catalyst layer,” *Electrochemistry*, vol. 79, no. 5, pp. 404–413, 2011.
- [131] N. Subramanian, T. Greszler, J Zhang, W Gu, and R Makharia, “Pt-oxide coverage-dependent oxygen reduction reaction (ORR) kinetics,” *Journal of The Electrochemical Society*, vol. 159, no. 5, B531, 2012.
- [132] K. Cooper and M. Smith, “Electrical test methods for on-line fuel cell ohmic resistance measurement,” *Journal of Power Sources*, vol. 160, no. 2, pp. 1088–1095, 2006, ISSN: 0378-7753.
- [133] S. Ge, X. Li, B. Yi, and I.-M. Hsing, “Absorption, Desorption, and Transport of Water in Polymer Electrolyte Membranes for Fuel Cells,” *Journal of The Electrochemical Society*, vol. 152, no. 6, A1149–A1157, 2005.
- [134] G. Janssen and M. Overvelde, “Water transport in the proton-exchange-membrane fuel cell: Measurements of the effective drag coefficient,” *Journal of Power Sources*, vol. 101, no. 1, pp. 117–125, 2001.
- [135] T Colinart, A Chenu, S Didierjean, O Lottin, and S Besse, “Experimental study on water transport coefficient in proton exchange membrane fuel cell,” *Journal of Power Sources*, vol. 190, no. 2, pp. 230–240, 2009.
- [136] J. G. Pharoah, B. Peppley, H. Atiyeh, E. Halliop, K. Karan, and A. Phoenix, “Investigating the Role of a Microporous Layer on the Water Transport and Performance of a PEMFC,” *ECS Transactions*, vol. 3, no. 1, p. 1227, 2006.
- [137] K. Karan, H. Atiyeh, A. Phoenix, E. Halliop, J. Pharoah, and B. Peppley, “An experimental investigation of water transport in PEMFCs: The role of microporous layers,” *Electrochemical and Solid-state Letters*, vol. 10, no. 2, B34, 2006.
- [138] A Thomas, G Maranzana, S Didierjean, J Dillet, and O Lottin, “Thermal effect on water transport in proton exchange membrane fuel cell,” *Fuel Cells*, vol. 12, no. 2, pp. 212–224, 2012.
- [139] X. Ye and C.-Y. Wang, “Measurement of water transport properties through membrane-electrode assemblies: I. membranes,” *Journal of The Electrochemical Society*, vol. 154, no. 7, B676, 2007.
- [140] A. Thomas, G. Maranzana, S. Didierjean, J. Dillet, and O. Lottin, “Measurements of electrode temperatures, heat and water fluxes in PEMFCs: conclusions about transfer mechanisms,” *Journal of The Electrochemical Society*, vol. 160, no. 2, F191, 2012.

- [141] P. Sauriol, D. S. Nobes, X. T. Bi, J. Stumper, D. Jones, and D. Kiel, “Design and validation of a water transfer factor measurement apparatus for proton exchange membrane fuel cells,” *Journal of Fuel Cell Science and Technology*, vol. 6, no. 4, p. 041 014, 2009.
- [142] T. C. Yau, P. Sauriol, X. T. Bi, and J. Stumper, “Experimental determination of water transport in polymer electrolyte membrane fuel cells,” *Journal of The Electrochemical Society*, vol. 157, no. 9, B1310, 2010.
- [143] M. Mench, Q. Dong, and C. Wang, “In situ water distribution measurements in a polymer electrolyte fuel cell,” *Journal of Power Sources*, vol. 124, no. 1, pp. 90–98, 2003.
- [144] Q Dong, J Kull, and M. Mench, “Real-time water distribution in a polymer electrolyte fuel cell,” *Journal of Power Sources*, vol. 139, no. 1-2, pp. 106–114, 2005.
- [145] A. M. Niroumand and M. Saif, “Two-phase flow measurement system for polymer electrolyte fuel cells,” *Journal of Power Sources*, vol. 195, no. 10, pp. 3250–3255, 2010.
- [146] B. Eriksson, H. Grimler, A. Carlson, H. Ekström, R. W. Lindström, G. Lindbergh, and C. Lagergren, “Quantifying water transport in anion exchange membrane fuel cells,” *International Journal of Hydrogen Energy*, vol. 44, no. 10, pp. 4930–4939, 2019.
- [147] J. T. Gostick, M. A. Ioannidis, M. W. Fowler, and M. D. Pritzker, “Wettability and capillary behavior of fibrous gas diffusion media for polymer electrolyte membrane fuel cells,” *Journal of Power Sources*, vol. 194, no. 1, pp. 433–444, 2009.
- [148] Y.-C. Chen, A. Berger, S. De Angelis, T. Schuler, M. Bozzetti, J. Eller, V. Tileli, T. J. Schmidt, and F. N. Büchi, “A method for spatial quantification of water in microporous layers of polymer electrolyte fuel cells by X-ray tomographic microscopy,” *ACS Applied Materials & Interfaces*, vol. 13, no. 14, pp. 16 227–16 237, 2021.
- [149] M. Sabharwal, F. N. Büchi, S. Nagashima, F. Marone, and J. Eller, “Investigation of the transient freeze start behavior of polymer electrolyte fuel cells,” *Journal of Power Sources*, vol. 489, p. 229 447, 2021.
- [150] I. V. Zenyuk and A. Z. Weber, “Understanding liquid-water management in PEFCs using X-ray computed tomography and modeling,” *ECS Transactions*, vol. 69, no. 17, p. 1253, 2015.
- [151] A. D. Shum, D. Y. Parkinson, X. Xiao, A. Z. Weber, O. S. Burheim, and I. V. Zenyuk, “Investigating phase-change-induced flow in gas diffusion layers in fuel cells with X-ray computed tomography,” *Electrochimica Acta*, vol. 256, pp. 279–290, 2017.

- [152] D. Kulkarni, S. J. Normile, L. G. Connolly, and I. V. Zenyuk, “Development of low temperature fuel cell holders for operando x-ray micro and nano computed tomography to visualize water distribution,” *Journal of Physics: Energy*, vol. 2, no. 4, p. 044 005, 2020.
- [153] A Bazylak, “Liquid water visualization in PEM fuel cells: A review,” *International Journal of Hydrogen Energy*, vol. 34, no. 9, pp. 3845–3857, 2009.
- [154] D. Kartouzian, A. Mohseninia, H. Markötter, J. Scholta, and I. Manke, “Neutron tomographic investigation of the effect of hydrophobicity gradients within mpl and mea on the spatial distribution and transport of liquid water in pem-fcs,” *ECS Transactions*, vol. 85, no. 13, p. 927, 2018.
- [155] F. S. Nanadegani, E. N. Lay, and B. Sunden, “Effects of an MPL on water and thermal management in a PEMFC,” *International Journal of Energy Research*, vol. 43, no. 1, pp. 274–296, 2019.
- [156] X. Zhang, X. Ma, S. Shuai, Y. Qin, and J. Yang, “Effect of micro-porous layer on pem fuel cells performance: Considering the spatially variable properties,” *International Journal of Heat and Mass Transfer*, vol. 178, p. 121 592, 2021.
- [157] J. T. Gostick, M. A. Ioannidis, M. D. Pritzker, and M. W. Fowler, “Impact of liquid water on reactant mass transfer in PEM fuel cell electrodes,” *Journal of The Electrochemical Society*, vol. 157, no. 4, B563, 2010.
- [158] A. Goshtasbi, P. García-Salaberri, J. Chen, K. Talukdar, D. G. Sanchez, and T. Eersal, “Through-the-membrane transient phenomena in PEM fuel cells: A modeling study,” *Journal of The Electrochemical Society*, vol. 166, no. 7, F3154, 2019.
- [159] I. V. Zenyuk, P. K. Das, and A. Z. Weber, “Understanding Impacts of Catalyst-Layer Thickness on Fuel-Cell Performance via Mathematical Modeling,” *Journal of The Electrochemical Society*, vol. 163, no. 7, F691, 2016.
- [160] S Culubret, M. Rubio, D. Sanchez, and A Urquia, “Dynamic modeling of the effect of water management on polymer electrolyte fuel cells performance,” *International Journal of Hydrogen Energy*, vol. 45, no. 9, pp. 5710–5722, 2020.
- [161] R. Vetter and J. O. Schumacher, “Free open reference implementation of a two-phase PEM fuel cell model,” *Computer Physics Communications*, vol. 234, pp. 223–234, 2019.
- [162] P. Carrere and M. Prat, “Liquid water in cathode gas diffusion layers of pem fuel cells: Identification of various pore filling regimes from pore network simulations,” *International Journal of Heat and Mass Transfer*, vol. 129, pp. 1043–1056, 2019.
- [163] S. Li, J. Yuan, G. Xie, and B. Sundén, “Effects of agglomerate model parameters on transport characterization and performance of PEM fuel cells,” *International Journal of Hydrogen Energy*, vol. 43, no. 17, pp. 8451–8463, 2018.

- [164] I. V. Zenyuk, E. Medici, J. Allen, and A. Z. Weber, “Coupling continuum and pore-network models for polymer-electrolyte fuel cells,” *International Journal of Hydrogen Energy*, vol. 40, no. 46, pp. 16 831–16 845, 2015.
- [165] D. J. Burnett, A. R. Garcia, and F. Thielmann, “Measuring moisture sorption and diffusion kinetics on proton exchange membranes using a gravimetric vapor sorption apparatus,” *Journal of Power Sources*, vol. 160, no. 1, pp. 426–430, 2006.
- [166] M. B. Satterfield and J. B. Benziger, “Non-Fickian water vapor sorption dynamics by Nafion membranes,” *The Journal of Physical Chemistry B*, vol. 112, no. 12, pp. 3693–3704, 2008.
- [167] T. A. Zawodzinski, C. Derouin, S. Radzinski, R. J. Sherman, V. T. Smith, T. E. Springer, and S. Gottesfeld, “Water uptake by and transport through Nafion<sup>®</sup> 117 membranes,” *Journal of The Electrochemical Society*, vol. 140, no. 4, p. 1041, 1993.
- [168] T. A. Zawodzinski Jr, M. Neeman, L. O. Sillerud, and S. Gottesfeld, “Determination of water diffusion coefficients in perfluorosulfonate ionomeric membranes,” *The Journal of Physical Chemistry*, vol. 95, no. 15, pp. 6040–6044, 1991.
- [169] S Tsushima, K Teranishi, and S Hirai, “Water diffusion measurement in fuel-cell SPE membrane by NMR,” *Energy*, vol. 30, no. 2-4, pp. 235–245, 2005.
- [170] A. M. Pivovar and B. S. Pivovar, “Dynamic behavior of water within a polymer electrolyte fuel cell membrane at low hydration levels,” *The Journal of Physical Chemistry B*, vol. 109, no. 2, pp. 785–793, 2005.
- [171] J.-C. Perrin, S. Lyonnard, and F. Volino, “Quasielastic neutron scattering study of water dynamics in hydrated Nafion membranes,” *The Journal of Physical Chemistry C*, vol. 111, no. 8, pp. 3393–3404, 2007.
- [172] M. Soniat and F. A. Houle, “How the hydrophobic interface between a perfluorosulfonic acid polymer and water vapor controls membrane hydration,” *ACS Applied Polymer Materials*, vol. 4, no. 5, pp. 3247–3258, 2022.
- [173] P. W. Majsztrik, M. B. Satterfield, A. B. Bocarsly, and J. B. Benziger, “Water sorption, desorption and transport in Nafion membranes,” *Journal of Membrane Science*, vol. 301, no. 1-2, pp. 93–106, 2007.
- [174] C. W. Monroe, T. Romero, W. Mérida, and M. Eikerling, “A vaporization-exchange model for water sorption and flux in Nafion,” *Journal of Membrane Science*, vol. 324, no. 1-2, pp. 1–6, 2008.
- [175] B. Kienitz, H. Yamada, N. Nonoyama, and A. Z. Weber, “Interfacial water transport effects in proton-exchange membranes,” *Journal of Fuel Cell Science and Technology*, vol. 8, no. 1, 2011.
- [176] Q. Zhao, P. Majsztrik, and J. Benziger, “Diffusion and interfacial transport of water in Nafion,” *The Journal of Physical Chemistry B*, vol. 115, no. 12, pp. 2717–2727, 2011.

- [177] M. Adachi, T. Navessin, Z. Xie, F. H. Li, S. Tanaka, and S. Holdcroft, "Thickness dependence of water permeation through proton exchange membranes," *Journal of Membrane Science*, vol. 364, no. 1-2, pp. 183–193, 2010.
- [178] X. Luo, A. Wright, T. Weissbach, and S. Holdcroft, "Water permeation through anion exchange membranes," *Journal of Power Sources*, vol. 375, pp. 442–451, 2018.
- [179] K Chadha, S Martemianov, and A Thomas, "Estimation of the effective water diffusion coefficient in Nafion<sup>®</sup> membrane by water balance measurements," *Fuel Cells*, vol. 21, no. 2, pp. 139–148, 2021.
- [180] P. Futerko and I.-M. Hsing, "Two-dimensional finite-element method study of the resistance of membranes in polymer electrolyte fuel cells," *Electrochimica Acta*, vol. 45, no. 11, pp. 1741–1751, 2000.
- [181] P. Berg, K. Promislow, J. S. Pierre, J. Stumper, and B. Wetton, "Water management in PEM fuel cells," *Journal of The Electrochemical Society*, vol. 151, no. 3, A341, 2004.
- [182] M. J. Cheah, I. G. Kevrekidis, and J. Benziger, "Effect of interfacial water transport resistance on coupled proton and water transport across Nafion," *The Journal of Physical Chemistry B*, vol. 115, no. 34, pp. 10 239–10 250, 2011.
- [183] V. Klika, J. Kubant, M. Pavelka, and J. B. Benziger, "Non-equilibrium thermodynamic model of water sorption in Nafion membranes," *Journal of Membrane Science*, vol. 540, pp. 35–49, 2017.
- [184] G. S. Hwang, D. Y. Parkinson, A. Kusoglu, A. A. MacDowell, and A. Z. Weber, "Understanding water uptake and transport in Nafion using X-ray microtomography," *ACS Macro Letters*, vol. 2, no. 4, pp. 288–291, 2013.
- [185] T. D. Myles, A. M. Kiss, K. N. Grew, A. A. Peracchio, G. J. Nelson, and W. K. Chiu, "Calculation of water diffusion coefficients in an anion exchange membrane using a water permeation technique," *Journal of The Electrochemical Society*, vol. 158, no. 7, B790, 2011.
- [186] M. Marino, J. Melchior, A Wohlfarth, and K. Kreuer, "Hydroxide, halide and water transport in a model anion exchange membrane," *Journal of Membrane Science*, vol. 464, pp. 61–71, 2014.
- [187] Y. Li, T. Zhao, and W. Yang, "Measurements of water uptake and transport properties in anion-exchange membranes," *International Journal of Hydrogen Energy*, vol. 35, no. 11, pp. 5656–5665, 2010.
- [188] J. Sim, M. Kang, H. Oh, E. Lee, J.-Y. Jyoung, and K. Min, "The effect of gas diffusion layer on electrochemical effective reaction area of catalyst layer and water discharge capability," *Renewable Energy*, vol. 197, pp. 932–942, 2022.
- [189] S. Motupally, A. J. Becker, and J. W. Weidner, "Diffusion of water in Nafion 115 membranes," *Journal of The Electrochemical Society*, vol. 147, no. 9, pp. 3171–3177, 2000.

- [190] A. Z. Weber and J. Newman, “Transport in Polymer-Electrolyte Membranes: II. Mathematical Model,” *Journal of The Electrochemical Society*, vol. 151, no. 2, A311, 2004.
- [191] I. Zenyuk, E. Kumbur, and S Litster, “Deterministic contact mechanics model applied to electrode interfaces in polymer electrolyte fuel cells and interfacial water accumulation,” *Journal of Power Sources*, vol. 241, pp. 379–387, 2013.
- [192] F Jinuntuya and W Kamsanam, “Effects of a microporous layer on water transport BEhaviour in PEM fuel cell gas diffusion layers,” *IOP Conference Series: Materials Science and Engineering*, vol. 886, no. 1, pp. 012–043, 2020.
- [193] M Lopez-Haro, L Guétaz, T Printemps, A Morin, S Escribano, P.-H. Jouneau, P Bayle-Guillemaud, F Chandezon, and G Gebel, “Three-dimensional analysis of Nafion layers in fuel cell electrodes,” *Nature Communications*, vol. 5, no. 1, p. 5229, 2014.
- [194] D. A. Cullen, K. Neyerlin, R. K. Ahluwalia, R. Mukundan, K. L. More, R. L. Borup, A. Z. Weber, D. J. Myers, and A. Kusoglu, “New roads and challenges for fuel cells in heavy-duty transportation,” *Nature Energy*, vol. 6, no. 5, pp. 462–474, 2021.
- [195] H Ishikawa, Y Sugawara, G Inoue, and M Kawase, “Effects of Pt and ionomer ratios on the structure of catalyst layer: A theoretical model for polymer electrolyte fuel cells,” *Journal of Power Sources*, vol. 374, pp. 196–204, 2018.
- [196] S. Lee, S Mukerjee, J. McBreen, Y. Rho, Y. Kho, and T. Lee, “Effects of Nafion impregnation on performances of PEMFC electrodes,” *Electrochimica Acta*, vol. 43, no. 24, pp. 3693–3701, 1998.
- [197] E Antolini, L Giorgi, A Pozio, and E Passalacqua, “Influence of Nafion loading in the catalyst layer of gas-diffusion electrodes for PEFC,” *Journal of Power Sources*, vol. 77, no. 2, pp. 136–142, 1999.
- [198] E Passalacqua, F Lufrano, G Squadrito, A Patti, and L Giorgi, “Nafion content in the catalyst layer of polymer electrolyte fuel cells: effects on structure and performance,” *Electrochimica Acta*, vol. 46, no. 6, pp. 799–805, 2001, ISSN: 0013-4686.
- [199] G. Li and P. G. Pickup, “Ionic conductivity of PEMFC electrodes: Effect of Nafion loading,” *Journal of The Electrochemical Society*, vol. 150, no. 11, p. C745, 2003.
- [200] G Sasikumar, J. Ihm, and H Ryu, “Optimum Nafion content in PEM fuel cell electrodes,” *Electrochimica Acta*, vol. 50, no. 2-3, pp. 601–605, 2004.
- [201] G Sasikumar, J. Ihm, and H Ryu, “Dependence of optimum Nafion content in catalyst layer on platinum loading,” *Journal of Power Sources*, vol. 132, no. 1, pp. 11–17, 2004, ISSN: 0378-7753.

- [202] Z. Xie, T. Navessin, K. Shi, R. Chow, Q. Wang, D. Song, B. Andreaus, M. Eikerling, Z. Liu, and S. Holdcroft, “Functionally Graded Cathode Catalyst Layers for Polymer Electrolyte Fuel Cells: II. Experimental Study of the Effect of Nafion Distribution,” *Journal of The Electrochemical Society*, vol. 152, no. 6, A1171, 2005.
- [203] D. Lee and S. Hwang, “Effect of loading and distributions of Nafion ionomer in the catalyst layer for PEMFCs,” *International Journal of Hydrogen Energy*, vol. 33, no. 11, pp. 2790–2794, 2008.
- [204] C.-M. Lai, J.-C. Lin, F.-P. Ting, S.-D. Chyou, and K.-L. Hsueh, “Contribution of Nafion loading to the activity of catalysts and the performance of PEMFC,” *International Journal of Hydrogen Energy*, vol. 33, no. 15, pp. 4132–4137, 2008.
- [205] J. Xie, F. Xu, D. L. Wood, K. L. More, T. A. Zawodzinski, and W. H. Smith, “Influence of ionomer content on the structure and performance of PEFC membrane electrode assemblies,” *Electrochimica Acta*, vol. 55, no. 24, pp. 7404–7412, 2010, ISSN: 0013-4686.
- [206] S Martin, P. Garcia-Ybarra, and J. Castillo, “High platinum utilization in ultra-low Pt loaded PEM fuel cell cathodes prepared by electrospraying,” *International Journal of Hydrogen Energy*, vol. 35, no. 19, pp. 10 446–10 451, 2010.
- [207] K.-H. Kim, K.-Y. Lee, H.-J. Kim, E. Cho, S.-Y. Lee, T.-H. Lim, S. P. Yoon, I. C. Hwang, and J. H. Jang, “The effects of Nafion<sup>®</sup> ionomer content in PEMFC MEAs prepared by a catalyst-coated membrane (CCM) spraying method,” *International Journal of Hydrogen Energy*, vol. 35, no. 5, pp. 2119–2126, 2010.
- [208] Q. Wang, M. Eikerling, D. Song, Z. Liu, T. Navessin, Z. Xie, and S. Holdcroft, “Functionally Graded Cathode Catalyst Layers for Polymer Electrolyte Fuel Cells: I. Theoretical Modeling,” *Journal of The Electrochemical Society*, vol. 151, no. 7, A950, 2004.
- [209] Y.-G. Yoon, T.-H. Yang, G.-G. Park, W.-Y. Lee, and C.-S. Kim, “A multi-layer structured cathode for the PEMFC,” *Journal of Power Sources*, vol. 118, no. 1, pp. 189–192, 2003.
- [210] K.-H. Kim, H.-J. Kim, K.-Y. Lee, J. Jang, S.-Y. Lee, E Cho, I.-H. Oh, and T.-H. Lim, “Effect of Nafion<sup>®</sup> gradient in dual catalyst layer on proton exchange membrane fuel cell performance,” *International Journal of Hydrogen Energy*, vol. 33, no. 11, pp. 2783–2789, 2008.
- [211] A. D. Taylor, E. Y. Kim, V. P. Humes, J. Kizuka, and L. T. Thompson, “Inkjet printing of carbon supported platinum 3-D catalyst layers for use in fuel cells,” *Journal of Power Sources*, vol. 171, no. 1, pp. 101–106, 2007.
- [212] M Srinivasarao, D Bhattacharyya, R Rengaswamy, and S Narasimhan, “Performance analysis of a PEM fuel cell cathode with multiple catalyst layers,” *International Journal of Hydrogen Energy*, vol. 35, no. 12, pp. 6356–6365, 2010.

- [213] M. Srinivasarao, D. Bhattacharyya, and R. Rengaswamy, "Optimization studies of a polymer electrolyte membrane fuel cell with multiple catalyst layers," *Journal of Power Sources*, vol. 206, pp. 197–203, 2012.
- [214] A. Kosakian and M. Secanell, "Estimating charge-transport properties of fuel-cell and electrolyzer catalyst layers via electrochemical impedance spectroscopy," *Electrochimica Acta*, vol. 367, p. 137 521, 2021.
- [215] M. Adachi, T. Romero, T. Navessin, Z. Xie, Z. Shi, W. Mérida, and S. Holdcroft, "Water Permeation Through Catalyst-Coated Membranes," *Electrochemical and Solid-State Letters*, vol. 13, no. 6, B51, 2010.
- [216] *BUCK RESEARCH INSTRUMENTS L.L.C. MODEL CR-2 HYGROMETER OPERATING MANUAL*, <https://www.hygrometers.com/wp-content/uploads/CR-1A-users-manual-2009-12.pdf>, Accessed: September 07th, 2023.
- [217] T. D. Gierke, G. Munn, and F. Wilson, "The morphology in Nafion perfluorinated membrane products, as determined by wide-and small-angle X-ray studies," *Journal of Polymer Science: Polymer Physics Edition*, vol. 19, no. 11, pp. 1687–1704, 1981.
- [218] R. M. Darling, J. D. Saraidaridis, C. Shovlin, and M. Fortin, "The influence of current density on transport of vanadium acetylacetonate through a cation-exchange membrane," *Journal of The Electrochemical Society*, vol. 169, no. 3, p. 030 514, 2022.
- [219] T. Uchiyama, M. Kato, Y. Ikogi, and T. Yoshida, "Mechanical degradation mechanism of membrane electrode assemblies in buckling test under humidity cycles," *Journal of Fuel Cell Science and Technology*, vol. 9, no. 6, 2012.
- [220] P Dobson, C Lei, T Navessin, and M Secanell, "Characterization of the PEM fuel cell catalyst layer microstructure by nonlinear least-squares parameter estimation," *Journal of The Electrochemical Society*, vol. 159, no. 5, B514, 2012.
- [221] R. Bock, A. Shum, X Xiao, H. Karoliussen, F. Seland, I. V. Zenyuk, and O. S. Burheim, "Thermal conductivity and compaction of GDL-MPL interfacial composite material," *Journal of The Electrochemical Society*, vol. 165, no. 7, F514, 2018.
- [222] O. S. Burheim, G. A. Crymble, R. Bock, N. Hussain, S. Pasupathi, A. du Plessis, S. le Roux, F. Seland, H. Su, and B. G. Pollet, "Thermal conductivity in the three layered regions of micro porous layer coated porous transport layers for the PEM fuel cell," *International Journal of Hydrogen Energy*, vol. 40, no. 46, pp. 16 775–16 785, 2015.
- [223] A. J. Wheeler and A. R. Ganji, *Introduction to Engineering Experimentation 2nd Edition*. Prentice Hall, 2004.
- [224] J. R. Taylor, *An Introduction to Error Analysis: The Study of Uncertainties in Physical Measurements 2nd Edition*. University Science Books, 1997.

- [225] The Sensirion Company, “Datasheet SHT85 Humidity and Temperature Sensor,” *Official Website*, March 2021.
- [226] F. Wei, A. Kosakian, J. Liu, J. Kracher, R. Khan, and M. Secanell, “Corrigendum to “Water transport in anion and proton exchange membranes” [J. Power Sources 557 (2023) 232494],” *Journal of Power Sources*, vol. 576, p. 233 214, 2023, ISSN: 0378-7753.
- [227] J. T. Hinatsu, M. Mizuhata, and H. Takenaka, “Water uptake of perfluoro-sulfonic acid membranes from liquid water and water vapor,” *Journal of The Electrochemical Society*, vol. 141, no. 6, pp. 1493–1498, 1994.
- [228] J. Peron, A. Mani, X. Zhao, D. Edwards, M. Adachi, T. Soboleva, Z. Shi, Z. Xie, T. Navessin, and S. Holdcroft, “Properties of Nafion<sup>®</sup> NR-211 membranes for PEMFCs,” *Journal of Membrane Science*, vol. 356, no. 1-2, pp. 44–51, 2010.
- [229] T. A. Zawodzinski, T. E. Springer, J. Davey, R. Jestel, C. Lopez, J. Valerio, and S. Gottesfeld, “A comparative study of water uptake by and transport through ionomeric fuel cell membranes,” *Journal of The Electrochemical Society*, vol. 140, no. 7, p. 1981, 1993.
- [230] A. Kusoglu, B. L. Kienitz, and A. Z. Weber, “Understanding the effects of compression and constraints on water uptake of fuel-cell membranes,” *Journal of The Electrochemical Society*, vol. 158, no. 12, B1504, 2011.
- [231] X. Luo, S. Rojas-Carbonell, Y. Yan, and A. Kusoglu, “Structure-transport relationships of poly (aryl piperidinium) anion-exchange membranes: Effect of anions and hydration,” *Journal of Membrane Science*, vol. 598, p. 117 680, 2020.
- [232] P. Majsztrik, A. Bocarsly, and J. Benziger, “Water permeation through Nafion membranes: The role of water activity,” *The Journal of Physical Chemistry B*, vol. 112, no. 51, pp. 16 280–16 289, 2008.
- [233] P. Virtanen, R. Gommers, T. E. Oliphant, M. Haberland, T. Reddy, D. Cournapeau, E. Burovski, P. Peterson, W. Weckesser, J. Bright, *et al.*, “SciPy 1.0: Fundamental algorithms for scientific computing in Python,” *Nature methods*, vol. 17, no. 3, pp. 261–272, 2020.
- [234] A. Hindmarsh, “ODEPACK. A collection of ODE system solvers,” Lawrence Livermore National Lab., CA (United States), Tech. Rep., 1992.
- [235] L. Petzold, “Automatic selection of methods for solving stiff and nonstiff systems of ordinary differential equations,” *SIAM Journal on Scientific and Statistical Computing*, vol. 4, no. 1, pp. 136–148, 1983.
- [236] R. P. Brent, *Algorithms for minimization without derivatives*. Courier Corporation, 2013.
- [237] W. H. Press, S. A. Teukolsky, W. T. Vetterling, and B. P. Flannery, *Numerical recipes: The art of scientific computing*, third edition. Cambridge University Press, 2007.

- [238] A. Kusoglu, A. Kwong, K. T. Clark, H. P. Gunterman, and A. Z. Weber, “Water uptake of fuel-cell catalyst layers,” *Journal of The Electrochemical Society*, vol. 159, no. 9, F530–F535, 2012.
- [239] T. Springer, T. Zawodzinski, and S. Gottesfeld, “Polymer electrolyte fuel cell model,” *Journal of The Electrochemical Society*, vol. 138, no. 8, pp. 2334–2342, 1991.
- [240] C. K. Mittelsteadt and H. Liu, “Conductivity, permeability, and ohmic shorting of ionomeric membranes,” in *Handbook of fuel cells: Fundamentals technology and applications: Advances in electrocatalysis, materials, diagnostics and durability*, W. Vielstich, H. A. Gasteiger, and H. Yokokawa, Eds., John Wiley & Sons: Springer New York, 2009, pp. 345–358.
- [241] H. Iden, K. Sato, A. Ohma, and K. Shinohara, “Relationship among microstructure, ionomer property and proton transport in pseudo catalyst layers,” *Journal of The Electrochemical Society*, vol. 158, no. 8, B987–B994, 2011.
- [242] K.-D. Kreuer, “The role of internal pressure for the hydration and transport properties of ionomers and polyelectrolytes,” *Solid State Ionics*, vol. 252, pp. 93–101, 2013.
- [243] S Naudy, F Collette, F ThomINETTE, G Gebel, and E. Espuche, “Influence of hygrothermal aging on the gas and water transport properties of Nafion<sup>®</sup> membranes,” *Journal of Membrane Science*, vol. 451, pp. 293–304, 2014.
- [244] S. Shi, A. Z. Weber, and A. Kusoglu, “Structure/property relationship of Nafion XL composite membranes,” *Journal of Membrane Science*, vol. 516, pp. 123–134, 2016.
- [245] D. Novitski, A. Kosakian, T. Weissbach, M. Secanell, and S. Holdcroft, “Electrochemical reduction of dissolved oxygen in alkaline, solid polymer electrolyte films,” *Journal of the American Chemical Society*, vol. 138, no. 47, pp. 15 465–15 472, 2016.
- [246] Y. Zheng, U. Ash, R. P. Pandey, A. G. Ozioko, J. Ponce-González, M. Handl, T. Weissbach, J. R. Varcoe, S. Holdcroft, M. W. Liberatore, *et al.*, “Water uptake study of anion exchange membranes,” *Macromolecules*, vol. 51, no. 9, pp. 3264–3278, 2018.
- [247] N. Ziv, A. N. Mondal, T. Weissbach, S. Holdcroft, and D. R. Dekel, “Effect of CO<sub>2</sub> on the properties of anion exchange membranes for fuel cell applications,” *Journal of Membrane Science*, vol. 586, pp. 140–150, 2019.
- [248] E. J. Dickinson and G. Smith, “Modelling the proton-conductive membrane in practical polymer electrolyte membrane fuel cell (PEMFC) simulation: A review,” *Membranes*, vol. 10, no. 11, p. 310, 2020.
- [249] A. Kusoglu, S. Savagatrup, K. T. Clark, and A. Z. Weber, “Role of mechanical factors in controlling the structure–function relationship of PFSA ionomers,” *Macromolecules*, vol. 45, no. 18, pp. 7467–7476, 2012.

- [250] S. C. Yeo and A. Eisenberg, “Physical properties and supermolecular structure of perfluorinated ion-containing (Nafion) polymers,” *Journal of applied polymer science*, vol. 21, no. 4, pp. 875–898, 1977.
- [251] *Maxima, a Computer Algebra System (official website)*, <http://maxima.sourceforge.net/>, Accessed September 07th, 2022.
- [252] A. C. Olesen, “Macroscopic modeling of transport phenomena in direct methanol fuel cells,” Ph.D. dissertation, Aalborg University, 2013.
- [253] M. P. Nielsen, A. C. C. Olesen, and A. Menard, “Modeling of membrane based humidifiers for fuel cell applications subject to end-of-life conditions,” in *Proceedings of the 55th Conference on Simulation and Modelling (SIMS 55), Modelling, Simulation and Optimization, 21-22 October 2014, Aalborg, Denmark*, Linköping University Electronic Press, 2014, pp. 101–110.
- [254] T. Okada, G. Xie, and M. Meeg, “Simulation for water management in membranes for polymer electrolyte fuel cells,” *Electrochimica Acta*, vol. 43, no. 14-15, pp. 2141–2155, 1998.
- [255] A. Kongkanand, “Interfacial water transport measurements in Nafion thin films using a quartz-crystal microbalance,” *The Journal of Physical Chemistry C*, vol. 115, no. 22, pp. 11 318–11 325, 2011.
- [256] Y. Tabuchi, R. Ito, S. Tsushima, and S. Hirai, “Analysis of in situ water transport in Nafion<sup>®</sup> by confocal micro-Raman spectroscopy,” *Journal of Power Sources*, vol. 196, no. 2, pp. 652–658, 2011.
- [257] T. Romero and W. Merida, “Water transport in liquid and vapour equilibrated Nafion membranes,” *Journal of Membrane Science*, vol. 338, no. 1-2, pp. 135–144, 2009.
- [258] Q. He, A. Kusoglu, I. T. Lucas, K. Clark, A. Z. Weber, and R. Kostecky, “Correlating humidity-dependent ionically conductive surface area with transport phenomena in proton-exchange membranes,” *The Journal of Physical Chemistry B*, vol. 115, no. 40, pp. 11 650–11 657, 2011.
- [259] M. W. Verbrugge, E. W. Schneider, R. S. Conell, and R. F. Hill, “The effect of temperature on the equilibrium and transport properties of saturated poly (perfluorosulfonic acid) membranes,” *Journal of The Electrochemical Society*, vol. 139, no. 12, p. 3421, 1992.
- [260] D. R. Morris and X. Sun, “Water-sorption and transport properties of Nafion 117 H,” *Journal of applied polymer science*, vol. 50, no. 8, pp. 1445–1452, 1993.
- [261] S. Shukla, D. Stanier, M. S. Saha, J. Stumper, and M. Secanell, “Analysis of Inkjet Printed PEFC Electrodes with Varying Platinum Loading,” *Journal of The Electrochemical Society*, vol. 163, no. 7, F677, 2016.
- [262] M. Mandal, A. Valls, N. Gangnus, and M. Secanell, “Analysis of Inkjet Printed Catalyst Coated Membranes for Polymer Electrolyte Electrolyzers,” *Journal of The Electrochemical Society*, vol. 165, no. 7, F543, 2018.

- [263] J Zhou, A Putz, and M Secanell, “A mixed wettability pore size distribution based mathematical model for analyzing two-phase flow in porous electrodes,” *Journal of The Electrochemical Society*, vol. 164, no. 6, F530, 2017.
- [264] M. N. Islam, U. Shrivastava, M. Atwa, X. Li, V. Birss, and K. Karan, “Highly ordered nanoporous carbon scaffold with controllable wettability as the microporous layer for fuel cells,” *ACS Applied Materials & Interfaces*, vol. 12, no. 35, pp. 39 215–39 226, 2020.
- [265] T. Tanuma, M. Kawamoto, and S Kinoshita, “Effect of properties of hydrophilic microporous layer (MPL) on PEFC performance,” *Journal of The Electrochemical Society*, vol. 164, no. 6, F499, 2017.
- [266] V. R. Ilie, S Martemianov, and A Thomas, “Investigation of the local temperature and overheat inside the membrane electrode assembly of PEM fuel cell,” *International Journal of Hydrogen Energy*, vol. 41, no. 34, pp. 15 528–15 537, 2016.
- [267] C. A. Schneider, W. S. Rasband, and K. W. Eliceiri, “NIH Image to ImageJ: 25 years of image analysis,” *Nature Methods*, vol. 9, no. 7, pp. 671–675, 2012.
- [268] P. Gode, F. Jaouen, G. Lindbergh, A. Lundblad, and G. Sundholm, “Influence of the composition on the structure and electrochemical characteristics of the pefc cathode,” *Electrochimica Acta*, vol. 48, no. 28, pp. 4175–4187, 2003.
- [269] Z. Yu, R. N. Carter, and J. Zhang, “Measurements of Pore Size Distribution, Porosity, Effective Oxygen Diffusivity, and Tortuosity of PEM Fuel Cell Electrodes,” *Fuel Cells*, vol. 12, no. 4, pp. 557–565, 2012.
- [270] I. V. Zenyuk, A. Lamibrac, J. Eller, D. Y. Parkinson, F. Marone, F. N. Büchi, and A. Z. Weber, “Investigating Evaporation in Gas Diffusion Layers for Fuel Cells with X-ray Computed Tomography,” *The Journal of Physical Chemistry C*, vol. 120, no. 50, pp. 28 701–28 711, 2016.
- [271] S Shukla, D Stanier, M. Saha, B Zahiri, M Tam, J Stumper, and M Secanell, “Characterization of Inkjet Printed Electrodes with Improved Porosity,” *ECS Transactions*, vol. 77, no. 11, pp. 1453–1463, 2017.
- [272] M. S. Saha, D. Malevich, E. Halliop, J. G. Pharoah, B. A. Peppley, and K. Karan, “Electrochemical activity and catalyst utilization of low Pt and thickness controlled membrane electrode assemblies,” *Journal of The Electrochemical Society*, vol. 158, no. 5, B562, 2011.
- [273] *U.S. Department of Energy Hydrogen Program: 2021 Annual Merit Review and Peer Evaluation Report*, <https://www.nrel.gov/docs/fy22osti/81192.pdf>, Accessed: 16th January, 2023.
- [274] C. Wang, M. Waje, X. Wang, J. M. Tang, R. C. Haddon, and Y. Yan, “Proton exchange membrane fuel cells with carbon nanotube based electrodes,” *Nano Letters*, vol. 4, no. 2, pp. 345–348, 2004.
- [275] E. Antolini, “Graphene as a new carbon support for low-temperature fuel cell catalysts,” *Applied Catalysis B: Environmental*, vol. 123, pp. 52–68, 2012.

- [276] A Smirnova, X Dong, H Hara, A Vasiliev, and N Sammes, “Novel carbon aerogel-supported catalysts for PEM fuel cell application,” *International journal of hydrogen energy*, vol. 30, no. 2, pp. 149–158, 2005.
- [277] W. S. Jung and B. N. Popov, “Improved durability of Pt catalyst supported on N-doped mesoporous graphitized carbon for oxygen reduction reaction in polymer electrolyte membrane fuel cells,” *Carbon*, vol. 122, pp. 746–755, 2017.
- [278] S. Ott, A. Orfanidi, H. Schmies, B. Anke, H. N. Nong, J. Hübner, U. Gernert, M. Gliech, M. Lerch, and P. Strasser, “Ionomer distribution control in porous carbon-supported catalyst layers for high-power and low Pt-loaded proton exchange membrane fuel cells,” *Nature Materials*, vol. 19, no. 1, pp. 77–85, 2020.
- [279] S. X. Chen, X. Zhang, and P. K. Shen, “Macroporous conducting matrix: Fabrication and application as electrocatalyst support,” *Electrochemistry Communications*, vol. 8, no. 5, pp. 713–719, 2006.
- [280] X. Tian, X. Zhao, Y.-Q. Su, L. Wang, H. Wang, D. Dang, B. Chi, H. Liu, E. J. Hensen, X. W. Lou, *et al.*, “Engineering bunched Pt-Ni alloy nanocages for efficient oxygen reduction in practical fuel cells,” *Science*, vol. 366, no. 6467, pp. 850–856, 2019.
- [281] L. Chong, J. Wen, J. Kubal, F. G. Sen, J. Zou, J. Greeley, M. Chan, H. Barkholtz, W. Ding, and D.-J. Liu, “Ultralow-loading platinum-cobalt fuel cell catalysts derived from imidazolate frameworks,” *Science*, vol. 362, no. 6420, pp. 1276–1281, 2018.
- [282] M. Li, Z. Zhao, T. Cheng, A. Fortunelli, C.-Y. Chen, R. Yu, Q. Zhang, L. Gu, B. V. Merinov, Z. Lin, *et al.*, “Ultrafine jagged platinum nanowires enable ultrahigh mass activity for the oxygen reduction reaction,” *Science*, vol. 354, no. 6318, pp. 1414–1419, 2016.
- [283] X. Huang, Z. Zhao, L. Cao, Y. Chen, E. Zhu, Z. Lin, M. Li, A. Yan, A. Zettl, Y. M. Wang, *et al.*, “High-performance transition metal-doped Pt<sub>3</sub>Ni octahedra for oxygen reduction reaction,” *Science*, vol. 348, no. 6240, pp. 1230–1234, 2015.
- [284] C. Chen, Y. Kang, Z. Huo, Z. Zhu, W. Huang, H. L. Xin, J. D. Snyder, D. Li, J. A. Herron, M. Mavrikakis, *et al.*, “Highly crystalline multimetallic nanoframes with three-dimensional electrocatalytic surfaces,” *Science*, vol. 343, no. 6177, pp. 1339–1343, 2014.
- [285] H. Zhang, S. Hwang, M. Wang, Z. Feng, S. Karakalos, L. Luo, Z. Qiao, X. Xie, C. Wang, D. Su, *et al.*, “Single atomic iron catalysts for oxygen reduction in acidic media: Particle size control and thermal activation,” *Journal of the American Chemical Society*, vol. 139, no. 40, pp. 14 143–14 149, 2017.
- [286] H. T. Chung, D. A. Cullen, D. Higgins, B. T. Sneed, E. F. Holby, K. L. More, and P. Zelenay, “Direct atomic-level insight into the active sites of a high-performance PGM-free ORR catalyst,” *Science*, vol. 357, no. 6350, pp. 479–484, 2017.

- [287] Z. Miao, X. Wang, M.-C. Tsai, Q. Jin, J. Liang, F. Ma, T. Wang, S. Zheng, B.-J. Hwang, Y. Huang, *et al.*, “Atomically dispersed Fe-Nx/C electrocatalyst boosts oxygen catalysis via a new metal-organic polymer supramolecule strategy,” *Advanced Energy Materials*, vol. 8, no. 24, p. 1 801 226, 2018.
- [288] J.-Y. Choi, L. Yang, T. Kishimoto, X. Fu, S. Ye, Z. Chen, and D. Banham, “Is the rapid initial performance loss of Fe/N/C non precious metal catalysts due to micropore flooding?” *Energy & Environmental Science*, vol. 10, no. 1, pp. 296–305, 2017.
- [289] A. Kosakian, “Transient numerical modeling of proton-exchange-membrane fuel cells,” Ph.D. dissertation, University of Alberta, 2021.
- [290] A. G. Wright, J. Fan, B. Britton, T. Weissbach, H.-F. Lee, E. A. Kitching, T. J. Peckham, and S. Holdcroft, “Hexamethyl-p-terphenyl poly (benzimidazolium): A universal hydroxide-conducting polymer for energy conversion devices,” *Energy & Environmental Science*, vol. 9, no. 6, pp. 2130–2142, 2016.
- [291] P. Fortin, T. Khoza, X. Cao, S. Y. Martinsen, A. O. Barnett, and S. Holdcroft, “High-performance alkaline water electrolysis using Aemion™ anion exchange membranes,” *Journal of Power Sources*, vol. 451, p. 227 814, 2020.
- [292] B. Shanahan, B. Britton, A. Belletti, S. Vierrath, and M. Breitwieser, “Performance and stability comparison of aemion™ and aemion+™ membranes for vanadium redox flow batteries,” *RSC Advances*, vol. 11, no. 22, pp. 13 077–13 084, 2021.
- [293] A. S. Gangrade, S. Cassegrain, P. C. Ghosh, and S. Holdcroft, “Permselectivity of ionene-based, Aemion® anion exchange membranes,” *Journal of Membrane Science*, vol. 641, p. 119 917, 2022.

# Appendix A: Supplementary Information for Chapter 3: Water Transport in Anion and Proton Exchange Membranes

## A.1 Mathematical model

### A.1.1 Water uptake

The water-uptake data for Nafion<sup>®</sup> N211 and N212 at 25–80 °C from references [228, 238, 243, 244] were fitted with eq. (3.10). The fitting was performed using the Sequential Least Squares Programming (SLSQP) algorithm in SciPy [233] by minimizing the root-mean-square deviation (RMSD)

$$\text{RMSD} = \sqrt{\frac{\sum_{i=1}^N (\lambda_{\text{eq}}^{\text{exp}}(a_{\text{w},i}^{\text{exp}}) - \lambda_{\text{eq}}^{\text{fit}}(a_{\text{w},i}^{\text{exp}}))^2}{N}} \quad (\text{A.1})$$

between the experimental data and the fitting function (3.10). Since multiple data sets were available, the overall fitting residual was defined as a root-mean square of RMSDs of the individual data sets:

$$\text{RMS} = \sqrt{\frac{\sum_{i=1}^M \text{RMSD}_i^2}{M}}, \quad (\text{A.2})$$

where  $M$  is the number of the data sets. The fitted coefficients of eq. (3.10) are provided in Table A.1. The coefficient of determination ( $R^2$ ) of the fit was at least 0.9784 (0.9917 on average).

Table A.1: Coefficients of the water-uptake curve eq. (3.10).

Membrane	$\alpha_0$	$\alpha_1$	$\alpha_2$	$\alpha_3$	Reference
Nafion <sup>®</sup> N11X	0.043	17.81	-39.85	36.0	Refs. [168, 239]
Nafion <sup>®</sup> N21X	0	14.25	-23.95	21.11	This work
Aemion <sup>®</sup> AH1-HNN8-50-X	0	18.31	-32.57	28.06	This work
Fumapem <sup>®</sup> FAA-3	0	12.11	-15.76	13.56	This work
Versogen <sup>™</sup> PiperION-A40	0	13.13	-14.81	14.41	This work

Water-uptake curves for the cast Nafion<sup>®</sup> N211 and N212 membranes at 25–80 °C from references [228, 238, 243, 244] are plotted in Figure A.1a along with their fit obtained in this work (eq. (3.10) and Table A.1) and the sorption isotherm for the extruded Nafion<sup>®</sup> N117 from references [168, 239] (also eq. (3.10) and Table A.1). The sorption isotherm fitted by Kosakian et al. [92, 289] for a variety of Nafion<sup>®</sup> membranes (mostly extruded),

$$\lambda_{\text{eq}} = \left( 18.37a_w - 37.46a_w^2 + 31.70a_w^3 \right) \cdot \exp \left[ -66.28 \left( \frac{1}{T} - \frac{1}{303.15} \right) \right], \quad (\text{A.3})$$

is shown in Figure A.1 for comparison. It can be seen from the figure that the water uptake by cast Nafion<sup>®</sup> membranes (N211, N212) is similar to that by extruded membranes (N117).

Water-uptake data for alkaline membranes are more scarce as compared with the Nafion<sup>®</sup> materials. Since Aemion<sup>®</sup> membranes are based on hexamethyl-*p*-terphenyl poly(methylbenzimidazolium) (HMT-PMBI) [290–293], water uptake by HMT-PMBI reported in references [245–247] was used to approximate that for Aemion<sup>®</sup> AH1-HNN8-50-X. The only data for HMT-PMBI in bicarbonate ( $\text{HCO}_3^-$ ) form were found in the work of Ziv et al. [247], where the uptake was reported for the RH of and above 50%. Since the minimum RH used in this work was 10%, sorption data at a wider range of water activity was required. Water uptake for the entire range of RH was reported by Novitski et al. [245] and Zheng et al. [246], but for HMT-PMBI in the hydroxide ( $\text{OH}^-$ ) form. The data reported by Ziv et al. [247] indicate that the

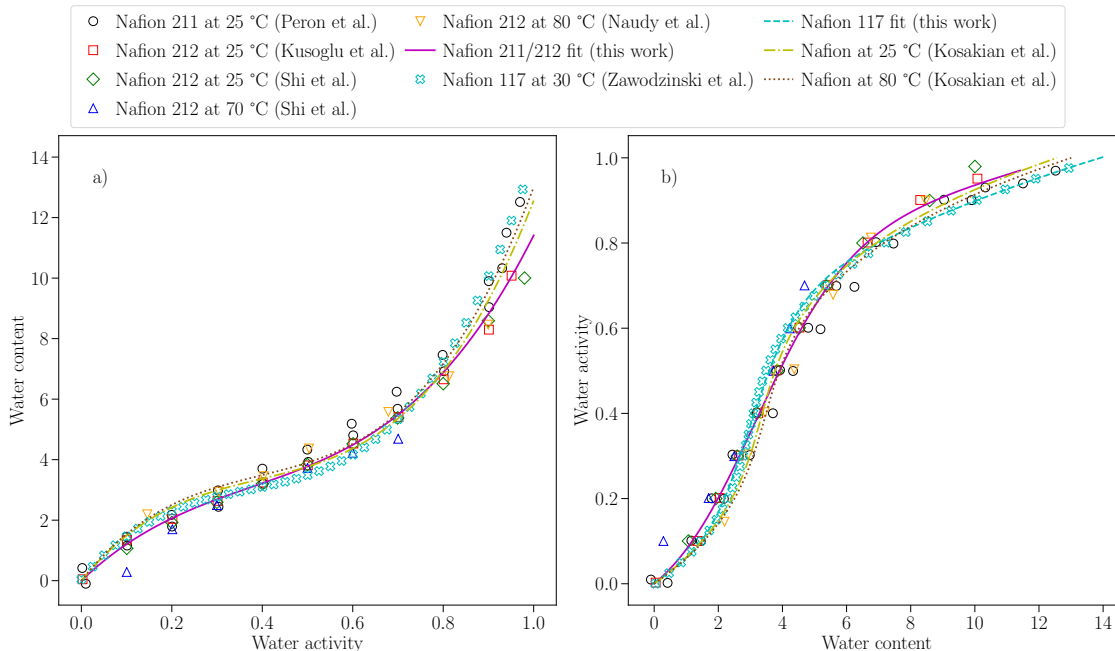


Figure A.1: Water-uptake curves for the cast Nafion<sup>®</sup> N211 and N212 membranes at 25–80 °C from references [228, 238, 243, 244] and their fit obtained in this work: a) the sorption isotherm (eq. (3.10) and Table A.1) and b) the inverse sorption isotherm (eq. (A.8) and Table A.2). Sorption isotherms for Nafion<sup>®</sup> N117 (eq. (3.10) and Table A.1) and a variety of Nafion membranes (eq. (A.3)) are also shown for comparison.

uptake by HMT-PMBI membranes in the bicarbonate form is approximately 8–13% higher than in the hydroxide form at 50–90% RH, and the difference is smaller at lower RH. In the absence of a complete data set for HMT-PMBI in the  $\text{HCO}_3^-$  form, water uptake in the  $\text{OH}^-$  form at 40–60 °C from references [245, 246] was used as an estimate. The data were fitted following the procedure discussed above for Nafion<sup>®</sup>, and the sorption isotherm obtained with  $R^2$  of at least 0.998 is provided in eq. (3.10) and Table A.1.

Ziv et al. [247] also reported water uptake by HMT-PMBI in the  $\text{OH}^-$  form at 50–90% RH. Fitting all three data sets [245–247] resulted in no significant change in the sorption isotherm in the entire range of RH as shown in Figure A.2a (the coefficient of determination for the original fit with respect to the data from Ziv et al. was reasonably high at 0.943). Fitting the inverted isotherm to compute water

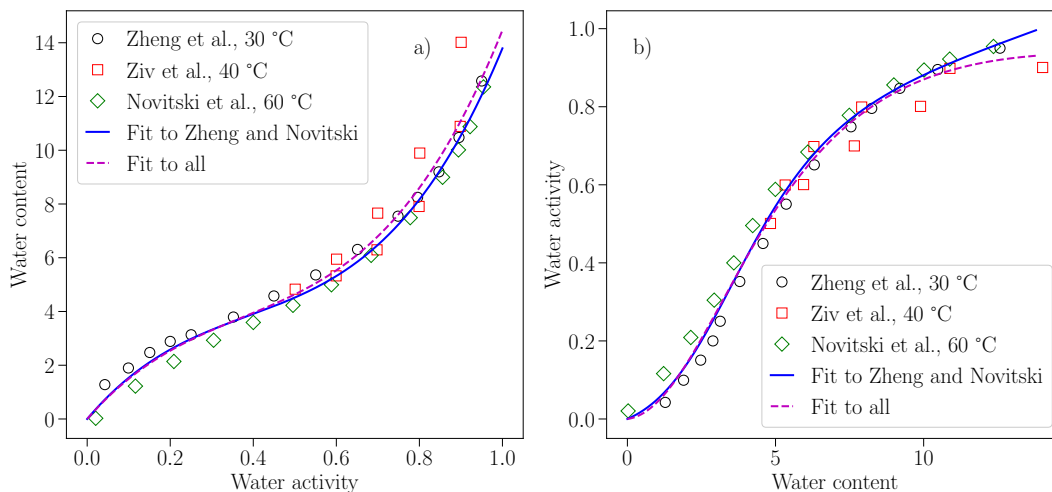


Figure A.2: Water-uptake curves for Aemion<sup>®</sup> AH1-HNN8-50-X (HMT-PMBI) membranes at 30–60 °C from references [245–247] and their fits obtained in this work: a) the sorption isotherm (eq. (3.10) and Table A.1) and b) the inverse sorption isotherm (eq. (A.8) and Table A.2).

diffusivity (see Section 3.2.3) also resulted in a water-activity curve that was nearly identical to the fit to only two data sets [245, 246] up to the water content of about 10 mol<sub>H<sub>2</sub>O</sub>/mol<sub>N<sup>+</sup></sub> (90% RH), as seen in Figure A.2b. However, the water-activity curve did not tend to unity at high water content, i.e., did not cover the entire range of RH, when the data from Ziv et al. [247] were included. For that reason, only the sorption isotherm obtained by fitting the data from Novitski et al. [245] and Zheng et al. [246] is reported in this work.

The experimentally measured water uptake by Fumapem<sup>®</sup> FAA-3 membranes in bicarbonate form at 25 and 40 °C from references [231, 247] was fitted with eq. (3.10) to give the polynomial coefficients in Table A.1 with  $R^2$  of 0.9773 and 0.9994. The resulting isotherm is plotted in Figure A.3a along with the original data [231, 247].

Only one reference for the water uptake by PiperION<sup>®</sup> membranes was found [231]. The sorption isotherm was measured for PAP-TP-85 [231] and was assumed in this work to be representative of Versogen<sup>™</sup> PiperION-A40. Fitting of the data (measured at 25 °C) with eq. (3.10) yielded the coefficients in Table A.1 with  $R^2$  of 0.9996. The experimental data and the plot of the fitted isotherm are shown in Figure A.4a.

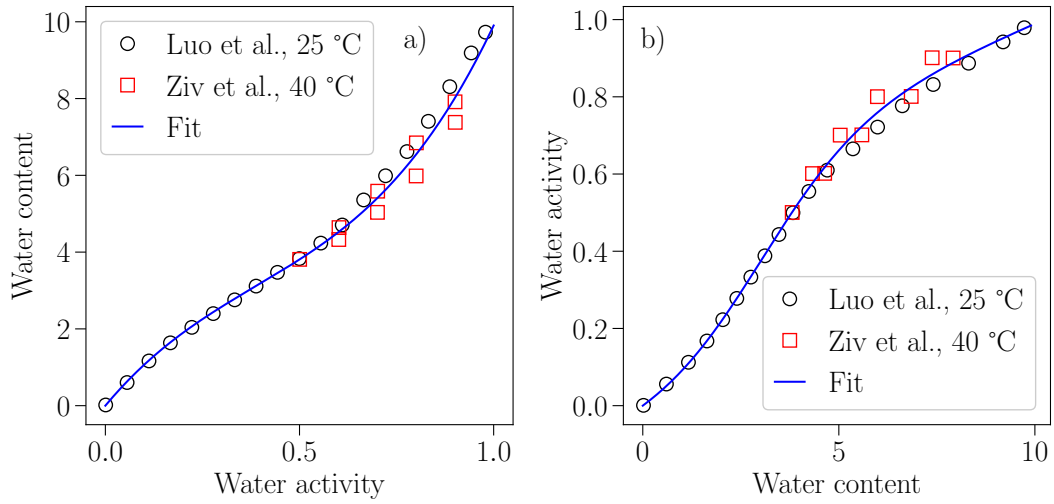


Figure A.3: Water-uptake curves for Fumapem<sup>®</sup> FAA3 membranes at 25 and 40 °C from references [231, 247] and their fit obtained in this work: a) the sorption isotherm (eq. (3.10) and Table A.1) and b) the inverse sorption isotherm (eq. (A.8) and Table A.2).

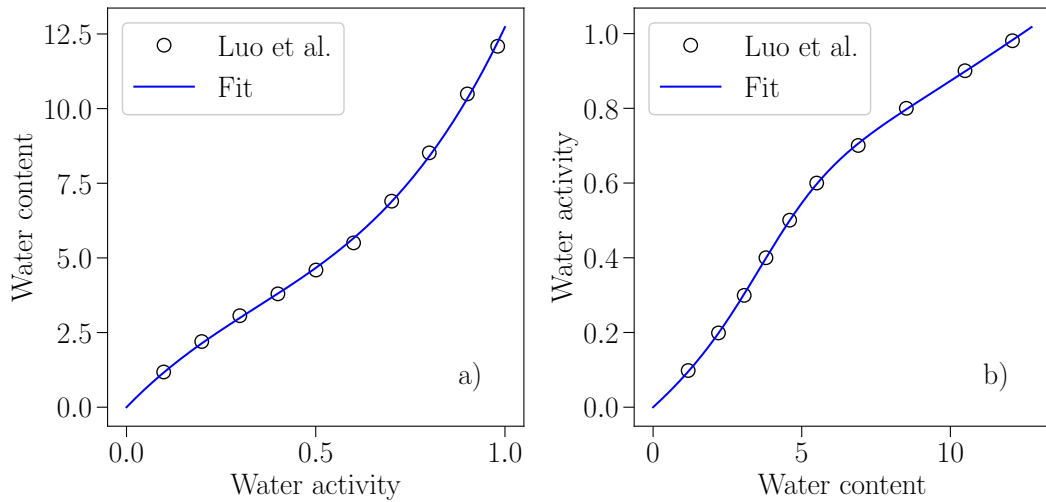


Figure A.4: Water-uptake curves for PiperION<sup>®</sup> PAP-TP-85 from reference [231] and its fit obtained in this work: a) the sorption isotherm (eq. (3.10) and Table A.1) and b) the inverse sorption isotherm (eq. (A.8) and Table A.2).

### A.1.2 Darken factor

In order to find an expression for water diffusivity in the polymer electrolyte, the flux of water due to the water-content gradient is equated in this work to the water flux due to the chemical-potential gradient [190, 239]:

$$\mathbf{N}_\lambda = \mathbf{N}_\mu = -D_\mu \frac{c_{\text{wv}}}{RT} \nabla \mu. \quad (\text{A.4})$$

Noting that concentration of water is related to the water content through

$$c_{\text{wv}} = \frac{\rho_{\text{m,dry}} \lambda}{EW},$$

using the definition of the chemical potential  $\mu = RT \ln a_w$  [239], and assuming isothermal conditions,

$$-D_\mu \frac{c_{\text{wv}}}{RT} \nabla \mu = -D_\mu \frac{\rho_{\text{m,dry}}}{EW} \lambda \nabla \ln a_w.$$

Application of the chain rule to the gradient in the equation above results in

$$\mathbf{N}_\mu = -D_\mu \frac{\rho_{\text{m,dry}}}{EW} \frac{\partial \ln a_w}{\partial \ln \lambda} \nabla \lambda. \quad (\text{A.5})$$

Since

$$\mathbf{N}_\lambda = -D_\lambda \frac{\rho_{\text{m,dry}}}{EW} \nabla \lambda, \quad (\text{A.6})$$

equating the water fluxes (A.4) gives

$$D_\lambda = \frac{\partial \ln a_w}{\partial \ln \lambda} D_\mu, \quad (\text{A.7})$$

a result often found in the fuel-cell literature [133, 168, 189, 190, 239].

One way to compute the Darken factor (eq. (3.12)) is to find the derivative  $\partial \lambda / \partial a_w$  from the sorption isotherm and then substitute it into

$$\mathcal{D} = \frac{\partial \ln a_w}{\partial \ln \lambda} = \left( \frac{a_w}{\lambda} \frac{\partial \lambda}{\partial a_w} \right)^{-1}.$$

This, however, results in a large expression that is a function of water activity, while, for modeling purposes, the Darken factor should be related to the water content. A

common approach to overcoming this issue is to differentiate the sorption isotherm  $\lambda_{\text{eq}}(a_w, T)$  plotted in the logarithmic scale and then to fit the resulting curve with an empirical relationship. The plateau at the intermediate water activity seen in Figures A.1a, A.3a, and A.4a results in a peak in the Darken factor, and the expressions for water diffusivity found through this method are separated into two parts, for low and high water contents [133, 189]. Apart from the inconvenience of having two diffusivity expressions instead of one, this approach also relies on two curve-fitting procedures, one for water uptake and one for diffusivity, each of which contributes to the overall numerical error in the final relationships.

As discussed in the main text, a different approach to computing the Darken factor was taken in this work that is free of the shortcomings of the aforementioned methods. The uptake data from references [228, 231, 238, 239, 243, 244, 247] were inverted, fitted, and the Darken factor was computed analytically. This approach results in a single relationship  $D_\lambda(\lambda, T)$  for the entire range of water content (or RH) that contains a numerical error associated with only one curve-fitting procedure.

The general expression used for fitting the inverted water-uptake curves was

$$a_w = \frac{\beta_1\lambda + \beta_2\lambda^2 + \beta_3\lambda^3}{\gamma_0 + \gamma_1\lambda + \gamma_2\lambda^2 + \gamma_3\lambda^3}. \quad (\text{A.8})$$

The fitted polynomial coefficients are listed in Table A.2. They were obtained with the  $R^2$  of at least 0.99998, 0.993, 0.999, 0.981, and 0.99996 for Nafion<sup>®</sup> N117, Nafion<sup>®</sup> N211, Aemion<sup>®</sup> AH1-HNN8-50-X, Fumapem<sup>®</sup> FAA-3-50, and Versogen<sup>™</sup> PiperION-A40, respectively. The inverted isotherms are shown in Figures A.1b, A.2b, A.3b, and A.4b alongside the original data. The analytically computed Darken factors are given in eq. (3.13) and Table A.3 and are plotted in Figure A.5.

The peak in the Darken factor at the water content of about 2–3 mol<sub>H<sub>2</sub>O</sub>/mol<sub>ion</sub> is due to the plateau in the sorption isotherms at the intermediate water activity (Figure 3.2). The Darken factors shown in Figure A.5 are extended beyond the maximum water content in vapor-equilibrated membranes at unit water activity found from the

Table A.2: Coefficients of the inverted water-uptake curve (A.8).

Membrane	$\beta_1$	$\beta_2$	$\beta_3$	$\gamma_0$	$\gamma_1$	$\gamma_2$	$\gamma_3$
Nafion <sup>®</sup> N11X	0.532	-0.245	0.0826	8.93	-3.41	0.488	0.0469
Nafion <sup>®</sup> N21X	1.77	0.121	0.0317	28.3	-5.32	0.907	0
Aemion <sup>®</sup> AH1-HNN8-50-X	1.32	0.341	0.0429	40.2	-7.25	1.35	0
Fumapem <sup>®</sup> FAA-3	2.37	-0.0662	0.0642	31.5	-6.63	1.17	0
Versogen <sup>™</sup> PiperION-A40	2.01	-0.371	0.0575	27.6	-7.08	0.897	0

sorption isotherms (eq. (3.10) and Table A.1) to the liquid-equilibrated water content from Table 3.1. In that region, the Darken factors are quasi-linear, in agreement with the results of Motupally et al. [189] and Ge et al. [133]. As in references [133, 189], it was assumed in this work that the derived Darken factors and thus diffusion coefficients of water were valid between the vapor-equilibrated and liquid-equilibrated water contents.

## A.2 Results and discussion

### A.2.1 Fitting

The experimentally measured crossover flux for each membrane and the corresponding fitted values are shown in Figures A.6 and A.7 for the example of model 2 (desorption). The coefficient of determination,  $R^2$ , was 0.900–0.983. It was higher, 0.972–0.994, when computed for the outlet vapor pressure (which was not fitted), as the measured data were not influenced by the inlet uncertainty. The measured and calculated outlet vapor pressure is illustrated in Figures A.8 and A.9.

Distributions of the fitting residual (3.15) around the fitted scaling factors  $\beta_D$ ,  $\beta_E$ , and  $\beta_d$  obtained with model 3 (diffusion and desorption; see Tables 3.3 and 3.4) are shown in Figures A.10 and A.11.

Diffusion coefficients of water in Nafion<sup>®</sup> fitted with model 3 (diffusion and desorption) are shown in Figure A.13. The obtained water diffusivity in Nafion<sup>®</sup> is higher

Table A.3: Coefficients of the Darken factor eq. (3.13). For all membranes,  $\delta_0 = \varepsilon_0 = 1$ .

Membrane	$\delta_1$	$\delta_2$	$\delta_3$	$\delta_4$	$\varepsilon_1$	$\varepsilon_2$	$\varepsilon_3$	$\varepsilon_4$	$\varepsilon_5$
Nafion <sup>®</sup> N11X	-0.9211	0.5870	-0.1291	0.01090	-0.8424	0.3858	-0.07920	$6.066 \cdot 10^{-3}$	$8.154 \cdot 10^{-4}$
Nafion <sup>®</sup> N21X	0.1367	0.008828	$-6.734 \cdot 10^{-3}$	$5.740 \cdot 10^{-4}$	-0.1196	0.03711	$-1.176 \cdot 10^{-3}$	$5.740 \cdot 10^{-4}$	0
Aemion <sup>®</sup> AH1-HNN8-50-X	0.5167	0.01733	-0.01172	$1.091 \cdot 10^{-3}$	0.07799	0.01949	$2.814 \cdot 10^{-3}$	$1.091 \cdot 10^{-3}$	0
Fumapem <sup>®</sup> FAA-3	-0.05586	0.05000	-0.01140	$1.006 \cdot 10^{-3}$	-0.2384	0.07011	-0.006739	$1.006 \cdot 10^{-3}$	0
Versogen <sup>™</sup> PiperION-A40	-0.3692	0.1007	-0.01468	$9.297 \cdot 10^{-4}$	-0.4411	0.1085	-0.01334	$9.297 \cdot 10^{-4}$	0

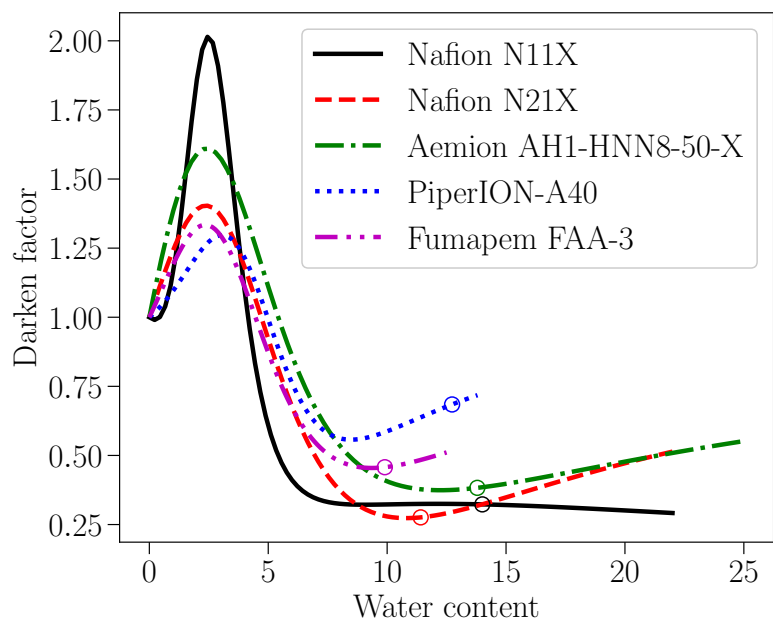


Figure A.5: Comparison of the Darken factors for Nafion<sup>®</sup> N11X, Nafion<sup>®</sup> N21X, Aemion<sup>®</sup> AH1-HNN8-50-X, Fumapem<sup>®</sup> FAA-3, and Versogen<sup>™</sup> PiperION-A40 membranes (eq. (3.13) and Table A.3). Markers correspond to the maximum water content in vapor-equilibrated membranes at unit water activity found from the sorption isotherms (eq. (3.10) and Table A.1).

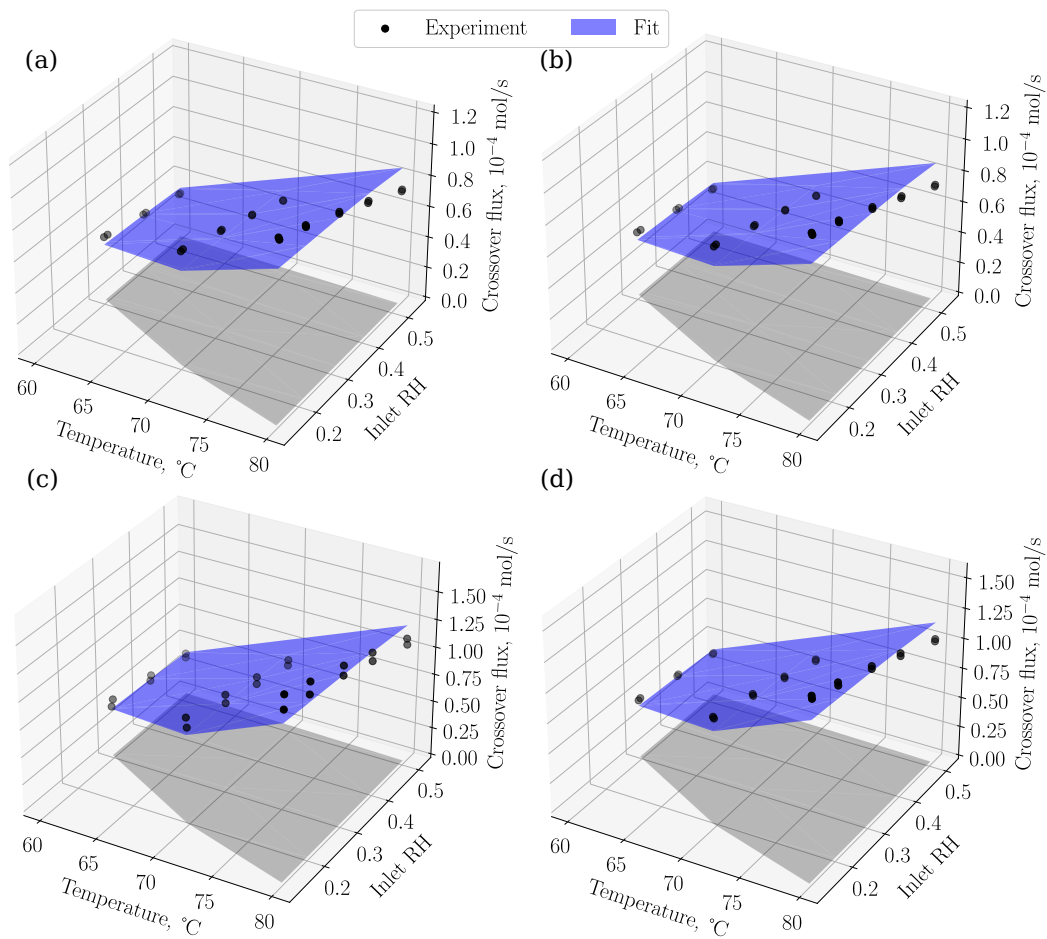


Figure A.6: Results of fitting the experimental crossover flux with model 2 (desorption only; see Table 3.3) for Nafion<sup>®</sup>: a) N115; b) N117; c) N211; and d) N212. The shadow is added to guide the eye through the experimental conditions.

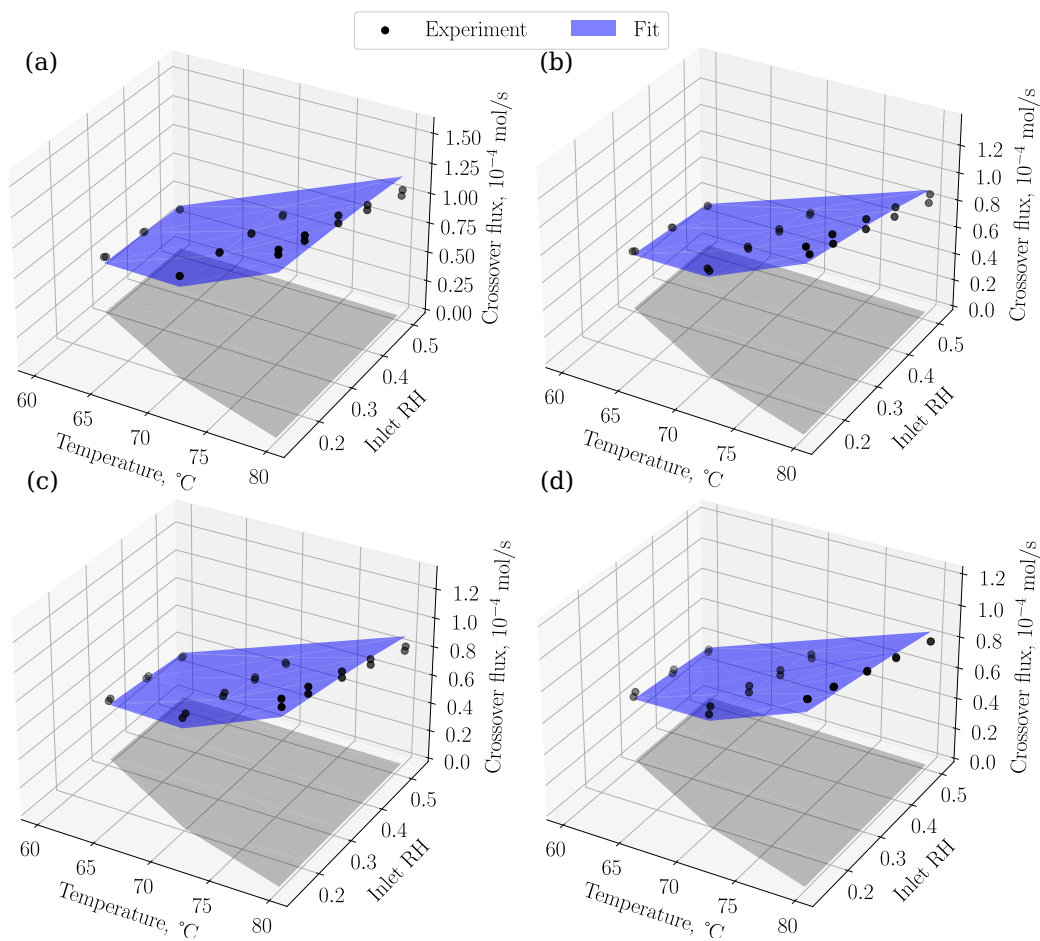


Figure A.7: Results of fitting the experimental crossover flux with model 2 (desorption only; see Table 3.4) for: a) Aemion<sup>®</sup> AH1-HNN8-50-X; b) Versogen<sup>™</sup> PiperION-A40; c) Fumapem<sup>®</sup> FAA-3-30; and d) Fumapem<sup>®</sup> FAA-3-50. The shadow is added to guide the eye through the experimental conditions.

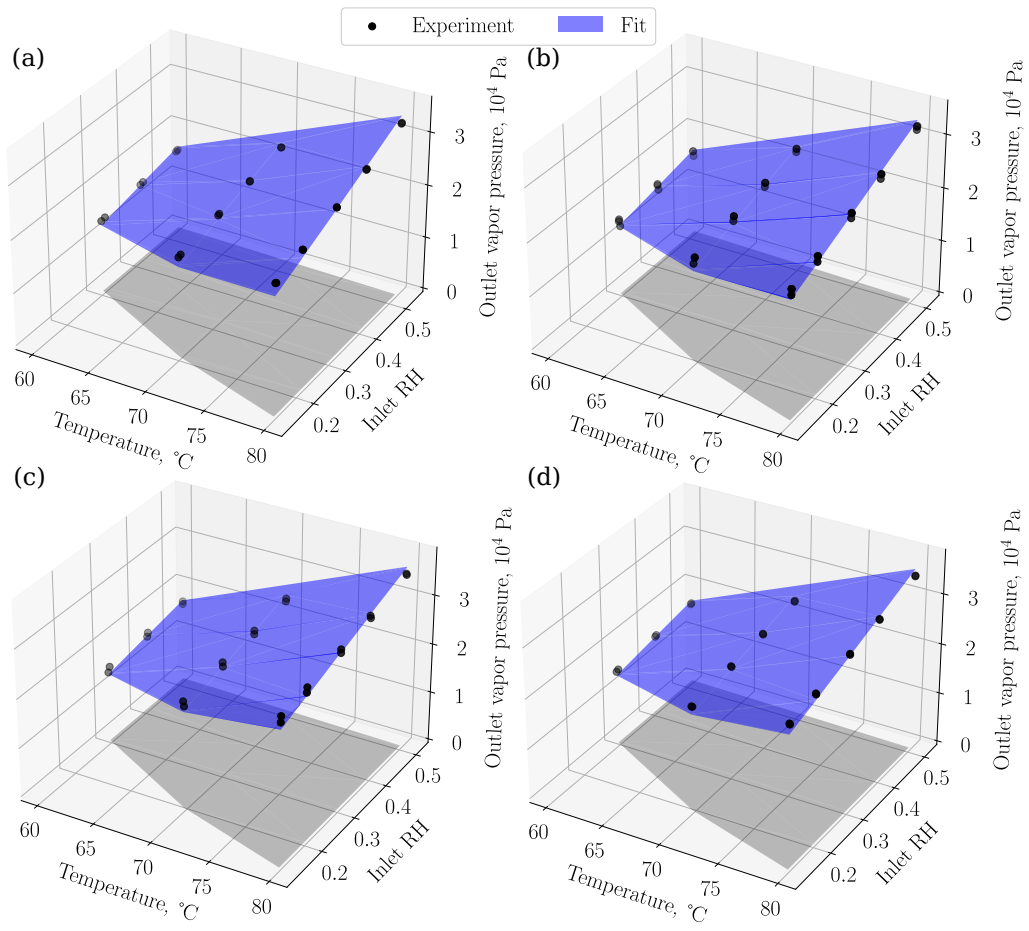


Figure A.8: Comparison of the measured and simulated outlet vapor pressure in the dry channel for the fitting results in Table 3.3 and Figure A.6 obtained with model 2 (desorption only) for Nafion<sup>®</sup>: a) N115; b) N117; c) N211; and d) N212. The shadow is added to guide the eye through the experimental conditions.

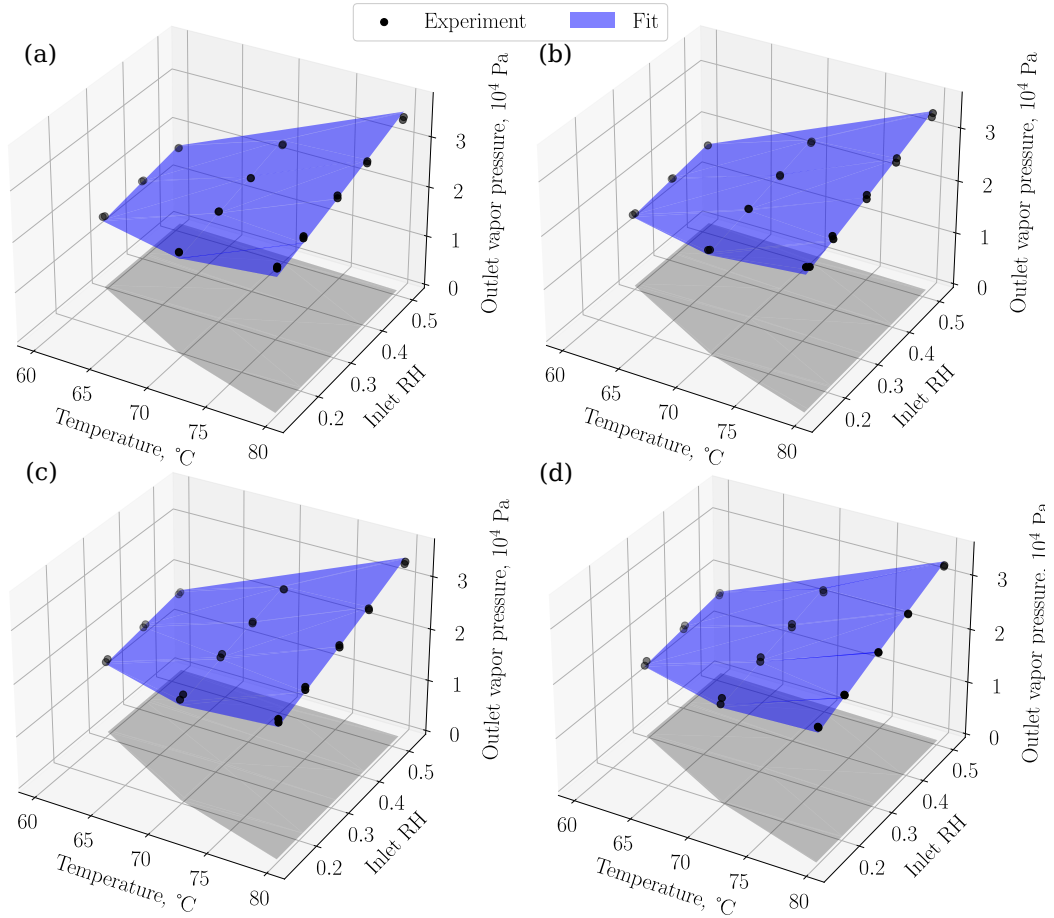


Figure A.9: Comparison of the measured and simulated outlet vapor pressure in the dry channel for the fitting results in Table 3.4 and Figure A.7 obtained with model 2 (desorption only) for: a) Aemion<sup>®</sup> AH1-HNN8-50-X; b) Versogen<sup>™</sup> PiperION-A40; c) Fumapem<sup>®</sup> FAA-3-30; and d) Fumapem<sup>®</sup> FAA-3-50. The shadow is added to guide the eye through the experimental conditions.

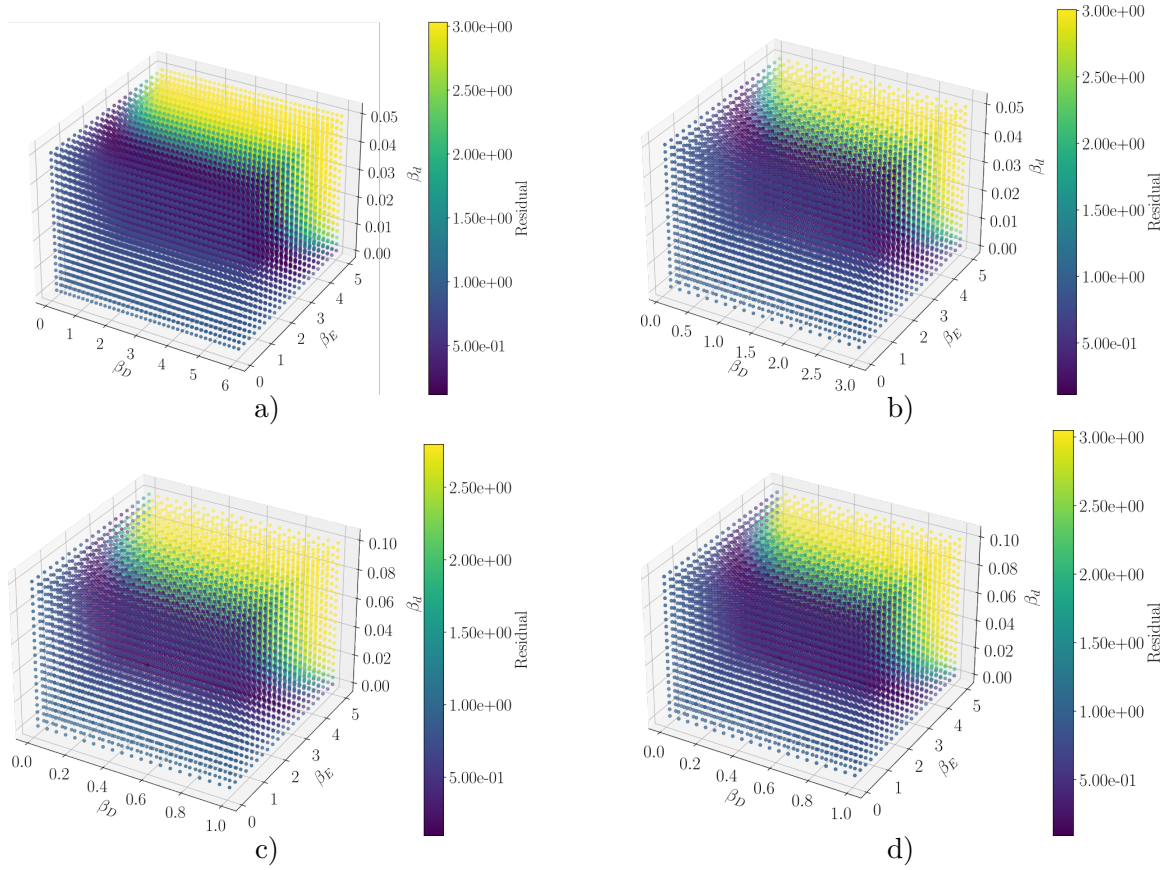


Figure A.10: Residual distributions around the fitted scaling factors in Tables 3.3 and 3.4 for Nafion<sup>®</sup>: a) N115; b) N117; c) N211; and d) N212.

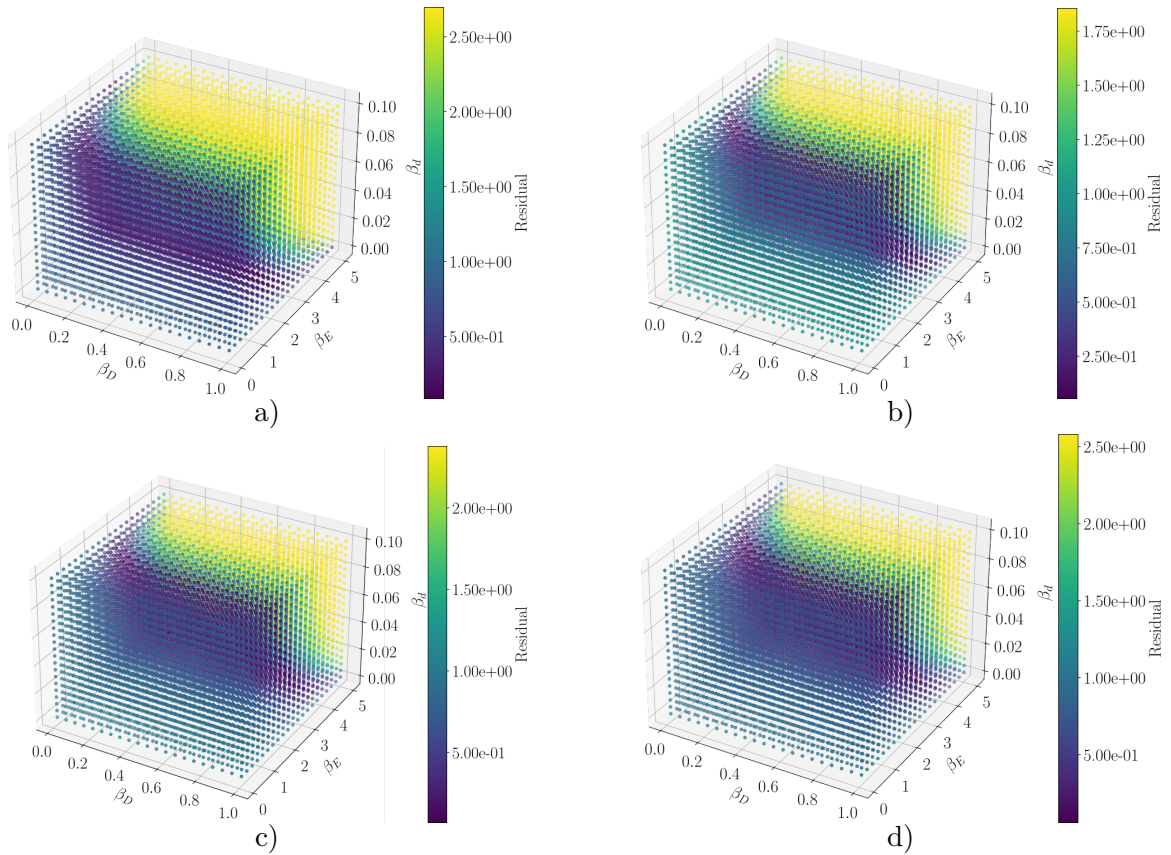


Figure A.11: Residual distributions around the fitted scaling factors in Tables 3.3 and 3.4 for: a) Aemion<sup>®</sup> AH1-HNN8-50-X; b) Versogen<sup>™</sup> PiperION-A40; c) Fumapem<sup>®</sup> FAA-3-30; and d) Fumapem<sup>®</sup> FAA-3-50.

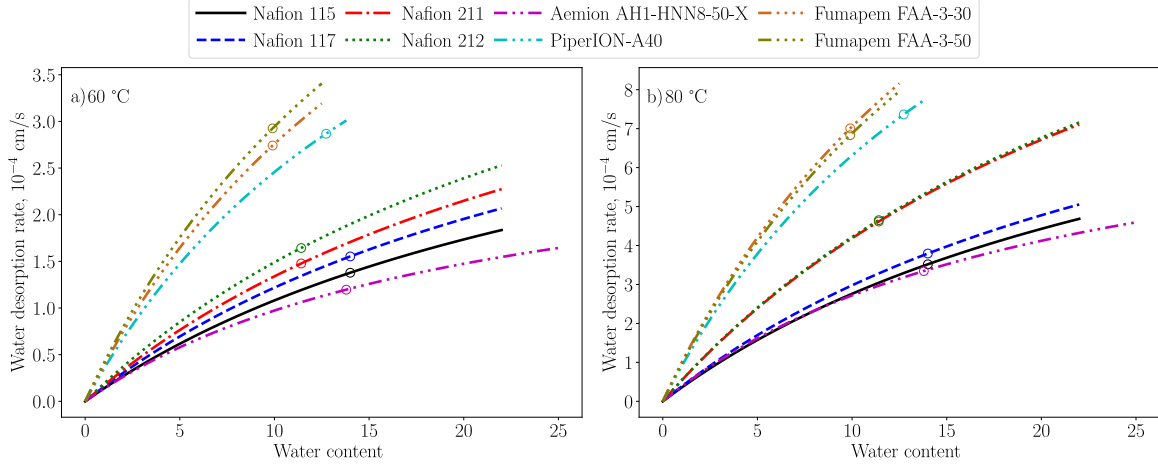


Figure A.12: Comparison of the fitted water-desorption rates for Nafion<sup>®</sup> N117, N211, N212, Aemion<sup>®</sup> AH1-HNN8-50-X, Fumapem<sup>®</sup> FAA-3-50, and Versogen<sup>™</sup> PiperION-A40 at a) 60 °C and b) 80 °C. The results were obtained with model 3 (diffusion and desorption). Markers indicate the vapor-equilibrated water content at 100% RH from Figure 3.2. Each graph is plotted up to the liquid-equilibrated water content from Table 3.1.

than reported in the literature [43, 133, 189, 239, 252, 253], especially at the elevated temperature. As discussed in the main text, this is because of the low sensitivity of the overall transport across membranes equilibrated with liquid water on one side to the bulk transport, which makes the determination of water diffusivity using liquid-vapor permeation setups challenging and potentially inaccurate. The desorption rate of water and its activation energy can still be estimated.

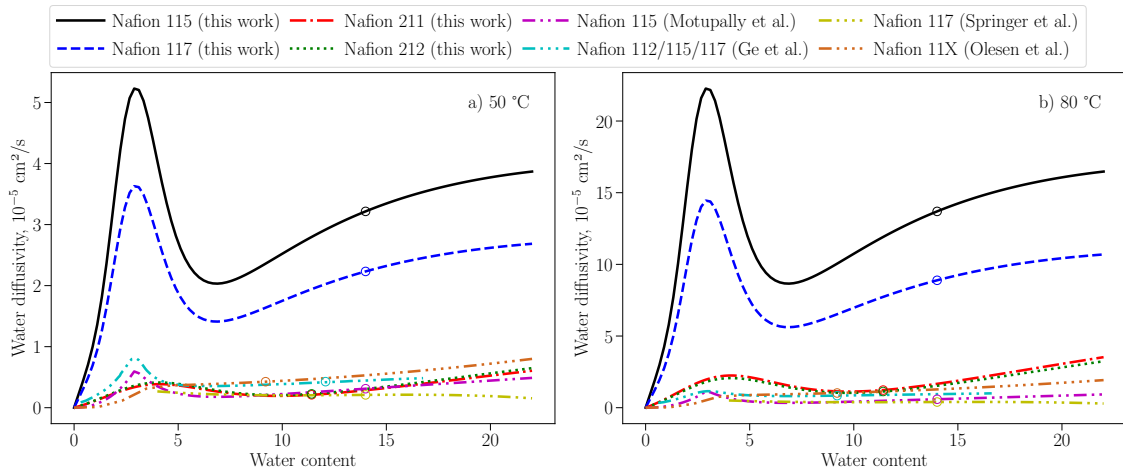


Figure A.13: Comparison of the water diffusivities fitted for Nafion<sup>®</sup> N117, N211, and N212 with the literature data at a) 50 °C and b) 80 °C. The results were obtained with model 3 (diffusion and desorption). Markers indicate the vapor-equilibrated water content at 100% RH from Figure 3.2. Each graph is plotted up to the liquid-equilibrated water content from Table 3.1. The literature data are from Refs. [133, 189, 239, 252, 253].